Ex libris
universitatis
albertaensis

QUAECUMQUE VERA

Digitized by the Internet Archive
in 2019 with funding from
University of Alberta Libraries

https://archive.org/details/Kolber1993

University of Alberta

Release Form

Name of Author:	Terrence Kolber
Title of Thesis:	Nonlinear evolution of scattering instabilities in laser produced plasmas.
Degree:	Doctor of Philosophy
Year This Degree Granted:	1993

Permission is hereby granted to the University of Alberta to reproduce single copies of this thesis and to lend or sell such copies for private, scholarly or scientific research purposes only.

The author reserves all other publication and other rights in association with the copyright in the thesis, and except as hereinbefore provided neither the thesis nor any substantial proportion thereof may be printed or otherwise reproduced in any material form whatever without the author's written permission.

University of Alberta

Nonlinear evolution of scattering instabilities in laser produced plasmas.

By

Terrence Kolber ©

A thesis submitted to the Faculty of Graduate Studies and Research in partial fulfillment of the requirements for the degree of Doctor of Philosophy in Theoretical Physics.

Department of Physics

Edmonton Alberta

Fall 1993

UNIVERSITY OF ALBERTA

FACULTY OF GRADUATE STUDIES AND RESEARCH

The undersigned certify that they have read, and recommend to the Faculty of Graduate Studies and Research for acceptance, a thesis entitled "Nonlinear evolution of scattering instabilities in laser produced plasmas." submitted by Terrence Kolber in partial fulfillment of the requirements for the degree of Doctor of Philosophy in Physics.

Abstract

Nonlinear theory of scattering processes during interaction of intense electromagnetic radiation with plasmas is studied. Our studies have concentrated on two instabilities: stimulated Raman (SRS) and Brillouin (SBS) scattering. A theoretical model based on the Zakharov-Maxwell equations is used to describe the evolution of SRS and SBS. The model includes nonlinear processes related to the coupling between Langmuir and ion waves. Numerical results obtained in a homogenous finite plasma have shown that the primary mechanism responsible for saturation of SRS in our theory is the parametric decay instability (PDI) of the resonantly driven Langmuir wave. The different spatial and temporal evolution of SRS and PDI leads to new physics in SRS nonlinear evolution, including disruption of the PDI cascade, localization of Langmuir fields, and burst like behavior of SRS reflectivity.

The nonlinear evolution of the Langmuir and ion acoustic waves provides a mechanism which broadens and enhances the Langmuir and ion acoustic wave spectra. These enhanced fluctuation levels contribute to secondary scattering processes such as enhanced Brillouin, forward Raman, and anti-Stokes forward and backward Raman scattering. Asymptotic saturation levels of stimulated Raman scattering are well approximated by a simple scaling law. This scaling predicts a proportionality of the Langmuir wave amplitude to the PDI threshold with dependence on the intensity and plasma interaction length. Scaling laws for the secondary scattering processes as well as criteria for their strong enhancement are given. The frequency spectra of enhanced Brillouin scattering shows Stokes and anti-Stokes components, where their relative intensities depend on the plasma density. Superthermal electron production is also studied in the asymptotic regime, providing limitations on

the interaction length and laser intensity in our model. Our theoretical results are consistent with many experimental observations providing new or alternate explanations for observed results.

Acknowledgements

I wish to thank my supervisor Wojciech Rozmus for his overwhelming enthusiasm during this project. His guidance, support and the occasional ’You must work hard ...’ enabled me to grow both as a scientist and as an individual. ’Obviously’ I would also like to thank Vladimir Tikhonchuk, whose patient explanations made even the most difficult subject understandable. The final form of this thesis has been greatly improved due to the many suggestions made by the external examiner. I would thus like to thank Tudor Johnston.

Many thanks must also go to John Samson and the Canadian Network for Space Research for providing the computers used for our simulations. I gratefully acknowledge Jeff Candy for the collaborative effort which led to the development of the numerical solver program of Appendix .2. My friendship with Jeff has led to many interesting conversations, both academic and otherwise, which made my graduate years much more enjoyable.

For their love and encouragement I wish to thank my parents. Their support over the years have made it possible for me to follow this chosen path. Finally special thanks are due Sandra Crawford for tolerating the long hours and late nights. Her love and friendship has brought me much joy and has helped me through this time in my life.

Table of Contents

page

Chapter 1. Introduction 1

Chapter 2. Basic concepts 24

Section 2.1 Derivation of basic equations 24

2.1.1 Equations describing electromagnetic field evolution 25

2.1.2 Hydrodynamic and electrostatic field equations 27

Section 2.2 Three wave interaction 41

2.2.1 Standard equations for three wave coupling 44

2.2.2 Absolute and convective instabilities 46

2.2.3 Finite interaction length 48

2.2.4 Intermediate asymptotic dependence of growth rate on length .. 50

Chapter 3. Analysis of stimulated Raman scattering evolution 54

Section 3.1 Typical evolution of the backward Raman scattering simulations 58

Section 3.2 Linear growth 60

Section 3.3 First saturation of stimulated Raman scattering by parametric decay instability 65

Section 3.4 Intermediate nonlinear regime 73

Section 3.5 Final asymptotic saturation 83

Section 3.6 Derivation of coherent and random phase reflectivity 91

Chapter 4. Laser light scattering from fluctuations enhanced by stimulated Raman scattering 97

Section 4.1 Enhancement of Brillouin and forward Raman 102

4.1.1 The frequency and wave number spectra of scattered radiation 115

Section 4.2 Anti-Stokes forward and backward Raman scattering 120

Chapter 5. Superthermal electron generation 130

Chapter 6. Correspondence between theory and experiments 138

Chapter 7. Summary and conclusions 157

Bibliography 164

Appendix .1 Thermal noise levels 173

Appendix .2 Partial/ordinary differential solver algorithm 179

Section .2.1 System of equations 175

Section .2.2 Inversion algorithm 179

Section .2.3 Derivative differencing 182

List of Tables

page

Table 2.1 Wave numbers associated with the three wave processes of Raman and Brillouin scattering as well as the Stokes coupling of PDI. 39

Table 2.2 Group velocities for the various linear wave modes and growth rates and thresholds for SRS, SBS, and PDI. 53

Table 3.1 Parameters used in simulations for equations (3.1)-(3.4). The symbols themselves are used in Figs. 3.18 and 3.19 58

Table 4.1 Parameters used in simulations of equations (2.57)-(2.61). The symbols are used in Figs. (4.5), (4.6) and (4.7) 98

List of Figures

page

Figure 1.1 Schematic diagram of the linear wave modes 3

Figure 1.2 Schematic diagram of possible three wave interactions 7

Figure 1.3 Schematic diagram of interaction processes in ICF 9

Figure 1.4 The linear instabilities described by the Zakharov equations 16

Figure 1.5 Schematic diagram of PDI cascade process 17

Figure 2.1 Schematic diagram of Stokes and anti-Stokes coupling of (a) SRS and (b) SBS 35

Figure 2.2 Schematic diagram of the SRS feedback mechanism 43

Figure 2.3 Deformation of the Fourier contour (a) and associated lowering of the Laplace contour (b) 47

Figure 3.1 SRS reflectivity as a function of time 59

Figure 3.2 Bursts of SRS reflectivity 60

Figure 3.3 Simulation results for the temporal evolution of SRS reflectivity 62

Figure 3.4 Examples of time evolution of the Fourier component at $k = k_L$ of the Langmuir field $E(x,t)$ 64

Figure 3.5 (a) SRS reflectivity time history and (b) Maximum of the electric field as a function of time. 65

Figure 3.6 Results from the numerical integration of equations (3.1)-(3.4) at $t = 12.12$ ps of Fig. 3.5 67

Figure 3.7 Comparison between the results obtained from the five-wave model equations (2.70), (2.72), and (3.8)-(3.10) (dashed curve) and from the full model equations (3.1)-(3.4) (dotted curve) 69

Figure 3.8 Results from the numerical integration of equations (3.1)-(3.4) for $t = 18.64$ ps of Fig. 3.5 71

Figure 3.9 Results from the numerical integration of equations (3.1)-(3.4) for $t = 19.82$ ps of Fig. 3.5 73

Figure 3.10 Results from the numerical integration of equations (3.1)-(3.4) for $t = 20.6$ ps of Fig. 3.5 75

Figure 3.11 Results from the numerical integration of equations (3.1)-(3.4) for $t = 23.54$ ps of Fig. 3.5 76

Figure 3.12 Time evolution of the Fourier component at $k = k_L$ of the Langmuir field $E(x, t)$ and density 79

Figure 3.13 Time evolution of the Fourier component at $k = k_L$ of the Langmuir field $E(x, t)$ and density 80

Figure 3.14 SRS reflectivity as a function of time 81

Figure 3.15 (a) SRS reflectivity time history and (b) Fourier components at k_L of the Langmuir field. 82

Figure 3.16 Results from the numerical integration of equations (3.1)-(3.4) for $t = 58.86$ ps of Fig. 3.5 85

Figure 3.17 Results from the numerical integration of equations (3.1)-(3.4) for $t = 34.3$ ps 86

Figure 3.18 SRS reflectivities plotted as a function of scaling formula 88

Figure 3.19 Time integral averaged asymptotic values of the Fourier transformed Langmuir field at $k = k_L$ plotted as a function of scaling formula 89

Figure 4.1 Reflectivity as a function of time: (a) SRS, (b) Brillouin, (c) forward Raman, (d) anti-Stokes backwards Raman, and (e) anti-Stokes forward Raman 99

Figure 4.2 (a) Electrostatic and (b) density spectra 101

Figure 4.3 Brillouin (dotted curves) and forward Raman (solid curves) reflectivities as a function of time 103

Figure 4.4 Electrostatic and density spectra obtained from numerical solutions of equations (2.57)-(2.61) at $t = 94.9$ps 107

Figure 4.5 Brillouin reflectivities plotted as a function of scaling formula .. 108

Figure 4.6 Forward Raman scattering reflectivities plotted as a function of scaling formula 109

Figure 4.7 SRS reflectivities plotted as a function of scaling formula 110

Figure 4.8 Parameter regime limits of our simulations $\Delta_B/\frac{2}{3}A = 1$ (dotted curves), $\Delta_{FR}/\frac{2}{3}A = 1$ (dashed curves), and $\Delta_{ub} = 1$ 116

Figure 4.9 Brillouin reflectivity frequency spectra obtained from numerical solutions of equations (2.57)-(2.61) 117

Figure 4.10 Brillouin reflectivity frequency and wave number spectra obtained from numerical solutions of equations (2.57)-(2.61) 118

Figure 4.11 Electrostatic spectra 121

Figure 4.12 Anti-Stokes forward Raman reflectivities plotted as a function of scaling formula 125

Figure 4.13 Anti-Stokes backward Raman reflectivities plotted as a function of scaling formula 126

Figure 4.14 Anti-Stokes forward Raman reflectivities plotted as a function of scaling formula 127

Figure 4.15 Anti-Stokes backward Raman reflectivities plotted as a function of scaling formula 128

Figure 5.1 Electron distribution evolution 133

Figure 5.2 Hot electron density n_H and $n_H v_H^2/v_{T_e}^2$ as a function of (a) length

($I = 5 \cdot 10^{14}\, W/cm^2$) and (b) laser intensity ($L \simeq 55\, \mu m$) 135

Figure 5.3 Parameter regime limits of our simulations in terms of the increase in effective Landau damping due to hot electron generation 137

Figure 6.1 Electrostatic spectra 140

Figure 6.2 Experimentally observed Brillouin reflectivity together with enhanced Brillouin reflectivity curves 142

Figure 6.3 Time history of SRS (solid curve), enhanced Brillouin (dotted curve) and three wave Brillouin (dashed curve) reflectivity 143

Figure 6.4 SRS reflectivity and Brillouin reflectivity as functions of time .. 145

Figure 6.5 (a) normalized Fourier spectrum of density fluctuations at time t=53.29 ps (cf. Fig. 6.3(a)). (b) contour plot of the Brillouin backscattered spectral intensity normalized to pump intensity. 147

Figure 6.6 (a) normalized Fourier spectrum of density fluctuations at time t= 49.07 ps (cf. Fig. 6.3(b)). (b) contour plot of the Brillouin backscattered spectral intensity normalized to pump intensity. 148

Figure 6.7 Simulation versus theoretical reflectivity values for SRS, forward Stokes,) and anti-Stokes Raman scattering 150

Figure 6.8 SRS, Brillouin and ABR reflectivity as a function of time 152

Figure 6.9 SRS reflectivity expressions (3.27) solid line, and (6.4) dotted line, as a function of density, ... 155

Figure .1 Schematic diagram of numerical solver program. 182

Figure .2 Centered difference 186

Figure .3 Unsymmetric difference for points (a) n = 2 and (b) n = NP-1 .. 187

Figure .4 Unsymmetric difference for boundary points 188

List of Symbols and Abbreviations

FR	Forward Raman
TWI	Three wave interaction
SRS	Stimulated Raman scattering
SBS	Stimulated Brillouin scattering
PDI	Parametric decay instability
TPD	Two plasmon decay
IAD	Ion acoustic decay
MI	modulational instability
ICF	Inertial confinement fusion
subscript 0	Laser pump component
subscript $R^{\mp}$	Stokes/anti-Stokes Raman component
subscript $B^{\mp}$	Stokes/anti-Stokes Brillouin component
subscript L	Langmuir component
subscript A	Ion acoustic component
subscript x	Parallel ($\hat{e}_x$) component
subscript $\perp$	Perpendicular ($\hat{e}_y, \hat{e}_z$) component
e	Electron charge
Z	Atomic number
c	Speed of light
n_α	Electron $\alpha = e$, and ion $\alpha = i$ density
n_0^α	Background electron $\alpha = e$, and ion $\alpha = i$ density
δn_α	Fluctuation in electron $\alpha = e$, and ion $\alpha = i$ density
v_α	Mean velocity for electrons $\alpha = e$, and ions $\alpha = i$
T_α	Temperature of electrons $\alpha = e$, and ions $\alpha = i$

m_α	Mass of electrons $\alpha = e$, and ions $\alpha = i$
L	Interaction length of plasma
$\omega_j, \Omega_j,\ k_j$	Frequency and wave number of mode j
γ_j	Damping coefficient of mode j
$\gamma_L(k_L),\ \gamma_A(k_A)$	Electron and ion Landau damping coefficients
Γ	General growth rate
$\epsilon,\ \lambda$	Expansion parameters
$\epsilon(k, \omega)$	Longitudinal dielectric permittivity
χ	Linear plasma susceptibility
$\delta\omega,\ \delta k$	Frequency and wave number mismatch
$\mu = Zm_e/m_i$	Mass ratio
$\omega_p = \sqrt{4\pi e^2 n_0^e/m_e}$	Plasma frequency
$k_D = \sqrt{4\pi e^2 n_0^e/T_e}$	Debye wave number
$v_{T_\alpha} = \sqrt{T_\alpha/m_\alpha}$	Thermal velocity for electrons $\alpha = e$, and ions $\alpha = i$
$v_H = \sqrt{T_H/m_e}$	Thermal velocity for hot electrons
$c_s = \sqrt{(ZT_e + 3T_i)/m_i}$	Ion acoustic velocity
$V_j = c^2 k_j/\omega_j$	Electromagnetic group velocity of mode j
$V_L = 3v_{T_e}^2 k_L/\omega_L$	Langmuir wave group velocity
$n_c = \omega_0^2 m_e/4\pi e^2$	Critical density
$E_{thr} = \sqrt{\frac{64\pi n_0^e T_e \gamma_A(k_A)\gamma_L(k_L)}{\omega_L \omega_A}}$	PDI threshold
$A = \Gamma_{SRS}^2 L/\gamma_L(k_L) \mid V_R \mid$	SRS amplification coefficient
$Z(t)$	Amplitude of Mathieu equation
$\vec{E}$	Electric field
$\varepsilon^2 = \mid E_x \mid^2 /4\pi n_0^e T_e$	Ratio of electrostatic to kinetic energy of plasma
$\vec{B}$	Magnetic field

ϕ	Electrostatic potential
$\vec{A}$	Magnetic Vector potential
E_j	Electrostatic or electromagnetic field amplitude of mode j
$v_j = eE_j/m_e\omega_j$	Quiver velocity of mode j
Ψ_j	Time averaged electromagnetic field of mode j
E	Time averaged Langmuir field
$N = \delta n_i/n_0^i$	Slowly varying normalized density fluctuation
a_j	TWI amplitude of mode j
$\langle ... \rangle$	Temporal, or ensemble average
$f_0(v)$	Maxwellian distribution function
$S_L(x,t)$	Langmuir thermal noise source
$S_A(x,t)$	Ion acoustic thermal noise source

Chapter 1

Introduction

Historically the term "plasma" is attributed to Tonks and Langmuir [1] who in 1929 used the expression to describe equal distributions of electrons and ions in the ionized portion of a gas in an arc like discharge. Over the last 65 years the expression "plasma" has evolved into a definition of what is often referred to as the fourth state of matter. A simplified progression in obtaining a plasma is by heating a solid to form a liquid, the liquid can then be heated to form a gas, and the gas heated to form a plasma. A more accurate description of a plasma is dependent on the plasma parameters of temperature, density and the collisional properties of the system, which will determine whether discrete particle or collective effects are the dominant processes. Because of the important role collective phenomena play in the physics of plasmas they must be included in any formal definition.

Many textbooks [2]-[14], presenting plasma physics from numerous view points and with varying degrees of complexity, have been written. Throughout most of these books one of the simplest phenomena associated with the collective behavior of plasmas is the development of linear wave modes or eigenmodes of the plasma dispersion relation. These eigenmodes, often called natural or normal modes, describe the linear response of the plasma to electromagnetic and electrostatic fields.

In the absence of external magnetic fields three linear modes can exist, two being electrostatic and the third electromagnetic. The two electrostatic waves are the high frequency Langmuir waves, often called the electron plasma waves (EPW) or plasmons which, in the long wavelength regime where $k \ll k_D$, satisfy the approximate linear dispersion relation (cf. [2], [3])

$$\omega_L^2(k) = \omega_p^2 + 3v_{T_e}^2 k^2 \tag{1.1}$$

and the low frequency ion acoustic waves (IAW) or phonons, which approximately satisfy (cf. [2], [3])

$$\omega_A(k) = c_s k \tag{1.2}$$

Here $\omega_p = \sqrt{4\pi e^2 n_0^e / m_e}$ is the electron plasma frequency, $k_D = \omega_p / v_{T_e} = \sqrt{4\pi e^2 n_0^e / T_e}$ is the Debye wave number, $v_{T_e} = \sqrt{T_e / m_e}$ is the electron thermal velocity and $c_s = \sqrt{(ZT_e + 3T_i)/m_i}$ is the ion acoustic velocity. T_e and T_i are the electron and ion temperatures in electron volts and n_0^e is the mean electron density. The plasma also supports the propagation of electromagnetic waves (EMW) or photons, which satisfy (cf. [2], [3])

$$\omega^2(k) = \omega_p^2 + c^2 k^2 \tag{1.3}$$

In simple diagrammatic form we represent each of the wave types by the symbols in Fig.1.1

In this study we investigate the evolution of a plasma in the presence of an intense electromagnetic wave. This EMW, in the form of a laser beam propagating through the plasma, can drive the plasma unstable by transferring EMW free energy to the electrostatic modes. This scenario is of great interest allowing the

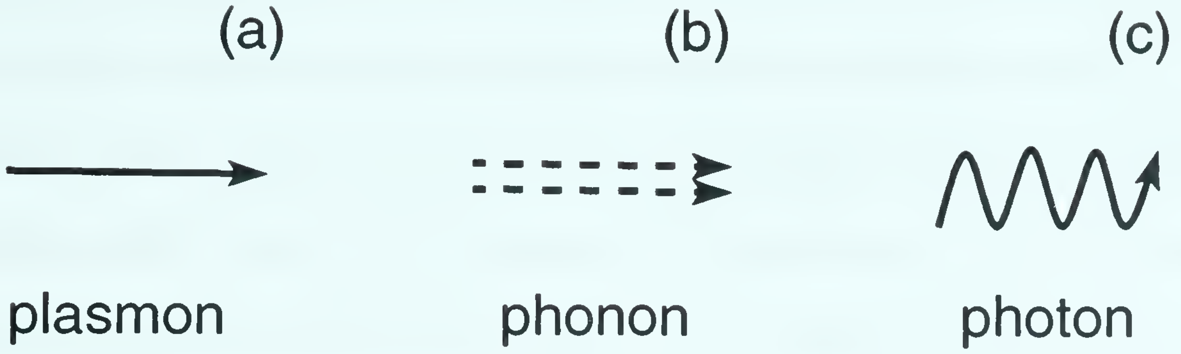

Figure 1.1: *Schematic diagram of the linear wave modes in an unmagnetized plasma*

study of wave-particle (see for example Ref. [4], [8]), wave-wave (see for example Ref. [3], [10]) and multi wave-particle interactions (see for example Ref. [11]). The first of these processes, the linear wave-particle interaction, allows for the transfer of energy between the electrostatic waves existing in the plasma and the charged particles themselves. One significant example of wave-particle interaction is collisionless Landau damping (for a good review see Ref. [9]). Landau damping provides a mechanism which can transfer wave energy to particles whose velocity is close to the phase velocity of the electrostatic modes present in the plasma. A more complete description of this process is modeled through quasilinear theory and allows for the heating of electrons in the plasma (cf. [4], [16]-[18]).

The second process, that of wave-wave interaction, contains a subgroup of important interactions usually classified under the broad heading of parametric instabilities (cf. [3], [10], [13]). Parametric instabilities are resonant processes which allow for unstable growth of the participating waves. In this investigation we will concentrate on the nonlinear evolution of parametric instabilities and in particular the saturation of stimulated Raman scattering (SRS). SRS is a three wave interaction, involving the decay of an EMW into a second EMW and a EPW, which we will describe shortly. We will show, in Chap. 3, that secondary parametric

processes, in particular the parametric decay instability (PDI), can disrupt and saturate SRS. This late time asymptotic saturation of SRS can be well described by simple scaling laws. In Chap. 4 we will show that during its nonlinear stage of evolution SRS excites a wide spectrum of plasma fluctuations from which secondary processes can scatter at enhanced levels. Simple scaling laws describing the reflectivity levels of these enhanced secondary processes will also be given.

Parametric instabilities have a physical analogue (which most individuals, as children, have experienced directly), of playing on a swing. The child's swing is commonly used to illustrate the concept of a parametric process. As the child pumps his legs at the appropriate rate, the child/swing system is carried higher with each successive period. From personal experience each individual is aware that one can gain altitude on a swing only if a specific pumping frequency is used.

To further understand what is happening we examine a mathematical description involving a modulated harmonic oscillator with an amplitude $Z(t)$ in the form of the Mathieu equation [13]

$$\frac{d^2Z(t)}{dt^2} + \Omega_0^2 \left[1 - 2\epsilon \cos(\omega_0 t)\right] Z(t) = 0 \tag{1.4}$$

where when $\epsilon \simeq 0$, Ω_0 is the natural frequency of the oscillator. The standard method (cf. [13] [15]) for examining (1.4) is to assume that $\epsilon \ll 1$ and that a perturbative approach can be applied. Taking the Laplace transform (cf. Ref. [13])

$$Z(\omega) = \int_0^\infty dt Z(t) \exp[i\omega t] \tag{1.5}$$

of (1.4) one can find linear solutions of the form $\exp[i\omega t]$ and $\exp[-i\omega t]$ which will give rise to perturbed solutions of the form $Z(\omega + (n-1)\omega_0)$ and $Z(\omega + (n+1)\omega_0)$

$n = 0, \pm 1, \pm 2, \pm 3...$ producing the recurrence relation

$$\left[(\omega + n\omega_0)^2 - \Omega_0^2\right] Z(\omega + n\omega_0) = \tag{1.6}$$

$$-\epsilon\Omega_0^2 \left[Z(\omega + (n+1)\omega_0) + Z(\omega + (n-1)\omega_0)\right]$$

Unstable solutions of the Mathieu equation which allow for the growth of the perturbations are restricted for $\mid \epsilon \mid \ll 1$ to regions for which solutions exist such that

$$\Omega_0 = \frac{n\omega_0}{2}; \qquad (n = \pm 1, \pm 2, \pm 3...) \tag{1.7}$$

Examining the $n = -1$ solution (i.e. $\omega_0 = 2\Omega_0$) with the dominant $Z(\omega - \omega_0)$, $Z(\omega)$ components produces the dispersion relation

$$\left(\omega^2 - \Omega_0^2\right)\left((\omega - \omega_0)^2 - \Omega_0^2\right) = \epsilon^2\Omega_0^4 \tag{1.8}$$

where $\omega_0 = 2\Omega_0$. If we wish to find unstable solutions we assume ω to be complex and, using $\omega = \Omega + i\Gamma$ one obtains the growth rate

$$\Gamma = \frac{\epsilon\Omega_0}{2} \tag{1.9}$$

In the child/swing system the natural frequency of the swing is modulated twice during each cycle, as the child pumps his legs at the frequency $\omega_0 = 2\Omega_0$. This modulation of the swings natural frequency allows the amplitude of the swing to grow at a rate of Γ. If damping is included in (1.4) then the growth rate (1.9) must exceed the damping threshold before growth can occur.

A similar process is observed in plasmas [13] for the coupling between three waves or four waves (the space-time version of 'resonances'). This allows for the

transfer of wave energy and action from one wave, such as an electromagnetic wave, to waves of the same or different type, such as Langmuir waves. Take for example a large amplitude wave, such as an intense electromagnetic pump wave, existing in a plasma. This strong wave can combine with the oscillating density variation associated with an electrostatic plasma wave giving rise to a source current for an EMW at the combination frequency. This second electromagnetic wave can then interact with the original EMW to produce a ponderomotive force which acts to increase the density variation. In this way, near resonance, both weak waves can grow at the expense of the strong wave. When such a system exists inside a plasma it is known as a parametric instability.

The most basic form of a parametric instability is that of a three wave interaction (3WI) known as the decay instability. In this process a pump wave of frequency ω_0 and wave number k_0 decays into two satellite with frequencies ω_1, ω_2 and wave number k_1, k_2. If the matching conditions

$$\delta\omega = \omega_1 + \omega_2 - \omega_0 \tag{1.10}$$

representing energy conservation and

$$\delta\vec{k} = \vec{k}_1 + \vec{k}_2 - \vec{k}_0 \tag{1.11}$$

representing conservation of momentum, are met exactly, ie. $\delta\omega = \delta\vec{k} = 0$ then the interaction is in exact resonance and the strongest possibility of unstable growth of the secondary waves occurs (cf. [10], [13]).

In the absence of external magnetic fields, six variations of the decay instability can take place involving the linear eigenmodes. With the symbols of Fig.1.1 we can illustrate these possibilities of

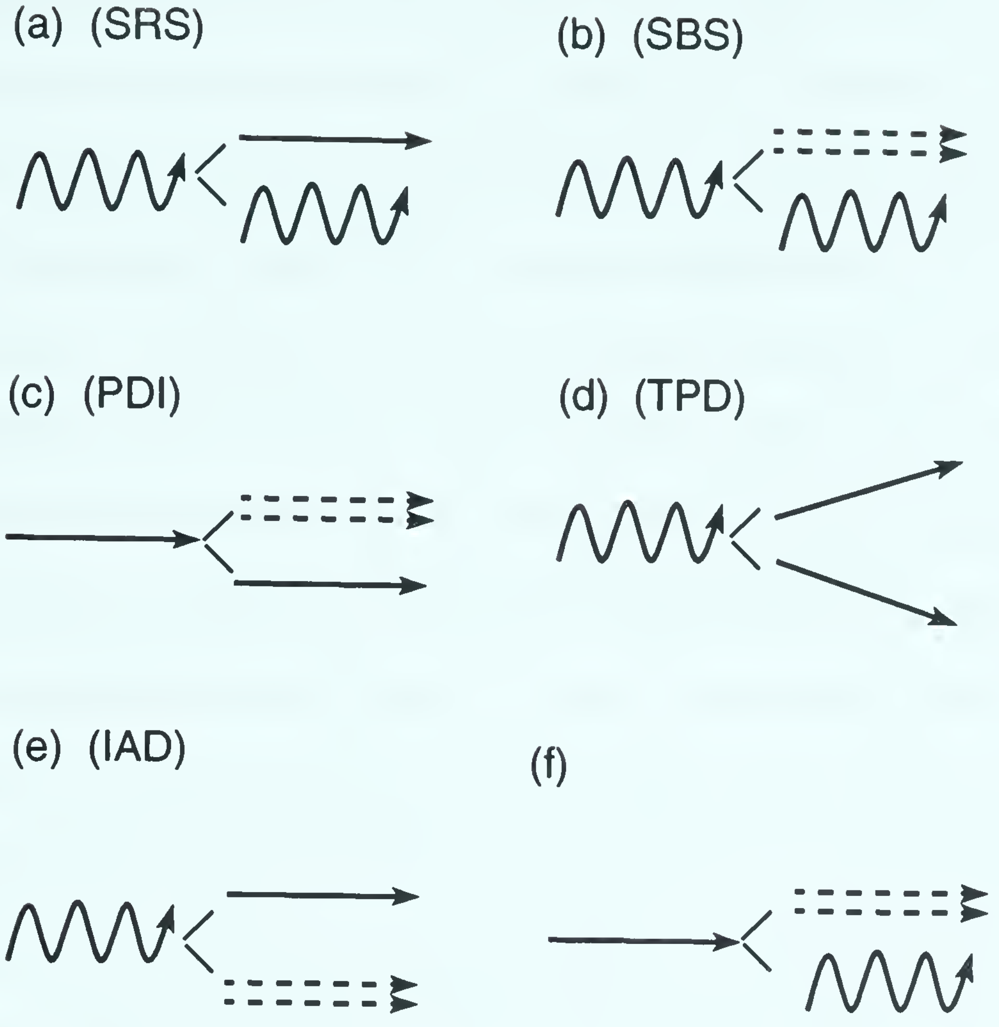

Figure 1.2: *Schematic diagram of possible three wave interactions using the linear wave modes of an unmagnetized plasma.*

(a) photon → photon + plasmon (Stimulated Raman scattering (SRS))

(b) photon → photon + phonon (Stimulated Brillouin scattering (SBS))

(c) plasmon → plasmon + phonon (Parametric decay instability (PDI))

(d) photon → plasmon + plasmon (Two plasmon decay (TPD))

(e) photon → plasmon + phonon (Ion acoustic decay (IAD))

(f) plasmon → photon + phonon

shown in a diagrammatic fashion in Fig.1.2

The invention of the laser and the notion of controlled fusion as an energy resource produced an increased interest in parametric instabilities and other wave interactions in plasma physics (see [6], [19], [20]). As lasers became more powerful, inertial confinement fusion (ICF) became a possible scheme for initiating and controlling fusion. ICF involves the use of intense laser light to compress a solid target initiating a fusion reaction. Two main types, direct and indirect drive designs, are used in ICF research, each having its own advantages and disadvantages. The basic processes involved in each of the systems are illustrated in Fig.1.3. In the direct drive system a solid target is symmetrically radiated with intense laser light. Ideally the incoming laser light strikes the outside surface of the capsule containing DT 'fuel', forming a plasma in which the laser energy is partly absorbed and partly reflected on passage through the plasma to the 'critical-density' surface layer. Further energy is absorbed at the critical surface where the laser energy is converted into thermal energy. The thermal energy is then transported inward as matter is ablated. The ablation of this inner surface produces extreme pressure, compressing the inner solid and producing a fusion reaction (cf. [21]).

In the indirect drive model the laser energy is delivered to the inside surface of a high-Z enclosure, called a hohlraum, which surrounds the fuel cell. The walls of the hohlraum then emit x-rays which are absorbed by the target. This energy is again used to drive the ablation process producing a fusion reaction.

Characteristic of both drive schemes is the production of a large volume of plasma in which many different interaction processes can occur below the critical surface. The critical surface is defined by a point n_c along the density gradient where the frequency of the incoming laser light ω_0 is equal to the plasma frequency preventing the laser light from propagating further into the plasma i.e.

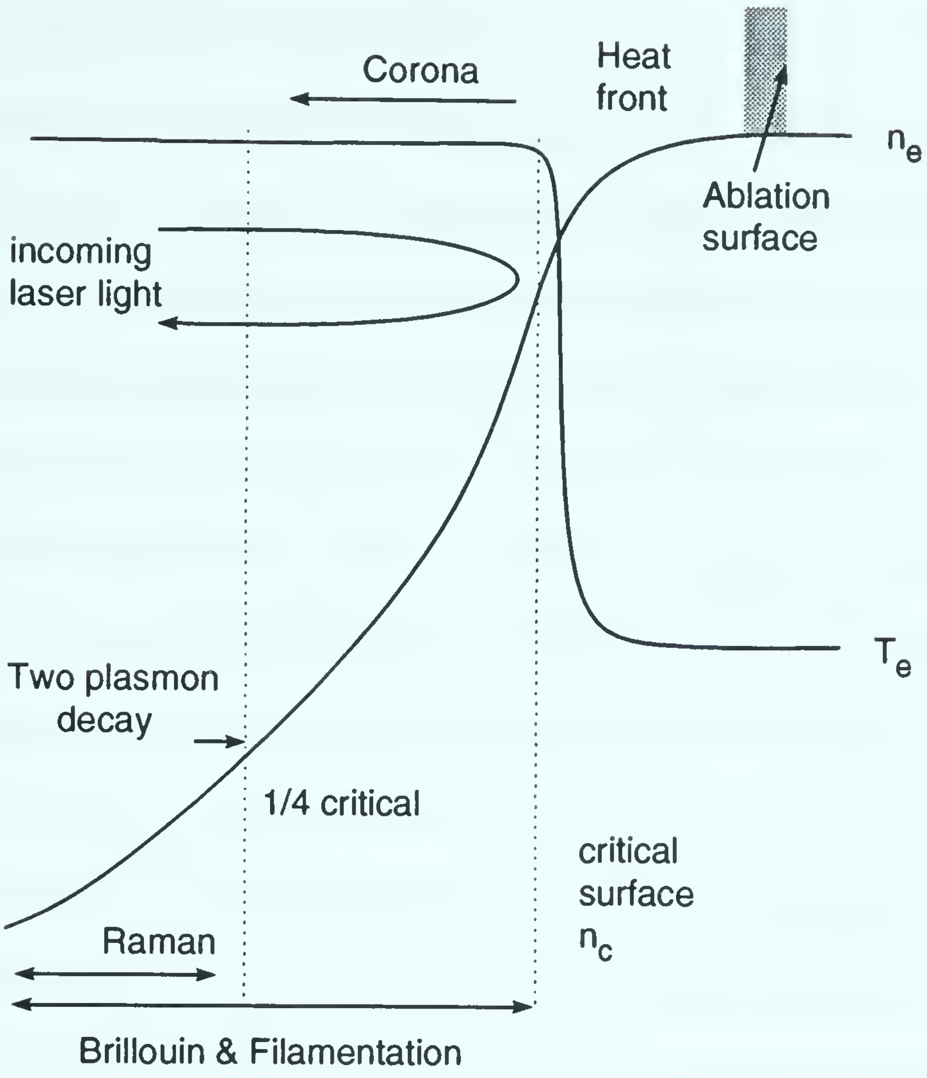
Corona
Heat front
n_e
Ablation surface
incoming laser light
T_e
Two plasmon decay
1/4 critical
critical surface n_c
Raman
Brillouin & Filamentation

Figure 1.3: *Schematic diagram of interaction processes in ICF*

$$n_c = \frac{\omega_0^2 m_e}{4\pi e^2} \simeq 10^{21}\lambda_\mu^{-2} electrons/cm^3 \tag{1.12}$$

Here λ_μ is the laser wavelength in microns.

The direct drive system is much more efficient in transporting energy to this critical surface, but is very sensitive to nonuniformities in the laser beam, and has the disadvantage of allowing the production of large density and velocity gradients. The indirect drive is not as sensitive to nonuniformities of the laser beam but the process generates a large volume of homogeneous plasma. This homogeneous plasma allows for stronger development of laser driven parametric instabilities which can

be extremely detrimental to drive efficiency.

In general the plasma, of both drive types, is itself nonlinear in nature, allowing for the development of wave-wave interactions. Some of these interactions, in the form of parametric instabilities, can scatter laser light, through processes such as SRS or SBS, greatly reducing the amount of energy which can reach the critical surface. Other interaction processes such as the heating of electrons to MeV energies can have detrimental effects on ICF by preheating the fusion core. Overall these processes present a problem for those searching for a means of producing controllable fusion, but these same processes have resulted in one of the most interesting areas of plasma physics referred to as laser-plasma interactions.

In the late 1960's and early 1970's many individuals began investigating parametric instabilities, first in the context of analysing experiments involving intense irradiation of the ionosphere [22], and then in the context of laser-plasma interactions(cf Ref. [23]-[28]). Of particular interest to us, and significant importance to ICF, are those parametric instabilities which can scatter the incoming laser light (cf. [29] for a recent review). Inherently the ICF interaction scheme depicted in Fig.1.3 produces a plasma density gradient extending from the vacuum level to the critical surface. Along this gradient various regimes exist allowing for different instabilities to develop. Stimulated Raman scattering (SRS) for instance can occur between the quarter critical density and very low densities, where $k \geq 0.3k_D$ producing very heavy Landau damping of the Langmuir waves. A second important instability, stimulated Brillouin scattering (SBS) can exist along the entire density gradient up to critical density. Both these instabilities have been extensively investigated theoretically (cf [30]-[34]). SBS was observed in the early 1970's [35]-[37] while SRS was not confirmed until 1978 when Watt et al [38] reported the

first direct spectral evidence of SRS. Since this time many experiments have been performed and a great deal of experimental evidence has been gathered (see [18], [39]-[42]and references there in).

Until recently, instabilities such as SRS and SBS have been treated theoretically as separate independent processes in the form of three wave interactions. From the analysis of experimental evidence it has become obvious that not only is a three wave model inadequate to properly explain the nonlinear evolution [43]-[45], but treating these instabilities as independent processes can lead to incorrect results. Within the last decade a great deal of attention has been focused on the interaction of simultaneous instabilities, such as the competition of SRS-SBS for pump energy [46]-[49]. It is thought that through the interaction of these individual instabilities various nonlinear phenomena, such as saturation mechanisms, can be explained. Prompted by experimental observations many studies (cf. [49], [64], [81], [95]) have been designed to isolate the mechanisms responsible for these nonlinear phenomena, such as SRS and SBS saturation. One possible mechanism for saturating SRS is via PDI, whereby the SRS driven Langmuir wave at ω_L, k_L decays into a second Langmuir wave at $\omega_L^{(1)}, k_L^{(1)}$ and an ion acoustic wave at $\omega_A^{(1)}, k_A^{(1)}$. The resultant resonant matching conditions are given by

$$\omega_L = \omega_L^{(1)} + \omega_A^{(1)} \tag{1.13}$$

and

$$k_L = k_L^{(1)} + k_A^{(1)} \tag{1.14}$$

Using (1.13), (1.14) and the linear dispersion relations (1.1) and (1.2) one can calculate the necessary wave numbers, a Langmuir wave at $k_L^{(1)} = \Delta k - k_L$ ($\Delta k = \frac{2}{3} k_D \sqrt{Z m_e / m_i}$) and an ion acoustic wave at $k_A^{(1)} = 2k_L - \Delta k$. PDI can be used to

saturate SRS by disrupting the resonant matching conditions of SRS through the production of density fluctuations in the plasma.

The present study is devoted, in part, to exploring SRS saturation through a one dimensional model coupling the three wave SRS process to the Zakharov equations. The Zakharov equations allow for the nonlinear coupling of the Langmuir field and ion density fluctuations [50]-[54]. For brevity we will refer to this nonlinear coupling of the Langmuir field and ion density fluctuations as the electron-ion coupling of the Zakharov equations. The Zakharov equations,which will be derived as an integral part of our full model in Chap. 2, can be written in dimensional form as

$$i(\frac{\partial E}{\partial T} + \gamma_L * E) + \frac{3}{2}\frac{v_{T_e}^2}{\omega_p}\frac{\partial^2 E}{\partial X^2} - \frac{\omega_p}{2} N E = 0, \tag{1.15}$$

$$\frac{\partial^2 N}{\partial T^2} + 2\gamma_A * \frac{\partial N}{\partial T} - c_s^2 \frac{\partial^2 N}{\partial X^2} = \frac{\partial^2}{\partial X^2}\left(\frac{\mid E \mid^2}{16\pi n_0^i m_i}\right), \tag{1.16}$$

Here $N = \delta n_i / n_0^i$ is the slowly varying ion density fluctuation, and E represents the slowly varying enveloped amplitude of the Langmuir field. $\gamma_L * E$ and $2\gamma_A * \partial N/\partial T$ are convolution operators which account for the phenomenological electron and ion Landau damping and collisional damping on the Langmuir waves.

Through these equations the high frequency Langmuir fields produce low frequency ponderomotive effects on the electrons which can influence the behavior of the ion density fluctuation evolution. The ion motion in turn affects the density sensitive plasma wave dispersion and thus the evolution of the Langmuir fields. The Zakharov equations permit the development of PDI as well as allowing for the nonlinear evolution of the Langmuir and ion acoustic waves. Other nonlinear effects such as the development of a PDI cascade [55], [56] can also occur. A PDI cascade occurs when the satellite Langmuir wave of PDI itself decays through

PDI producing a progression of ion acoustic and Langmuir waves towards the long wavelength region of the wave spectra. These waves can then interact producing resonant and quasimode components in the wave spectra. The quasimode components are defined as waves which do not satisfy the linear dispersion relations (1.1) and (1.2).

If the PDI cascade is strongly driven, or the wave number of the driven wave is sufficiently small, the Langmuir wave energy will accumulate in the long wavelength region of the spectra where Landau damping has little effect. Under these circumstances the modulational instability (MI) [57], [58] will be the characteristic instability. In its linear form MI is a four-wave nonresonant process which involves a Langmuir pump wave (twice), both the Stokes and anti-Stokes Langmuir satellites and an ion acoustic quasimode. The Langmuir pump drives the ion quasimode to produce an instability, modulating the shape of the primary Langmuir wave. As the system evolves and becomes nonlinear the modulated Langmuir wave will produce localized regions of strong electrostatic fields. This nonlinear evolution of MI leads to a regime designated as strong Langmuir turbulence. Dubois, Rose and their colleagues have extensively studied the Zakharov equations in this and other context [52]-[54], [59]-[62]. In such a regime the localized regions of the high frequency electrostatic field will use the ponderomotive potential $\sim\mid E \mid^2$ to push out the plasma from these local areas, producing density cavities or cavitons. The localized Langmuir field will then remain locked together with the density cavities, localizing further as the density focuses the Langmuir field through the nonlinear coupling $\sim NE$. As the scale length of the localized structures decreases the wave numbers increase allowing for strong Landau damping of the electrostatic fields. In one dimension the localization process will produce soliton like structures which, in

higher dimensions, collapse to very short spatial scales leaving the density cavities unsupported.

To classify whether a process is characterized as a modulational or parametric decay instability it is advantageous to examine the linear response and growth rates of the Zakharov equations. To this end a rapid review of the one dimensional linear theory [51] is presented here. The linear growth rates can be found by assuming that a finite amplitude Langmuir mode of the form $E_L \exp[i(k_L x - \Omega_L t)]$ exists inside the plasma. Infinitesimal plane wave modes $E_\pm \exp[i(k_\pm x - \Omega_\pm t)]$ for the Langmuir waves and $\frac{1}{2}(N_1 \exp[i(k_A x - \Omega_A t)] + c.c.)$ for the ion density waves, are also assumed to exist, resulting in the linearized system of equations

$$\left(i\gamma_L(k_L) + \Omega_L - \frac{3}{2}\frac{v_{T_e}^2 k_0^2}{\omega_p}\right) E_L = \frac{\omega_p}{4}(E_1 N_1 + N_1^* E_+) \tag{1.17}$$

$$\left(i\gamma_{L_\pm}(k_\pm) + \Omega_\pm - \frac{3}{2}\frac{v_{T_e}^2 k_\pm^2}{\omega_p}\right) E_\pm = \frac{\omega_p}{4}(S_+ E_L N_1 + S_- E_L N_1^*) \tag{1.18}$$

$$\left(2i\Omega_A \gamma_A(k_A) + \Omega_A^2 - c_s^2 k_A^2\right) N_1 = \frac{c_s^2 k_A^2}{8\pi n_0^e T_e}(E_L E_-^* + E_+ E_L^*) \tag{1.19}$$

where the asterisk denotes complex conjugate, $\gamma_L(k_L)$, $\gamma_{L_\pm}(k_\pm)$, $\gamma_A(k_A)$ denote the linear damping coefficients, $S_+(S_-) = 1$ for $E_+(E_-)$ and zero for $E_-(E_+)$. We have also defined

$$\Omega_\pm = \Omega_L \pm \Omega_A \tag{1.20}$$

$$k_\pm = k_L \pm k_A \tag{1.21}$$

Eliminating $E_\pm$ we have the dispersion relation

$$\left(2i\Omega_A\gamma_A(k_A) + \Omega_A^2 - c_s^2k_A^2\right) = \frac{\omega_p c_s^2 k_A^2}{32\pi n_0^e T_e} \mid E_L \mid^2 \tag{1.22}$$
$$\times \left(\frac{1}{i\gamma_{L_+}(k_{L_+}) + \Omega_+ - 3v_{T_e}^2 k_+^2/2\omega_p} + \frac{1}{-i\gamma_{L_-}(k_{L_-}) + \Omega_-^* - 3v_{T_e}^2 k_-^2/2\omega_p}\right)$$

Figure 1.4 presents a diagram illustrating the various linear regimes possible. In the event that the process involves both the Stokes and anti-Stokes components a modulational instability develops (regions III and IV Fig.1.4). Should the linear process only involve the Stokes Langmuir satellite the process is classified as a PDI (regions I and II Fig.1.4). The two regimes for each instability are further classified by the strength of the Langmuir pump wave where regions II and III are strongly driven and regions I and IV represent weakly driven regimes.

In regimes where the anti-Stokes component E_+ can be neglected we have using $\Omega_- = 3v_{T_e}^2 k_-^2/2\omega_p + i\Gamma$ and $\Omega_A = \omega_A + i\Gamma$, the dispersion relation

$$(-2\Gamma\gamma_A(k_A) - \Gamma^2 + 2i\omega_A[\Gamma + \gamma_A(k_A)])(-i\Gamma - i\gamma_L(k_L)) = \frac{\omega_p c_s^2 k_A^2}{32\pi n_0^e T_e} \mid E_L \mid^2 \tag{1.23}$$

When $\omega_A \gg \Gamma$ no modification to the dispersion relations of the linear wave modes occurs producing the approximate PDI growth rate in the weakly driven regime in region I of Fig.1.4. The decay instability thus has a growth rate of

$$\Gamma_{PDW} = \left(\frac{\omega_p\omega_A \mid E_L \mid^2}{64\pi n_0^e T_e}\right)^{1/2} \tag{1.24}$$

where we have ignored the linear damping for convenience. If damping is present the Langmuir pump must be large enough to overcome the PDI threshold of

$$E_{thr}^2 = \frac{64\pi n_0^e T_e \gamma_A(k_A)\gamma_L(k_L)}{\omega_L\omega_A}, \tag{1.25}$$

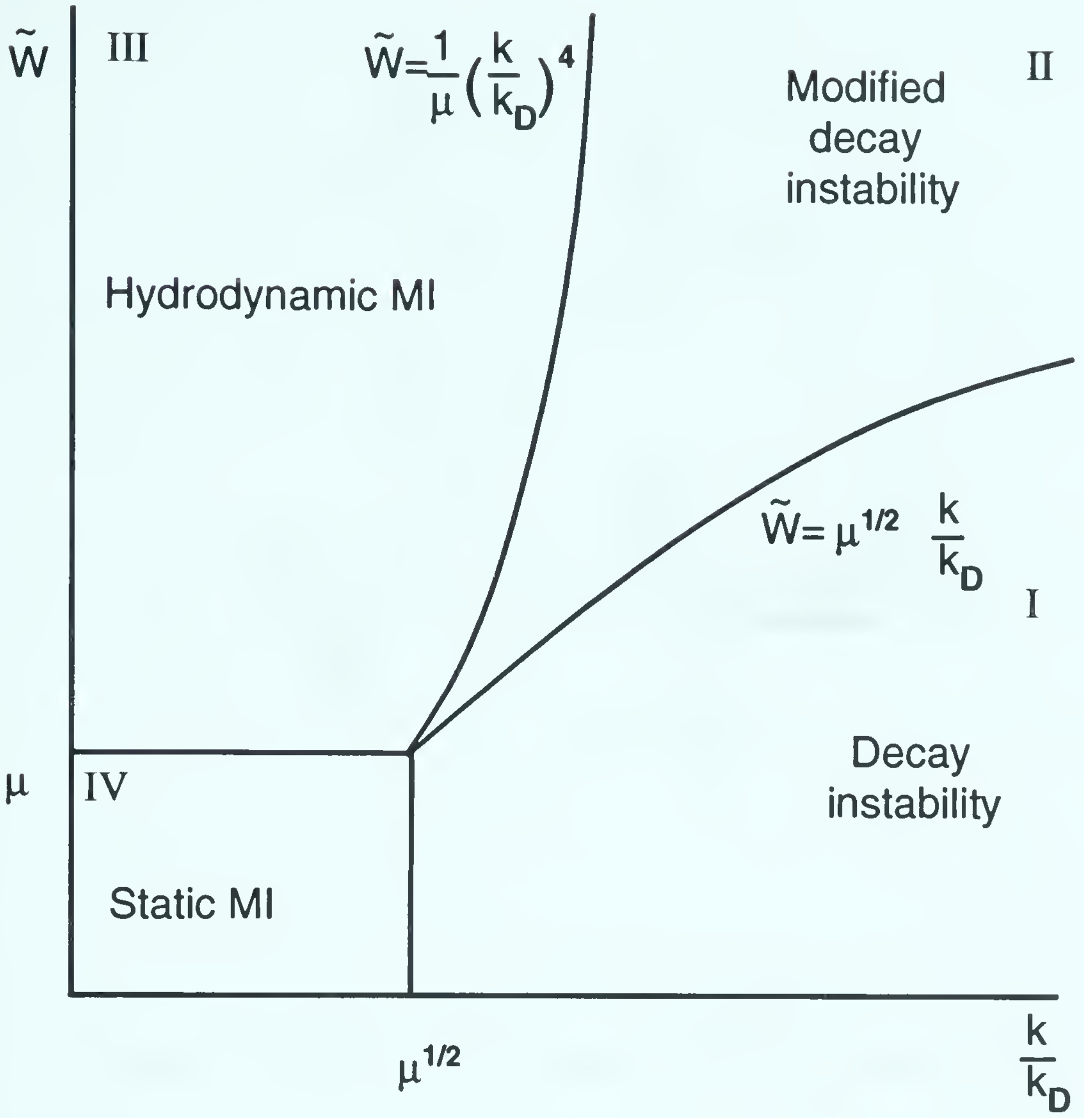

Figure 1.4: *The linear instabilities described by the Zakharov equations (1.15)-(1.16) for the parameters of the electrostatic electric field* $\tilde{W} = \hat{E}^2 = E^2/(4\pi n_0^e T_e)$ *versus* k/k_D, *where* $\mu = Zm_e/m_i$, *and* $k_D = (4\pi e^2 n_0^e/T_e)^{1/2}$ *is the Debye wave number.*

If the amplitude of the primary Langmuir wave is well above the PDI threshold a cascade of resonant decays can occur, producing waves at $k_L^{(2n-1)} = (2n-1)\Delta k - k_L$ and $k_L^{(2n)} = k_L - 2n\Delta k$ for the Langmuir waves and $k_A^{(n)} = 2k_L - (2n-1)\Delta k$ for the ion acoustic waves. This process is illustrated in diagrammatic form in Fig.1.5.

Using $\omega_A = c_s k_A \gg \Gamma$ the limit for this weakly driven regime is given by

$$k_A \gg \frac{\omega_p \mid E_L \mid^2}{64 c_s \pi n_0^e T_e} = \frac{\omega_p}{16 c_s}\tilde{W} \tag{1.26}$$

where we have defined

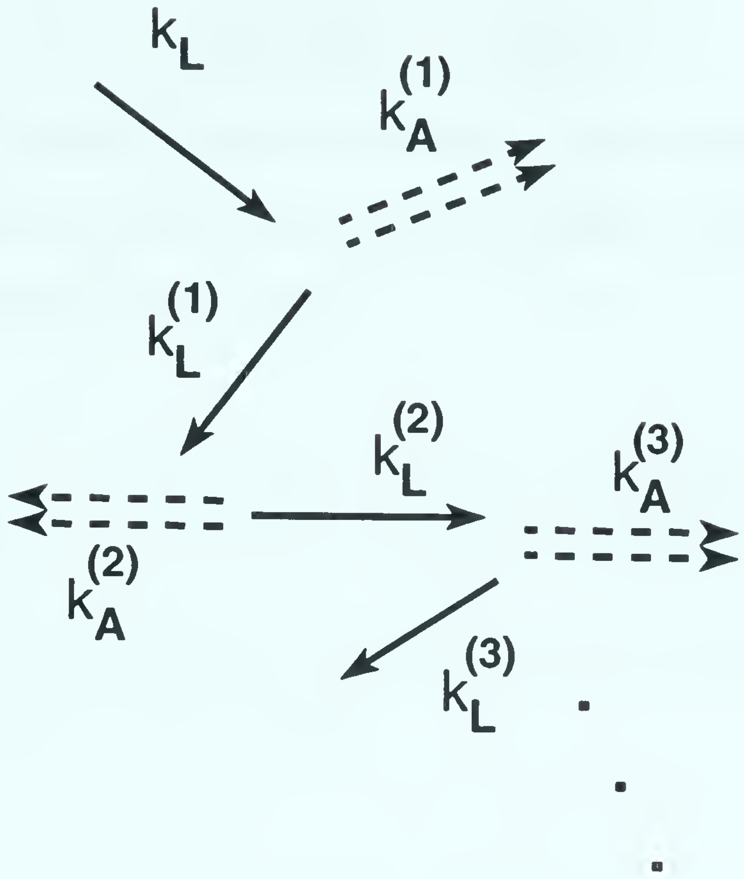

Figure 1.5: *Schematic diagram of PDI cascade process*

$$\tilde{W} \equiv \frac{\mid E_L \mid^2}{4\pi n_0^e T_e} \tag{1.27}$$

In the event that the ion acoustic growth is strongly driven ie. $\omega_A \leq \Gamma$ the ion acoustic frequency will be modified and we are in region II of Fig.1.4. Here the decay instability is also modified producing the growth rate of

$$\Gamma_{PDS} = \frac{\sqrt{3}}{2} \left(\frac{\omega_p c_s^2 k_A^2 \mid E_L \mid^2}{32\pi n_0^e T_e} \right)^{1/3} \tag{1.28}$$

where again we have ignored the linear damping. Once again should the primary wave E_L be well above threshold cascading can occur. In this case the frequency of the ion acoustic wave will be modified by the strong growth. One can still estimate the regime where the strongly driven PDI growth will be observed by the expression

$$k_A \ll 3^{1.5}\frac{\omega_p \mid E_L \mid^2}{256 c_s \pi n_0^e T_e} = 3^{1.5}\frac{\omega_p}{64 c_s}\tilde{W} \tag{1.29}$$

In regimes where the modulational instability occurs we require that both the Stokes and anti-Stokes contributions in (1.22) are resonant simultaneously. Thus in the absence of damping (1.22) becomes

$$\left(\Omega_A^2 - c_s^2 k_A^2\right)\left(\left[\Omega_A - \frac{3v_{T_e}^2 k_A k_L}{\omega_p}\right]^2 - \frac{9}{4}\frac{v_{T_e}^4 k_A^4}{\omega_p^2}\right) = \frac{3v_{T_e}^2 c_s^2 k_A^4}{32\pi n_0^e T_e} \mid E_L \mid^2 \tag{1.30}$$

At this point no condition has been set on either k_L or k_A. In the adiabatic regime we take $k_A \gg k_L$ and set $k_L \sim 0$ to obtain

$$\left(\Omega_A^2 - c_s^2 k_A^2\right)\left(\Omega_A^2 - \frac{9}{4}\frac{v_{T_e}^4 k_A^4}{\omega_p^2}\right) = \frac{3v_{T_e}^2 c_s^2 k_A^4}{32\pi n_0^e T_e} \mid E_L \mid^2 \tag{1.31}$$

Looking for stationary solutions where $\Omega_{Real} \sim 0$ and using $\Omega_A \sim i\Gamma$ so that we have purely growing solutions will produce a threshold of

$$\tilde{W} > 6\left(\frac{k_A}{k_D}\right)^2 \tag{1.32}$$

In the strongest driven regime of MI where

$$\Gamma^2 > \frac{9}{4}\frac{v_{T_e}^4 k_A^4}{\omega_p^2} \tag{1.33}$$

the growth rate is approximately

$$\Gamma^4 = \frac{3v_{T_e}^2 c_s^2 k_A^4}{32\pi n_0^e T_e} \mid E_L \mid^2 \tag{1.34}$$

leading to the condition that in this regime

$$\tilde{W} > \frac{27m_i}{2Zm_e}\left(\frac{k_A}{k_D}\right)^4 \simeq \frac{1}{\mu}\left(\frac{k_A}{k_D}\right)^4 \tag{1.35}$$

which is region III of Fig.1.4 the hydrodynamic MI regime. Here we have defined $\mu = Zm_e/m_i$. In the solutions we have examined the sound waves are quasimodes enslaved to the nonlinear ponderomotive force in (1.16). This ponderomotive force drives the density fluctuations, which in turn focuses the Langmuir field. A similar process occurs in region IV of Fig.1.4, the static MI regime, where the growth rate is much smaller than the ion acoustic frequency $\Gamma^2 < c_s^2 k_A^2$. It is also assumed that $\frac{9}{4} v_{T_e}^4 k_A^4/\omega_p^2 < c_s^2 k_A^2$ resulting in the limit

$$\frac{2}{3}\sqrt{\frac{Zm_e}{m_i}} \simeq \mu^{1/2} > \left(\frac{k_A}{k_D}\right) \tag{1.36}$$

with a growth rate of

$$\Gamma^2 = \frac{3v_{T_e}^2 k_A^2}{8}\tilde{W} \tag{1.37}$$

and bounded above by

$$\mu > \tilde{W} \tag{1.38}$$

The linear analysis itself remains valid for only a limited time, and as the small amplitude waves grow, becomes inadequate to describe the evolution of the system. As the system evolves into the nonlinear regime it becomes obvious that describing the saturation of SRS by using only the first stage of the PDI cascade is inadequate. The many different processes, such as the interaction of the PDI cascade components or the nonlinear focusing of MI, makes using a model containing the

electron-ion coupling of the Zakharov equations a necessity when describing the nonlinear evolution of the plasma. In order to account for these nonlinear processes we have included the Zakharov equation in our theoretical description of SRS. The model used in our investigation is based on the Aldrich et al. [63] and Rozmus et al. [64] models. The investigation itself, studying the saturation of SRS in the presence of the electron-ion interaction of the Zakharov model, has been conducted in parallel with the Los Alamos group of Bezzerides, Dubois and Rose who are investigating a similar model in the context of strong Langmuir turbulence [65]. Our theoretical model is derived from the system of Maxwell's and fluid equations, where we have enveloped in time the rapidly varying quantities corresponding to the electromagnetic and electrostatic fields, so that all field amplitudes vary on the ion acoustic timescale. We will restrict our analysis to a one-dimensional geometry and concentrate on a parameter regime such that a fluid description of the plasma is possible.

In Chap. 2 we will derive the basic theoretical model used in our simulations. The final model is based on the system of Zakharov-Maxwell equations and uses the electron-ion coupling of the Zakharov equations to produce saturation of SRS. Chapter 2 also provides a review of the basic three wave interaction results. These results are used to analyse the early stages of the full model simulations, permitting the identification of the dominate physical processes.

In Chap. 3 we will analyse our theoretical model in the absence of SBS and anti-Stokes Raman couplings, from both a numerical and an analytical view point. The typical evolution of SRS saturation will be documented, describing the initial linear growth and initial saturation of SRS by PDI. The intermediate nonlinear regime which can lead to an immediate final saturated state or a quasiperiodic

repeating [66] of the first two stages of development will be discussed. Finally the asymptotic quasistationary saturated state will be discussed in detail where we will present scaling laws describing the asymptotic levels of Langmuir fields and SRS reflectivity [67].

The evolution described in Chap. 3. has been seen to hold in the presence of the SBS coupling as long as the parameters are restricted to those regimes in which SBS does not grow absolutely or the timescale of the simulations prohibit domination by SBS. The analysis in Chap. 4 will thus contain our full model with the SBS [68] and anti-Stokes Raman coupling intact. The information gained in Chap. 3 regarding the asymptotic state of the Langmuir waves will be used in Chap. 4 to produce expressions describing the ion density and Langmuir spectra. These spectral expressions can then be used to describe enhancement of various scattering processes, which produce reflectivity levels far in excess of the expected 3WI predictions. Such scattering processes include enhanced Brillouin and forward Raman scattering, as well as anti-Stokes components of backward and forward Raman.

The Langmuir spectra calculated in Chap. 4 can also be used to analysis the production of hot electrons which can have serious consequences in limiting the validity of our fluid model. Using a simple model describing linear wave-particle interactions we examine in Chap. 5 the effect of the asymptotic Langmuir waves on the evolution of a Maxwellian distribution function. With these results, further limits can now be placed on the plasma interaction lengths and intensities for which our fluid model and hence our investigation remains valid.

In Chap. 6 we will explore the applicability of our analytical and numerical work to explain experimental observations. Numerous experiments involving SRS,

SBS and their evolution are studied, providing a large body of evidence to which our calculations can be compared. Reasonable agreement between theory and experiment has been found for many different experiments allowing us to offer new or alternate explanations for observed results. Finally in Chap. 7 we summarize our results and present a final discussion and conclusions. We also discuss the limitations of the present analysis and present possible ways in which the current investigation could be expanded.

All our numerical simulations have been performed using the numerical partial/ordinary differential equation solver described in appendix .2. The core of this algorithm was designed to accommodate an arbitrary number of nonlinear partial and ordinary differential equations for an initial value problem with nonperiodic boundary conditions. The code itself uses a five point centered difference spatial derivative approximation and is solved implicitly in time for a two point forward difference temporal derivative. To solve for the spatial dependence a penta-block diagonal inversion scheme (a variation of the standard tridiagonal inversion algorithm) is used.

To test the algorithm we have applied the solver program to many different systems. Exact analytical solutions of the test problems have been verified by numerical simulations. These test problems have included both linear problems for which analytical expressions are easily found, as well as nonlinear problems, such as the nonlinear Schrödinger equation and Zakharov equations, for which specific nonlinear solutions are known. Excellent agreement between the analytical and numerical solutions have been obtained for these problems. The accumulation of numerical errors has been found to be very small and easily controlled. For example in our full theoretical model, which will be described in Chap. 2, we added the

phenomenological thermal noise sources of appendix .1. These noise source terms were always much greater in magnitude than any numerical error observed in our test runs.

Chapter 2

Basic concepts

2.1 Derivation of basic equations

In our investigation, in order to derive our theoretical model, we start with the standard fluid equations coupled with Maxwell's equations. The resultant system describes the nonlinear evolution of SRS in the presence of the electron-ion coupling of the Zakharov equations. The nonlinear coupling of the Zakharov equations allows for the development of PDI and its nonlinear evolution, which has been found to be the primary mechanism of SRS saturation in the parameter regimes studied in this investigation. The more complete description of the interaction of the Langmuir fields and ion density fluctuations, allowed by the Zakharov equations permits the development of a more accurate model describing SRS saturation. Similar theoretical models have been previously used to describe scattering instabilities in terms of periodic boundary conditions [63], [64], finite geometry simulations of CO_2 experiments [49], and other systems [65].

The plasma itself will be assumed homogeneous with a one-dimensional geometry. We will concentrate on a parameter regime such that a fluid description of the plasma is possible. The temperature and laser intensities are chosen such that relativistic effects can be ignored, and densities are in a regime where quantum

effects are negligible. The final system of equations is solved numerically for a finite plasma in a parameter regime consistent with today's laser-plasma interaction experiments.

2.1.1 Equations describing electromagnetic field evolution

In order to derive an equation describing the interaction of electromagnetic waves with the plasma we start by examining Maxwell's equations. Choosing a Coloumb gauge $\vec{\nabla} \cdot \vec{A} = 0$ and using Ampere's law in the form

$$\vec{\nabla} \times \vec{B} = \frac{1}{c}\frac{\partial \vec{E}}{\partial t} + \frac{4\pi}{c}\vec{J} \tag{2.1}$$

together with

$$\vec{E} = -\vec{\nabla}\phi - \frac{1}{c}\frac{\partial \vec{A}}{\partial t}; \qquad \vec{B} = \vec{\nabla} \times \vec{A} \tag{2.2}$$

one obtains

$$\frac{\partial^2 \vec{A}}{\partial t^2} + c^2 \vec{\nabla} \times \vec{\nabla} \times \vec{A} = c\left(4\pi \vec{J} - \frac{\partial \vec{\nabla}\phi}{\partial t}\right) \tag{2.3}$$

where $\vec{J} \equiv \Sigma q_\alpha n_\alpha \vec{v}_\alpha$ is used to describe the current. Here n_α is the density, $\vec{v}_\alpha$ is the mean local velocity and $\alpha = e, i$ denotes the electron or ion species. To obtain the evolution of these quantities we proceed using the standard fluid equations where the continuity equation is defined as

$$\frac{\partial n_\alpha}{\partial t} + \vec{\nabla} \cdot (n_\alpha \vec{v}_\alpha) = 0 \tag{2.4}$$

and the second hydrodynamical equation is written in the form

$$\frac{\partial n_\alpha \vec{v}_\alpha}{\partial t} + \vec{\nabla} \cdot (n_\alpha \vec{v}_\alpha \vec{v}_\alpha) + \gamma_\alpha v_{T_\alpha}^2 \vec{\nabla} n_\alpha - \frac{q_\alpha n_\alpha}{m_\alpha} \left(\vec{E} + \frac{1}{c} \vec{v}_\alpha \times \vec{B} \right) = 0 \tag{2.5}$$

where we have assumed that the pressure tensor can be represented by the isothermal equation of state $P_\alpha = n_\alpha T_\alpha$. Here v_{T_α} is the thermal velocity for the electron ($\alpha = e$) or ion ($\alpha = i$) species. By using the vector identity

$$\vec{v} \cdot \vec{\nabla} \vec{v} = \frac{1}{2} \vec{\nabla} (\vec{v} \cdot \vec{v}) - \vec{v} \times \vec{\nabla} \times \vec{v} \tag{2.6}$$

and defining the velocity vector $\vec{h}_\alpha \equiv \vec{v}_\alpha + q_\alpha \vec{A} / m_\alpha c$, equation (2.5) can be rewritten as

$$\frac{\partial \vec{h}_\alpha}{\partial t} - \vec{v}_\alpha \times \vec{\nabla} \times \vec{h}_\alpha = -\vec{\nabla} \left(\frac{q_\alpha \phi}{m_\alpha} + \frac{\vec{v}_\alpha^2}{2} + \gamma_\alpha v_{T_\alpha}^2 ln(n_\alpha) \right) \tag{2.7}$$

which will permit easier identification of the relevant variables. Assuming a one dimensional geometry with $\vec{\nabla} = \hat{e}_x \partial / \partial x$ equations (2.3) and (2.7) can be separated into the parallel ($\hat{e}_x$) and the perpendicular ($\hat{e}_y, \hat{e}_z$) directions. Equation (2.7) can thus be written as

$$\frac{\partial h_{\alpha x}}{\partial t} = -\frac{\partial}{\partial x} \left(\frac{q_\alpha \phi}{m_\alpha} + \frac{v_{\alpha x}^2}{2} + \frac{v_{\alpha \perp}^2}{2} + \gamma_\alpha v_{T_\alpha}^2 ln(n_\alpha) \right) \tag{2.8}$$

and

$$\frac{\partial h_{\alpha \perp}}{\partial t} - v_{\alpha x} \frac{\partial h_{\alpha \perp}}{\partial x} = 0 \tag{2.9}$$

$A_\perp$ and $v_{\alpha \perp}$ are transverse components corresponding to electromagnetic fields and the quiver velocity response to such fields. As a simple estimate of (2.9) we

identify $h_{\alpha\perp} \propto \exp[ikx - i\omega t]$ where we have the approximate electromagnetic dispersion relation $\omega \simeq ck$, which is valid in very underdense plasmas. This estimate produces the result

$$(\omega - v_{\alpha x}k)h_{\alpha\perp} = (c - v_{\alpha x})kh_{\alpha\perp} = 0 \tag{2.10}$$

If one is in the nonrelativistic limit where $v_{\alpha x} \ll c$, then $h_{\alpha\perp} \simeq 0$ resulting in the relation $v_{\alpha\perp} = -q_\alpha A_\perp / m_\alpha c$. By assuming $v_{i\perp} \simeq 0$ and using Poisson's equation in the form

$$n_e = Zn_i - \frac{1}{4\pi e}\frac{\partial E_x}{\partial x} \tag{2.11}$$

equation (2.3) reduces to

$$\frac{\partial^2 v_{e\perp}}{\partial t^2} - c^2\frac{\partial^2 v_{e\perp}}{\partial x^2} = -\frac{4\pi e^2 Z n_i}{m_e}v_{e\perp} + \frac{e}{m_e}\frac{\partial E_x}{\partial x}v_{e\perp} \tag{2.12}$$

which describes the evolution of the electron quiver velocity in the electromagnetic wave field. The first term on the right hand side of (2.12) will produce a nonlinear coupling to low frequency ion acoustic modes in the plasma, while the second term produces a nonlinear coupling to high frequency Langmuir modes.

2.1.2 Hydrodynamic and electrostatic field equations

To produce an appropriate equation describing the evolution of the electrostatic components, it is first necessary to clarify which nonlinear terms will significantly affect the evolution of our system in the parameter regime of interest. Due to the large mass difference between the electrons and ions, two distinct timescales will be observed. The electrons will contain both high frequency motion oscillating near the plasma frequency ω_p as well as motion in response to the low frequency

movement of the ions within the ion acoustic timescale $1/\omega_A$. Because of this low frequency response, nonlinear high frequency terms may affect the ion evolution.

In order to separate the two scales it becomes necessary to find the slow time average variation of the enveloped high frequency oscillations of these nonlinear terms. The contribution of a linear high frequency term on the slow ion acoustic timescale will be zero. For an example we write the electron density as

$$n_e = n_0^e + \delta n_e^h + \delta n_e^l \tag{2.13}$$

The electron density contains both high ($\delta n_e^h \sim \delta \tilde{n}^h(\tau)\exp[-i\omega_p t]$) and low ($\delta n_e^l \sim \delta \tilde{n}^l(\tau)$) frequency fluctuations around a constant background density n_0^e. The variation on the ion acoustic timescale represented by τ is held approximately constant over the short time interval $2\pi/\omega_p$. We then average over the fast timescale by integrating from t to $t + 2\pi/\omega_p$, represented by $\langle ... \rangle$. This process will give

$$\langle \delta n_e^l \rangle = \frac{\omega_p}{2\pi}\int_t^{t+2\pi/\omega_p} \tilde{n}^l(\tau)dt = \delta n_e^l \tag{2.14}$$

$$\langle \delta n_e^h \rangle = \frac{\omega_p}{2\pi}\int_t^{t+2\pi/\omega_p} \tilde{n}^h(\tau)\exp[-i\omega_p t]dt = 0 \tag{2.15}$$

The ions are also assumed to contain low frequency fluctuations (δn_i^l) around a constant background density n_0^i and can be written as

$$n_i = n_0^i + \delta n_i^l \tag{2.16}$$

One method of obtaining an equation describing the high frequency evolution of the electrostatic modes is to take the divergence of (2.5) for electrons, and use the continuity equation to produce

$$\frac{\partial^2 n_e}{\partial t^2} - \gamma_e v_{T_e}^2 \frac{\partial^2 n_e}{\partial x^2} = \frac{\partial}{\partial x}\left[v_{ex}\frac{\partial}{\partial x}(n_e v_{ex}) + n_e \frac{\partial}{\partial x}(\frac{v_{ex}^2}{2} + \frac{{v_{e\perp}}^2}{2}) - \frac{q_e n_e}{m_e}E_x\right] \tag{2.17}$$

By ignoring all third order nonlinear terms and using (2.11) in (2.17) we get

$$\begin{aligned}\left(\frac{\partial^2}{\partial t^2} - \gamma_e v_{T_e}^2 \frac{\partial^2}{\partial x^2}\right) Zn_i = &-\frac{1}{4\pi e}\frac{\partial}{\partial x}\left[\frac{\partial^2 E_x}{\partial t^2} - \gamma_e v_{T_e}^2 \frac{\partial^2 E_x}{\partial x^2}\right] \\ &+\frac{\partial}{\partial x}\left[n_0^e \frac{\partial}{\partial x}(v_{ex}^2 + \frac{{v_{e\perp}}^2}{2}) + \frac{Zen_iE_x}{m_e} - \frac{E_x}{4\pi m_e}\frac{\partial E_x}{\partial x}\right]\end{aligned} \tag{2.18}$$

Removing the obvious low frequency linear contributions $\sim Zn_i$ and assuming the high frequency part of the nonlinear hydrodynamical terms $E_x \partial E_x / \partial x$ and $v_{ex} \partial v_{ex} / \partial x$ can be ignored we arrive at the high frequency equation

$$\frac{\partial^2 E_x}{\partial t^2} - 3v_{T_e}^2 \frac{\partial^2 E_x}{\partial x^2} + \frac{4\pi e n_0^e}{2}\frac{\partial v_{e\perp}^2}{\partial x} + \omega_p^2 \left(1 + \frac{\delta n_i^l}{n_0^i}\right) E_x = 0 \tag{2.19}$$

Here the Langmuir field is coupled nonlinearly to the ion motion through the low frequency density fluctuation δn_i^l, where we have assumed $n_0^e \simeq Zn_0^i$.

To identify the low frequency contributions of (2.18) to the ion motion we find the fast time average producing the equation varying over the ion acoustic scales of

$$\begin{aligned}\frac{\partial^2 Zn_i}{\partial t^2} - v_{T_e}^2 \frac{\partial^2 Zn_i}{\partial x^2} = \\ \frac{\partial}{\partial x}\left[n_0^e \frac{\partial}{\partial x}((\langle v_{ex}^2\rangle + \frac{\langle {v_{e\perp}}^2\rangle}{2}) + \frac{Ze\langle n_iE_x\rangle}{m_e} - \frac{1}{8\pi m_e}\frac{\partial \langle E_x^2\rangle}{\partial x}\right]\end{aligned} \tag{2.20}$$

where $\langle E_x \rangle = 0$. By using the divergence of (2.5) for ions and the ion continuity equation one produces the equation

$$\frac{\partial^2 n_i}{\partial t^2} - 3v_{T_i}^2 \frac{\partial^2 n_i}{\partial x^2} = -\frac{\partial}{\partial x}\left[\frac{Ze\langle n_i E_x\rangle}{m_i}\right] \tag{2.21}$$

where we have used $v_{i\perp} \simeq 0$, ignored $v_{ix}\partial v_{ix}/\partial x$ and assumed that E_x can only contribute terms varying on the slow timescale. Equations (2.20) and (2.21) are multiplied by their respective masses to produce the slowly varying density equation of

$$\left(\frac{\partial^2}{\partial t^2} - c_s^2\frac{\partial^2}{\partial x^2}\right)\frac{\delta n_i}{n_0^i} = \frac{\partial^2}{\partial x^2}\left[\frac{Zm_e}{m_i}\langle v_{e\perp}^2\rangle + \frac{1}{8\pi m_i n_0^i}\langle E_x^2\rangle\right] \tag{2.22}$$

In equation (2.22) we have used the linear approximation

$$\mid v_{ex} \mid^2 = \mid \frac{eE_x}{m_e\omega_p} \mid^2 \tag{2.23}$$

to eliminate v_{ex}.

In deriving expression (2.18) we assumed that the nonlinear hydrodynamical terms $v_{ex}\partial v_{ex}/\partial x$ and $E_x\partial E_x/\partial x$ could be ignored. To justify this we return to equation (2.8) for electrons and identify $v_{ex} = h_{ex}$ producing the equation

$$\frac{\partial v_{ex}}{\partial t} + \frac{1}{2}\frac{\partial}{\partial x}\left({v_{ex}}^2 + {v_{e\perp}}^2\right) + \frac{\gamma_e v_{T_e}^2}{n_e}\frac{\partial n_e}{\partial x} - \frac{q_e}{m_e}E_x = 0 \tag{2.24}$$

We assume that the nonlinear couplings can be treated as weak and that a perturbative approach is considered valid. In the linear limit the high frequency electron components of (2.24) will oscillate near the plasma frequency ω_p ie: $E_x, v_{ex} \propto \exp[-i\omega_p t + ik_L x]$ and hence one has the approximation

$$v_{ex} \sim \frac{e \mid E_x \mid}{m_e\omega_p} = \varepsilon v_{T_e} \tag{2.25}$$

where we have defined the electrostatic plasma energy density as $\varepsilon^2 = \mid E_x \mid^2 /4\pi n_0^e T_e$. The term $v_{ex}\partial v_{ex}/\partial x$, the hydrodynamical nonlinearity which leads to high frequency harmonic generation in the Langmuir fields and steepening of the density profile, can be compared to the linear temporal derivative term in (2.24) producing

$$v_{ex}\frac{\partial v_{ex}}{\partial x}/\frac{\partial v_{ex}}{\partial t} \sim \frac{k v_{ex}}{\omega_p} = \frac{k}{k_D}\varepsilon \tag{2.26}$$

Using the linear approximation (2.25) leads to identical results for $E_x\partial E_x/\partial x$ in (2.18), and hence when $\varepsilon k/k_D \ll 1$ the high frequency contribution of these convective terms can be ignored in relation to the linear components. The physical system that we wish to examine contains an intense electromagnetic laser pump which will act through the ponderomotive force term $v_{e\perp}^2$. The efficient coupling of such a pump with the thermal noise can produce strong instabilities thus necessitating the inclusion of the nonlinear electromagnetic term $v_{e\perp}^2$ in the high frequency electrostatic equation.

In the derivation of the slowly varying density equation we neglected the hydrodynamical nonlinearity $v_{ix}\partial v_{ix}/\partial x$. In order to determine the approximate regime where this omission remains valid we assume a slight departure from quasineutrality and allow a slowly varying electrostatic potential ϕ^s to be present. The full electrostatic potential containing both high and low frequency components is thus written as

$$\phi = \phi^f + \phi^s \tag{2.27}$$

and the electron quiver velocity in the $\hat{e}_x$ direction as

$$v_{ex} = v_{ex}^{f} + v_{ex}^{s} \tag{2.28}$$

Here the superscripts refer to the fast and slow timescale variations. To estimate the slow variation of the electrons we use (2.27) and (2.28) in expression (2.8) and separate the slow and fast variation by time averaging over the fast timescale. Ignoring electron inertia effects ($m_e \rightarrow 0$) results in the expression for the slowly varying electron density component of

$$n_e = n_0^e \exp[\frac{e\phi^s}{T_e}] \tag{2.29}$$

Poisson's equation for the slowly varying electrostatic field becomes

$$\frac{\partial^2 \phi^s}{\partial x^2} = 4\pi e \left(n_0^e \exp[\frac{e\phi^s}{T_e}] - Z n_0^i - Z \delta n_i^l \right) \tag{2.30}$$

Using the fact that the slight departure from quasineutrality means $e\phi^s/T_e \ll 1$ we expand the variables in a perturbation series

$$\begin{aligned} \phi^s &= \lambda \phi^{(1)} + \lambda^2 \phi^{(2)} ... \qquad (2.31) \\ \delta n_i^l &= \lambda \delta n^{(1)} + \lambda^2 \delta n^{(2)} ... \qquad (2.32) \end{aligned}$$

producing

$$\frac{\partial^2 \phi^{(1)}}{\partial x^2} = 4\pi e n_0^e \left(\frac{e\phi^{(1)}}{T_e} - \frac{\delta n^{(1)}}{n_0^i} + \lambda \left[\left(\frac{e\phi^{(1)}}{T_e} \right)^2 + \frac{e\phi^{(2)}}{T_e} - \frac{\delta n^{(2)}}{n_0^i} \right] \right) \tag{2.33}$$

where we have used $Z n_0^i = n_0^e$. By assuming that the spatial variation of ϕ^s is very small

$$\frac{1}{k_D^2}\partial^2\phi^{(1)}/\partial x^2 \sim \lambda\phi^{(1)} \tag{2.34}$$

and using a linear waveform for $v_{ix}, \delta n_i^l \propto \exp[-i\omega_A t + ik_A x]$ where $\omega_A = c_s k_A$ is the ion acoustic frequency, produces

$$\left(\frac{k_A}{k_D}\right)^2 = \lambda \tag{2.35}$$

Separating orders of λ also allows us to equate

$$\frac{e\phi^{(1)}}{T_e} = \frac{\delta n^{(1)}}{n_0^i} \tag{2.36}$$

Using the same type of expansion as (2.31) for v_{ix} allows us to expand equation (2.8) for ions as

$$\frac{\partial v_{ix}^{(1)}}{\partial t} + \frac{Ze}{m_i}\frac{\partial\phi^{(1)}}{\partial x} + \frac{3v_{T_i}^2}{n_0^i}\frac{\partial\delta n^{(1)}}{\partial x} + \lambda\left[v_{ix}^{(1)}\frac{\partial v_{ix}^{(1)}}{\partial x} + O(f^{(2)})\right] \tag{2.37}$$

where $O(f^{(2)})$ refers to all other second order quantities. Using the linear waveform $v_{ix}^{(1)}, \delta n^{(1)} \propto \exp[-i\omega_A t + ik_A x]$ produces

$$v_{ix}^{(1)} \sim \frac{c_s\delta n^{(1)}}{n_0^i} \tag{2.38}$$

and thus the convective term is of the order given by

$$v_{ix}^{(1)}\frac{\partial v_{ix}^{(1)}}{\partial x}/\frac{\partial v_{ix}^{(1)}}{\partial t} \sim \frac{k_A v_{ix}^{(1)}}{\omega_A} = \frac{\delta n^{(1)}}{n_0^i} \tag{2.39}$$

The ion convective term is of an order λ smaller than the temporal derivative and hence $\delta n^{(1)}/n_0^i$ is also of the order λ. In order that we may neglect the nonlinear hydrodynamic and other second order terms in (2.33) and (2.37)

$$\frac{\delta n^{(1)}}{n_0^i} \sim \left(\frac{k_A}{k_D}\right)^2 \ll 1 \tag{2.40}$$

If (2.40) is satisfied then one can ignore the ion convective term $v_{ix}\partial v_{ix}/\partial x$ responsible for the steepening of the ion density and generation of ion harmonics.

Finally introducing phenomenological collisional and Landau damping terms we obtain from equations (2.12), (2.19) and (2.22) the system of equations

$$\frac{\partial^2 v_{e\perp}}{\partial t^2} + 2\gamma_j^c \frac{\partial v_{e\perp}}{\partial t} - c^2 \frac{\partial^2 v_{e\perp}}{\partial x^2} + \omega_p^2 \frac{n_i}{n_0^i} v_{e\perp} = \frac{e}{m_e} \frac{\partial E_x}{\partial x} v_{e\perp} \tag{2.41}$$

$$\frac{\partial^2 E_x}{\partial t^2} + 2\gamma_L * \frac{\partial E_x}{\partial t} - 3v_{T_e}^2 \frac{\partial^2 E_x}{\partial x^2} + \frac{4\pi e n_0^e}{2} \frac{\partial v_{e\perp}^2}{\partial x} + \omega_p^2 \frac{n_i}{n_0^i} E_x = 0 \tag{2.42}$$

and

$$\frac{\partial^2 n_i^l}{\partial t^2} + 2\gamma_A * \frac{\partial n_i^l}{\partial t} - c_s^2 \frac{\partial^2 n_i^l}{\partial x^2} = \frac{Z m_e n_0^i}{2m_i} \frac{\partial^2 \langle v_{e\perp}^2 \rangle}{\partial x^2} + \frac{1}{8\pi m_i} \frac{\partial^2 \langle E_x^2 \rangle}{\partial x^2} \tag{2.43}$$

Equations (2.41)-(2.42) represent the high frequency evolution of the Langmuir and electromagnetic components, and permits both the Stokes and anti-Stokes coupling of electromagnetic and electrostatic waves.

In our investigation there are three categories of wave interactions which we will be interested in studying: (a) The Stokes and anti-Stokes coupling of Raman scattering, (b) The Stokes and anti-Stokes coupling of Brillouin scattering, and (c) the Stokes coupling of the PDI cascade components. In Chap. 1 we described the three wave interaction and discussed the six possible decay instabilities, where a pump wave decays into two satellite components. The Stokes coupling of Raman and Brillouin scattering are the decay instabilities corresponding to Fig. 1.2(a) and Fig. 1.2(b) respectively, while the Stokes coupling of PDI corresponds to

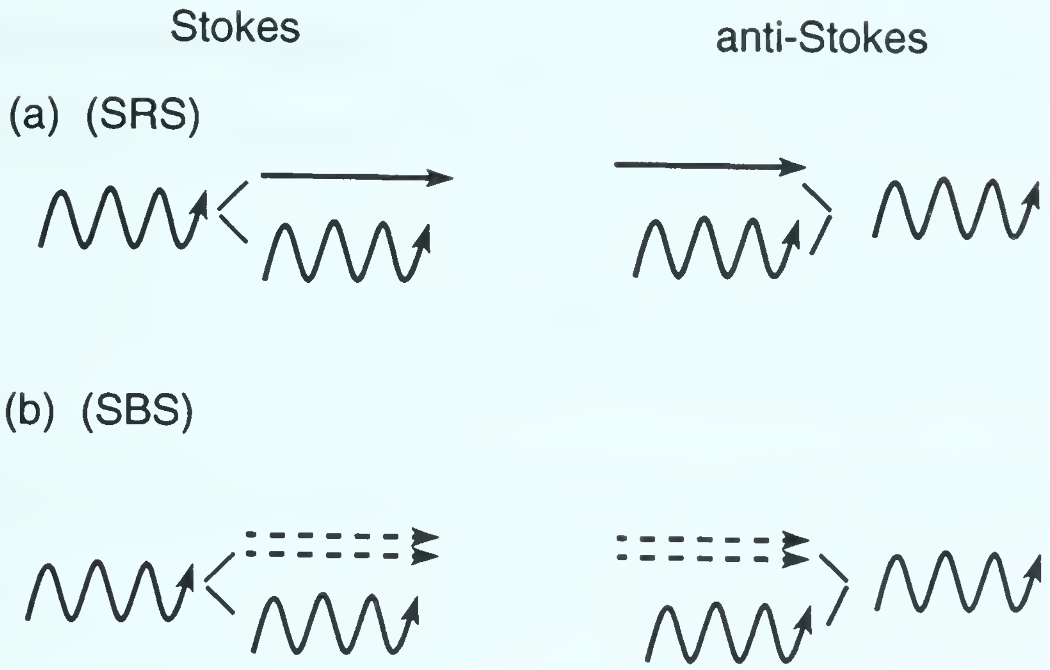

Figure 2.1: *Schematic diagram of Stokes and anti-Stokes coupling of (a) SRS and (b) SBS*

Fig. 1.2(c). In contrast to the decay instability an anti-Stokes coupling requires two existing waves to combine together to produce a third wave. The difference between the Stokes and anti-Stokes coupling is illustrated in diagrammatic form in Fig. 2.1 for (a) Raman and (b) Brillouin scattering. Because of conservation of energy the anti-Stokes coupling by itself cannot be unstable, and hence the amplitude of the scattered wave will be determined by the waves already existing inside the plasma. Although the Langmuir wave associated with the Stokes Raman scattering is mismatched for the production of anti-Stokes Raman coupling, other processes creating Langmuir waves can produce a Langmuir wave which will be resonant for the production of anti-Stokes scattering.

In each of the three wave interactions we are examining the wave modes are assumed to satisfy the linear dispersion relations (1.1)-(1.3). This assumption allows us to easily calculate the approximate wave number of each wave. The wave number of the electromagnetic pump wave in a vacuum is well known as $k_0^v = \omega_0/c$ and is calculated in the plasma to be

$$k_0 = \frac{\omega_0}{c}\sqrt{1 - \frac{n_0}{n_c}} \tag{2.44}$$

where $n_0/n_c = \omega_p^2/\omega_0^2$.

Using the matching conditions (1.11) with $\delta k = 0$ the scattered electromagnetic wave number for the Stokes components is approximately

$$k_R = \pm\frac{\omega_0}{c}\sqrt{1 - 2\sqrt{n_0/n_c}} \tag{2.45}$$

while for the anti-Stokes component it is given by

$$k_{R^+} = \pm\frac{\omega_0}{c}\sqrt{1 + 2\sqrt{n_0/n_c}} \tag{2.46}$$

Here the positive root refers to forward Raman scattering and the negative root refers to backward Raman scattering. The Langmuir wave for both couplings is thus found by

$$k_L = k_0 - k_R \tag{2.47}$$

for the Stokes components and

$$k_{L^+} = k_{R^+} - k_0 \tag{2.48}$$

for the anti-Stokes components. When it is necessary to distinguish between the backward and forward component of Raman scattering we adopt the convention k_L, k_R; k_L^{FR}, k_{FR} for the Stokes components and k_L^{BR+}, k_{R+}; k_L^{FR+}, k_{FR+} for the anti-Stokes components respectively.

The Brillouin backward scattering wave numbers for both the Stokes and anti-Stokes can also be easily estimated. Because the ion acoustic frequency is very small, the scattered light will have approximately the same frequency as the laser light, thus for both the Stokes and anti-Stokes Brillouin scattered light the wave number is given by

$$k_B \sim -k_0; \qquad k_{B+} \sim -k_0 \tag{2.49}$$

respectively. The ion acoustic wave number associated with the Brillouin scatter will thus be given by

$$k_A = k_0 - k_B \sim 2k_0; \qquad k_{A+} = k_{B+} - k_0 \sim -2k_0 \tag{2.50}$$

for the Stokes and anti-Stokes components respectively.

In our investigation we assume that the pump wave associated with PDI is supplied by the SRS driven Langmuir wave. As was shown in Chap. 1 the satellite components are given by

$$k_L^{(1)} = \Delta k - k_L \tag{2.51}$$

for the Langmuir satellite, where $\Delta k = \frac{2}{3} k_D \sqrt{Z m_e / m_i}$ and

$$k_A^{(1)} = k_L - k_L^{(1)} = 2k_L - \Delta k \tag{2.52}$$

for the ion acoustic satellite. The Langmuir satellite of PDI can also decay producing a cascade of waves. In general the satellites of the $n+1$ stage of the cascade can be calculated as

$$k_L^{(n+1)} = (-1)^n \Delta k - k_L^{(n)} \tag{2.53}$$

for the Langmuir wave and

$$k_A^{(n+1)} = k_L^{(n)} - k_L^{(n+1)} \tag{2.54}$$

for the ion acoustic wave. The wave numbers for all the processes are summarized in table 2.1

In our investigation we wish to examine the behavior of (2.41)-(2.43) only on the ion acoustic timescale. To reduce the system to this single timescale we introduce the quantities

$$\begin{aligned} E_x &= \frac{1}{2}(E \exp[-i\omega_p t] + c.c) && (2.55) \\ v_{e\perp} &= \frac{1}{2}(\Psi_0 \exp[-i\omega_0 t] + \Psi_R \exp[-i(\omega_0 - \omega_p)t] \\ &\quad + \Psi_{R+} \exp[-i(\omega_0 + \omega_p)t] + c.c.) && (2.56) \end{aligned}$$

and average over the fast timescale. Here E and Ψ_j are assumed to vary only on a slow timescale related to the ion dynamics. Thus with $n_i = n_0^i + \delta n_i^l$ and by dropping second order time derivatives of the slowly varying components we obtain our basic equations

$$\begin{aligned} & i(\frac{\partial E}{\partial t} + \gamma_L * E) + \frac{3}{2}\frac{v_{T_e}^2}{\omega_p}\frac{\partial^2 E}{\partial x^2} - \frac{\omega_p}{2} N E && (2.57) \\ & \qquad = \frac{\pi e n_0^e}{\omega_p}\frac{\partial}{\partial x}(\Psi_0 \Psi_R^* + \Psi_0^* \Psi_{R+}) + S_L(x,t), \end{aligned}$$

	wave numbers		
SRS Stokes	$k_0 = \frac{\omega_0}{c}\sqrt{1-\frac{n_0}{n_c}}$	$k_R = \pm\frac{\omega_0}{c}\sqrt{1-2\sqrt{\frac{n_0}{n_c}}}$	$k_L = k_0 - k_R$
SRS anti-Stokes	$k_0 = \frac{\omega_0}{c}\sqrt{1-\frac{n_0}{n_c}}$	$k_{R^+} = \pm\frac{\omega_0}{c}\sqrt{1+2\sqrt{\frac{n_0}{n_c}}}$	$k_{L^+} = k_{R^+} - k_0$
SBS Stokes	$k_0 = \frac{\omega_0}{c}\sqrt{1-\frac{n_0}{n_c}}$	$k_B \sim -k_0$	$k_A^B \sim 2k_0$
SBS anti-Stokes	$k_0 = \frac{\omega_0}{c}\sqrt{1-\frac{n_0}{n_c}}$	$k_{B^+} \sim -k_0$	$k_A^{B^+} \sim -2k_0$
PDI	k_L	$k_L^{(n+1)} = (-1)^n \Delta k - k_L^{(n)}$	$k_A^{(n+1)} = k_L^{(n)} - k_L^{(n+1)}$

Table 2.1: *Wave numbers associated with the three wave processes of the Stokes and anti-Stokes coupling of SRS, and SBS as well as the Stokes coupling of PDI. Here* $\Delta k = \frac{2}{3}k_D(Zm_e/m_i)^{1/2}$

$$\begin{aligned}
&\frac{\partial^2 N}{\partial t^2} + 2\gamma_A * \frac{\partial N}{\partial t} - c_s^2\frac{\partial^2 N}{\partial x^2} \\
&\qquad = \frac{\partial^2}{\partial x^2}\left(\frac{\mid E\mid^2}{16\pi n_0^i m_i} + \frac{Zm_e}{4m_i}\mid \Psi_0 \mid^2\right) + S_A(x,t),
\end{aligned} \tag{2.58}$$

$$\begin{aligned}
&i(\frac{\partial \Psi_0}{\partial t} + \gamma_0^c \Psi_0) + \frac{c^2}{2\omega_0}\frac{\partial^2 \Psi_0}{\partial x^2} - \frac{\omega_p^2 - \omega_0^2}{2\omega_0}\Psi_0 \\
&\qquad = \frac{\omega_p^2}{2\omega_0} N \Psi_0 - \frac{e}{4\omega_0 m_e}\left(\Psi_R \frac{\partial E}{\partial x} + \Psi_{R^+}\frac{\partial E^*}{\partial x}\right),
\end{aligned} \tag{2.59}$$

$$\begin{aligned}
&i(\frac{\partial \Psi_R}{\partial t} + \gamma_R^c \Psi_R) + \frac{c^2}{2(\omega_0 - \omega_p)}\frac{\partial^2 \Psi_R}{\partial x^2} - \frac{\omega_p^2 - (\omega_0 - \omega_p)^2}{2(\omega_0 - \omega_p)}\Psi_R \\
&\qquad = \frac{\omega_p^2}{2(\omega_0 - \omega_p)} N \Psi_R - \frac{e}{4(\omega_0 - \omega_p) m_e}\Psi_0 \frac{\partial E^*}{\partial x},
\end{aligned} \tag{2.60}$$

$$i(\frac{\partial \Psi_{R^+}}{\partial t} + \gamma_{R^+}^c \Psi_{R^+}) + \frac{c^2}{2(\omega_0 + \omega_p)}\frac{\partial^2 \Psi_{R^+}}{\partial x^2} - \frac{\omega_p^2 - (\omega_0 + \omega_p)^2}{2(\omega_0 + \omega_p)}\Psi_{R^+} \tag{2.61}$$

$$= \frac{\omega_p^2}{2(\omega_0+\omega_p)} N\Psi_{R^+} - \frac{e}{4(\omega_0+\omega_p)m_e}\Psi_0\frac{\partial E}{\partial x},$$

where Ψ_j represents the electromagnetic quiver velocity wave amplitudes with $j = 0, R, R^+$ representing the laser pump, Raman Stokes and anti-Stokes components respectively, E is the electrostatic field amplitude, and $N = n^i/n_0^i - 1$ is the low frequency ion density wave amplitude. The asterisk denotes complex conjugate. One can extract the Zakharov equations from the above system by ignoring the electromagnetic components. Thus the left hand side of (2.57) is easily recognizable as the Langmuir equation (1.15). (1.16) is also recognized in (2.58) by removing the electromagnetic ponderomotive potential.

In the electromagnetic evolution equations γ_j^c represent the collisional damping terms. Similarly in the equation describing Langmuir evolution $\gamma_L(k)$ includes the collisional damping as well as the Landau damping term which is defined by

$$\gamma_L(k) = \sqrt{\frac{\pi}{8}}\omega_p\frac{k_D^3}{k^3}\exp[-\frac{1}{2}(3+\frac{k_D^2}{k^2})] + \frac{\nu_e}{2}. \tag{2.62}$$

In the heavily damped Landau regime where $k \geq k_D$ the Landau operator was replaced by a linear dependence on k. In (2.62) ν_e represents the electron-ion collision rate. The ion acoustic wave damping is attributed to Landau damping and is represented by

$$\gamma_A(k) = \sqrt{\frac{\pi}{8}}c_s k\left(\sqrt{\frac{Zm_e}{m_i}} + \left(\frac{ZT_e}{T_i}\right)^{3/2}\exp[-(\frac{3}{2}+\frac{ZT_e}{2T_i})]\right), \tag{2.63}$$

The electron-ion temperature ratio dependence of the ion Landau damping can greatly affect the nonlinear saturation behavior of SRS causing for example, strong quasi-periodic pulsations or bursting of SRS reflectivity (see Chap. 3). Both the electron and ion damping in (2.57) and (2.58) are convolution operators applied in

Fourier space [70].

The electrostatic source terms for the Langmuir waves $S_L(x,t)$ and the ion acoustic waves $S_A(x,t)$ are derived from the linearized electrostatic equations (see appendix I for details). The random amplitudes of these modes are introduced at values consistent with thermal equilibrium levels with the intention of modeling, in the absence of an electromagnetic pump, a plasma at thermal equilibrium [71], [72].

To model a realistic plasma, finite geometry boundary conditions in (2.59)-(2.61) are imposed. Such conditions allow an electromagnetic pump wave to enter on the left boundary at a constant amplitude and leave freely on the right boundary. The left boundary also allows Brillouin backscatter to exit freely. Similarly the remaining electromagnetic equations allow for both forward and backward traveling components to exit freely from the right and left boundaries respectively. Langmuir and ion acoustic waves in (2.57) and (2.58) also have outgoing boundary conditions with narrow regions of artificial damping added at both ends to prevent reflections back into the plasma.

2.2 Three wave interaction

The parametric instability known as the three wave interaction is a common model used to describe wave evolution in a plasma. One well known example of three wave interaction is stimulated Raman scattering which is found by using the Stokes coupling of Raman scattering. The anti-Stokes Raman coupling, though a three wave process, is not an instability and will not grow exponentially. To illustrate the difference between the two couplings we examine only the Raman coupling of equations (2.41)-(2.42) by setting $n_i = n_0^i$ =constant and using

$$v_{e\perp} = v_0 + v_R \tag{2.64}$$

Here v_0 corresponds to the laser pump and v_R corresponds to the Raman scattered wave. Ignoring the harmonic generation terms v_0^2 and v_R^2 as well as the damping coefficients we have

$$\frac{\partial^2 v_0}{\partial t^2} - c^2 \frac{\partial^2 v_0}{\partial x^2} + \omega_p^2 v_0 = \frac{e}{m_e} \frac{\partial E_x}{\partial x} v_R \tag{2.65}$$

$$\frac{\partial^2 v_R}{\partial t^2} - c^2 \frac{\partial^2 v_R}{\partial x^2} + \omega_p^2 v_R = \frac{e}{m_e} \frac{\partial E_x}{\partial x} v_0 \tag{2.66}$$

and

$$\frac{\partial^2 E_x}{\partial t^2} - 3v_{T_e}^2 \frac{\partial^2 E_x}{\partial x^2} + \omega_p^2 E_x = -\frac{4\pi e n_0^e}{2} \frac{\partial}{\partial x}(v_0 v_R) \tag{2.67}$$

For the Stokes coupling of Raman scattering there exists a feedback mechanism which can lead to an instability. Figure 2.2 illustrates this mechanism in diagrammatic form. In Fig. 2.2 an initial electron density fluctuation δn_e produces a transverse current $\propto \delta n_e v_0$ corresponding to the oscillatory motion of the electrons in the laser field. This transverse current in turn produces a reflected light wave v_R. The reflected light wave can then couple with the laser light wave producing a ponderomotive force $\propto v_R v_0$ which enhances the initial density fluctuation and leads to exponential growth. In contrast the anti-Stokes coupling will not produce the feedback mechanism of Fig. 2.2. Because of the coupling process the initial density perturbation must combine with the laser pump to produce the anti-Stokes Raman scattered light wave. Instead of being enhanced the density fluctuation is reduced as energy from the Langmuir wave is transferred to the anti-Stokes light

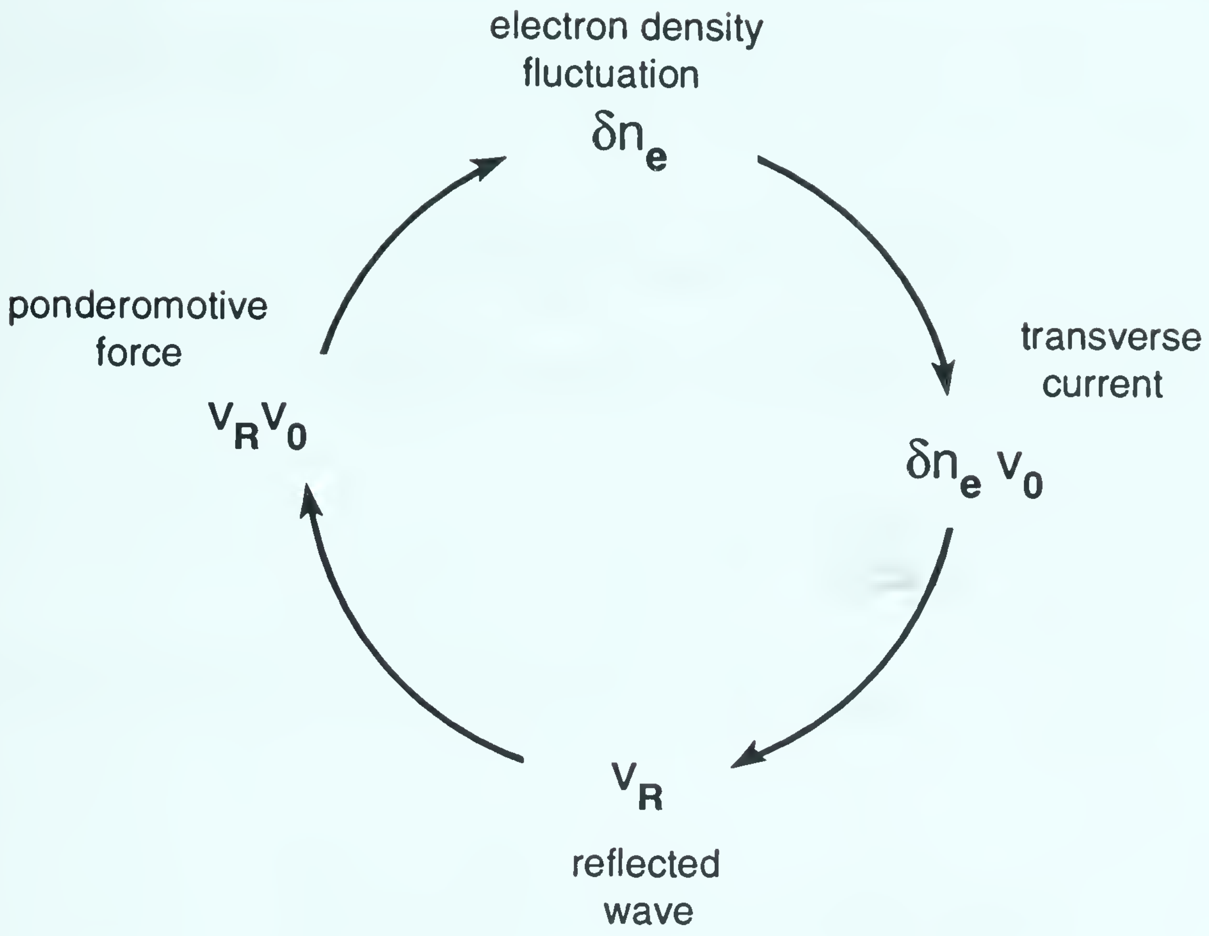
electron density
fluctuation
δn_e
transverse
current
$\delta n_e\, v_0$
v_R
reflected
wave
ponderomotive
force
$v_R v_0$

Figure 2.2: *Schematic diagram of the stimulated Raman scattering feedback mechanism*

wave. Thus the amplitude of the anti-Stokes Raman wave can grow only if there already exists large levels of Langmuir waves in the plasma, which can transfer energy to the anti-Stokes component. For this reason a three wave interaction usually refers only to the Stokes coupling of the scattering processes.

As an example of the three wave interaction model we derive the relevant equations for stimulated Raman scattering. To derive the three wave equations we return to our equations (2.41)-(2.43) and assume that the dependent variables can be represented in terms of slowly varying amplitudes $E_j(x,t)$ of the plasma eigenmodes. The fast time (short length scale) behavior of these modes is characterized by frequencies $\omega_j(k_j)$ (wave numbers k_j) satisfying linear dispersion relations (1.1)-

(1.3). For SRS the electromagnetic and electrostatic components of (2.41) - (2.42) are represented by

$$v_{e\perp} = \frac{1}{2}(\frac{eE_0(x,t)}{m_e\omega_0}\exp[i(k_0x-\omega_0(k)t)]$$
$$+\frac{eE_R(x,t)}{m_e\omega_R}\exp[i(k_Rx-\omega_R(k)t)]+c.c.) \tag{2.68}$$

$$E_x = \frac{1}{2}(E_L(x,t)\exp[i(k_Lx-\omega_L(k)t)]+c.c.) \tag{2.69}$$

and when inserted in (2.41)-(2.42) produce the results

$$\begin{aligned}
\frac{\partial E_0}{\partial t}+V_0\frac{\partial E_0}{\partial x}+\gamma_0E_0 &= -\frac{1}{4}\frac{e}{m_e}\frac{k_L}{\omega_R}E_RE_L && (2.70)\\
\frac{\partial E_L}{\partial t}+V_L\frac{\partial E_L}{\partial x}+\gamma_LE_L &= \frac{1}{4}\frac{e}{m_e}\frac{k_L\omega_p^2}{\omega_R\omega_0\omega_L}E_0E_R^* && (2.71)\\
\frac{\partial E_R}{\partial t}+V_R\frac{\partial E_R}{\partial x}+\gamma_RE_R &= \frac{1}{4}\frac{e}{m_e}\frac{k_L}{\omega_0}E_0E_L^* && (2.72)
\end{aligned}$$

where $V_L = 3v_{T_e}^2k_L/\omega_L$ and $V_j = c^2k_j/\omega_j; j = 0, R$, are the group velocities of the Langmuir field and the pump and backscattered electromagnetic components respectively and γ_j represents the appropriate damping coefficient. In producing (2.70)-(2.72) all second order derivatives of slowly varying components were assumed to be very small and dropped from the equations. The derivatives of slowly varying components involved in nonlinear coupling terms were also assumed to be small and were ignored.

2.2.1 Standard equations for three wave coupling

By making the substitutions

$$E_0 = a_0; \qquad E_L = a_1 \frac{\omega_p}{\sqrt{\omega_0 \omega_L}}; \qquad E_R = a_2 \sqrt{\frac{\omega_R}{\omega_0}}; \qquad \tilde{\Gamma} = \frac{e \omega_p k_L}{4 m_e \omega_0 \sqrt{\omega_R \omega_L}} \tag{2.73}$$

and relabeling

$$V_0 = c_0; \quad V_L = c_1; \quad V_R = c_2; \quad \gamma_L = \gamma_1; \quad \gamma_R = \gamma_2 \tag{2.74}$$

the SRS three wave equations can be written in the standard form of

$$\frac{\partial a_0}{\partial t} + c_0 \frac{\partial a_0}{\partial x} + \gamma_0 a_0 = -\tilde{\Gamma} a_1 a_2 \tag{2.75}$$

$$\frac{\partial a_1}{\partial t} + c_1 \frac{\partial a_1}{\partial x} + \gamma_1 a_1 = \tilde{\Gamma} a_0 a_2^* \tag{2.76}$$

$$\frac{\partial a_2}{\partial t} + c_2 \frac{\partial a_2}{\partial x} + \gamma_2 a_2 = \tilde{\Gamma} a_1^* a_0 \tag{2.77}$$

All three wave interactions can be written in this form allowing one to analyze general properties of the system. By assuming that a_0 represents a constant finite amplitude pump one can linearize (2.75)-(2.77) producing

$$\frac{\partial a_1}{\partial t} + c_1 \frac{\partial a_1}{\partial x} + \gamma_1 a_1 = \Gamma a_2^* \tag{2.78}$$

$$\frac{\partial a_2}{\partial t} + c_2 \frac{\partial a_2}{\partial x} + \gamma_2 a_2 = \Gamma a_1^* \tag{2.79}$$

This system describes the linear interaction of two small amplitude waves interacting with a constant finite amplitude wave and can be used to discuss the absolute and convective nature of 3WI as well as illustrate an asymptotic intermediate regime which has length dependent growth rates. Here we have defined $\Gamma = \tilde{\Gamma} a_0$ which is found to be equivalent to the maximum growth rate of the system.

2.2.2 Absolute and convective instabilities

The terms absolute and convective are used in the literature to classify linear interactions into either temporally (absolute) or spatially (convective) growing instabilities. Formally one can define an absolute or convective instability in terms of the physical characteristics of a localized pulse propagating through an unstable medium (cf. [12]). This pulse can grow in one of two ways: (a) If the pulse originally located at the origin, grows in time but propagates away from the origin, so that eventually the disturbance at the origin disappears then the instability is classified as convective. (b) If the pulse grows in time and spreads through space such that at some asymptotic late time the pulse encompasses all space then it is referred to as an absolute instability.

In a more mathematical form one can define an absolute instability as follows: It is assumed that a linear dispersion relation

$$D(k, \omega(k)) = 0 \tag{2.80}$$

has unstable roots $\Im(\omega) > 0$ for some real wave number k. For an absolute instability to exist there must be two solutions of (2.80) for some k requiring that $D(k, \omega) = 0$ and $\partial D(k, \omega)/\partial k = 0$ to exist for some ω. These wave numbers must lie on opposite sides of the complex wave number contour C_k (see Fig. 2.3(a)) which will coalesce to pinch that contour at the same k_0 when one approaches the correct solution for ω with $\Im(\omega) > 0$ by lowering the complex frequency contour C_ω (see Fig. 2.3(b)). If these conditions are met then one has a nonconvective or absolute instability. If these conditions are not met only a convective instability is possible.

To examine these concepts more closely, we derive the various growth rates for

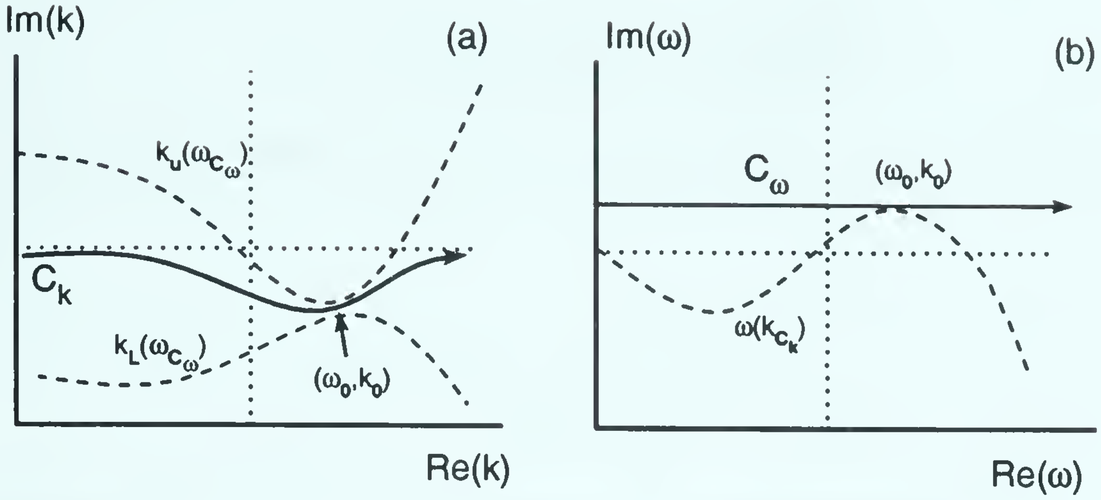

Figure 2.3: *Deformation of the Fourier contour (a) and associated lowering of the Laplace contour (b)*

the general linearized 3WI equations in an infinite regime. To derive the growth rates in a simple manner we start by assuming the ansatz $a_1 = A_1 \exp[i(kx - \omega t)]$ and $a_2 = A_2 \exp[-i(kx - \omega^* t)]$ where A_1, A_2 are constants, and ω, (k) vary on the slow time, (large length) scales. Here we again use the asterisk to denote complex conjugate and we have assumed a priori that k is real and ω complex. This ansatz leads to the following dispersion relation for equations (2.78), and (2.79) of [12]:

$$D(k,\omega) = (\omega - c_1 k + i\gamma_1)(\omega - c_2 k + i\gamma_2) + \Gamma^2 = 0 \tag{2.81}$$

For an absolute instability to be possible requires that a double root of the appropriate form $D(k,\omega) = 0$ and $\partial D(k,\omega)/\partial k = 0$ exist. Using $\partial D(k,\omega)/\partial k = 0$ yields

$$k = \{\omega(c_1 + c_2) + i(c_1\gamma_2 + c_2\gamma_1)\} \times \frac{1}{2c_1c_2} \tag{2.82}$$

which produces the frequency

$$\omega = -i\frac{(c_1\gamma_2 - c_2\gamma_1)}{c_1 - c_2} \pm \Gamma\frac{2\sqrt{c_1c_2}}{\mid c_1 - c_2 \mid} \tag{2.83}$$

Notice that equation (2.83) can only be unstable if $c_1c_2 < 0$ and has a threshold given by

$$\Gamma^2 > \frac{(\mid c_1 \mid \gamma_2 + \mid c_2 \mid \gamma_1)^2}{4 \mid c_1c_2 \mid} = \gamma_a^2 \tag{2.84}$$

The maximum growth rate for the undamped system is given by

$$\Gamma_{abs} = \Gamma\frac{2\sqrt{c_1c_2}}{\mid c_1 \mid + \mid c_2 \mid} \tag{2.85}$$

If $c_1c_2 > 0$ then an absolute instability is not possible, however one can still have a convective instability if the threshold $\Gamma^2 > \gamma_2\gamma_1 = \gamma_c^2$ is met. The maximum convective growth rate can be easily found by simply solving equation (2.81) for the static solution where $\omega_{Real} = k = 0$ producing a growth rate of

$$\Gamma_{conv} = -\frac{(\gamma_1 + \gamma_2)}{2} \pm \frac{1}{2}\left[(\gamma_1 - \gamma_2)^2 + 4\Gamma^2\right]^{1/2} \tag{2.86}$$

This growth rate may be observed in an infinitely extended plasma or during the time period required by the fastest moving modes to identify where the boundaries are located.

2.2.3 Finite interaction length

In Chap. 2.2.2, growth rates for an infinitely extended plasma were developed. The introduction of a finite length however produces a critical length below which instabilities will no longer grow exponentially. Returning to equations (2.78) and (2.79) and demanding $c_1c_2 < 0$ and $\Gamma^2 > \gamma_a^2$ so that we are in the absolute regime we assume combinations of waves in the form of $\exp[pt + ikx]$ and $\exp[pt - ik^*x]$

$$a_1 = A\exp[pt + ikx] + B\exp[pt - ik^*x] \tag{2.87}$$

$$a_2 = C\exp[pt + ikx] + D\exp[pt - ik^*x] \tag{2.88}$$

where p is the effective absolute growth rate. By defining $\alpha = \Gamma/\sqrt{c_1 c_2}$ and $P = p/\Gamma_{abs} + \gamma_a/\Gamma$ together with the boundary conditions $a_1(0) = 0, a_2(L_I) = 0$ yields simple solutions of the form

$$a_1 = A_1 \exp[pt - \lambda x]\sin(\beta x) \tag{2.89}$$

$$a_2 = A_2 \exp[pt - \lambda x]\cos(\beta x) \tag{2.90}$$

where $\beta = \{\alpha^2(1 - P^2)\}^{1/2}$ and $\lambda = (p + \gamma_1)/2c_1 - (p + \gamma_2)/2 \mid c_2 \mid$. To meet the boundary conditions we require

$$\beta L_I = \{\alpha^2(1 - P^2)\}^{1/2} L_I = (2n + 1)\frac{\pi}{2} \qquad n = 0, 1, 2... \tag{2.91}$$

where L_I is the interaction length associated with the absolute instability. Since $0 \leq P \leq 1$ the smallest possible length for instability [73], [74] is

$$L_{cr} = \frac{\pi}{2\alpha} = \frac{\pi}{2}\frac{\sqrt{c_1 \mid c_2 \mid}}{\Gamma} \tag{2.92}$$

where the effect of damping is to increase the critical length of the instability. Finding the spatial maxima of a_1 and a_2, we see that the reflected wave a_2 has an amplitude maximum at $x = 0$ and a_1 has an amplitude maximum at $x = \frac{1}{\beta}\tan^{-1}(\beta/\lambda)$. Since a_1 is exponentially damped, $\sin(\beta x)^2 = \frac{1}{2}[1 - \cos(2\beta x)]$ shows that most of the energy of a_1 should reside between 0 and $2L_{cr}$. Equations (2.91)

and (2.92) allow us to calculate the maximum growth rate for a finite interaction length predicting a rate

$$p = \Gamma_{abs}\sqrt{1 - \left(\frac{L_{cr}}{L_I}\right)^2} - \frac{\Gamma_{abs}\gamma_a}{\Gamma} \tag{2.93}$$

which will be very sensitive to short interaction lengths.

2.2.4 Intermediate asymptotic dependence of growth rate on length

If the interaction length of the plasma is sufficiently long an intermediate regime which is characterized by a length dependent growth rate is asymptotically obtainable. To examine this asymptotic form we return to equations (2.78) and (2.79) and assuming that $\mid c_1 \mid \ll \mid c_2 \mid$, $\mid c_1 \partial a_1/\partial x \mid \ll \mid \partial a_1/\partial t \mid$, $\mid c_2 \partial a_2/\partial x \mid \gg \mid \partial a_2/\partial t \mid$ and ignoring damping for simplicity

$$\begin{aligned} \frac{\partial a_1}{\partial t} &= \Gamma a_2^* && (2.94) \\ c_2\frac{\partial a_2^*}{\partial x} &= \Gamma a_1. && (2.95) \end{aligned}$$

Taking the spatial derivative of (2.94), using (2.95) and a Laplace transform over time results in a simple ordinary differential equation which can be integrated spatially from 0 to L resulting in

$$A = A_0 \exp\left[\frac{\Gamma^2 L}{izc_2}\right]. \tag{2.96}$$

Here

$$A = \int_0^\infty a_1 \exp[-izt]dt \tag{2.97}$$

is the Laplace transform of a_1. Inverting the Laplace transform and making the change of variables $i\alpha y = izt$ where $\alpha = \Gamma\sqrt{Lt/c_2}$ yields

$$a_2 = \frac{A_0\alpha}{t}\int_C \exp\left[\alpha(y - \frac{1}{y})\right] dy \tag{2.98}$$

The integrand of equation (2.98) is a generator for Bessel functions thus producing

$$a_2 = \frac{A_0\alpha}{t} I_1(2\alpha) \tag{2.99}$$

which has the asymptotic form

$$a_2 = \frac{A_0\sqrt{\Gamma\sqrt{Lt/c_2}}}{t}\exp[2\Gamma\sqrt{Lt/c_2}] \tag{2.100}$$

The effective growth rate in the intermediate regime is thus given by

$$\Gamma_{int} \simeq \Gamma\sqrt{L/c_2 t} \tag{2.101}$$

Our simple expression is in agreement with similar work by Mounaix et al. [75] who used a Green's function analysis in the context of short pulse, long scale length, Brillouin experiments for which Brillouin scattering was below absolute threshold. Under such circumstances one observes the intermediate growth rate for times $L/c_2 < t < L/c_1$ and a convective stationary regime for times greater than $t > L/c_1$ where the energy growth Γ_{int} balances the damping of the waves γ_1 resulting in the characteristic spatial growth $\sim \exp[\Gamma^2 L/\gamma_1 c_2]$. However when one is above the absolute threshold this stationary regime is excluded and the absolute growth dominates asymptotically. For most of our full model simulation runs we remain above the absolute threshold and absolute growth of the plasma can occur. Once the absolute growth rate $\Gamma_{abs} \simeq 2\Gamma\sqrt{c_1/c_2}$ exceeds the intermediate growth,

it dominates the evolution of the plasma. By equating (2.101) with this absolute growth rate one can estimate the time at which this occurs as

$$t \simeq \frac{L}{4c_1} \tag{2.102}$$

In order to summarize the parametric instabilities which will dominate the analysis of this study, a summary of the linear wavemode group velocities and the various growth rates for the SRS, SBS and PDI three wave interactions is presented in Table 2.2.4. Also given are the convective and absolute thresholds for the three instabilities. For the instabilities involving electromagnetic wave modes the laser pump amplitude is given by $v_o = \Psi_0(x=0) = eE_0/m_e\omega_0$. The Langmuir pump wave for PDI is assumed to be represented by E_L which in the case of SRS saturation by PDI is the amplitude of the SRS driven Langmuir mode.

	electromagnetic	electrostatic	ion acoustic
Group velocity	$V_j = \frac{k_j c^2}{\omega_j};\ j = 0, R, B$	$V_L = \frac{3v_{T_e}^2 k_L}{\omega_L}$	$c_s = \sqrt{\frac{(ZT_e+3T_i)}{m_i}}$

	Growth rates		
	SRS	SBS	PDI
Convective	$\Gamma_{SRS} = \frac{k_L v_0 \omega_p}{4\sqrt{\omega_L \omega_R}}$	$\Gamma_{SBS} = \omega_p v_0 \sqrt{\frac{\omega_A}{8\omega_B v_T^2}}$	$\Gamma_{PDI} = \sqrt{\frac{\omega_p \omega_A \lvert E_L\rvert^2}{64\pi n_0^e T_e}}$
Intermediate	$\Gamma_{int} \simeq \Gamma_{SRS}\sqrt{\frac{L}{\lvert V_R\rvert t}}$	$\Gamma_{int} \simeq \Gamma_{SBS}\sqrt{\frac{L}{\lvert V_B\rvert t}}$	$\Gamma_{int} \simeq \Gamma_{PDI}\sqrt{\frac{L}{\lvert V_L\rvert t}}$
Absolute	$\Gamma_{abs} = \Gamma_{SRS}\frac{2\sqrt{V_L\lvert V_R\rvert}}{\lvert V_L\rvert+\lvert V_R\rvert}$	$\Gamma_{abs} = \Gamma_{SBS}\frac{2\sqrt{c_s\lvert V_B\rvert}}{\lvert c_s\rvert+\lvert V_B\rvert}$	$\Gamma_{abs} = \Gamma_{PDI}\frac{2\sqrt{c_s V_L}}{\lvert c_s\rvert+\lvert V_L\rvert}$

	Thresholds		
	SRS	SBS	PDI
Convective	$\Gamma_{SRS}^2 > \gamma_L(k_L)\gamma_R$	$\Gamma_{SBS}^2 > \gamma_A(k_A^B)\gamma_B$	$\frac{E_L^2}{4\pi n_0^e T_e} > \frac{16\gamma_A(k_A^{(1)})\gamma_L(k_L)}{\omega_L \omega_A^{(1)}},$
Absolute	$\frac{(\lvert V_L\rvert\gamma_R+\lvert V_R\rvert\gamma_L(k_L))^2}{4\lvert V_L V_R\rvert}$	$\frac{(\lvert c_s\rvert\gamma_B+\lvert V_B\rvert\gamma_A(k_A^B))^2}{4\lvert c_s V_B\rvert}$	$\frac{(\lvert c_s\rvert\gamma_L(k_L)+\lvert V_L\rvert\gamma_A(k_A^{(1)}))^2}{4\lvert c_s V_L\rvert}$

Table 2.2: *Group velocities for the various linear wave modes and growth rates and thresholds for SRS, SBS, PDI in the convective, intermediate and absolute regimes.*

Chapter 3

Analysis of stimulated Raman scattering evolution

The spatial and temporal evolution of SRS has been investigated by many authors, and although a great deal of information has been accumulated, a large number of questions remain unanswered. In particular, the mechanisms responsible for the saturation of SRS as well as other instabilities are still poorly understood. It has been suspected for many years that the interaction of the Langmuir field with ion density fluctuations is one mechanism which can lead to saturation of SRS. Numerous early studies have investigated this possibility using various models [55], [56], [76], [77], [78]. While meeting with limited success in properly explaining the saturation process by in effect removing the SRS driven Langmuir waves through a crude PDI model, these early studies fail in the details as will be seen, for example in Chap. 3.4. The primary reason for this lack of progress appears to be linked to the description of SRS saturation through PDI. In their investigation of SRS saturation Heikkinen and Karttunen [78] used a five wave interaction (5WI) model which consisted of a slowly varying amplitude approximation for the three SRS wave modes with the addition of the first PDI cascade satellites. Such a description does not allow for the production of quasimode components or further evolution of

the PDI cascade.

In recent years, it began to be understood that some model between the coherent mode coupling models and the large velocity distribution function codes had to be found in order to test these concepts over the long times necessary for the ion motion to affect SRS. A major advance in this area was introduced by Aldrich et al. [63] who in 1986 proposed a model which coupled the electromagnetic components of stimulated scattering processes to the more accurate Zakharov description of electron-ion coupling. The Zakharov description is more accurate because it allows one to examine the entire electrostatic wave number spectra without the necessity of describing each individual wave mode. This model was also used in later research to investigate SRS-SBS competition [49] within the context of such experimental observations by Walsh et al. [46], [47], [48]. Competition between SRS and SBS for laser pump energy is another process that can produce saturation of SRS. Investigations done by Kruer and his colleagues [16], [79], [80], used particle in cell (PIC) simulations to study this evolution of SRS and SBS and other related phenomena. A very similar but slightly more general model based on the Aldrich model was used by Rozmus et al. [64] to investigate simultaneous SRS-SBS evolution and the resultant effect on particle heating.

Other models which include the electron-ion coupling were investigated by Bonnaud et al. [81], [82], [83] who studied the saturation of SRS by PDI. In this study an appropriate saturation mechanism for SBS was absent, limiting the investigation to short time behavior. Collisional damping, which may be a very important experimental consideration [84], [85], [86], [87], and which we have found to be important in determining the level of SRS saturation [67], [68], was missing in the simulations.

In 1990 Drake and Batha [43], to explain experimental observations, used a scaling model for the saturation of the SRS reflectivity which was proportional to the PDI threshold. This scaling law was derived from a five wave model of SRS saturation by PDI [78], and is limited by this simple model. The more complete representation of the electron-ion evolution supplied by the Zakharov model allows us to produce a more accurate description of SRS saturation, and permits us to improve upon this scaling law.

In regimes where the plasma is in a turbulent state, called strong Langmuir turbulence, the Zakharov model can be used to describe the characteristic collapsing solutions of high frequency plasma waves trapped in self consistent density cavities. An investigation of strong Langmuir turbulence acting as a saturation mechanism of SRS is being conducted by Bezzerides et al. [65], in parallel with our present study, and is examining a much more turbulent regime of parameters than those examined here. Until our present study the evolution of SRS and its saturation by PDI in weakly and more strongly driven regimes had not been described in great detail and a reasonable analytical analysis was lacking. In order to improve on the SRS reflectivity scaling law proposed by Drake and Batha and to explore the early and late time evolution of SRS in long scale length plasmas, for which an accurate description of electron-ion evolution is present, we have studied SRS evolution in the presence of the Zakharov coupling.

To expand our understanding of SRS evolution we have investigated SRS saturation in a homogeneous, one dimensional plasma slab, using a limited form of our full theoretical model (2.57)-(2.61) namely

$$i(\frac{\partial E}{\partial t} + \gamma_L * E) + \frac{3}{2}\frac{v_{T_e}^2}{\omega_p}\frac{\partial^2 E}{\partial x^2} - \frac{\omega_p}{2} N E \tag{3.1}$$

$$= \frac{\pi e n_0^e}{\omega_p} \frac{\partial}{\partial x} (\Psi_0 \Psi_R^*) + S_L(x,t),$$

$$\frac{\partial^2 N}{\partial t^2} + 2\gamma_A * \frac{\partial N}{\partial t} - c_s^2 \frac{\partial^2 N}{\partial x^2} \tag{3.2}$$

$$= \frac{\partial^2}{\partial x^2} \left(\frac{\mid E \mid^2}{16\pi n_0^i m_i} \right) + S_A(x,t),$$

$$i(\frac{\partial \Psi_0}{\partial t} + \gamma_0^c \Psi_0) + \frac{c^2}{2\omega_0} \frac{\partial^2 \Psi_0}{\partial x^2} - \frac{\omega_p^2 - \omega_0^2}{2\omega_0} \Psi_0 \tag{3.3}$$

$$= -\frac{e}{4\omega_0 m_e} \Psi_R \frac{\partial E}{\partial x},$$

$$i(\frac{\partial \Psi_R}{\partial t} + \gamma_R^c \Psi_R) + \frac{c^2}{2(\omega_0 - \omega_p)} \frac{\partial^2 \Psi_R}{\partial x^2} - \frac{\omega_p^2 - (\omega_0 - \omega_p)^2}{2(\omega_0 - \omega_p)} \Psi_R \tag{3.4}$$

$$= -\frac{e}{4(\omega_0 - \omega_p) m_e} \Psi_0 \frac{\partial E^*}{\partial x}$$

In this model the nonlinear terms allowing for the production of SBS have been omitted by removing the ponderomotive force $\sim\mid \Psi_0 \mid^2$ term in Eq. (2.58) and density coupling $\sim N\Psi_0$ term in Eq. (2.59). The anti-Stokes Raman equation (2.61) and coupling in (2.57) was also ignored.

In our early analysis of SRS saturation many simulations were performed using the system (3.1)-(3.4) (see table 3.1). These early simulations and all others were performed at densities below quarter critical $n_0^e < 0.25 n_c$. The electromagnetic pump energy was always chosen so that we remained above the absolute SRS threshold $(2\Gamma_{SRS}/\gamma_L(k_L))\sqrt{V_L / \mid V_R \mid} > 1$, and all runs were performed for interaction lengths L for which L was at least a few times the critical length $L_{cr} = \pi \sqrt{V_L \mid V_R \mid} / 2\Gamma_{SRS}$.

The relatively strong collisional damping of the Langmuir waves is a characteristic feature of the short wave length laser-plasmas for which most of the simulations are performed. The rest of Chap. 3 is devoted to discussing the evolution of SRS in the presence of electron-ion coupling through the use of the Zakharov equations,

symbol	n_0/n_{cr}	T_e(keV)	ZT_e/T_i	λ_0(μm)	I(W/cm^2)	L(μm)	Z
▼	.1	1.25	4-11	0.53	3 10^{15}	25	4-11
◇	.1	.5	10-30	0.53	1 10^{15}	25-75	5
◁	.2	2.5	50	0.35	4.2 10^{14}	15	50
○	.2	3.5	50	0.53	2 10^{15}	25-50	50
●	.2	.5	10-30	0.53	5 10^{14}	25	2
◆	.1	1.0	10	0.53	3-10$10^{14}$	50	5
▲	.1	1.5	10	.53	3 10^{15}	25	10

Table 3.1: *Parameters used in simulations for equations (3.1)-(3.4). The symbols themselves are used in Figs. 3.18 and 3.19*

and outlines the typical evolutionary sequence. The simulations in this analysis were performed without the SBS or anti-Stokes Raman coupling where the of parameters explored is illustrated in table 3.1.

3.1 Typical evolution of the backward Raman scattering simulations

By analysing many simulations we have identified two typical scenarios of SRS temporal evolution. SRS evolves through a linear development stage which is easily recognizable as that of three wave evolution. Once the SRS driven Langmuir wave amplitude is above the PDI threshold (1.25)

$$E_{thr}^2 = \frac{64\pi n_0^e T_e \gamma_A(k_A^{(1)}) \gamma_L(k_L)}{\omega_L \omega_A^{(1)}}, \tag{3.5}$$

SRS evolves into a stage where the PDI process can produce a sharp saturation of SRS. Depending on the parameter regime the two scenarios now separate. The

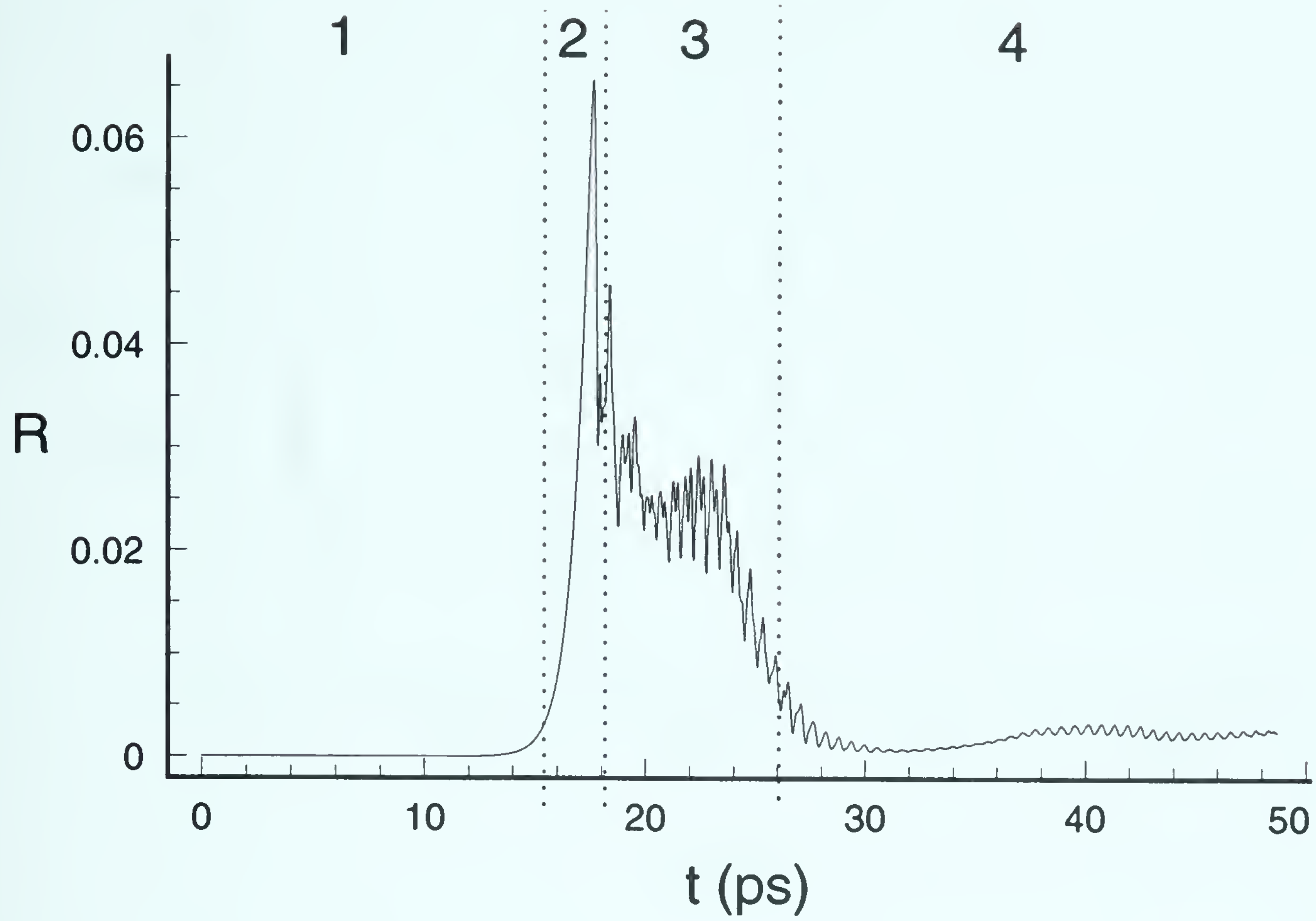

Figure 3.1: *SRS reflectivity as a function of time obtained from numerical solutions of equations (3.1)-(3.4) for the parameters* $L = 60\,\mu m$, $I = 2.5 \cdot 10^{14}\,W/cm^2$, $n_0^e/n_c = 0.2$, $T_e = 1\,keV$, $ZT_e/T_i = 8$, $Z = 3$, $\lambda_0 = 0.531\,\mu m$. *Various regimes in SRS evolution correspond to (1) linear growth, (2) a sharp first saturation, (3) transient nonlinear intermediate regime and (4) an asymptotic quasistationary saturation.*

first scenario is illustrated in Fig. 3.1 where after the initial first strong flash of SRS reflectivity, a transient nonlinear regime evolves into a final quasistationary saturated state. In the second scenario the strong reflectivity flashes are repeated (Fig. 3.2) producing a sequence of events that we refer to as bursts or pulsations of SRS. During these bursts of reflectivity the regions 1 and 2 of Fig. 3.1 are repeated quasiperiodically before a final saturation state is achieved. This intermediate behavior is classified as region 3 where the transient nonlinear evolution is examined. This behavior will eventually lead to the same asymptotic saturation (region 4) as in the first case.

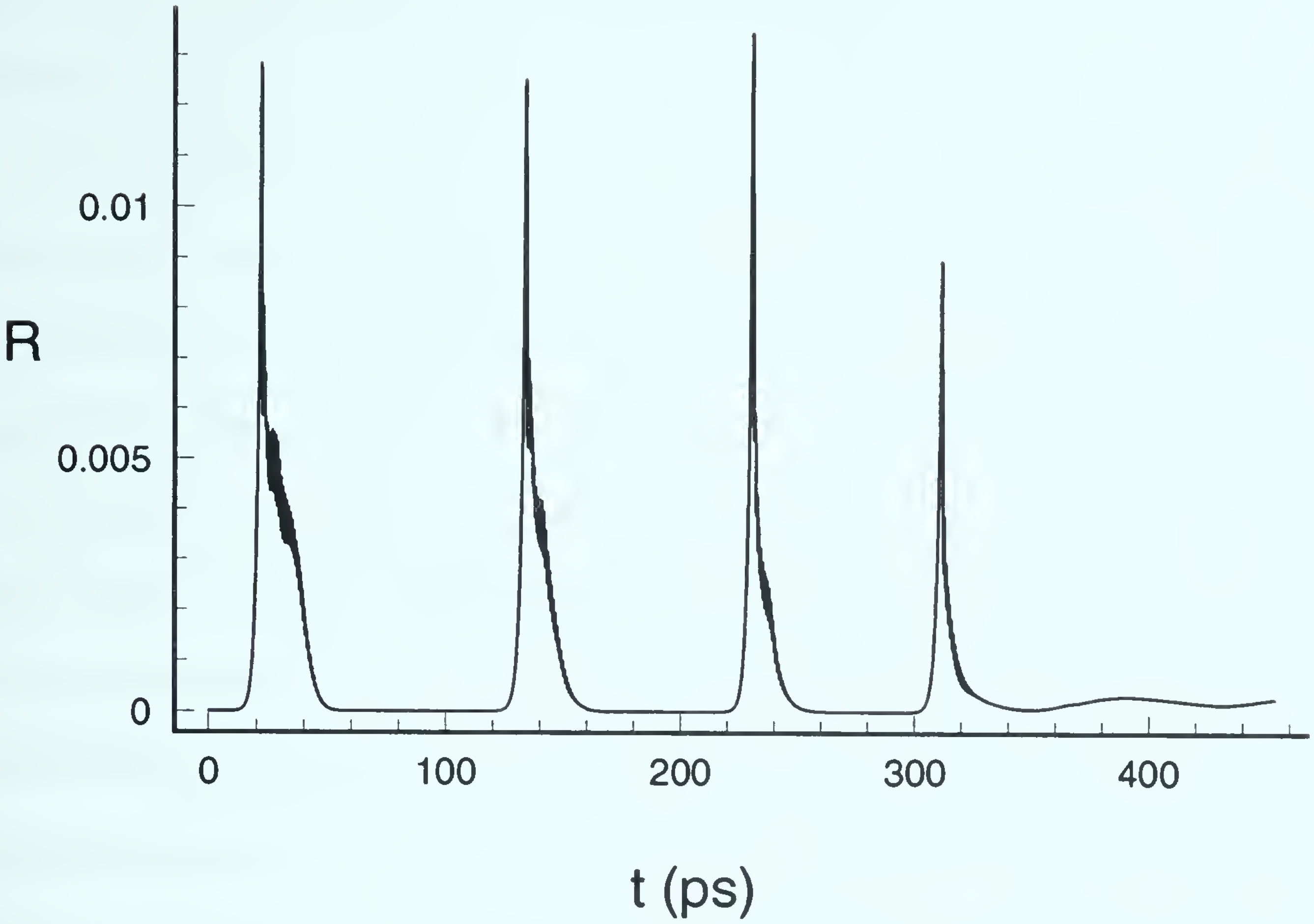

Figure 3.2: *Bursts of SRS reflectivity obtained from numerical solutions of equations (3.1)-(3.4) for the parameters* $L = 25\,\mu m$, $I = 4.8 \cdot 10^{14}\,W/cm^2$, $n_0^e/n_c = 0.2$, $T_e = 0.5\,keV$, $ZT_e/T_i = 30$, $Z = 2$, $\lambda_0 = 0.531\,\mu m$.

In summary both scenarios see a progression of SRS through four stages of development, appropriately labeled as: (1) linear growth, (2) a sharp first saturation, (3) transient nonlinear intermediate regime and (4) an asymptotic quasistationary saturation. All four intervals are easily identified in Fig. 3.1 and Fig. 3.2. Each stage is now examined in greater detail.

3.2 Linear growth

By making use of the investigation in Chap. 2.2, and assuming a constant amplitude pump, we can to estimate the linear growth rates in various regimes of the SRS evolution process. To effectively illustrate these linear regimes of SRS evolution we examine in detail simulations which produce the temporal evolution

in the linear regime of interest. Figure 3.3 illustrates the various regimes of the SRS interaction for parameters $L = 60\,\mu m$, $I = 2.5 \cdot 10^{14}\,W/cm^2$, $n_0^e/n_c = 0.2$, $T_e = 1\,keV$, $ZT_e/T_i = 8$, $Z = 3$, $\lambda_0 = 0.531\,\mu m$. Three different wave interaction codes were used to find the temporal evolution of the reflectivity: (a) a linearized three wave interaction code given by equations (2.78) and (2.79) (long dashed curve) in the context of SRS evolution (b) the full three wave interaction model for SRS equations (2.70)-(2.72) (dotted curve) where, if one is above the absolute threshold, pump depletion is the only method to saturate the instability and (c) our full system of equations (3.1)-(3.4) (solid curve) which permits saturation of SRS through the electron-ion interaction of the Zakharov equations. Each code was run using identical initial conditions and parameters, and except for extremely early time behavior of the full code, exhibit identical temporal evolution during the linear stages of development. In Fig. 3.3 the short dashed curves represent the various analytical approximations.

The electromagnetic pump in our simulations is initialized as a square pulse extending across the plasma. The plasma wave will grow at the convective growth rate $\propto \exp[\Gamma_{SRS} t]$ during the time period required for the initial backscattered wave to travel the length of the plasma (Fig. 3.3 dashed line from $0 - t \sim L/\mid V_R \mid= 0.56$ ps). Because $\Gamma_{SRS} L/\mid V_R \mid\ll 1$, the e-folding time is less than the propagation time, and this phase of SRS has no further effect on the evolution of the instability. If this were not the case the the inclusion of the temporal derivative of the electromagnetic waves would be necessary to correctly describe the subsequent evolution. For all our simulations $\Gamma_{SRS} L/\mid V_R \mid\ll 1$ and hence the time derivatives of the electromagnetic components were ignored.

Once the electromagnetic waves reach the boundaries of the plasma convective

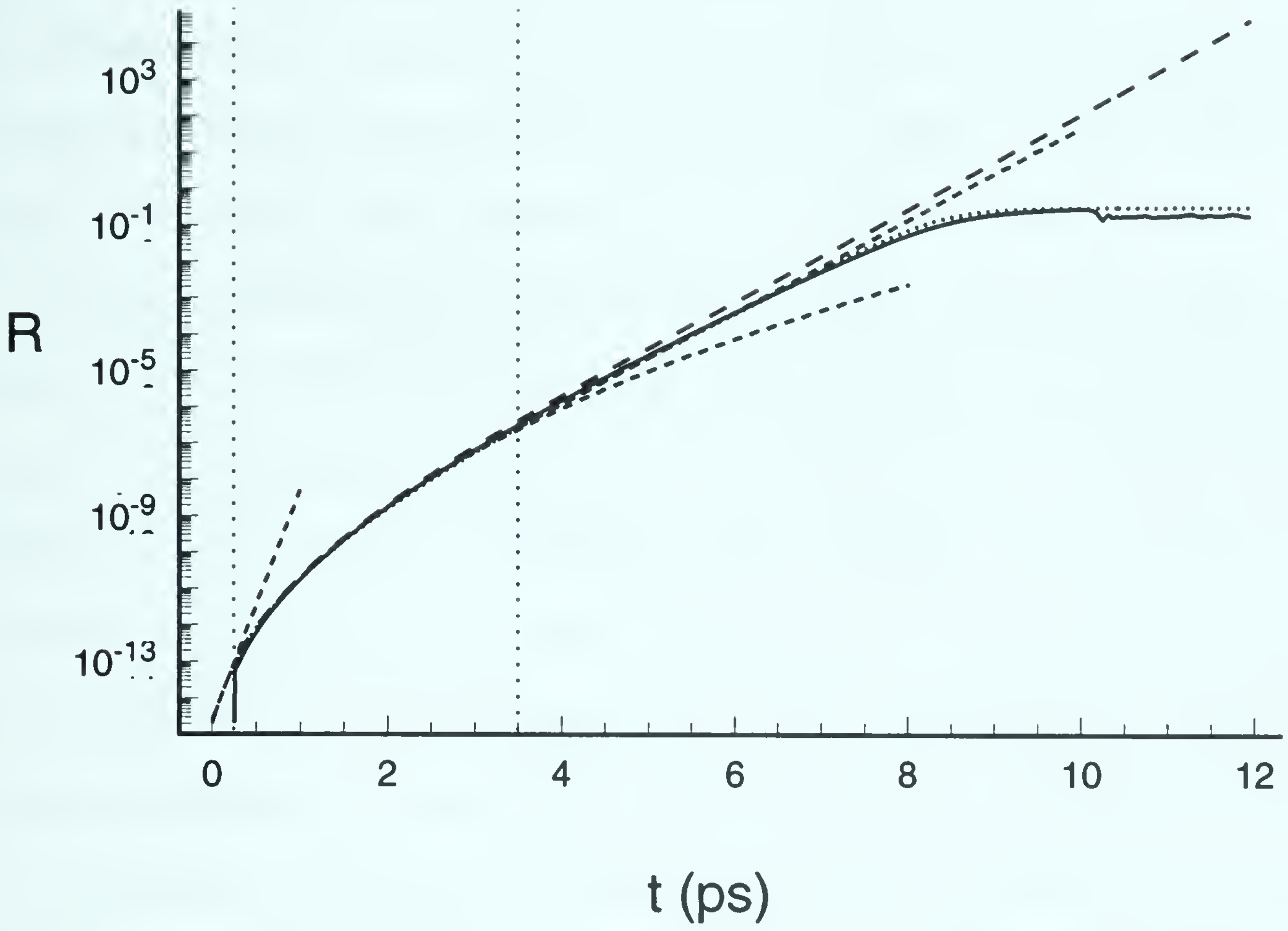

Figure 3.3: *Simulation results for the temporal evolution of SRS reflectivity using the parameters* $L = 60\,\mu m$, $I = 2.5 \cdot 10^{14}\,W/cm^2$, $n_0^e/n_c = 0.2$, $T_e = 1\,keV$, $ZT_e/T_i = 8$, $Z = 3$, $\lambda_0 = 0.531\,\mu m$ *for: (a) Linearized 3WI code equations (2.78) and (2.79) (long dashed curve), (b) 3WI code equations (2.70)-(2.72) (dotted curve), and (c) full model code equations (3.1)-(3.4) (solid curve). Also shown are relevant theoretical growth rates (dashed curves): (1)convective regime equation (2.86)* $t = 0$ *-* 0.56 *ps, (2)intermediate regime equation (2.101)* $t = 0.56$ *-* 3.5 *ps, and (3) absolute regime equation (2.85)* $t > 3.5$

losses will modify the growth rate of SRS producing an interaction length dependent growth rate, with a maximum growth $\propto \exp[2\Gamma_{SRS}\sqrt{Lt/\mid V_R \mid}]$. The effective growth rate is defined by $\mid \partial E/\partial t \mid / \mid E \mid = \Gamma_{int} = \Gamma_{SRS}\sqrt{L/\mid V_R \mid t}$ and hence decreases with time. In the intermediate regime $L/V_R < t < L/4V_L$ (Fig. 3.3 dashed line from 0.56 ps to 3.5 ps) a length dependent growth rate is observed. If one is below the absolute threshold a stationary convective instability will develop once the intermediate growth rate is reduced to a level where it balances the Langmuir damping ie.$\Gamma_{int} \simeq \gamma_L(k_L)$. At this point the SRS instability will saturate at a

level $\propto \exp[\Gamma^2_{SRS} L/\gamma_L(k_L) \mid V_R \mid]$. This regime has never been observed in our full model simulations because we are always above the absolute threshold. Instead we observe a conversion into an absolute growth rate $\propto \exp[2\Gamma_{SRS}\sqrt{V_L/\mid V_R \mid}t]$ which begins at $t \sim L/4V_L$ and continues until nonlinear effects come into play.

In order to demonstrate the intermediate growth rates explicit length dependence we have plotted the time history of three different interaction lengths in Fig. 3.4. All other parameters $I = 4.8 \cdot 10^{14}\, W/cm^2$, $n_0^e/n_c = 0.2$, $T_e = 0.5\, keV$, $ZT_e/T_i = 30$, $Z = 2$, $\lambda_0 = 0.531\, \mu m$ in Fig. 3.4 are identical except for the interaction length where the fastest growing mode corresponds to a length of $L = 150\lambda_0$(dotted curve) the second curve was obtained with $L = 100\lambda_0$(solid curve), and finally the slowest growth was observed for $L = 50\lambda_0$(dashed curve).

The necessity of including the Zakharov interaction in describing the later evolution of SRS is illustrated by Fig. 3.5. As long as the SRS driven Langmuir mode E_{k_L} dominates the evolution, ie. up to the moment of first saturation, the behavior of the SRS reflectivity R Fig. 3.5(a) follows closely the behavior of the maximum value of the electrostatic field $\mid E \mid^2_{max}$ Fig. 3.5(b). Once other nonlinear processes in the plasma begin to affect the evolution, $\mid E \mid^2_{max}$ deviates substantially from the SRS reflectivity evolution, where in Fig. 3.5 strong maxima in $\mid E \mid^2_{max}$ produce little change in R. This deviation indicates that in addition to SRS there are other process present driving the Langmuir evolution.

In the case of the electromagnetic modes for very underdense plasmas the linear dispersion relation (1.3) will depend on ω_p only very slightly thus

$$\omega \simeq ck \tag{3.6}$$

and hence a monochromatic EMW should be approximately described by a single

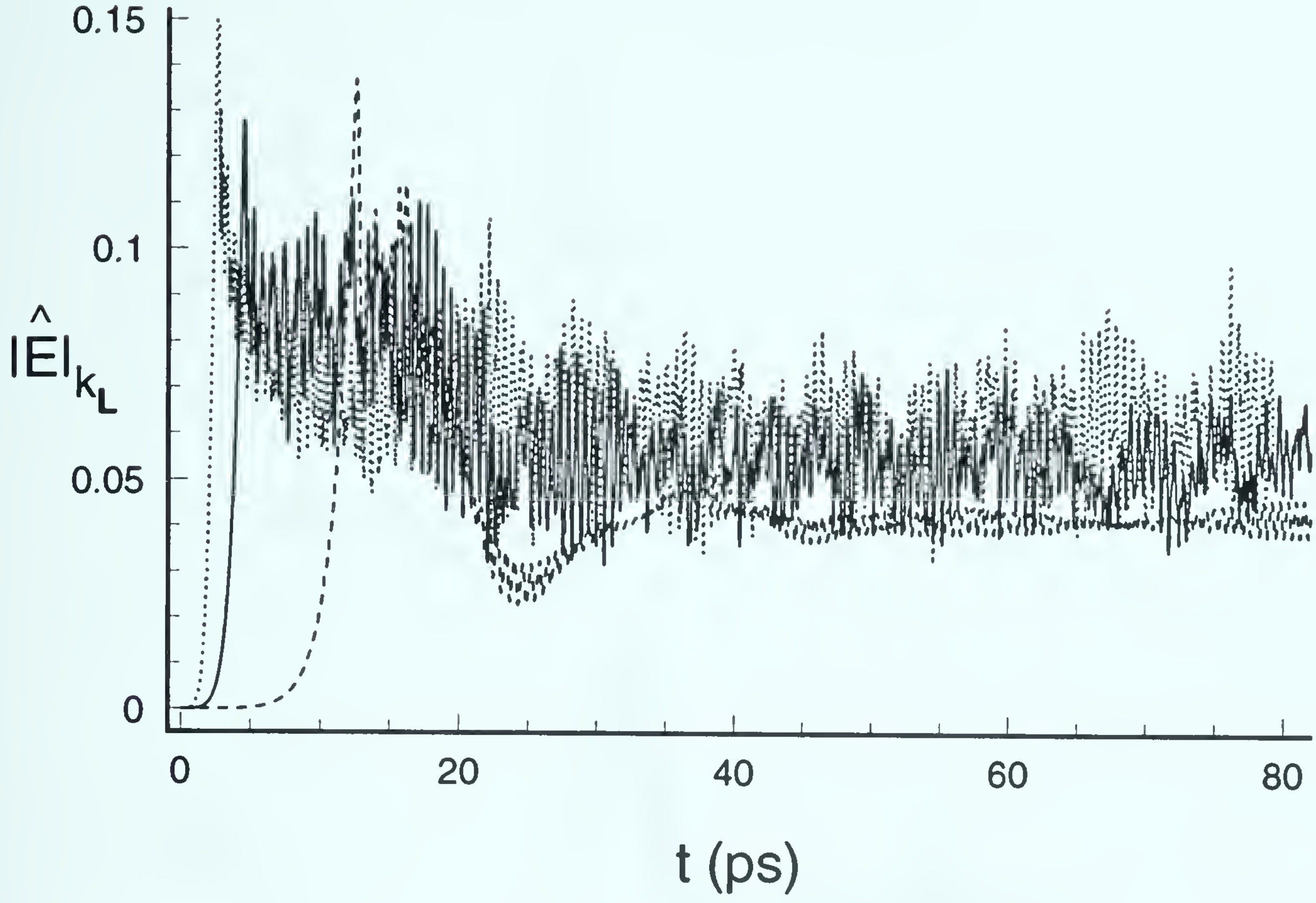

Figure 3.4: *Examples of time evolution of the Fourier component at* $k = k_L$ *of the Langmuir field* $E(x,t)$ *obtained from numerical solutions of equations (3.1)-(3.4) for the plasma interaction lengths: (a) dashed curve* $L = 25\,\mu m$*, (b) solid curve* $L = 50\,\mu m$*, (c) dotted curve* $L = 75\,\mu m$ *for parameters* $I = 4.8 \cdot 10^{14}\,W/cm^2$*,* $n_0^e/n_c = 0.2$*,* $T_e = 0.5\,keV$*,* $ZT_e/T_i = 30$*,* $Z = 2$*,* $\lambda_0 = 0.531\,\mu m$*.*

mode when propagating through the plasma. In fact this is the observed result in our simulations. The pump and backscattered Raman waves can be described by single modes throughout the simulation. If we were not interested in analysing forward Raman or Brillouin scattering the electromagnetic components of our full code could be replaced, as was done for example in [49] by spatially enveloped variables which vary only on long scale lengths.

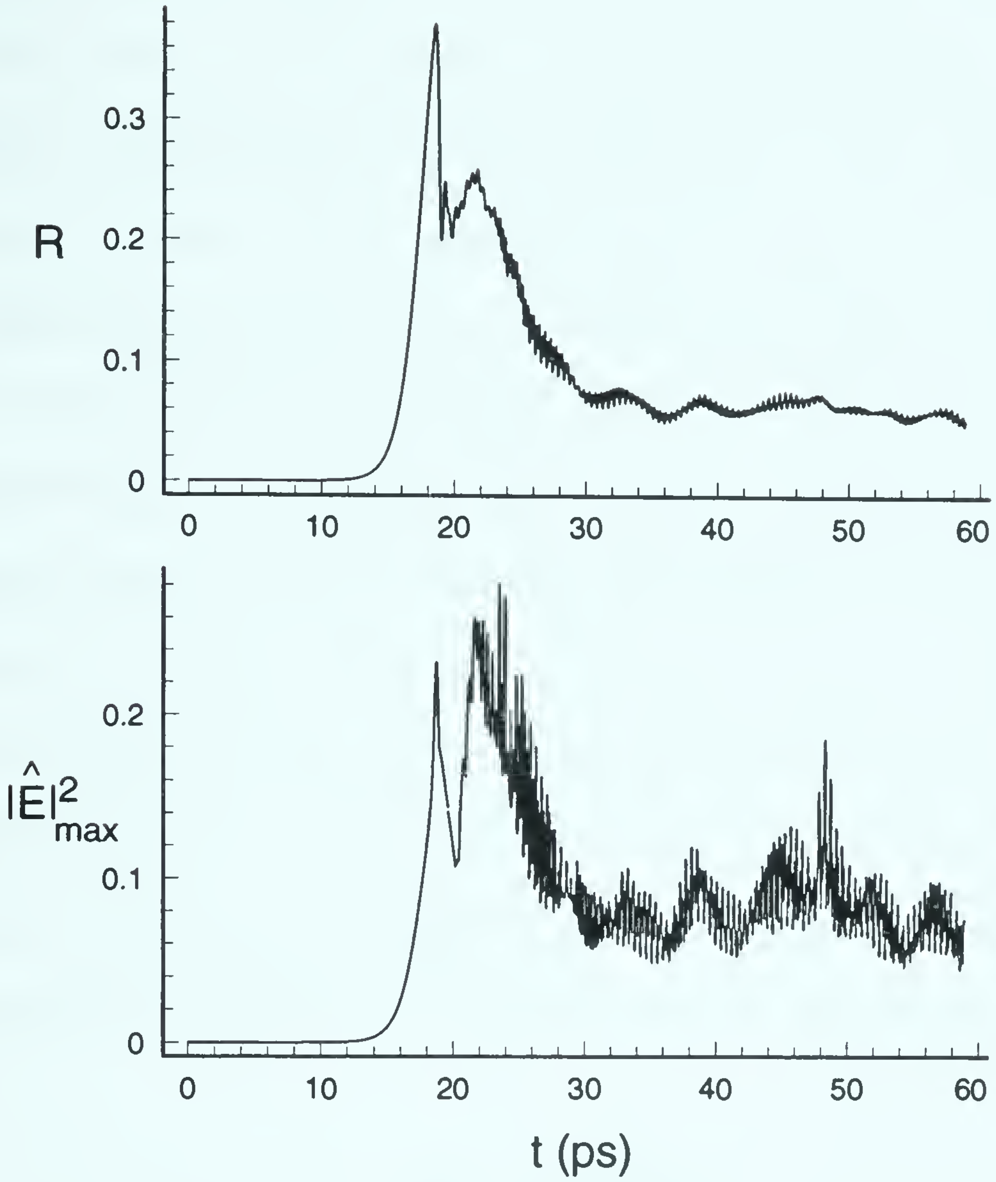

Figure 3.5: *Results from numerical integration of equations (3.1)-(3.4) for the parameters* $L = 50\,\mu m$, $I = 3.3 \cdot 10^{14}\,W/cm^2$, $n_0^e/n_c = 0.1$, $T_e = 1\,keV$, $ZT_e/T_i = 10$, $Z = 5$, $\lambda_0 = 0.531\,\mu m$. *(a) SRS reflectivity time history and (b) Maximum of the electric field as a function of time. The field values are normalized to the average thermal energy* $\mid \hat{E}_{max} \mid^2 = \mid E_{max} \mid^2 / (4\pi n_0^e T_e)$.

3.3 First saturation of stimulated Raman scattering by parametric decay instability

As SRS evolves through its linear stages of growth, the slowly varying spatial envelope of the Langmuir wave field will interact with the ion density through the electron-ion coupling of the Zakharov equations. Even though the ion density does not grow temporally in this phase of the evolution it will respond adiabatically to the presence of the electrostatic fields. This response is illustrated in Fig. 3.6

for the parameters $L = 50\,\mu m$, $I = 3.3 \cdot 10^{14}\,W/cm^2$, $n_0^e/n_c = 0.1$, $T_e = 1\,keV$, $ZT_e/T_i = 10$, $Z = 5$, $\lambda_0 = 0.531\,\mu m$ for $t = 12.12$ ps of Fig. 3.5 . The electrostatic field is below the PDI threshold of $E_{thr}^2/4\pi n_0^e T_e \simeq 1.7 \cdot 10^{-3}$ and hence only the single mode at k_L (Fig. 3.6(a)) will contribute to the smooth variation of $\mid E \mid^2$ in Fig. 3.6(b) (left hand scale). The ion density noise source $S_A(x,t)$ around k_A can be seen as the random ion density fluctuation of Fig. 3.6(b) (right hand scale). Also clearly visible is the response of the ion density fluctuations to the presence of the Langmuir field ($x \leq 15\mu m$). This response can be seen in the density spectra as the strong $k_A \simeq 0$ peak in Fig. 3.6(a). The third peak, $k_A \simeq 0.4k_D$, which can be seen in the density spectra of Fig. 3.6(a) is associated with the nonresonant coupling of the ponderomotive force term associated with the Zakharov equations.

In order to understand the density response we ignore the temporal derivative in equation (2.58) and derive the approximate relation for the density response of

$$N_{nt} \sim -\frac{\mid E \mid^2}{8\pi m_i n_0^i c_s^2} \tag{3.7}$$

resulting in a coherent source term for the background density. The density N_{nt} will be driven by the ponderomotive force (3.7) until such time that the Langmuir fields are above the PDI threshold $\mid E_{thr} \mid^2$. As the SRS driven Langmuir wave approaches the PDI threshold this increase in background density and its effect on the Langmuir noise levels will drastically alter the initial noise levels for PDI, creating density fluctuations far in excess of thermal levels [71]. N_{nt} through its interaction with the Langmuir fields will also produce changes in the Langmuir noise levels, making predictions of exact noise levels difficult. These noise levels will play a critical role in determining the timing and saturation amplitude of the first termination of SRS growth. This nonstationary transient regime is subject to

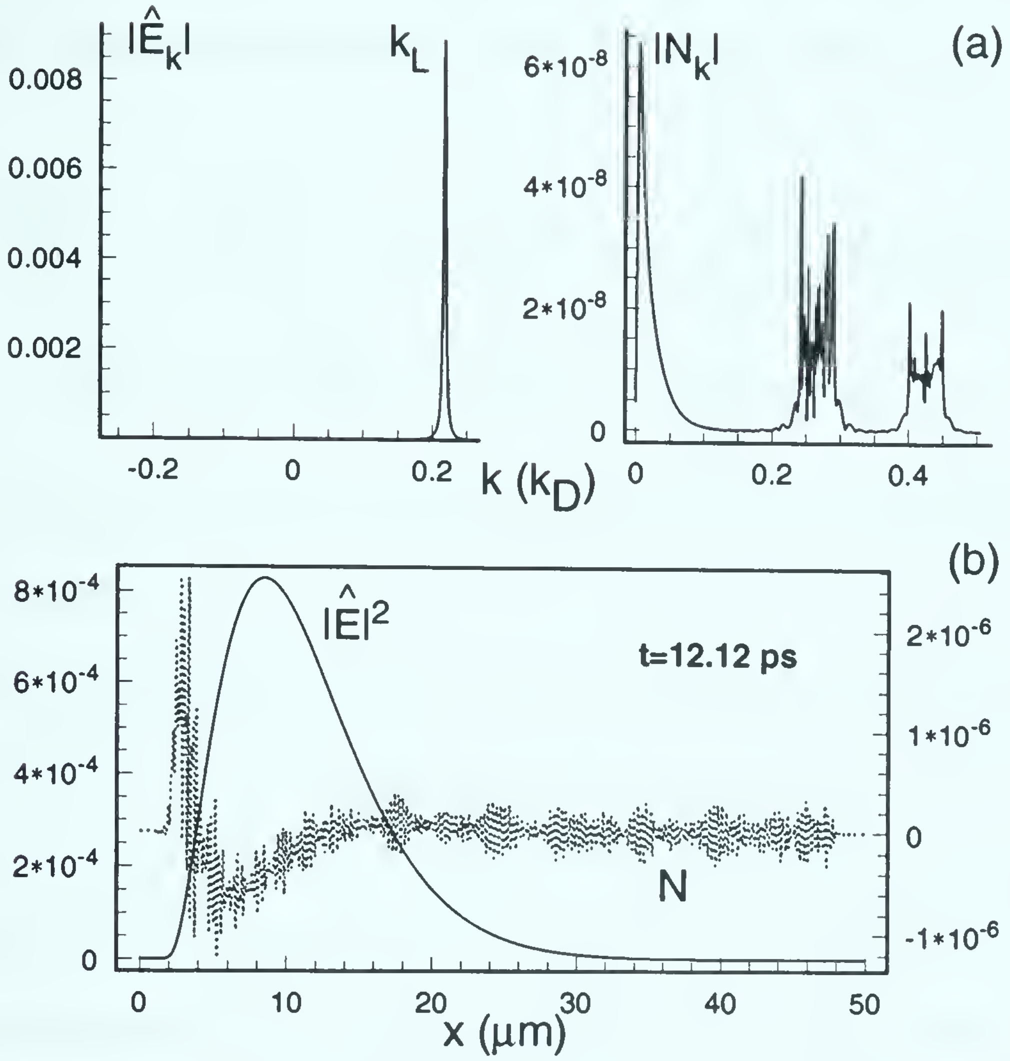

Figure 3.6: *Results from the numerical integration of equations (3.1)-(3.4) at* $t = 12.12$ *ps of Fig. 3.5 for parameters* $L = 50\,\mu m$, $I = 3.3 \cdot 10^{14}\,W/cm^2$, $n_0^e/n_c = 0.1$, $T_e = 1\,keV$, $ZT_e/T_i = 10$, $Z = 5$, $\lambda_0 = 0.531\,\mu m$. *(a) Fourier spectrum of the electrostatic electric field* $\hat{E}_k = E_k/(4\pi n_0^e T_e)^{1/2}$ *and density* N_k. *(b) Spatial profiles of the electrostatic electric field* $|\hat{E}|^2 = |E|^2/(4\pi n_0^e T_e)$ *and density.*

the initial conditions imposed on the plasma as well as the nontemporal evolution of the ion density creating difficult problems in predicting the exact time and amplitude of first saturation.

The approximate five wave coupling model which should describe the main features of the initial SRS-PDI interaction is based on equations (2.70)-(2.72) with the addition of a density coupling in (2.71) producing the equation

$$\frac{\partial E_L}{\partial t} + V_L \frac{\partial E_L}{\partial x} + \gamma_L E_L = \frac{1}{4} \frac{e}{m_e} \frac{k_L \omega_p^2}{\omega_R \omega_0 \omega_L} E_0 E_R^* - \frac{\omega_p^2}{4\omega_L} N_A^{(1)} E_L^{(1)} \tag{3.8}$$

and two extra equations describing the slowly varying evolution of the PDI satellites

$$\frac{\partial N_A^{(1)}}{\partial t} + c_s \frac{\partial N_A^{(1)}}{\partial x} + \gamma_A(k_A^{(1)}) N_A^{(1)} = \frac{k_A^{(1)2}}{16\pi n_0^i m_i \omega_A^{(1)}} E_L E_L^{(1)*} \tag{3.9}$$

$$\frac{\partial E_L^{(1)}}{\partial t} + V_L^{(1)} \frac{\partial E_L^{(1)}}{\partial x} + \gamma_L^{(1)} E_L^{(1)} = \frac{\omega_p^2}{4\omega_L^{(1)}} E_L N_A^{(1)*} \tag{3.10}$$

where $\omega_A^{(1)} = c_s k_A^{(1)}$, $N_A^{(1)}$ is the first ion acoustic daughter wave and $E_L^{(1)}$ is the first Langmuir daughter wave.

As is illustrated in region 2 of Fig. 3.1 the first saturation of SRS takes the form of a sharp burst of reflectivity which can reach very high values. This abrupt peak is caused by the competition of the SRS and PDI processes, as energy supplied to the Langmuir mode at k_L is now balanced by the energy absorbed by the first PDI Langmuir satellite at $k_L^{(1)}$. In region 2 of the SRS evolution, which begins once E_L exceeds the PDI threshold E_{thr} (3.5), SRS can be approximately described by a five wave interaction model (cf. [76]-[78]). The previously mentioned spatial response of the density to the presence of the Langmuir field evolution supplied by the Zakharov equations limits the applicability of the five wave model, but does permit a discussion of the basic physical processes involved in region 2 of the SRS temporal evolution.

In principle the first saturation of SRS by PDI should be reproducible by the five wave mode coupling equations (2.70), (2.72), and (3.8)-(3.10). Attempts at reproducing the first two stages of the full model evolution through the use of five wave model have emphasized the necessity of the inclusion of the initial evolution of the electrostatic noise levels. The linear stages of evolution are easily reproducible

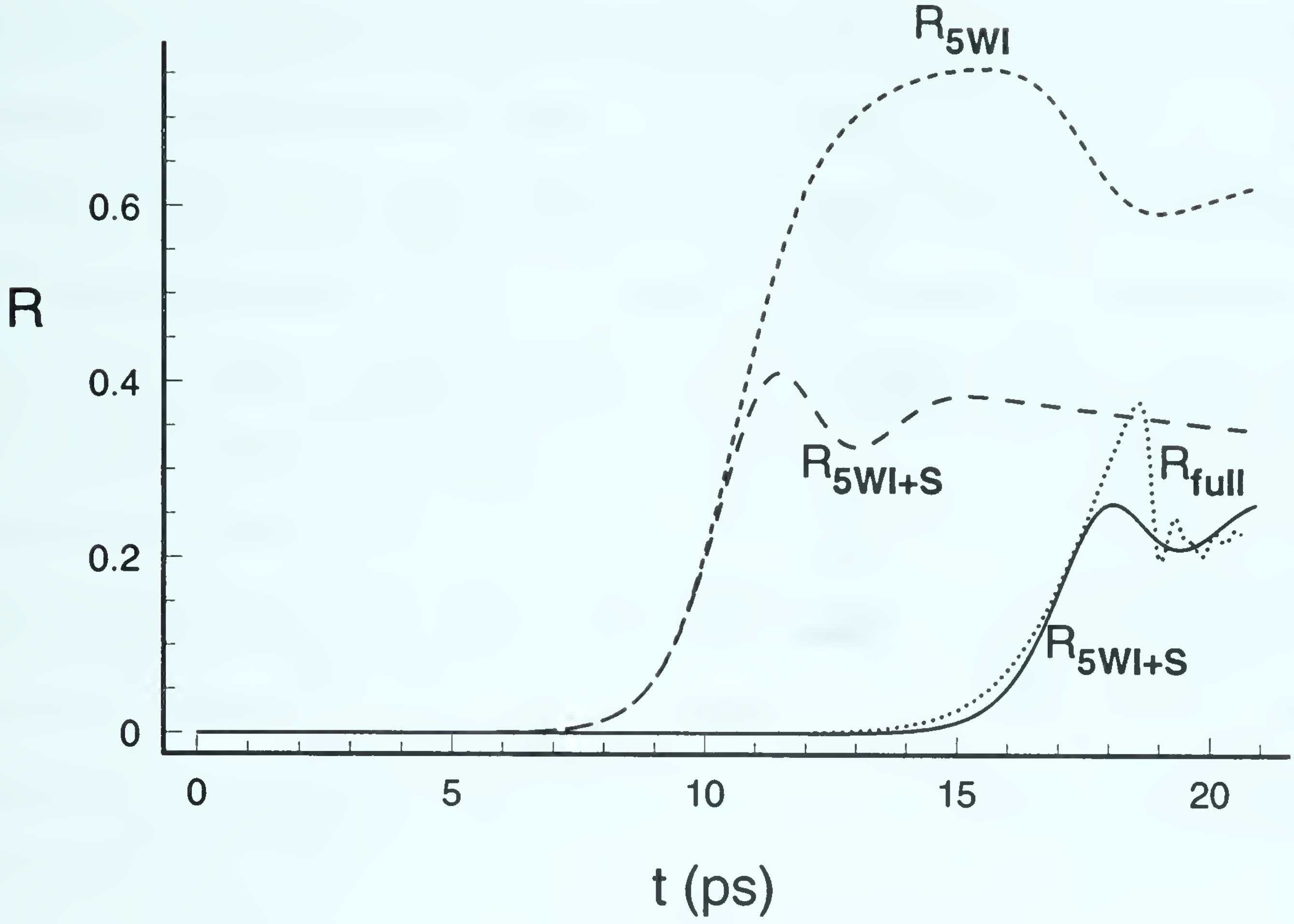

Figure 3.7: *Comparison between the results obtained from the five-wave (5WI) model equations (2.70), (2.72), and (3.8)-(3.10) (dashed curve) and from the full model (full) equations (3.1)-(3.4) (dotted curve) for the same parameters as in Fig. 3.5. The long dashed and solid curves correspond to the five-wave model with an extra source term proportional to E_L in equation (3.10) (5WI+S). The latter models in a crude way, the effect of nonresonant wave coupling present in the Zakharov model.*

and are in good agreement between the two models. The subsequent timing and maximum amplitude of the SRS saturation are however quite different. Figure 3.7 illustrates the difference between the reflectivity evolution of the five wave (dashed curve) and the full model (dotted) simulations. All parameters and initial conditions were identical $L = 50\,\mu m$, $I = 3.3{\cdot}10^{14}\,W/cm^2$, $n_0^e/n_c = 0.1$, $T_e = 1\,keV$, $ZT_e/T_i = 10$, $Z = 5$, $\lambda_0 = 0.531\,\mu m$ producing markedly different saturation evolution. The five wave model does not contain the sharp saturation of the full model, and has the characteristic slow saturation usually associated with pump

depletion as the primary saturation mechanism. To approximate the correct results we added to equation (3.10) a source term proportional to E_L, which was varied in strength until a more correct reflectivity curve was obtained. As is illustrated by the long dashed curve of Fig. 3.7 by varying the strength of the source term in (3.10) we were able to produce the correct level of SRS reflectivity. However the time when this peak occurred did not correspond to the occurrence of the maximum SRS reflectivity of the full model (3.1)-(3.4) (dotted curve). By varying the initial density fluctuation we were able to correct this timing error, but this resulted in an incorrect value for the peak reflectivity (solid curve). To reproduce the exact evolution of the full model through the use of the five wave model is quite difficult emphasizing how an analysis by the five wave model may lead to incorrect results.

Figure 3.8 illustrates full model simulation results at $t = 18.64$ ps (cf. also Fig. 3.5) just after the first saturation for run parameters $L = 50\,\mu m$, $I = 3.3 \cdot 10^{14}\,W/cm^2$, $n_0^e/n_c = 0.1, T_e = 1\,keV$, $ZT_e/T_i = 10$, $Z = 5$, $\lambda_0 = 0.531\,\mu m$. Each of the three electrostatic components involved in the PDI process are clearly visible in Fig. 3.8(a) where the SRS driven Langmuir wave at ω_L, k_L has decayed into the Langmuir component at $\omega_L^{(1)}, k_L^{(1)} = \Delta k - k_L$ and the ion acoustic component at $\omega_A^{(1)}, k_A^{(1)} = 2k_L - \Delta k$. Fig. 3.8(b) shows the spatial dependence of $\mid \hat{E} \mid^2 = \mid E \mid^2 / 4\pi n_0^e T_e$ and N at the same moment in time. Two distinct spatial regions are noticeable: in the right part of the interaction region ($x > 12\mu m$) only one electrostatic mode is excited producing the smooth variation of $\mid \hat{E} \mid^2$. In the left region the short scale variation is produced by the beating of the two Langmuir components k_L and $k_L^{(1)}$.

PDI itself begins evolving at the maximum of the Langmuir field, which is dependent on the pump amplitude and linear damping rate, and is reasonably

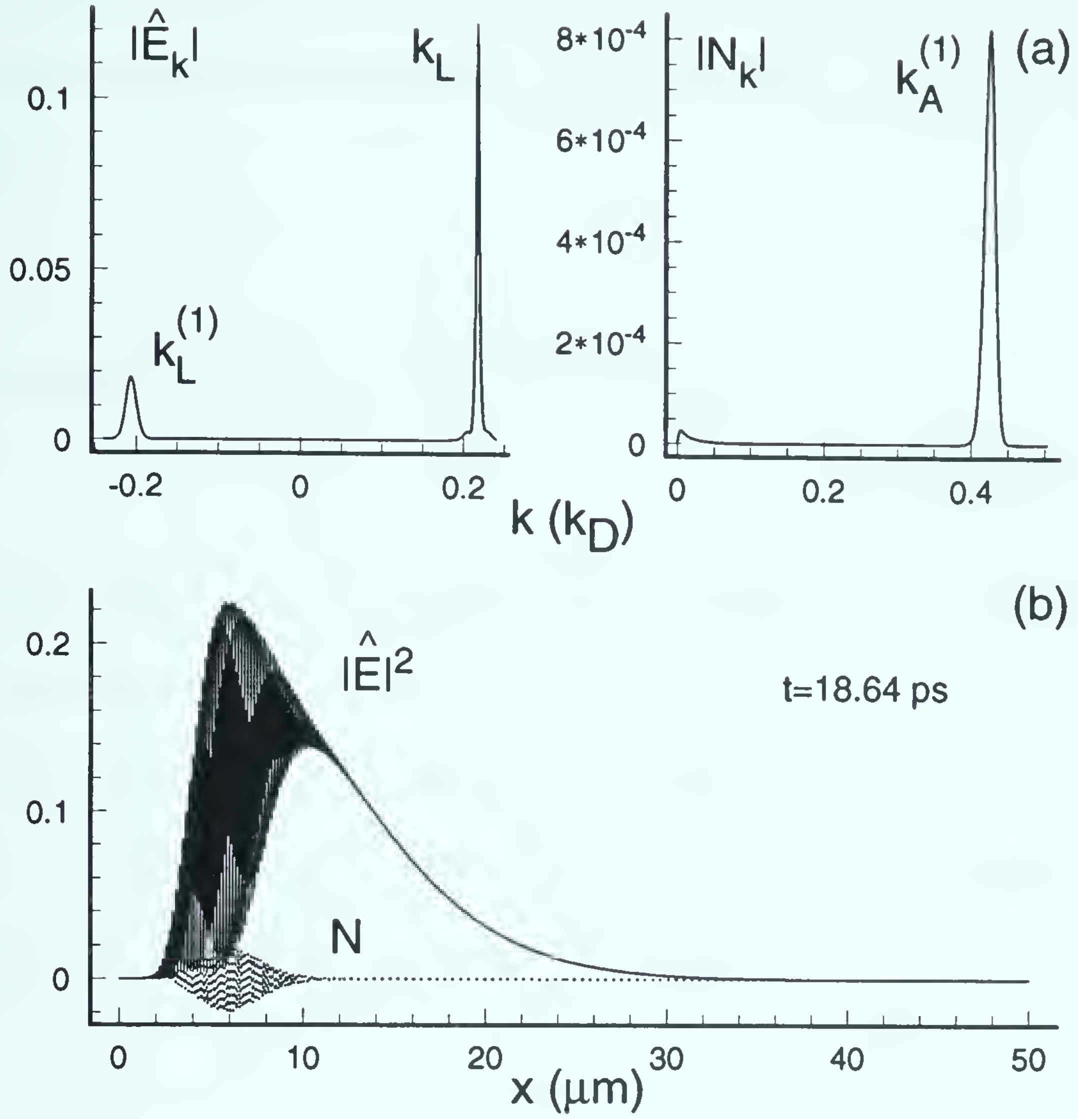

Figure 3.8: *Results from the numerical integration of equations (3.1)-(3.4) for* $t = 18.64$ *ps of Fig. 3.5 for parameters* $L = 50\,\mu m$, $I = 3.3 \cdot 10^{14}\,W/cm^2$, $n_0^e/n_c = 0.1$, $T_e = 1\,keV$, $ZT_e/T_i = 10$, $Z = 5$, $\lambda_0 = 0.531\,\mu m$. *(a) Fourier spectrum of the electrostatic electric field* $\hat{E}_k = E_k/(4\pi n_0^e T_e)^{1/2}$*and density* N_k. *(b) Spatial profiles of the electrostatic electric field* $|\hat{E}|^2 = |E|^2/(4\pi n_0^e T_e)$ *and density.*

approximated by $x_{max} \simeq L_{cr} = \pi\sqrt{V_L \mid V_R \mid}/2\gamma_L(k_L)$, and spreads through the interaction region at the rate of the Langmuir group velocity. The region of PDI activity spreads at a much slower rate than that of SRS. Stimulated Raman scattering spreads through the interaction region at the electromagnetic group velocity, quickly producing an instability that is modified by the loss of energy due to the convection of electromagnetic energy through the plasma boundary. In contrast, due to the slower propagation of electrostatic modes, PDI evolves at a rate pro-

portional to that of a plasma of infinite extent. The appropriate growth rate Γ_{PDI} can be found from the PDI dispersion relation of Chap. 1 equation (1.23) which is given by

$$(-2\Gamma_{PDI}\gamma_A(k_A^{(1)}) - \Gamma_{PDI}^2 + 2i\omega_A^{(1)}[\Gamma_{PDI} + \gamma_A(k_A^{(1)})])(-i\Gamma_{PDI} - i\gamma_L(k_L)) = \frac{\omega_p c_s^2 k_A^2}{32\pi n_0^e T_e} \mid E_L \mid^2 \quad (3.11)$$

As the PDI modes grow, a greater portion of the energy supplied to the SRS driven Langmuir mode E_L, will be absorbed by the PDI Langmuir satellite $E_L^{(1)}$. This energy sink provides an effective damping of E_L resulting in its eventual saturation. At the moment of saturation we can thus approximately balance the variation of $\mid E_L \mid^2$ by the increase in $\mid E_L^{(1)} \mid^2$ producing

$$\tilde{\Gamma}_{SRS} \mid E_L^{sat} \mid^2 \simeq \Gamma_{PDI} \mid E_L^{sat(1)} \mid^2 \quad (3.12)$$

where $\tilde{\Gamma}_{SRS}$ is the appropriate SRS growth rate, which depending on the length and intensity will be either the intermediate or absolute growth rate. Here Γ_{PDI} is the PDI growth rate found from (1.23). Through the use of numerical calculations the electrostatic field amplitudes are found to be $\mid E_L^{sat} \mid^2 \gg \mid E_L^{sat(1)} \mid^2$ revealing that $\Gamma_{PDI} \gg \tilde{\Gamma}_{SRS}$ at the moment of first saturation. This difference in growth rates produces the sharp peak in reflectivity when PDI reduces the SRS driven Langmuir wave to the PDI threshold (3.5) on a short time scale of the order of $\Delta t \sim 1/\Gamma_{PDI}$. This saturation of SRS initially applies only to a small fraction of the interaction length L and begins to slowly propagate through the rest of the plasma (cf. Fig. 3.9

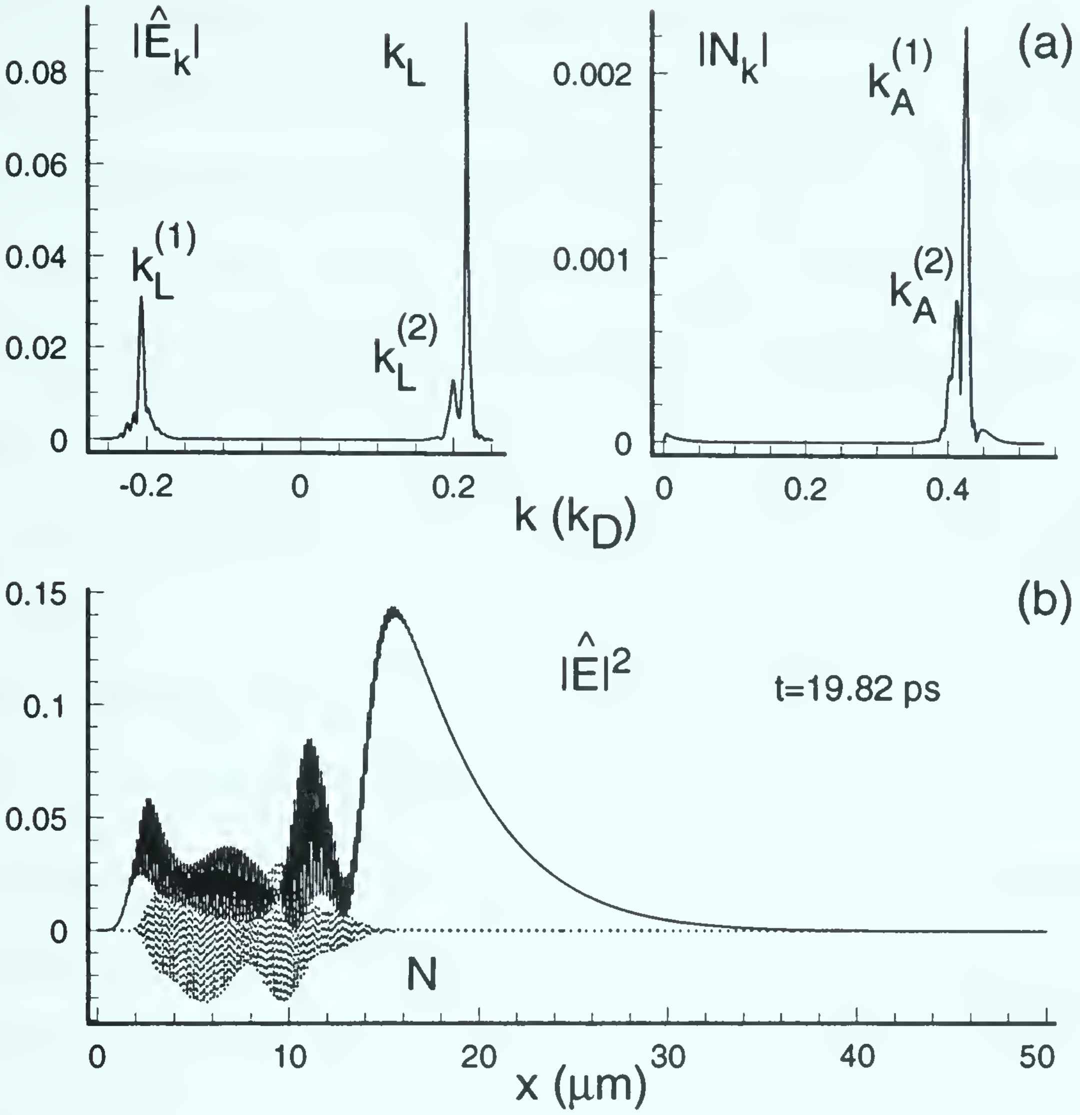

Figure 3.9: *Results from the numerical integration of equations (3.1)-(3.4) for* $t = 19.82$ *ps of Fig. 3.5 for same parameters as Fig 3.7. (a) Fourier spectrum of the electrostatic electric field* $\hat{E}_k = E_k/(4\pi n_0^e T_e)^{1/2}$*and density* N_k*. (b) Spatial profiles of the electrostatic electric field* $|\hat{E}|^2 = |E|^2/(4\pi n_0^e T_e)$ *and density.*

3.4 Intermediate nonlinear regime

After the first saturation of SRS the cascade process will continue, producing Langmuir waves at $k_L^{(n+1)} = (-1)^{(n)}\Delta k - k_L^{(n)}$ and ion acoustic waves at $k_A^{(n+1)} = k_L^{(n)} - k_L^{(n+1)}$. The third stage itself can evolve in two distinct ways: (1) the Langmuir fields localize and truncate PDI cascading producing a slow transition into a final asymptotic state or (2) if the Langmuir waves are still well above PDI threshold after the first saturation then the ion density fluctuations continue to grow. This also

affects the SRS coupling and, because under these circumstances $\Gamma_{PDI} \gg \gamma_A(k_A^{(1)})$, the secondary satellite continues to grow after first saturation. This will produce a strong energy sink for the SRS driven Langmuir wave energy and hence acts to effectively damp this wave. The combination of this effective damping and the interference with the SRS coupling will reduce the Langmuir energy to approximately noise level from which stages 1 and 2 repeat quasiperiodically, producing pulsations of SRS reflectivity, until Γ_{PDI} is reduced to a level where asymptotic saturation occurs.

The PDI cascading process occurs at a fairly rapid pace, where the presence of $k_L^{(2)}$ and $k_A^{(2)}$ at $t = 19.82$ps is shown in Fig. 3.9. The appearance of the second Langmuir satellite at $k_L^{(2)}$ is very important in the evolutionary process of SRS. Unlike the multi-wave mode coupling models of Heikkinen and Karttunen the Zakharov interaction allows the PDI cascade components to interact producing quasimodes which would not otherwise exist in the plasma. Of particular importance is the ponderomotive coupling of k_L and $k_L^{(2)}$ to produce an ion acoustic mode at $k_A = 2\Delta k$ which will couple with the Langmuir field to produce waves at $k > k_L$ and $k < k_L^{(1)}$. Figure 3.10 shows this characteristic behavior for $| \hat{E} |^2$ in the form of the superposition of k_L and $k_L^{(2)}$ producing the longscale length modulation of $| \hat{E} |^2$ in the right section of the interaction region $x \simeq 16 - 24\mu m$. These modulations of characteristic wavelength $2\pi/2\Delta k$ proceed the PDI because the Langmuir mode at $k_L^{(2)}$ propagates to the right and interacts with the k_L mode before $k_L^{(2)}$ has a chance to decay parametrically.

As the evolution continues the modulation of the pump Langmuir wave results in localization of the high frequency electrostatic fields with periodicity $2\pi/2\Delta k$ (cf Fig. 3.11). The PDI produced density fluctuations are phase shifted with respect to

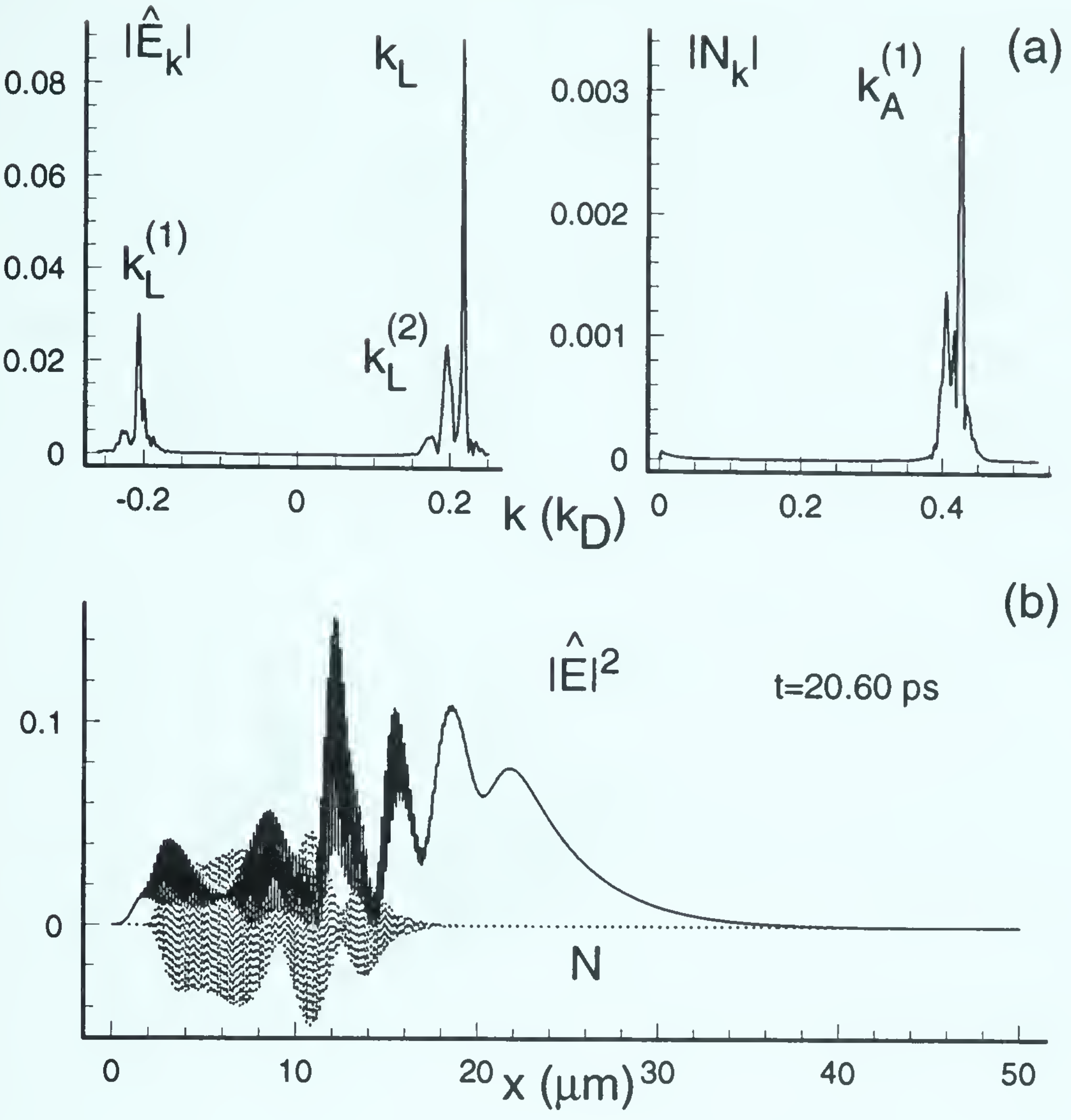

Figure 3.10: *Results from the numerical integration of equations (3.1)-(3.4) for* $t = 20.6$ *ps of Fig. 3.5 for same parameters as Fig 3.7. (a) Fourier spectrum of the electrostatic electric field* $\hat{E}_k = E_k/(4\pi n_0^e T_e)^{1/2}$*and density* N_k*. (b) Spatial profiles of the electrostatic electric field* $|\hat{E}|^2 = |E|^2/(4\pi n_0^e T_e)$ *and density.*

the Langmuir fields resulting in a configuration for which the density and Langmuir field maximum are anti-correlated. Such a field configuration corresponds to a Fourier spectra with components at $k_L \pm m2\Delta k$ and $k_L^{(1)} \pm m2\Delta k$ which is a clear indication of the localization process for which the slow scale modulation $\sim 2\pi/2\Delta k$ plays an important role. The presence of the density modulations allows for the partial decoupling of the SRS process allowing the Zakharov equations to play a more prominent role.

As can be seen in Fig. 3.11 the PDI density components in region $12-25\mu m$ are

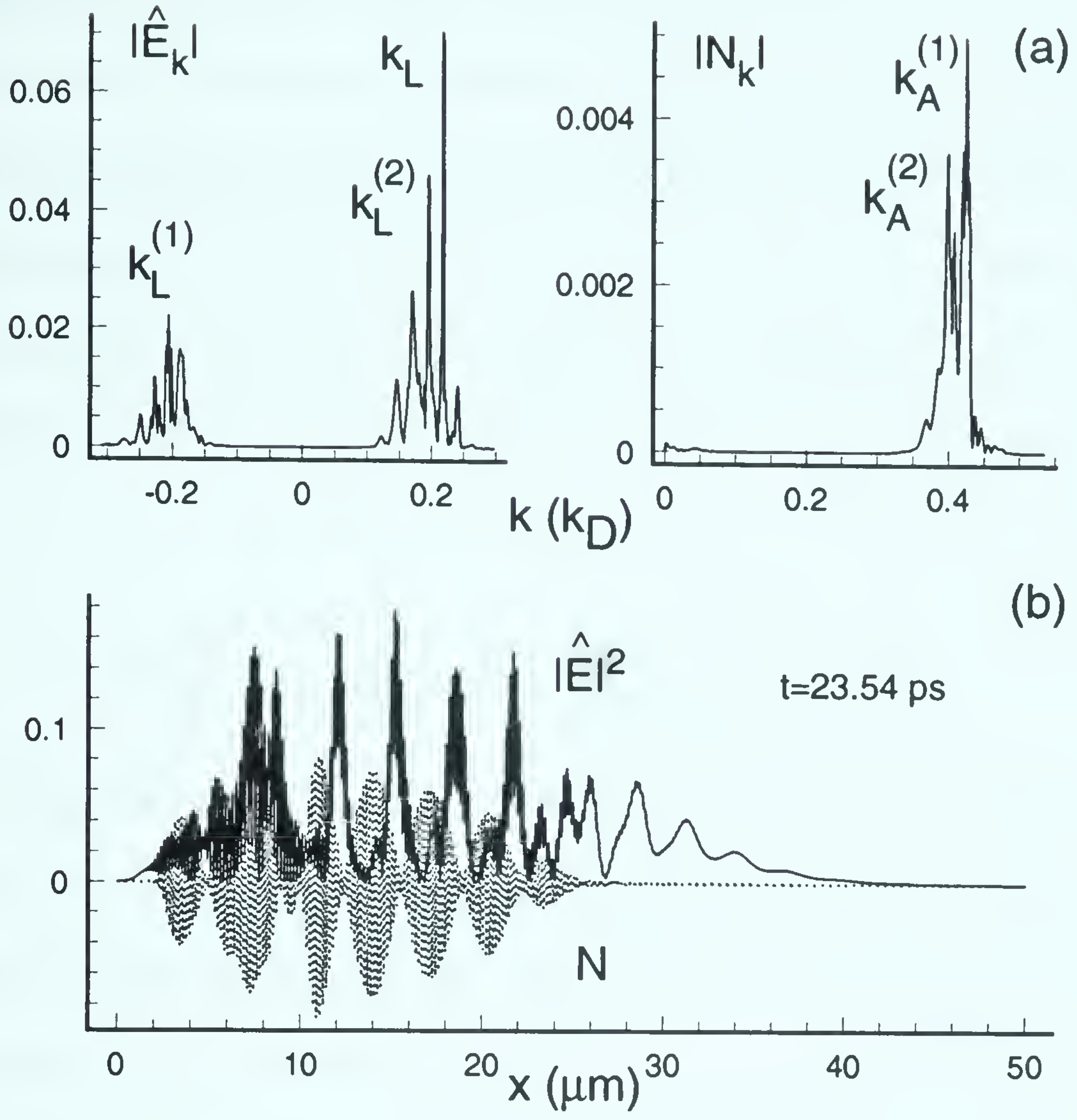

Figure 3.11: *Results from the numerical integration of equations (3.1)-(3.4) for* $t = 23.54$ *ps of Fig. 3.5 for same parameters as Fig 3.7. (a) Fourier spectrum of the electrostatic electric field* $\hat{E}_k = E_k/(4\pi n_0^e T_e)^{1/2}$*and density* N_k. *(b) Spatial profiles of the electrostatic electric field* $| \hat{E} |^2 = | E |^2 / (4\pi n_0^e T_e)$ *and density.*

phase shifted by 180 degrees from the large Langmuir field components. In these periodic regions of high density SRS evolution has been quenched. Competition between the SRS coupling and the Zakharov interaction are clearly evident, producing a transitory stage of evolution which will last until SRS has been partially decoupled through out the plasma. This transient time of evolution is related to the time needed for PDI active region to spread from the left to the right end of the interaction region.

To obtain quantitative estimates of the intermediate nonlinear regime of SRS we

use simplified versions of (2.57)-(2.60). To determine whether one obtains pulsating bursts of reflectivity or monotonic behavior one must examine the relationship of the ion acoustic damping to the parametric growth rate. Should $\gamma_A(k_A^{(1)})/\Gamma_{PDI} \ll 1$ then quasiperiodic bursts are possible. In contrast if the ion damping is a large fraction of the growth rate then only a single burst of reflectivity will be observed. Both of these possibilities can be examined by using an approximate version of (3.9)

$$\frac{\partial N_A^{(1)}}{\partial t} + \gamma_A(k_A^{(1)}) N_A^{(1)} = \frac{k_A^{(1)2}}{16\pi n_0^i m_i \omega_A^{(1)}} E_L E_L^{(1)*} \tag{3.13}$$

where the spatial derivative is omitted because the ion damping length $c_s/\gamma_A(k_A^{(1)})$ is much smaller than the PDI active region. During the transient nonlinear regime PDI is well developed allowing us to assume $E_L^* = E_L^{(1)*}$ which has an accuracy to an order of magnitude, and allows us to write

$$\frac{\partial N_A^{(1)}}{\partial t} + \gamma_A(k_A^{(1)}) N_A^{(1)} = \frac{\omega_A^{(1)}}{4} \mid \hat{E}_L \mid^2 \tag{3.14}$$

where $\mid \hat{E}_L \mid^2 = \mid E_L \mid^2 / 4\pi n_0^e T_e$

In the non-pulsating cases, the density during the transient and saturation stages is maintained at approximately a constant level so that in the first order approximation of the asymptotic state the time derivative can be ignored producing

$$N_A^{(1)} = \frac{\omega_A^{(1)}}{4\gamma_A(k_A^{(1)})} \mid \hat{E}_L^{as} \mid^2 = \frac{4\gamma_L(k_L)}{\omega_p} \frac{\mid \hat{E}_L^{as} \mid^2}{\mid \hat{E}_{thr} \mid^2} \tag{3.15}$$

where $\mid \hat{E}_L^{as} \mid^2$ is the approximate Langmuir field energy in the asymptotic regime, region 4 of Fig. 3.1. The variation of $N_A^{(1)}$ during the transient regime should be larger than the damping effects allowing us to approximate $N_A^{(1)}$ in this region as

$$N_A^{(1)} = \frac{\omega_A^{(1)}}{4\gamma_A(k_A^{(1)})} \mid \hat{E}_L \mid^2 (t - t_{sat}) \tag{3.16}$$

where the solution is restricted to the time interval $\Delta t < 1/\gamma_A(k_A^{(1)})$. This gives us the approximate relation between $N_A^{(1)}$ and $\mid \hat{E}_L \mid^2$ in the transient regime and is approximately valid for the interval $\Gamma_{PDI}/\gamma_A(k_A^{(1)}) < \gamma_A(k_A^{(1)})(t - t_{sat}) < 1$ where $t_{sat} = 1/\Gamma_{PDI}$ is the duration of the first peak. If the density varies only slowly as the transient regime moves into the saturation state, we can equate (3.15) and (3.16) to yield the variation of the intermediate Langmuir field in relation to the asymptotic state

$$\mid \hat{E}_L \mid^2 = \frac{\mid \hat{E}_L^{as} \mid^2}{\gamma_A(k_A^{(1)})(t - t_{sat})} \tag{3.17}$$

This is in good agreement with simulations of the non-bursting type where SRS reflectivity always follows closely the evolution of E_L and has been observed in simulations to decay on the ion acoustic damping timescale. All our simulations have the characteristic decay of the transient regime comparable to $2/\gamma_A(k_A^{(1)})$.

Equation (3.17) can be used to produce a more accurate description of the density fluctuations if one substitutes (3.17) back into (3.14). Ignoring the damping one observes that

$$N \sim \ln[\gamma_A(k_A^{(1)})(t - t_{sat})] \tag{3.18}$$

where the density during the transient regime evolves at approximately a logarithmic rate. This slow evolution can be observed in Fig. 3.12 for which the spectral density component oscillates slowly about a constant saturation value. In contrast to this development the temporal evolution of the density fluctuation during a pulsation is quite different in character. As one observes in Fig. 3.13 which presents

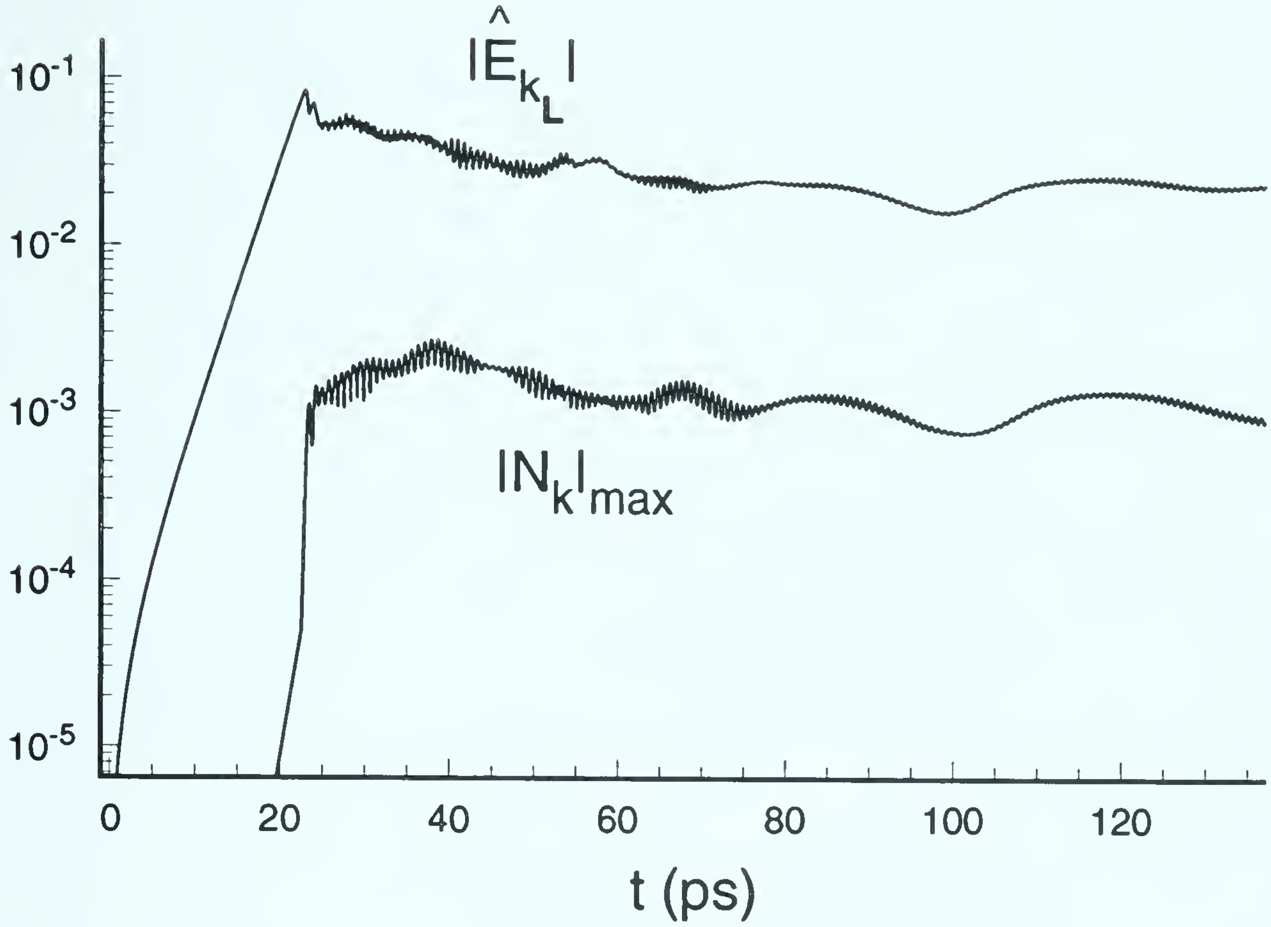

Figure 3.12: *Time evolution of the Fourier component at* $k = k_L$ *of the Langmuir field* $E(x,t)$ *and density obtained from numerical solutions of equations (3.1)-(3.4) for the parameters* $L = 25\,\mu m$, $I = 4.8 \cdot 10^{14}\,W/cm^2$, $n_0^e/n_c = 0.2$, $T_e = 0.5\,keV$, $ZT_e/T_i = 10$, $Z = 2$, $\lambda_0 = 0.531\,\mu m$.

the temporal evolution of the spectral components of E_{k_L} and N_{k_A} for run parameters of Fig. 3.2 , the density continues to grow at an exponential rate even after the first saturation. For this to occur the PDI growth rate Γ_{PDI} must be much larger than the ion damping rate $\gamma_A(k_A^{(1)})$ and the transfer rate of energy to other modes.

As we observed earlier the production of the density fluctuations together with the growth of secondary Langmuir waves can act as an effective damping on the SRS driven Langmuir wave, and together with the decoupling of SRS, damp the wave to thermal noise levels. Figure 3.13 illustrates this behavior for the pulsating run of Fig. 3.2. Once E_L passes through its first saturation the ion density component

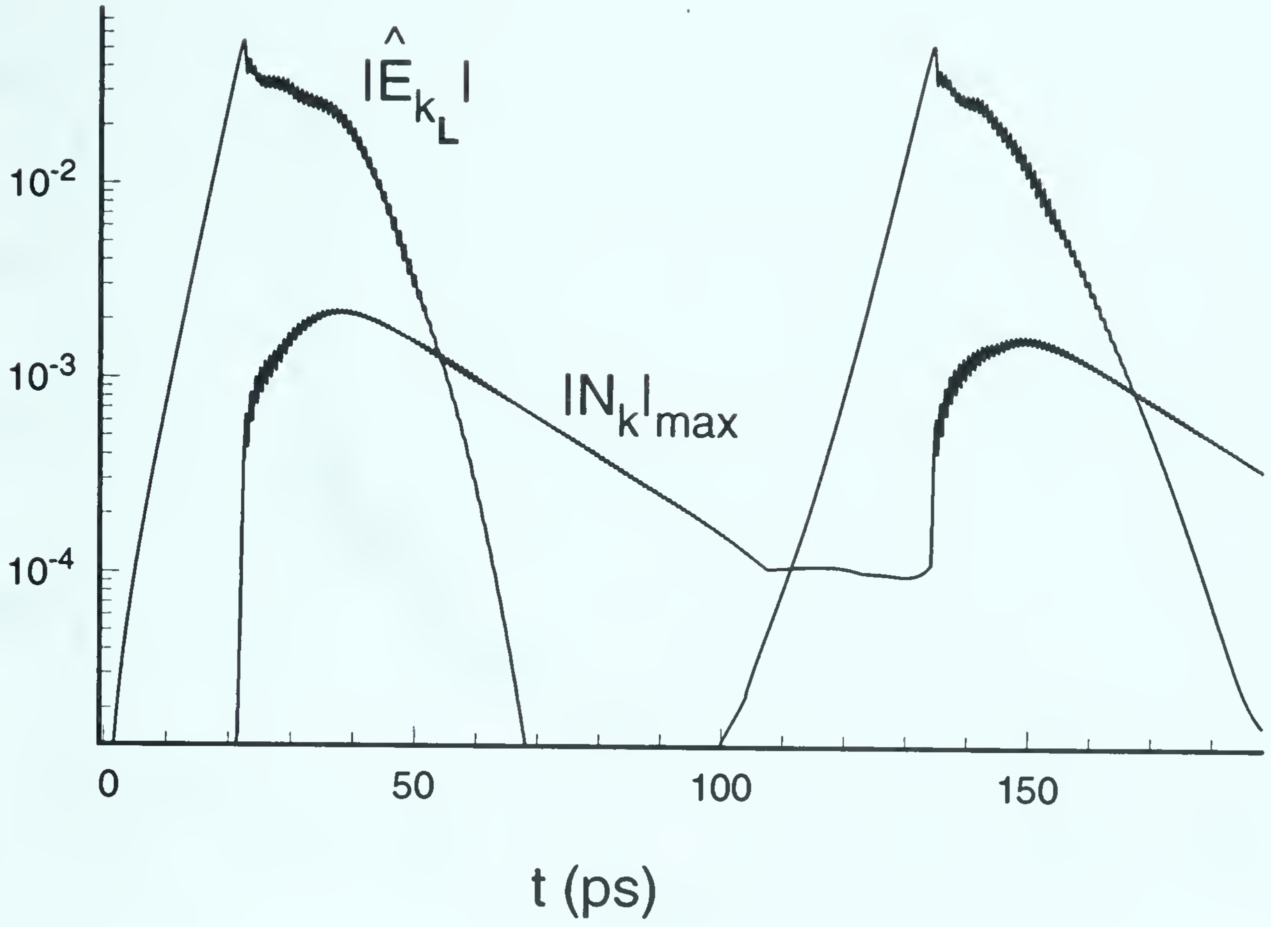

Figure 3.13: *Time evolution of the Fourier component at $k = k_L$ of the Langmuir field $E(x, t)$ and density obtained from numerical solutions of equations (3.1)-(3.4) for the parameters of Fig. 3.2*

continues to grow, decoupling SRS. As $N_A^{(1)}$ and $E_L^{(1)}$ continue to grow, further energy is drained from E_L. As the energy of E_L is drained away the PDI growth rate is reduced eventually leading to a saturation of the secondary satellites. Unlike the nonpulsating runs, a high enough level of density fluctuations have been built up as compared to the rate of dissipation due to ion damping, so that these density fluctuations continue to exist, maintaining the SRS decoupling, for sufficient time permitting E_L to be damped back down to noise level. The ion density then continues to damp eventually allowing SRS to once again establish itself and the sequence repeats itself. During subsequent bursts E_L will usually reach smaller and smaller values at first saturation until PDI growth rate Γ_{PDI} is of a value that will not produce pulsations and the SRS evolves into its asymptotic quasistationary

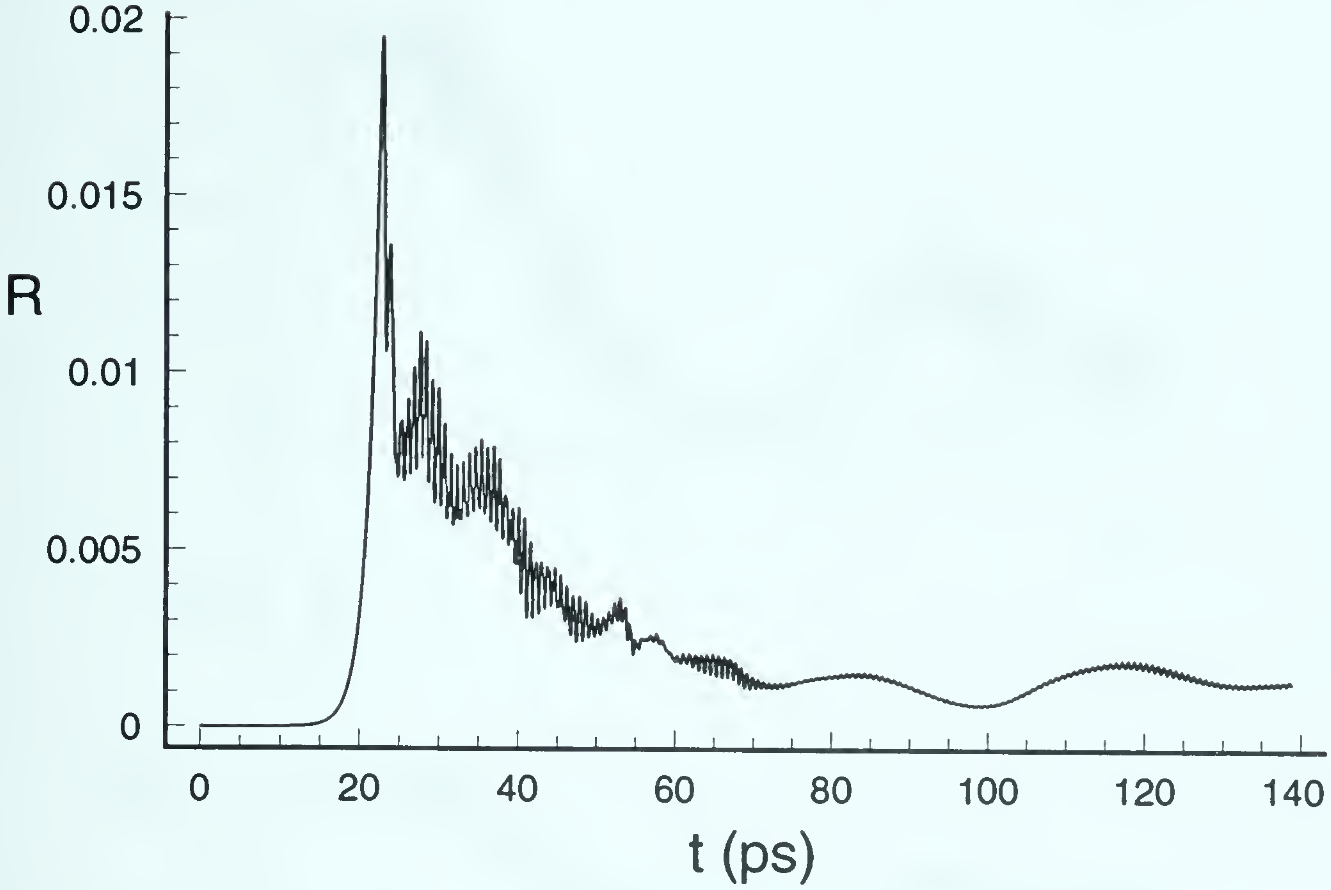

Figure 3.14: *SRS reflectivity as a function of time obtained from numerical solutions of equations (3.1)-(3.4) for the parameters of Fig. 3.12*

saturated state.

The dependence of the two evolution scenarios on the ratio $\Gamma_{PDI}/\gamma_A(k_A^{(1)})$ is illustrated in Fig. 3.14 where only a monotonic SRS burst is obtained. Figure 3.14 was obtained by running identical parameters to Fig. 3.2 except for the electron-ion temperature ratio. In this case ZT_e/T_i was lowered from $ZT_e/T_i = 30$ in Fig. 3.2 to $ZT_e/T_i = 10$ in Fig. 3.14, thus raising the ion acoustic damping rate. We were always able to change the behavior of our simulation runs from monotonic to quasiperiodic like behavior by reducing the ion wave damping and/or by increasing the ratio $\Gamma_{PDI}/\gamma_A(k_A^{(1)})$.

An example of the transition from monotonic to pulsating bursts by only changing $\Gamma_{PDI}/\gamma_A(k_A^{(1)})$ is illustrated in Fig. 3.15 These two simulations were run for

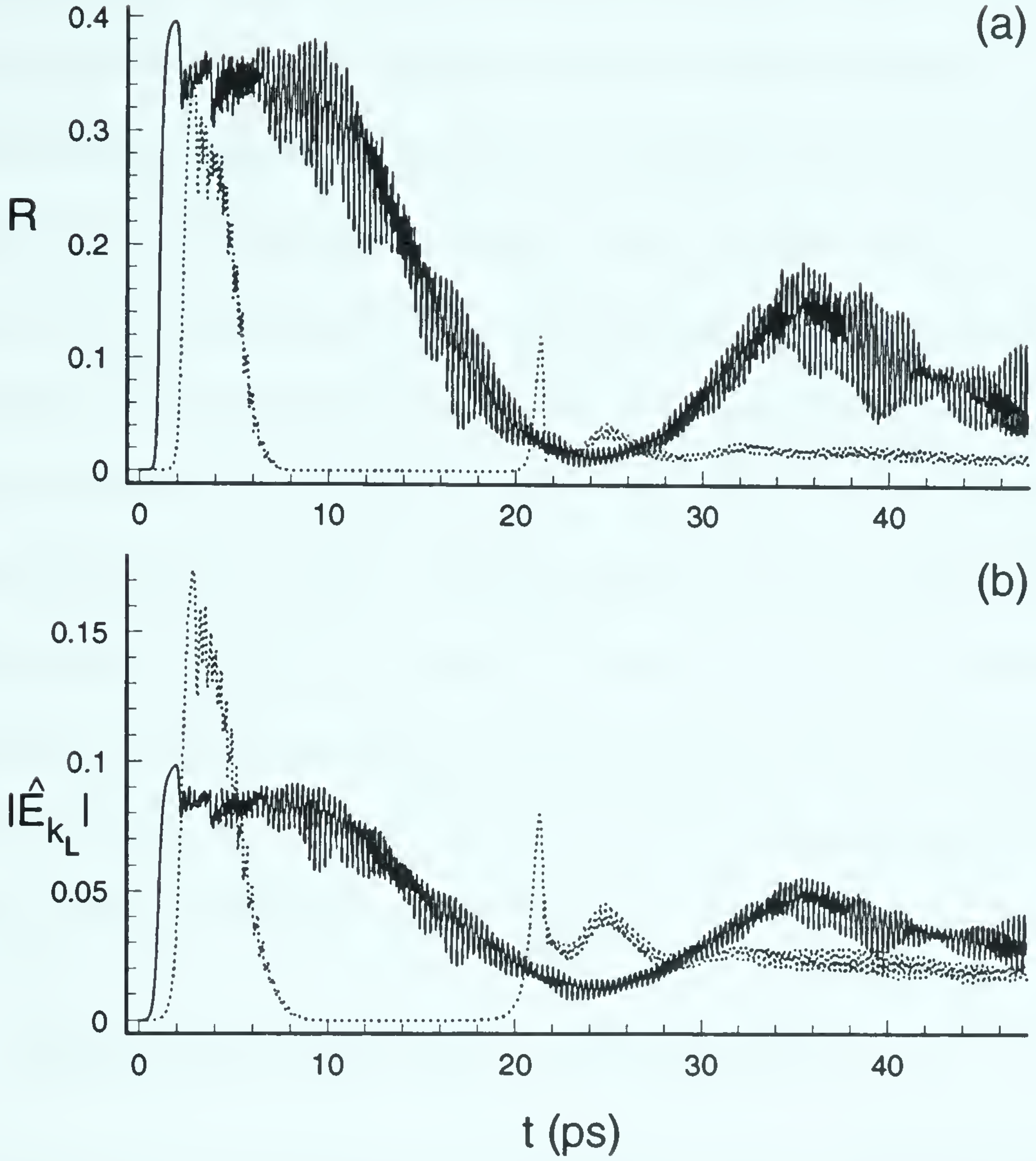

Figure 3.15: *Results from numerical integration of equations (3.1)-(3.4) for the parameters* $I = 2 \cdot 10^{15}\, W/cm^2$, $n_0^e/n_c = 0.2$, $T_e = 3.5\, keV$, $ZT_e/T_i = 50$, $Z = 50$, $\lambda_0 = 0.531\, \mu m$ *for lengths:* $L = 25\, \mu m$, *(dotted curve) and* $L = 50\, \mu m$ *(solid curve) displaying (a) SRS reflectivity time history and (b) Fourier components at* k_L *of the Langmuir field.*

identical parameters except for the interaction length L was changed from $25\mu m$ (dotted curve) to $50\mu m$ (solid curve). Note that this is consistent with the value of $\Gamma_{PDI}/\gamma_A(k_A^{(1)})$ which is larger for $25\mu m$ because of the larger value of $E_{k=k_L}$ (see Fig. 3.15(b)) in the intermediate nonlinear regime. Physically, PDI is much more effective in the termination of SRS leading to bursts in reflectivity when the region of its activity corresponds to a large fraction of the interaction length, as in the shorter box run.

In summary, the intermediate nonlinear evolution of SRS depends on the further development of the PDI cascade, which is usually disrupted in our runs after the second stage. The localization of the Langmuir waves that accompanies the truncation of the PDI cascade is related to the spatial evolution of the instability that starts locally and spreads in the plasma during the quasistationary evolution of reflectivity. The decay of the Langmuir wave amplitude and of the reflectivity toward the stationary asymptotic values takes place on the scale defined by the ion wave damping $1/\gamma_A(k_A^{(1)})$. For large values of $\Gamma_{PDI}/\gamma_A(k_A^{(1)})$, SRS occurs in bursts and while it is difficult to predict the value of this parameter in an absolute sense (Γ_{PDI} depends on the noise level and value of $\mid E_L \mid$ at first saturation) we can always change SRS behavior from monotonic to pulsating by decreasing the damping coefficient of the ion-acoustic wave.

3.5 Final asymptotic saturation

As the PDI active region spreads through out the interaction length of the plasma, and the localization of the electrostatic fields truncates the cascade, a final asymptotic quasistationary saturated state is reached. All simulation runs eventually reach this well defined asymptotic state, which produces an almost stationary level of reflectivity. To obtain a simple estimate of this stationary state, the two nonlinear terms in (3.8) are assumed to balance each other producing the expression

$$\frac{1}{4}\frac{e}{m_e}\frac{k_L\omega_p^2}{\omega_R\omega_0\omega_L}E_0E_R^* - \frac{\omega_p^2}{4\omega_L}N_A^{(1)}E_L^{(1)} = 0 \tag{3.19}$$

Here $N_A^{(1)}$ and $E_L^{(1)}$ correspond to the density and Langmuir field only in an average sense. The numerical results (Fig. 3.16) show a random distribution of $\mid \hat{E} \mid^2$ and N at later times. These turbulent Langmuir and density fields are very similar to

those shown in Fig. 3.17 which used the same parameters except for a doubling of laser intensity. The spectral results of Fig. 3.17(a) however contain a broader spread in the spectrum, and appear to have a much stronger continuous component. This suggests the presence of localization of the Langmuir fields, usually associated with a Langmuir collapse. However the most pronounced part of the spectrum is still associated with the discrete components of PDI during the first two stages of cascading. Thus without invoking the mechanism of strong Langmuir turbulence we can obtain expressions for the reflectivity scaling which are in good agreement with numerical results. Our parameters were always such that we remained in the weakly driven Langmuir regimes where strong Langmuir turbulence was avoided,

In order to accomplish this we again approximate $E_L^* \simeq E_L^{(1)*}$, disregard the phase variation and use (3.15) in (3.19) to produce the "average" expression

$$E_L^{as} = E_{thr}\hat{E}_R^{\frac{1}{3}} \tag{3.20}$$

where we assume $E_L^{as} > E_{thr}$ and we have introduced the normalized scattered field amplitude

$$\hat{E}_R = \frac{E_R}{E_{thr}}\frac{\omega_p}{\omega_R}\frac{k_L v_0}{4\gamma_L(k_L)} \tag{3.21}$$

As we have shown the electromagnetic components are well approximated by single modes and hence in the stationary regime the evolution of the backscattered electromagnetic component can be approximated by the equation

$$V_R\frac{\partial E_R}{\partial x} = \frac{k_L v_0}{4}E_L^* \tag{3.22}$$

In the present derivation we will assume that no pump depletion occurs allowing us to treat the electromagnetic pump as a constant. Combining (3.20),(3.21) and,

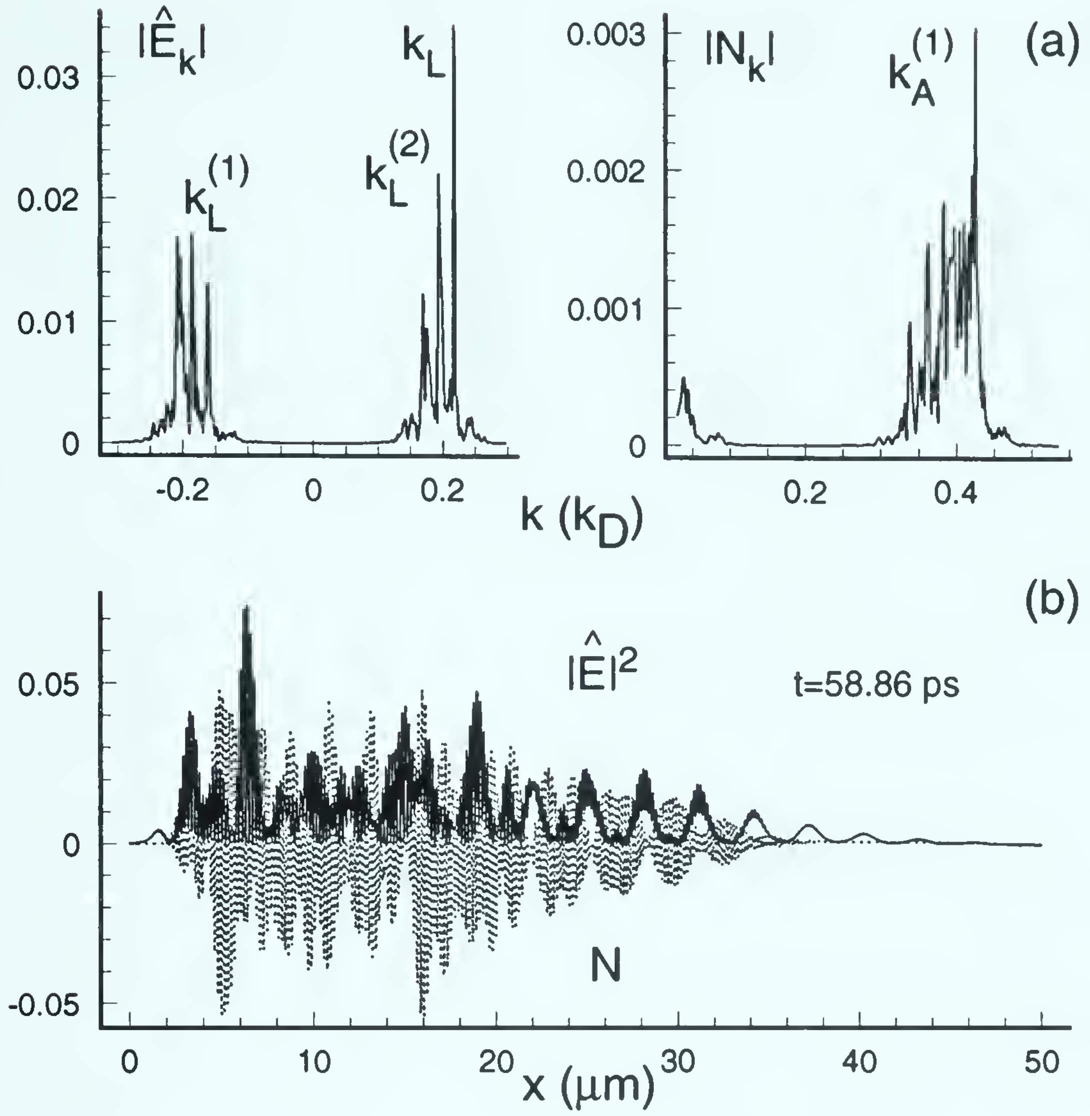

Figure 3.16: *Results from the numerical integration of equations (3.1)-(3.4) for* $t = 58.86$ *ps of Fig. 3.5 for same parameters as Fig 3.7. (a) Fourier spectrum of the electrostatic electric field* $\hat{E}_k = E_k/(4\pi n_0^e T_e)^{1/2}$ *and density* N_k. *(b) Spatial profiles of the electrostatic electric field* $|\hat{E}|^2 = |E|^2/(4\pi n_0^e T_e)$ *and density.*

(3.22) produces the resulting equation

$$\frac{\partial \hat{E}_R}{\partial x} = -\frac{\Gamma_{SRS}^2}{\gamma_L(k_L) \mid V_R \mid} \hat{E}_R^{\frac{1}{3}} \tag{3.23}$$

which can be integrated with the boundary conditions $\hat{E}_R(x = L) = 0$ to obtain for the backscattered electromagnetic component at the left boundary

$$\hat{E}_R(x = 0) = \left(\frac{2}{3} \frac{\Gamma_{SRS}^2 L}{\gamma_L(k_L) \mid V_R \mid} \right)^{\frac{3}{2}} = \left(\frac{2}{3} A \right)^{\frac{3}{2}} \tag{3.24}$$

Here we define the amplification coefficient for convective SRS as

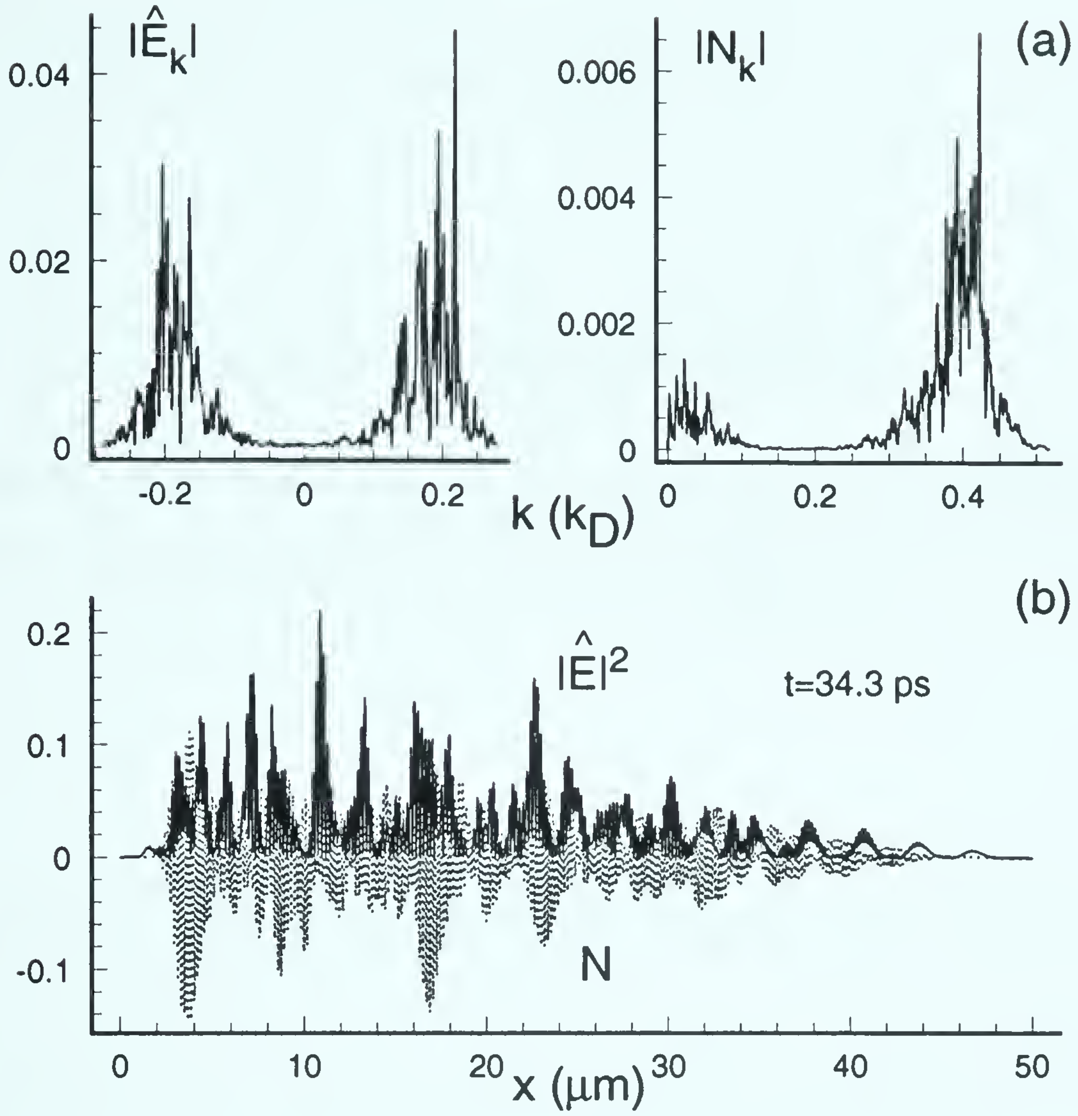

Figure 3.17: *Results from the numerical integration of equations (3.1)-(3.4) for* $t = 34.3$ *ps for same parameters as Fig. 3.7. except for a doubling of laser intensity(a) Fourier spectrum of the electrostatic electric field* $\hat{E}_k = E_k/(4\pi n_0^e T_e)^{1/2}$*and density* N_k*. (b) Spatial profiles of the electrostatic electric field* $\mid \hat{E} \mid^2 = \mid E \mid^2 /(4\pi n_0^e T_e)$ *and density.*

$$A \equiv \frac{\Gamma_{SRS}^2 L}{\gamma_L(k_L) \mid V_R \mid} \tag{3.25}$$

By defining the reflectivity

$$R = \frac{\mid V_R \mid}{V_0} \frac{\mid E_R(x=0) \mid^2}{\mid E_0(x=0) \mid^2} \tag{3.26}$$

we obtain an asymptotic scaling law for SRS reflectivity

$$R = R_c \left(\frac{2}{3}A\right)^3 \tag{3.27}$$

where

$$R_c = \frac{(k_L v_{T_e})^2 \gamma_L^3(k_L)\gamma_A(k_A^{(1)})\omega_p \mid V_R \mid}{\Gamma_{SRS}^4 \omega_0^2 \omega_A V_0} \tag{3.28}$$

This scaling law is linearly dependent on the laser intensity and proportional to L^3. With this, the Langmuir field can now be estimated for the asymptotic state giving

$$E_L^{as} = E_{thr} \left(\frac{2}{3}A\right)^{\frac{1}{2}} \tag{3.29}$$

It is important to note that the final SRS reflectivity and Langmuir field does not depend explicitly on the linear electron damping coefficients thus the linear damping will affect the way the energy is distributed through out the plasma but will not affect the final saturation value. This result different from the scaling laws proposed by Drake and Batha [43] who approximated the SRS saturated reflectivity with the PDI threshold. Bezzerides et al. [65] have also proposed SRS scaling which is dependent on the linear electron damping, however in their report the parameter regime studied allowed for the development of strong Langmuir turbulence.

Our results have been tested against many numerical simulations producing the results illustrated in Fig. 3.18. As one can easily see Fig. 3.18 illustrates the validity of (3.27) presenting evidence which gives reasonable agreement between our analytical theory and numerical simulation. Table 3.1 gives the range of parameters under which the early simulations, equations (3.1)-(3.4) which did not contain the SBS or anti-Stokes coupling, were performed.

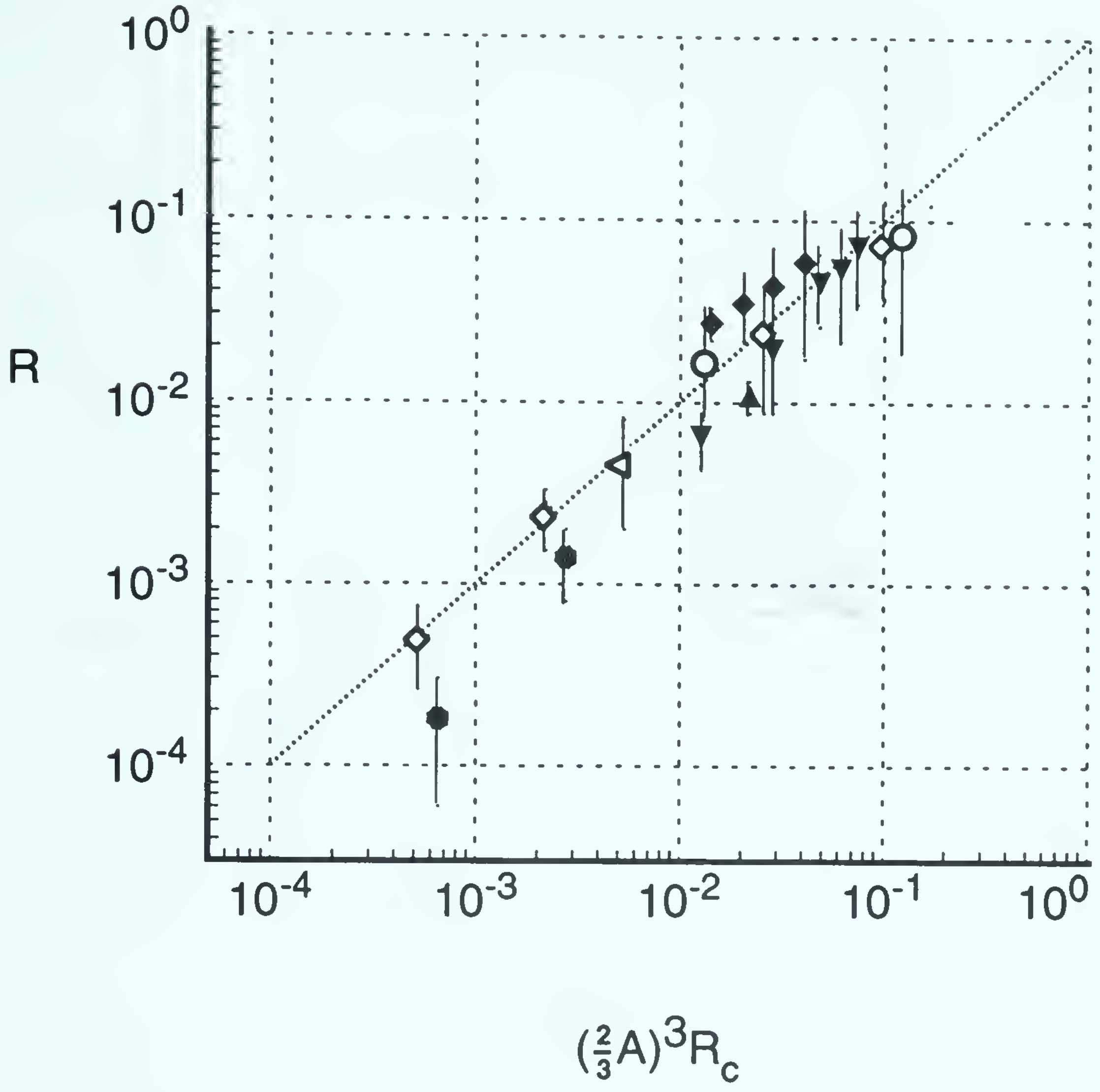

Figure 3.18: *Time integral averaged asymptotic SRS reflectivities plotted as a function of scaling formula, Equation(3.27). Explanations for the different symbols are given in table 3.1. Vertical error bars denote the maximum and minimum fluctuations during the asymptotic regime.*

In the recently proposed explanation [43] of the nonlinear properties of SRS, (for example the spectral gap observed in many experiments,) Drake and Batha assumed that the resonant Langmuir wave saturates exactly at the PDI threshold value E_{thr}. We have plotted our results for the Fourier spectrum component $\mid E_{k_L} \mid$ of the Langmuir fields as a function of the PDI threshold (Fig. 3.19)

It is quite apparent from Fig. 3.19 that $\mid E_{k_L} \mid$ scales in good approximation with E_{thr}. It is also obvious that the saturation levels of the Langmuir wave amplitudes depend on the laser intensity and the plasma interaction length. Several points from Fig. 3.19 were obtained for different interaction lengths or laser in-

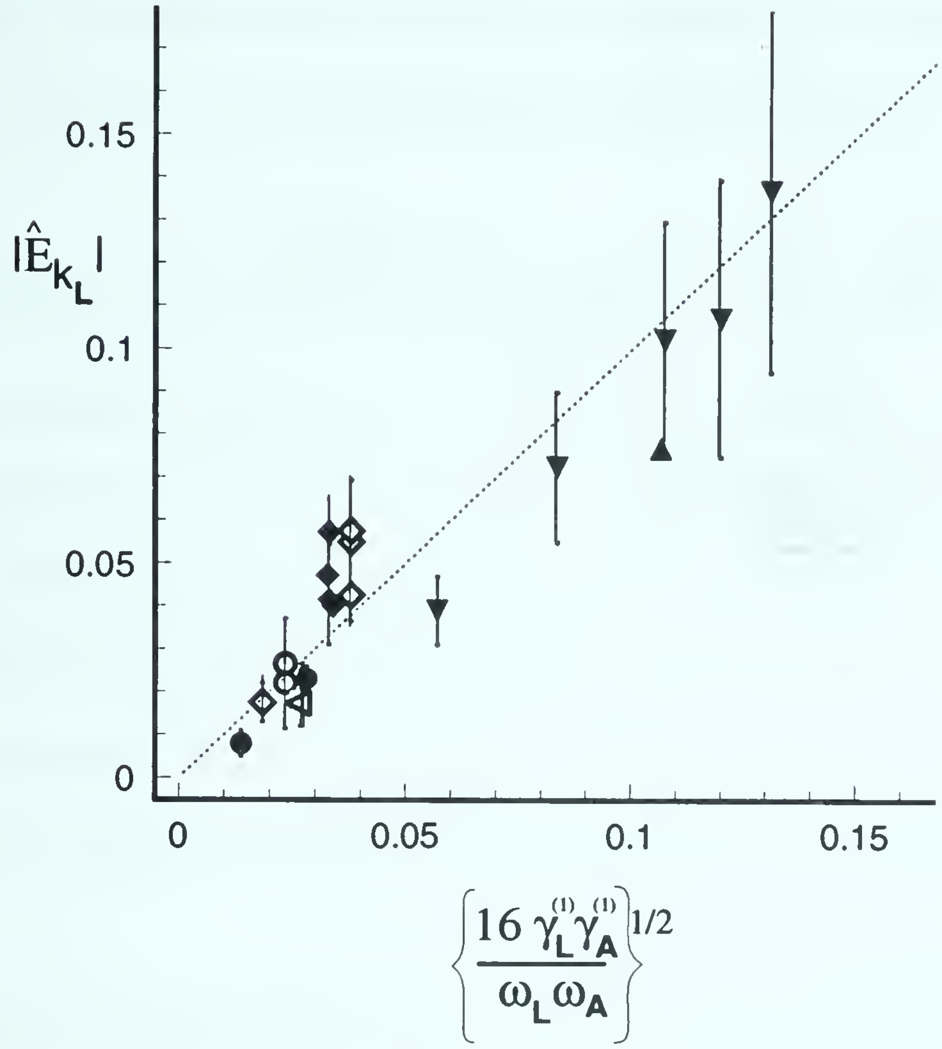

Figure 3.19: *Time integral averaged asymptotic values of the Fourier transformed Langmuir field at $k = k_L$ plotted as a function of scaling formula, Equation(3.29). Explanations for the different symbols are given in table 3.1. Vertical error bars denote the maximum and minimum fluctuations during the asymptotic regime.*

tensities while the remaining parameters were held constant. These points depart systematically from the simple scaling law proposed in [43] which is represented by the diagonal line. The more refined relation (3.29) contains a dependence on length and intensity, but because the numerical values of $\sqrt{A}$ are not very far from unity, it will give a very similar result compared to a simple scaling with the PDI threshold.

In more practical units (3.27) can be written as

$$R = 6.54\ 10^{-10} T_e \lambda_0^2 I_{14} \frac{\gamma_A(k_A^{(1)})}{\omega_A} \frac{L^3}{\lambda_0^3} \Xi(\frac{n_0}{n_c}) \tag{3.30}$$

where T_e is the electron temperature in electron volts, I_{14} is the laser intensity in $10^{14} W/cm^2$, and λ_0 and L are the wave length and the interaction length in μm respectively. The density dependent function Ξ is given by

$$\Xi(\frac{n_0}{n_c}) = \frac{n_0}{n_c}\frac{(1-\sqrt{n_0/n_c})^{1/2}\left[(1-n_0/n_c)^{1/2}+(1-2\sqrt{n_0/n_c})^{1/2}\right]^4}{(1-2\sqrt{n_0/n_c})(1-n_0/n_c)^{1/2}} \qquad (3.31)$$

Using equation (3.29) one can also estimate an upper bound for the intensity and length of the interaction region by enforcing $E_L^2/4\pi n_0^e T_e < 1$ which is one of the limiting parameters associated with the validity of the Zakharov model [51]. Under such restrictions, simulation runs, which both met this criterion and for which strong Langmuir turbulence was observed, were extremely rare for the parameter regimes investigated. In practical units this criterion is given by

$$3.05\ 10^{-4} I_{14}\lambda_0^2 \frac{L}{\lambda_0}\frac{\gamma_A(k_A^{(1)})}{\omega_A}\frac{\left[(1-n_0/n_c)^{1/2}+(1-2\sqrt{n_0/n_c})^{1/2}\right]^2}{(1-2\sqrt{n_0/n_c})^{1/2}} < 1, \qquad (3.32)$$

Here L and λ_0 are in μm and $\gamma_A(k_A^{(1)})$ is given by (2.63).

In the parameter regime where pump depletion can no longer be ignored, the saturation value for SRS reflectivity and the corresponding value for E_L must be recalculated. When pump depletion is included SRS reflectivity can be found by solving the simple ordinary differential equation

$$\frac{\partial R(x)}{\partial x} = -\frac{2\Gamma_{SRS}^2}{\gamma_L(k_L) \mid V_R \mid} R_{cr}^{\frac{1}{3}} \left[R^2(x)\left(C+\frac{\omega_0}{\omega_R}R(x)\right)^2\right]^{\frac{1}{3}} \qquad (3.33)$$

where R_{cr} is given by expression (3.28) and $C = 1 - \omega_0 R(0)/\omega_R$. Similarly the electrostatic field E_L can be found by solving the integral equation

$$\mid E_L \mid^2 = \frac{2A}{3}E_{thr}^2\left[1-\frac{\omega_0}{\omega_R}R(0)+\frac{2\omega_0}{L\omega_R}\int_0^L R(x)dx\right] \qquad (3.34)$$

Both these equations are evaluated using a shooting code and are necessary once the asymptotic SRS reflectivity is above $\simeq 10-15\%$. By using (3.33) and (3.34) the agreement between our analytical theory and numerical simulation is also slightly improved for parameters that do not lead to pump depletion.

3.6 Derivation of coherent and random phase reflectivity

In deriving expressions (3.27) and (3.33) for the SRS saturation it was assumed that the three wave modes producing SRS interact in a coherent manner throughout the entire interaction region. The final asymptotic state is the result of balancing the incoming laser energy with the conversion of this energy into Langmuir and ion acoustic modes and the subsequent damping of such modes. The process responsible for this, namely PDI cascading creates a broad spectrum of resonant and quasimode waves. Physically it is conceivable, especially for very large laser intensities or very long interaction regions, that the SRS process may not remain coherent for the entire interaction length. The spectrum itself, for high laser intensities, becomes turbulent, restricting the actual coherence length L_I to some length much smaller than the length of the plasma $L_I \ll L$. As the system becomes more turbulent the coherence length decreases, eventually reaching zero at which point the phases are considered to be completely random. The two different phase approximations, coherent and random, represent the upper and lower bounds for the length dependence of our system. We will examine the SRS reflectivity from both extremes allowing us to determine to what extent each of the models applies to our analysis. Because a similar analysis of which model, random or coherent, will be necessary in Chap. 4, we proceed using the general 3WI forms of the respective

phase approximations.

For a system of three waves with coherent-phase wave-packets (cf. Ref. [4], [5]) one has the equations

$$\left(\frac{\partial}{\partial t}+V_1\frac{\partial}{\partial x}\right)A_{k_1}=-\eta_1\int\int dk_2dk_3A_{k_2}A_{k_3}\delta(k_1-k_2-k_3)\exp(i\Delta\Phi t)\quad(3.35)$$

$$\left(\frac{\partial}{\partial t}+V_2\frac{\partial}{\partial x}\right)A_{k_2}=\eta_2\int\int dk_1dk_3A_{k_1}A^*_{k_3}\delta(k_1-k_2-k_3)\exp(-i\Delta\Phi t)\quad(3.36)$$

$$\left(\frac{\partial}{\partial t}+V_3\frac{\partial}{\partial x}\right)A_{k_3}=\eta_3\int\int dk_2dk_1A^*_{k_2}A_{k_1}\delta(k_1-k_2-k_3)\exp(-i\Delta\Phi t)\quad(3.37)$$

where $A_{k_j}; j=1,2$ represent the electromagnetic component spectral amplitudes, A_{k_3} is the electrostatic spectral amplitude, and $\Delta\Phi=\omega_1-\omega_2-\omega_3$ is the phase mismatch. For SRS $\eta_1=e(\omega_2+\omega_3)\omega_p^2k_3/2m_e\omega_1\omega_2\omega_3$, $\eta_2=e(\omega_1-\omega_3)\omega_p^2k_3/2m_e\omega_1\omega_2\omega_3$, and $\eta_3=e\omega_p^2k_3/4m_e\omega_1\omega_2\omega_3$. If we assume that the wave packets of the spectral components are very narrow around some specific wave number then we can make the approximation $\int dkA_k\sim\tilde{A}_k$. Taking the appropriate integral over k and finding stationary solution to (3.35) and (3.36) produces the equations

$$V_1\frac{\partial}{\partial x}\tilde{A}_{k_1}=-\eta_1\tilde{A}_{k_2}\tilde{A}_{k_3}\quad(3.38)$$

$$V_2\frac{\partial}{\partial x}\tilde{A}_{k_2}=\eta_2\tilde{A}_{k_1}\tilde{A}^*_{k_3}\quad(3.39)$$

where after integrating the delta function $k_1=k_2+k_3$, and $\omega_1=\omega_2+\omega_3$. To produce a more general form of the reflectivity derivation in Chap. 3.5, which can

be also used to discuss work in Chap. 4, we rewrite (3.38) and (3.39) in terms of the ponderomotive potential amplitude P and phase ϕ [65], [94] where

$$\frac{Pe^{i\phi}}{2} \equiv \mid \tilde{A}_{k_1}\tilde{A}^*_{k_2} \mid e^{i\phi} \tag{3.40}$$

producing the equation

$$\frac{\partial P}{\partial x} = 2\zeta \left[C^2 + \frac{P^2}{\omega_1\omega_0 \mid V_0 V_1 \mid} \right]^{\frac{1}{2}} \Re[\Phi] \tag{3.41}$$

where

$$\Phi = \tilde{A}_{k_3} \exp[-i\phi] \tag{3.42}$$

Here $C = -(\mid \tilde{A}_{k_1}(0) \mid^2 / \omega_1 V_2) + (\mid \tilde{A}_{k_2}(0) \mid^2 / \omega_2 V_1)$, $P(0) = 2I\sqrt{V_1 R / V_2}$ and $P(L) = 0$. For SRS the subscripts 1, 2 represent the laser pump and Raman backscattered wave while the subscript 3 refers to the Langmuir mode, here also for SRS $\zeta = e\omega_p^2 k_L / 2\omega_L m_e$. Integrating (3.41), one can produce the expression for reflectivity of

$$\begin{aligned} R = \frac{\mid V_2 \mid\mid \tilde{A}_{k_2} \mid^2}{V_1 \mid \tilde{A}_{k_1} \mid^2} &= \frac{\omega_2}{\omega_1} \tanh^2 \left[\alpha \int_0^L \tilde{A}_{k_3} \exp[-i\phi] dx \right] \\ &\simeq \frac{\omega_2}{\omega_1} \mid \alpha \int_0^L \tilde{A}_{k_3} \exp[-i\phi] dx \mid^2 \end{aligned} \tag{3.43}$$

where for SRS $\alpha = e\omega_p k_L / 2m_e c^2 \sqrt{k_0 k_R}$. In deriving (3.43) it has been assumed that $\tilde{A}_{k_3}$ is essentially independent of P. If a strong dependence on P occurs then (3.43) takes the form of an iterative equation with $\tilde{A}_{k_3} = \tilde{A}_{k_3}(R)$. For convenience of this discussion we assume that the phase of $\tilde{A}_{k_3}$ is ϕ and that $\tilde{A}_{k_3}$ is independent of x producing the approximate expression

$$R \propto | \tilde{A}_{k_3} |^2 L^2 \tag{3.44}$$

Examining the equations describing the evolution of the random phase wave packets (cf. Ref. [4], [5]) we have

$$\left(\frac{\partial}{\partial t} + V_1 \frac{\partial}{\partial x}\right) | A_{k_1} |^2 = -\beta_1 \int\int dk_2 dk_3 \delta(k_1 - k_2 - k_3)\delta(\Delta\Phi t) \times \left[\frac{| A_{k_2} |^2 | A_{k_1} |^2}{\omega_1\omega_2} - \frac{2 | A_{k_2} |^2 | A_{k_3} |^2}{\omega_3\omega_2} + \frac{2 | A_{k_3} |^2 | A_{k_1} |^2}{\omega_1\omega_3}\right] \tag{3.45}$$

$$\left(\frac{\partial}{\partial t} + V_2 \frac{\partial}{\partial x}\right) | A_{k_2} |^2 = -\beta_2 \int\int dk_1 dk_3 \delta(k_1 - k_2 - k_3)\delta(\Delta\Phi t) \times \left[\frac{| A_{k_2} |^2 | A_{k_1} |^2}{\omega_1\omega_2} - \frac{2 | A_{k_2} |^2 | A_{k_3} |^2}{\omega_3\omega_2} + \frac{2 | A_{k_3} |^2 | A_{k_1} |^2}{\omega_1\omega_3}\right] \tag{3.46}$$

$$\left(\frac{\partial}{\partial t} + V_3 \frac{\partial}{\partial x}\right) | A_{k_3} |^2 = -\beta_3 \int\int dk_2 dk_1 \delta(k_1 - k_2 - k_3)\delta(\Delta\Phi t) \times \left[\frac{| A_{k_2} |^2 | A_{k_1} |^2}{\omega_1\omega_2} - \frac{2 | A_{k_2} |^2 | A_{k_3} |^2}{\omega_3\omega_2} + \frac{2 | A_{k_3} |^2 | A_{k_1} |^2}{\omega_1\omega_3}\right] \tag{3.47}$$

For SRS $\beta_1 = e^2\omega_p^2 k_3^2/2m_e^2\omega_3\omega_2$, $\beta_2 = e^2\omega_p^2 k_3^2/2m_e^2\omega_3\omega_1$, and $\beta_3 = e^2\omega_p^2 k_3^2/16m_e^2\omega_3^2\omega_2\omega_1$. Ignoring the nonresonant nonlinear terms, calculating the integrals and finding stationary solutions produces:

$$V_1 \frac{\partial}{\partial x} | A_{k_1} |^2 = -\frac{\beta_1}{V_2\omega_2\omega_3} | A_{k_2} |^2 | A_{k_3} |^2 \tag{3.48}$$

$$V_2 \frac{\partial}{\partial x} | A_{k_2} |^2 = -\frac{\beta_2}{V_1\omega_2\omega_3} | A_{k_1} |^2 | A_{k_3} |^2 \tag{3.49}$$

which can be manipulated in terms of an analogous ponderomotive potential

$$\frac{P_1}{2} \equiv \mid A_{k_1} \mid^2 \mid A_{k_2} \mid^2 \tag{3.50}$$

producing the reflectivity expression

$$\begin{aligned} R = \frac{\mid V_2 \mid \mid A_{k_2} \mid^2}{V_1 \mid A_{k_1} \mid^2} &= \frac{\mid V_2 \mid}{V_1} \frac{\omega_2}{\omega_1} \tanh \left[\alpha_r \int_0^L \mid A_{k_3} \mid^2 dx \right] \\ &\simeq \frac{\mid V_2 \mid}{V_1} \frac{\omega_2}{\omega_1} \left[\alpha_r \int_0^L \mid A_{k_3} \mid^2 dx \right] \end{aligned} \tag{3.51}$$

where $\alpha_r = e^2 k_3^2 / m_e^2 \omega_1 \omega_2 \mid V_2 \mid V_1$. If we again assume that amplitude is independent of x and performing an integration over the wave numbers of k_3 we arrive at the reflectivity expression

$$R \propto \int dk_3 \mid \tilde{A}_{k_3} \mid^2 L = \langle A^2 \rangle L \tag{3.52}$$

where $\langle A^2 \rangle$ is the average spatial amplitude.

If the width of the coherent wave packet is relatively narrow, (3.44) for SRS is approximately proportional to our expression (3.27) where $\tilde{A}_{k_3}$ is given by (3.29), and hence would produce a linear dependence on intensity and cubic dependence on length. In contrast should a turbulent description be more consistent with our simulations one would expect to find a reflectivity with a length dependence other than cubic. In the case of completely random phases one would expect a reflectivity linearly dependent on the interaction length.

As is easily observable from Fig. 3.18 the correspondence between the simulation and theoretical reflectivities is in good agreement with a coherent wave description. However should the intensity regime or other changes in our parameter space produce a much more turbulent spectrum, then it may be necessary to

modify our analytical results. For example, the recent study by Bezzerides et al. [65] has explored regimes for which strong Langmuir turbulence is identified as the saturation mechanism of SRS and hence an approach tending towards a turbulent description may provide a more accurate scaling for their results than our analytical expressions. For the parameter regimes examined here, a coherent wave description proved adequate. However, in the next chapter we examine enhancement of parametric processes occurring simultaneously with SRS. Under these circumstances forward Raman and Brillouin scattering appear to be well approximated by a more turbulent system somewhere in between a coherent and completely random phase description, while the anti-Stokes Raman components appear to be described by an almost completely random phase.

Chapter 4

Laser light scattering from fluctuations enhanced by stimulated Raman scattering

In general, the PDI cascade and the interaction of resonant waves and quasimodes created during the saturation of SRS will produce broad Langmuir and density spectra. The spectral width in each case will be dependent on the laser intensity and interaction length through the asymptotic amplitude of the SRS driven Langmuir wave (3.29). Depending on the strength of the SRS amplification coefficient A, the spectrum can range in nature from a narrow pedestal like structure around the primary PDI wave numbers k_L, $k_L^{(1)}$ and $k_A^{(1)}$, to a continuous spectrum overlaid with discrete components. Should sufficient noise levels be generated, there exists the possibility of scattering large amounts of laser light through other known resonant channels such as Brillouin [88], [89], [69] or forward Raman [92], [100]. Resonant processes stable to small perturbations such as the anti-Stokes Raman scattering components may also be affected by these enhanced noise levels. The possibility of scattering light from these enhanced levels of electrostatic fluctuations can thus lead to explanations of experimental observations of anti-Stokes Raman reflectivity. Such a concept could also be applied to the experimental observation

symbol	n_0/n_{cr}	T_e(keV)	ZT_e/T_i	λ_0(μm)	I(W/cm^2)	L(μm)	Z
▼	.05	.05	5	10	$5\ 10^{12}$	250	3
◇	.04-.08	.3-.6	6-10	1	$.5\text{-}6\ 10^{14}$	60-500	2-6
▽	.1-.12	.5-.7	7-8	1	$5\text{-}9\ 10^{13}$	60-250	2
▲	.1-.15	1-1.2	5-10	1,0.53	$.5\text{-}10\ 10^{14}$	25-250	2-5
□	.14	2.0	8	0.53	$1\ 10^{15}$	30-100	4
◆	.2	.5-.75	6-8	1	$.5\text{-}2.5\ 10^{14}$	50-100	2-5
△	.2	1-1.5	4-8	1,0.53	$.2\text{-}5\ 10^{14}$	25-250	2-8
■	.2-.212	2.0	8-10	0.53	$.4\text{-}3\ 10^{14}$	30-100	5-8

Table 4.1: *Parameters used in simulations of equations (2.57)-(2.61). The symbols are used in Figs. (4.5), (4.6) and (4.7)*

of anomalously high levels of Brillouin reflectivity and forward Raman scattering. This chapter is devoted to studying under what conditions the enhancement of these secondary processes will take place in our model. Numerous sets of parameters (see table 4.1) were used to examine different regimes for which this enhancement may apply. Even though the parameter regime is extensive, simple criteria for strong enhancement are found and reflectivity scaling laws are provided.

To illustrate how the enhancement process may affect other parametric processes occurring simultaneously with SRS, Fig. 4.1 contains a typical time history of the SRS reflectivity and the other processes of Brillouin, and forward Raman scattering as well as the anti-Stokes forward and backward Raman scattering. Initially SRS (Fig. 4.1(a)) is observed evolving through the linear stage of its development in region 1, which then proceeds into the first sharp saturation caused by PDI in region 2. At this point the enhancement of the secondary scattering processes

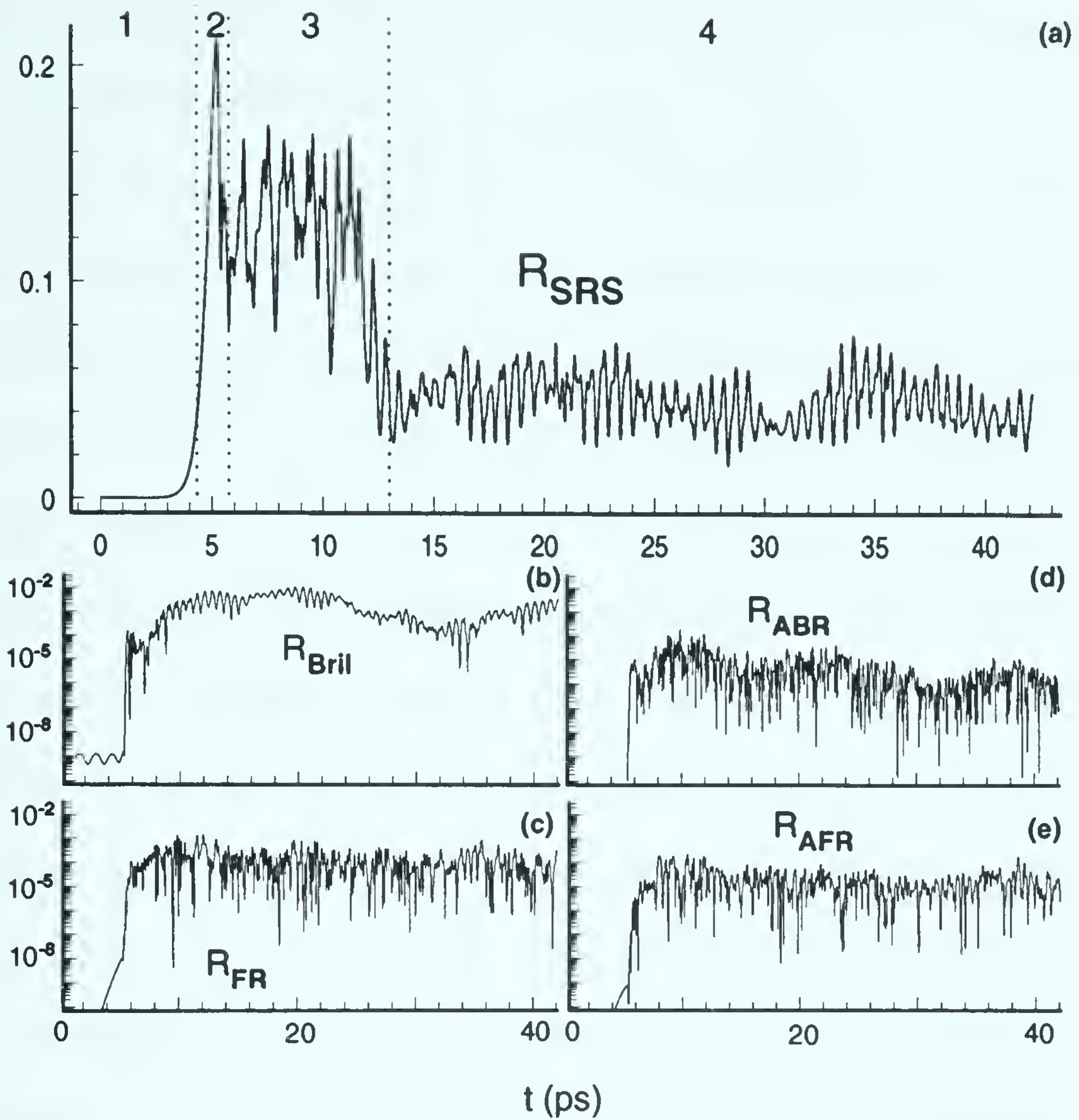

Figure 4.1: *Reflectivity as a function of time obtained from numerical solutions of equations (2.57)-(2.61) for the parameters* $L = 60\,\mu m$, $I = 2.5 \cdot 10^{14}\,W/cm^2$, $n_0^e/n_c = 0.2, T_e = 1\,keV$, $ZT_e/T_i = 8$, $Z = 3$, $\lambda_0 = 0.531\,\mu m$; *(a)SRS, (b)Brillouin, (c)forward Raman, (d)anti-Stokes backwards Raman, and (e)anti-Stokes forward Raman*

begins, producing a very rapid increase in the reflectivity levels of Brillouin (Fig. 4.1(b)), and forward Raman (Fig. 4.1(c)), as well as anti-Stokes backward (ABR) (Fig. 4.1(d)) and forward Raman (AFR) (Fig. 4.1(e)). As SRS evolves through its third stage the decay cascade continues, eventually producing broad Langmuir and ion acoustic spectra of quasimodes and resonant modes. With this broadening of the spectra the reflectivity level of the secondary components continues to increase until SRS saturation occurs in region 4.

As the simulations pass through the transient nonlinear phase into the asymptotic regime, the Langmuir and ion density spectra broaden due to PDI and the

interaction of quasimodes and resonant waves eventually reaching a quasistationary state. A typical example, with parameters $L = 30\,\mu m$, $I = 2 \cdot 10^{14}\,W/cm^2$, $n_0^e/n_c = 0.2$, $T_e = 1.5\,keV$, $ZT_e/T_i = 8$, $Z = 3$, $\lambda_0 = 0.531\,\mu m$, of the electrostatic spectrum is presented in Fig. 4.2(a) with the ion density spectra for the same case appearing in Fig. 4.2(b). As one observes the regions, in which PDI dominates, are composed of large spikes overlaying a much lower continuous spectra. Quasimodes, which do not satisfy (1.1) and (1.2), can be seen broadening the spectra around the PDI induced peaks. The discrete components of the PDI cascade are easily identifiable and are separated by $\Delta k = \frac{2}{3}k_D\sqrt{Zm_e/m_i}$ in the Langmuir wave spectrum and $2\Delta k$ in the density spectrum. In Fig. 4.2 we have identified the various wave numbers associated with our investigation. Here k_L^{FR} refers to the Stokes coupling of forward Raman while the components $k_L^{BR^+} \sim -0.27k_D$ (not shown) and $k_L^{FR^+} \sim k_L^{FR}$ refer to the Langmuir waves describing anti-Stokes backward and forward Raman scattering respectively (see table 2.1). In the density spectra $k_A^{(1)}$ is the first PDI daughter wave and k_A^B is the Brillouin density component.

Through many simulations an exponential decrease in the spectral amplitudes of the Langmuir and density cascades in the PDI active regions have been determined. The maximum amplitudes of the spectra occur at $N_{k=k_A^{(1)}}$ in the ion acoustic spectra and $E_{k=k_L}$ in the Langmuir spectra, and are well approximated by the expression (3.15) and (3.29) for which (3.29) is used to estimate the density amplitude. The spread of the spectra can be approximated by

$$\Delta k_{spr} = \Gamma_{PDI}/c_s \tag{4.1}$$

where Γ_{PDI} is the PDI growth rate, c_s is the ion sound speed, and Δk_{spr} is the spread of the wave spectrum. Using (4.1) the electrostatic wave number spectra

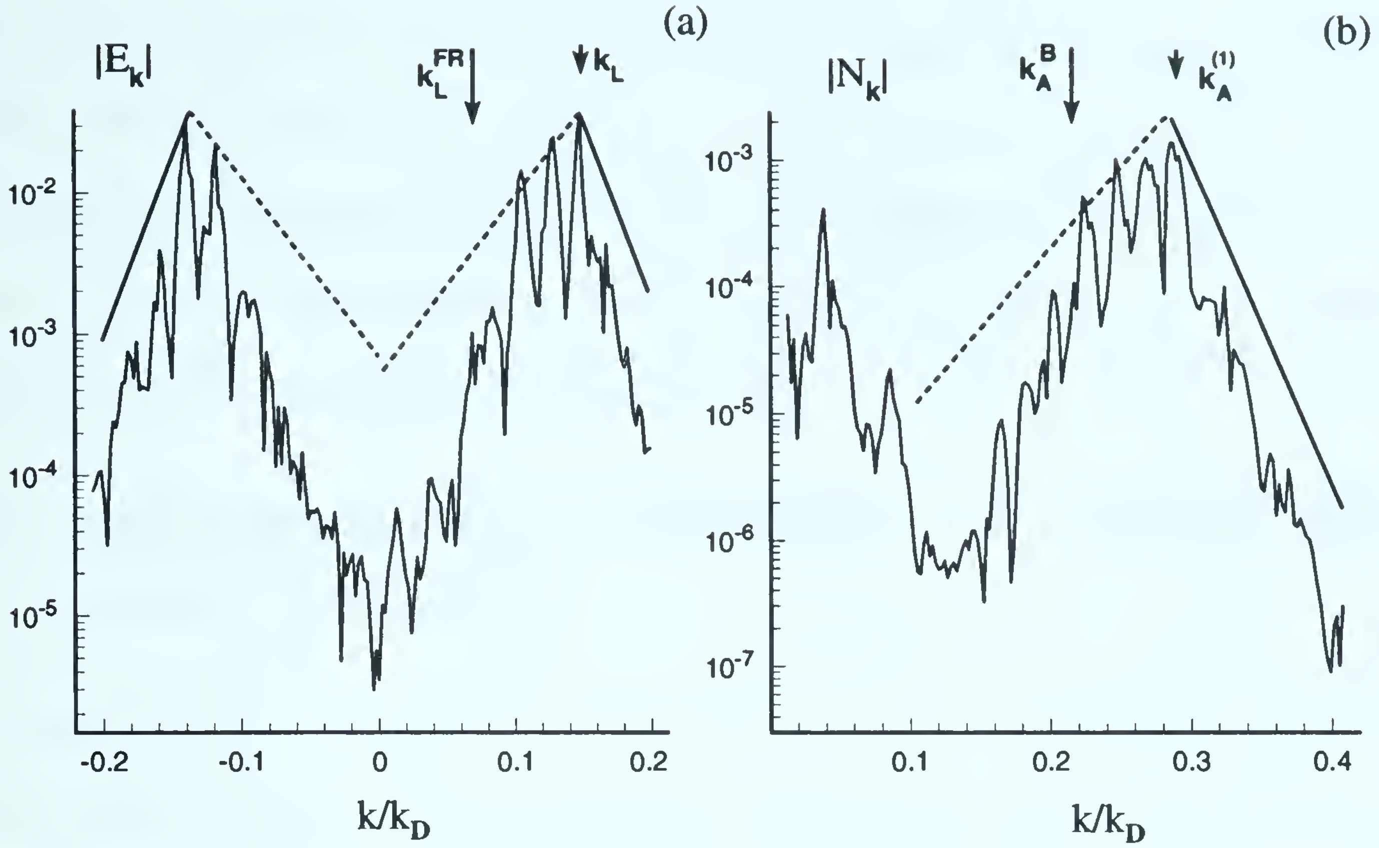

Figure 4.2: *(a) Electrostatic and (b) density spectra obtained from numerical solutions of equations (2.57)-(2.61) at* $t = 62.4ps$ *for run parameters* $L = 30\,\mu m$, $I = 2 \cdot 10^{14}\, W/cm^2$, $n_0^e/n_c = 0.2$, $T_e = 1.5\,keV$, $ZT_e/T_i = 8$, $Z = 3$, $\lambda_0 = 0.531\,\mu m$

can now be approximated by the expression

$$E_k = \frac{E_L}{\sqrt{2}} \exp[-\beta \left(\frac{\mid k - k_L \mid}{\Delta k_{spr}} \right)], \tag{4.2}$$

for the Langmuir spectra and

$$N_k = \frac{1}{8} \frac{\omega_A^{(1)}}{\gamma_A(k_A^{(1)})} \frac{\mid E_L \mid^2}{4\pi n_0^e T_e} \exp[-\beta \left(\frac{\mid k - k_A^{(1)} \mid}{\Delta k_{spr}} \right)]. \tag{4.3}$$

for the ion acoustic spectra. Here k_L is the resonantly driven SRS Langmuir mode, $\omega_A^{(1)}$ and $\gamma_A(k_A^{(1)})$ are the frequency and ion Landau damping coefficients associated with the first PDI ion mode. β is a parameter used to determine the slope of the spectra. In the region where the PDI cascade dominates $\beta \simeq 1$ Fig. 4.2 (dotted line) and $\beta \simeq 2$ in the strongly driven regions where the PDI cascade is absent Fig. 4.2 (solid line).

Good correspondence with numerical data can be achieved if the exact solution of the PDI dispersion relation (1.23) is used. In (1.23) E_L is determined by using the appropriate expression (3.29) or (3.34) and by using the PDI growth rate from (1.23) for which the appropriate weakly coupled ($\Gamma_{PDI} < k_A c_s$) or the strongly driven ($\Gamma_{PDI} > k_A c_s$) growth rate can be found.

4.1 Enhancement of Brillouin and forward Raman scattering

As was illustrated in Fig. 4.1 the enhancement of the various secondary scattering processes closely follows the nonlinear development of SRS. Beginning with the first saturation of SRS a very rapid increase in the Brillouin (Fig. 4.1(b)) and forward Raman (Fig. 4.1(c)) reflectivities is observed. Figure 4.3 compares the Brillouin and forward Raman reflectivities together with the respective reflectivities produced from the standard three wave interaction model using identical parameters, and thermal noise levels. The six orders of magnitude difference in the respective levels of Brillouin reflectivity demonstrate the importance of including simultaneous nonlinear processes in any description of laser-plasma interaction.

To obtain analytical results for the enhanced Brillouin and forward Raman scattering the same procedure as in Chap. 3.6 is used. Again it is assumed that the electromagnetic waves can be represented by single discrete modes. For Brillouin scattering we now expand Ψ_0 in terms of slowly varying amplitudes for the pump and Brillouin backscattered components

$$\Psi_0 = \frac{eE_0}{m_e\omega_0}\exp[ik_0x] + \frac{eE_B}{m_e\omega_B}\exp[ik_Bx] \tag{4.4}$$

which, when applied to equation (2.59), produces the stationary equations

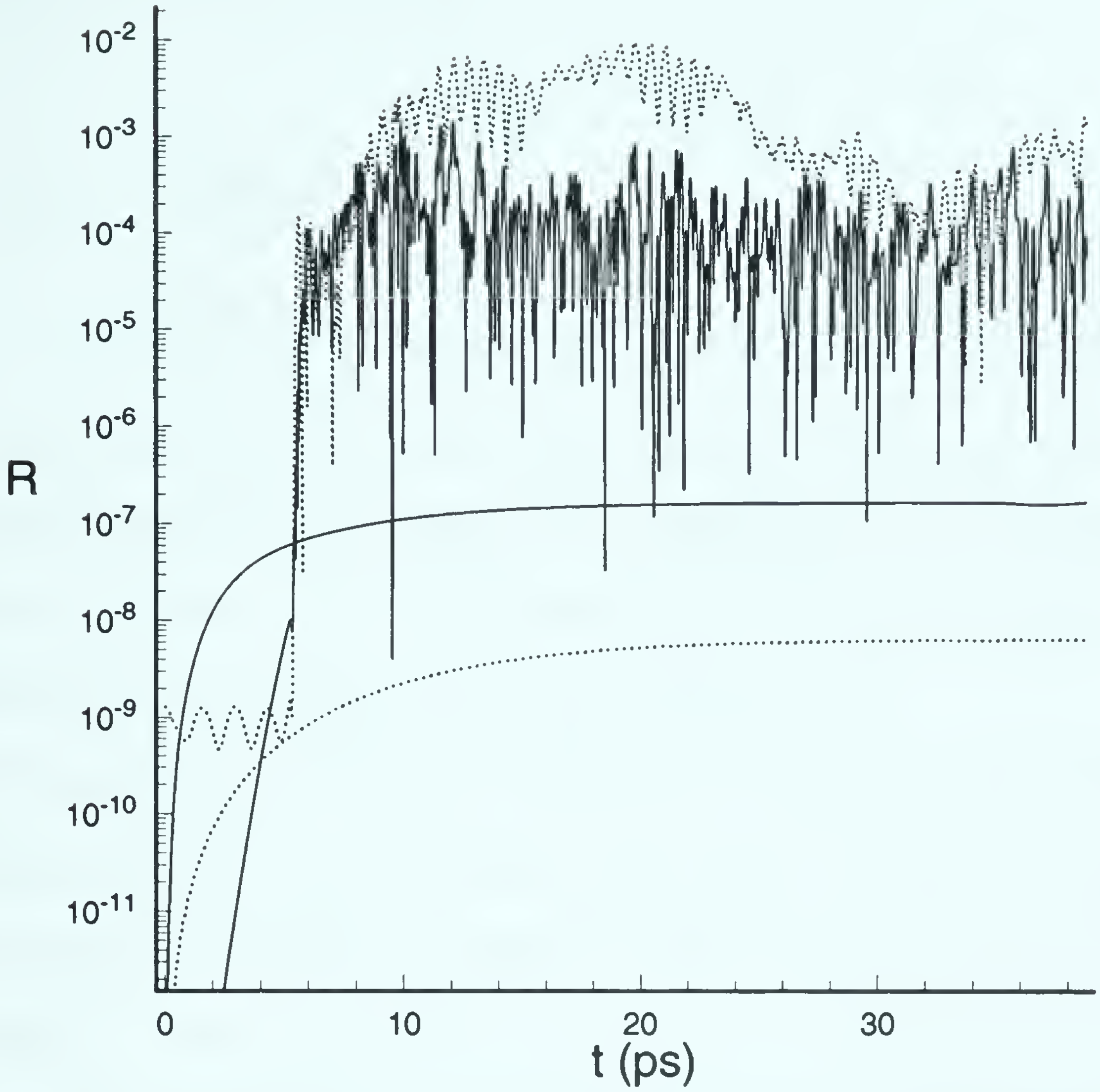

Figure 4.3: *Brillouin (dotted curves) and forward Raman (solid curves) reflectivities as a function of time obtained from numerical solutions of equations (2.57)-(2.61) for same parameters as in Fig. 4.1, together with the simulation results of the standard three wave interaction model equations (2.75)-(2.77) for identical parameters.*

$$V_B \frac{\partial E_B}{\partial X} = \frac{\omega_p^2}{2\omega_0} N E_0 \exp[ik_A^B x] \tag{4.5}$$

$$V_0 \frac{\partial E_0}{\partial X} = \frac{\omega_p^2}{2\omega_B} N E_0 \exp[-ik_A^B x] \tag{4.6}$$

At this point N is still the full amplitude wave function associated with (2.58) and $V_j = k_j c^2/\omega_j; j = 0, B$ are the group velocities of the pump and Brillouin electromagnetic waves respectively. The previous method, used in Chap. 3.6, of introducing a ponderomotive potential (3.40) can again be employed to produce

the Brillouin reflectivity expression

$$\begin{aligned} R_B &= \frac{\mid V_B \mid\mid E_B \mid^2}{V_0 \mid E_0 \mid^2} \\ &= \frac{\omega_B}{\omega_0} \tanh^2 \left[\alpha_B \int_0^L N \exp[-ik_A^B x - i\phi] dx \right] \simeq \mid \alpha_B N_{k_A^B} L \mid^2 \end{aligned} \tag{4.7}$$

where we have used (3.43) with $\alpha_B = \omega_p^2/2\omega_0 V_0$, $N_{k_A^B} = \tilde{A}_{k_3}$ and the subscripts 1, 2, and 3 refer to the electromagnetic pump, backscatter and electrostatic density fluctuation respectively. The actual reflectivity can then be estimated by using expression (4.3) at $k = k_A^B$ to evaluate the amplitude $N_{k_A^B}$.

As the amplification coefficient A (3.25) is increased the number of quasimodes and resonant modes in the spectra will also increase, creating circumstances for which the coherence length of the Brillouin reflectivity may be less than the interaction length L. Once again as was demonstrated in Chap. 3.6 one could produce an expression illustrating the lower limit for the reflectivity using a random phased wave packet (3.51), resulting in an expression which is linearly dependent on L and an ensemble averaged density amplitude $\langle N^2 \rangle$. The coherent and random phase approaches thus provide the limiting cases in which the reflectivity could be classified. In the event that the amplification coefficient A is not large enough to properly enhance the spectra, expressions (4.2) and (4.3) will not produce an accurate description of the spectra but instead provide an upper bound for the reflectivity.

The procedure used in Chapter 3.6 can also be used to produce an expression for the forward Raman reflectivity, resulting in

$$R_{FR} \simeq \mid \alpha_{FR} E_{k=k_L^{FR}} L \mid^2 \tag{4.8}$$

where $\alpha_{FR} = ek_L^{FR}/4m_e\omega_0\sqrt{V_0V_R}$, and the subscripts 1, 2, 3 now refer to the electromagnetic pump and forward Raman scatter, and the Langmuir wave component respectively. We also use $E_{k=k_L^{FR}} = \tilde{A}_{k_3}$ which is evaluated using (4.2) at $k = k_L^{FR}$. Similar restrictions to those acting on enhanced Brillouin scattering will apply to the enhancement of forward Raman scattering and thus a random phase approach could also be found to describe the lower limit of the reflectivity. In the present investigation it has been assumed that a coherent phase approach provides a sufficient analysis of the system, producing expressions (4.7) and (4.8) as reasonable approximations for the Brillouin and forward Raman reflectivities.

To determine the enhanced reflectivities it is necessary to know not only the overall shape of the wave spectra, but also the extent of the enhanced region. If expressions (4.2) and (4.3) are to be considered valid choices for use in (4.7) and (4.8), the PDI cascade must extend into the spectral region where Brillouin or forward Raman are naturally in resonance. To estimate the number of stages in the PDI cascade [55] one can use $m = E_L^2/E_{th}^2 = \frac{2}{3}A$ to predict the appropriate number of cascades in the Langmuir and ion acoustic Fourier spectra. The PDI density cascade peaks are separated by an amount $2\Delta k$ thus if the separation between the primary ion wave at $k_A^{(1)}$ and the Brillouin component at k_A^B is less than the number of cascade components ie.

$$\frac{2}{3}A > \frac{(k_A^B - k_A^{(1)})}{2\Delta k} = \frac{(\mid 2k_R \mid - \Delta k)}{2\Delta k} = \Delta_B, \tag{4.9}$$

then the cascade will continue past the Brillouin ion wave number and hence Brillouin will be strongly enhanced.

Similarly in the Langmuir spectra the PDI cascade components are separated by Δk and hence if the separation between the Langmuir wave numbers corresponding

to forward Raman at k_L^{FR} and backward Raman at (k_L) is less than the number of cascades ie.

$$\frac{2}{3}A > \frac{(k_L - k_L^{FR})}{\Delta k} = \frac{\mid 2k_R \mid}{\Delta k} = \Delta_{FR}. \tag{4.10}$$

forward Raman will also be strongly enhanced.

To illustrate the enhancement criterion Fig. 4.2 is re-examined where it can be seen at k_A^B that $2.18\Delta_B = \frac{2}{3}A$, and at k_L^{FR}, $0.94\Delta_{FR} = \frac{2}{3}A$, which would produce strongly enhanced Brillouin but would have to be considered only a marginal case for enhancement of forward Raman reflectivity. Figure 4.4 contain further examples of the Langmuir and ion density spectra. Once again the dotted lines illustrate (4.2) and (4.3) for the cascade region $\beta \simeq 1$ and the solid lines the noncascade region $\beta \simeq 2$ where $\mid k \mid > \mid k_L \mid$ and $\mid k \mid > \mid k_A \mid$. The corresponding values of $2.47\Delta_B = \frac{2}{3}A$ and $1.12\Delta_{FR} = \frac{2}{3}A$ at k_A^B and k_L^{FR} respectively are produced for the run parameters $L = 60\,\mu m$, $I = 9 \cdot 10^{13}\,W/cm^2$, $n_0^e/n_c = 0.12$, $T_e = 0.7\,keV$, $ZT_e/T_i = 7$, $Z = 2$, $\lambda_0 = 1\,\mu m$ (Fig. 4.4(a)). The density spectra are fully developed even though the Langmuir spectra remains pedestal like.

Figure 4.4(b) illustrates an example of conditions approaching a turbulence spectra which is produced at $t = 18.1$ps for run parameters $L = 60\,\mu m$, $I = 2.5 \cdot 10^{14}\,W/cm^2$, $n_0^e/n_c = 0.2$, $T_e = 1\,keV$, $ZT_e/T_i = 8$, $Z = 3$, $\lambda_0 = 0.531\,\mu m$. One notices how the peak density spectra are now several times less than that predicted by expression (3.15). Here one would expect that an approach in which the phases were not completely coherent would produce a more accurate result. Once again the corresponding levels $4.2\Delta_B = \frac{2}{3}A$ and $1.75\Delta_{FR} = \frac{2}{3}A$ at k_A^B and k_L^{FR} are produced for the enhancement criterion of the density and electrostatic spectra allowing for the strong enhancement of both instabilities.

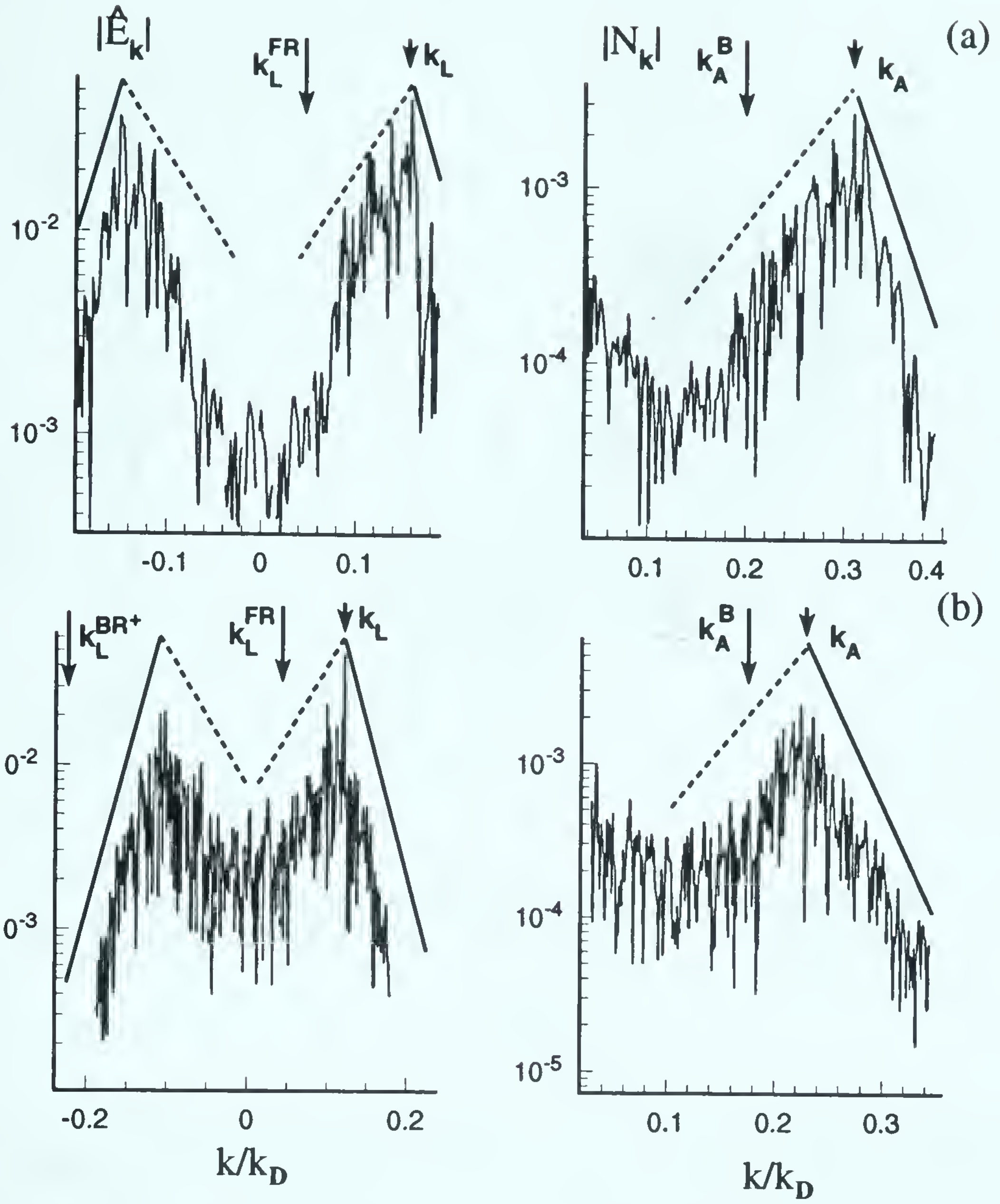

Figure 4.4: *Electrostatic and density spectra obtained from numerical solutions of equations (2.57)-(2.61) at* $t = 94.9ps$ *for run parameters (a)* $L = 60\,\mu m$, $I = 9 \cdot 10^{13}\,W/cm^2$, $n_0^e/n_c = 0.12$, $T_e = 0.7\,keV$, $ZT_e/T_i = 7$, $Z = 2$, $\lambda_0 = 1\,\mu m$ *and at* $t = 18.1ps$ *for run parameters (b)* $L = 60\,\mu m$, $I = 2.5 \cdot 10^{14}\,W/cm^2$, $n_0^e/n_c = 0.2$, $T_e = 1\,keV$, $ZT_e/T_i = 8$, $Z = 3$, $\lambda_0 = 0.531\,\mu m$

Earlier in our analysis it was assumed that both Brillouin and forward Raman could be represented by single modes for which the phases remain coherent. If the enhancement criterion is strictly adhered to and marginal cases ignored, a comparison between the theoretical reflectivities (4.7) and (4.8) and their simulation counterparts yields the plot in Fig. 4.5 and Fig. 4.6 giving good agreement between our numerical simulations and analytical theory. The simulations were run for the parameters of table 4.1. A further comparison for the SRS scaling law (3.27) for

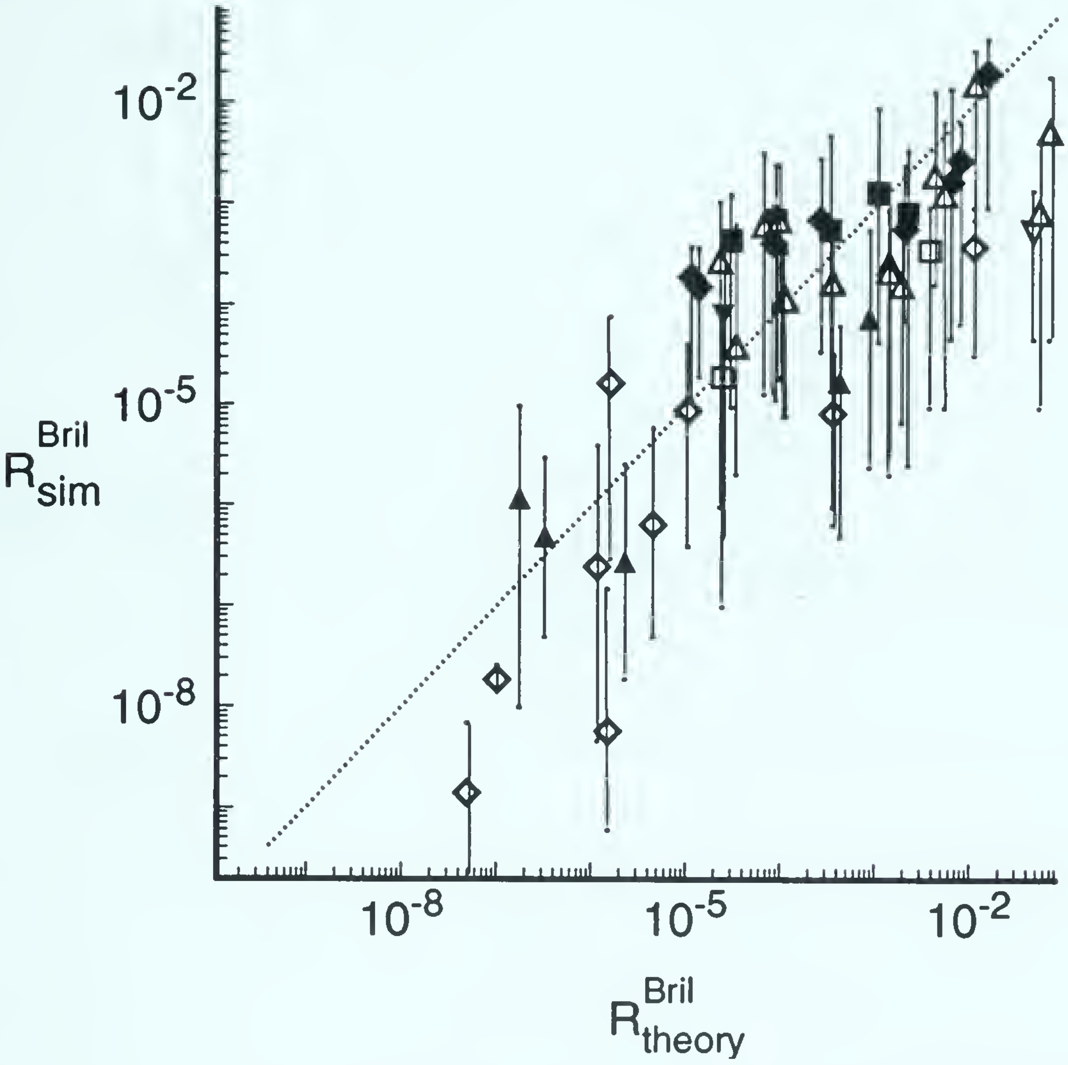

Figure 4.5: *Time integral averaged asymptotic Brillouin reflectivities plotted as a function of scaling formula, Equation(4.7). Explanations for the different symbols are given in table 4.1. Vertical error bars denote the maximum and minimum fluctuations during the asymptotic regime.*

full model simulation is also given in Fig. 4.7, showing that the introduction of the Brillouin coupling does not affect the SRS scaling law. The parameters of table 4.1 for the enhanced quantities and table 3.1 which examine only SRS saturation, were chosen so that we were able to explore the largest possible experimental regimes for which our theory may be applied.

The enhanced reflectivity expressions (4.7) and (4.8) can be rewritten in a more practical form becoming for Brillouin scattering

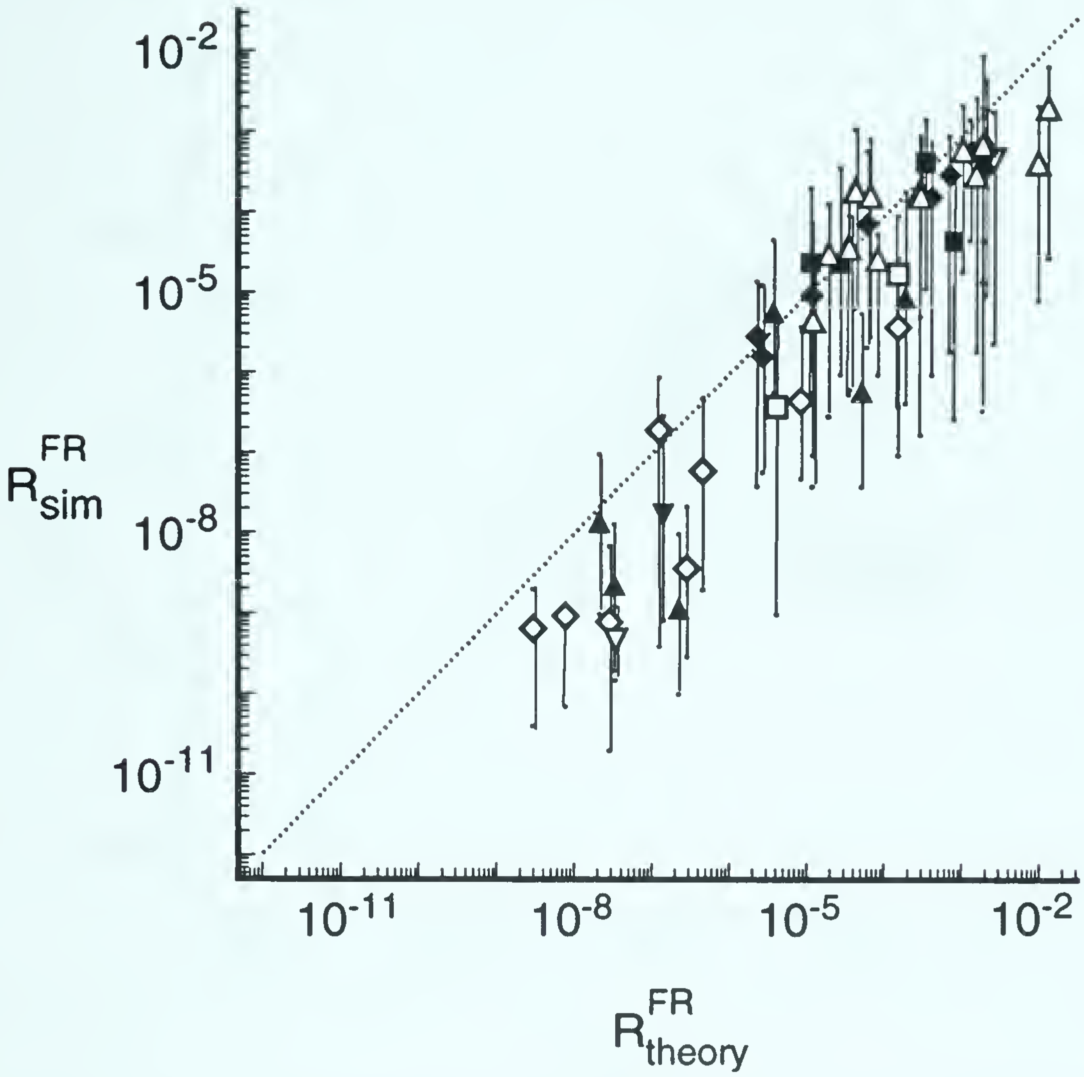

Figure 4.6: *Time integral averaged asymptotic forward Raman reflectivities plotted as a function of scaling formula, Equation(4.8). Explanations for the different symbols are given in table 4.1. Vertical error bars denote the maximum and minimum fluctuations during the asymptotic regime.*

$$R_B = 1.43\ 10^{-8} I_{14}^2 \lambda_0^4 \left(\frac{L}{\lambda_0}\right)^4 \exp[-2\beta\left(\frac{\mid 2k_R - \Delta k \mid}{\Delta k_{spr}}\right)]\Xi_B(\frac{n_0}{n_c}) \tag{4.11}$$

where

$$\Xi_B(\frac{n_0}{n_c}) = (\frac{n_0}{n_c})^2 \frac{\left[(1-n_0/n_c)^{1/2} + (1-2\sqrt{n_0/n_c})^{1/2}\right]^4}{(1-2\sqrt{n_0/n_c})(1-n_0/n_c)} \tag{4.12}$$

and for forward Raman scattering

$$R_{FR} = 1.47\ 10^{-9} I_{14} \lambda_0^2 \left(\frac{L}{\lambda_0}\right)^3 \frac{\gamma_A(k_A^{(1)})}{\omega_A^{(1)}} \exp[-2\beta\left(\frac{\mid 2k_R \mid}{\Delta k_{spr}}\right)]\Xi_{FR}(\frac{n_0}{n_c}) \tag{4.13}$$

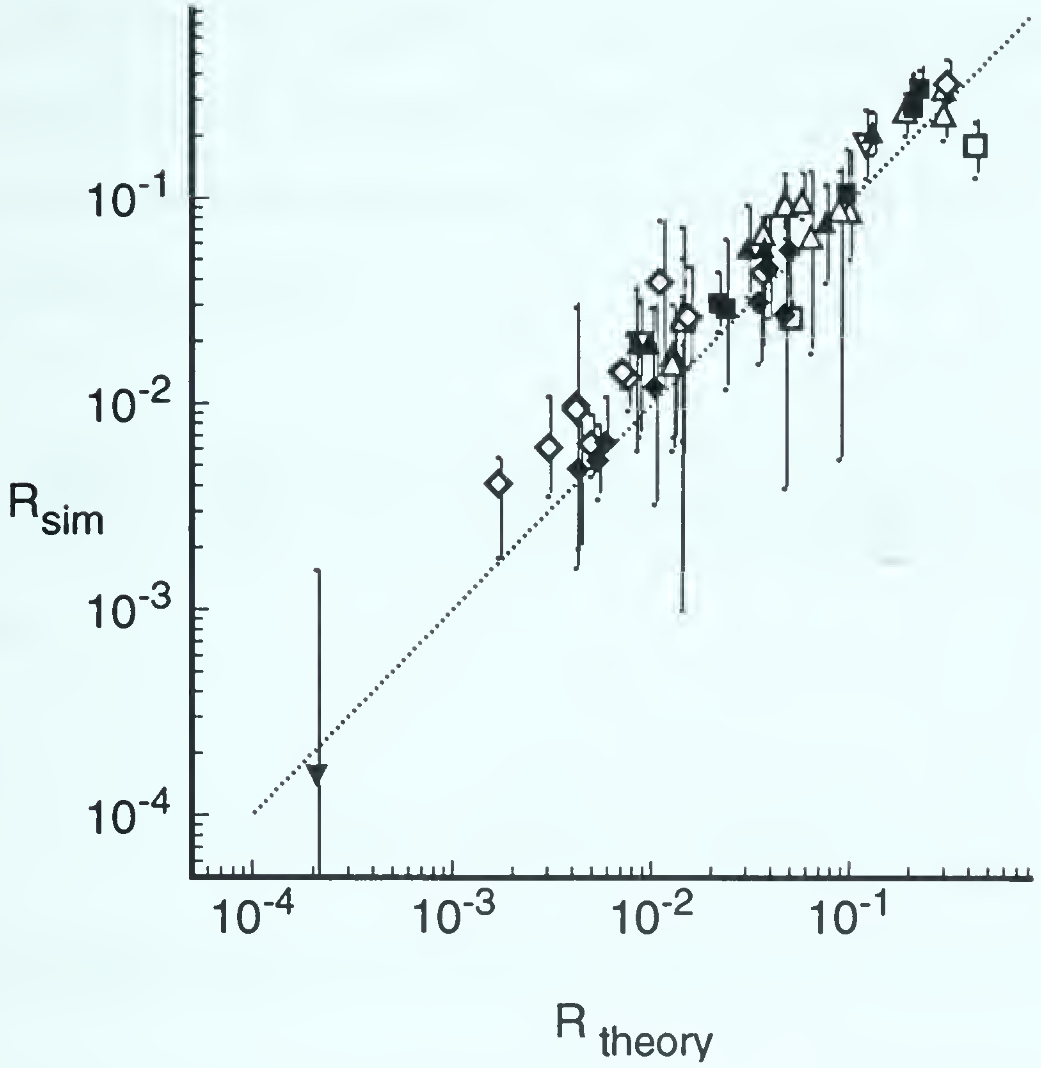

Figure 4.7: *Time integral averaged asymptotic SRS reflectivities plotted as a function of scaling formula, Equation(3.27). Explanations for the different symbols are given in table 4.1. Vertical error bars denote the maximum and minimum fluctuations during the asymptotic regime.*

where

$$\Xi_{FR}(\frac{n_0}{n_c}) = (\frac{n_0}{n_c})\frac{\left[(1-n_0/n_c)-(1-2\sqrt{n_0/n_c})\right]^2(1-\sqrt{n_0/n_c})}{(1-2\sqrt{n_0/n_c})(1-n_0/n_c)^{1/2}} \tag{4.14}$$

In these expressions L, and λ_0 are in μm, $\gamma_A(k_A^{(1)})/\omega_A^{(1)}$ can be found using (2.63) and I_{14} is the laser intensity in $10^{14} W/cm^2$. It is to be noted that the expression for Brillouin reflectivity depends on the electron and ion damping only through the spread of the wave spectra Δk_{spr} (4.1). Similarly forward Raman is dependent on the electron damping only through the spread of the waves. To evaluate the PDI

growth rate appearing in (4.2) and (4.3) without the use of numerical methods one can approximate the expression (1.23) in the absence of damping for the weakly driven case $\Gamma_{PDW} < k_A c_s$ using expression (1.24). With the approximation $k_A^{(1)} \sim 2k_L$ the inverse of the argument of the exponential for both (4.11) and (4.13) can be written in the form

$$\frac{\Delta k_{spr}}{2k_R} = \frac{\Gamma_{PDW}}{2c_s k_R} = 5.4 \cdot 10^{-7}\left[I_{14}\lambda_0^2 \frac{2}{ZT_e}\frac{L}{\lambda_0}\frac{\gamma_A(k_A^{(1)})}{\omega_A^{(1)}}\Xi_{PDW}(\frac{n_0}{n_c})\right]^{1/2} \tag{4.15}$$

where

$$\Xi_{PDW}(\frac{n_0}{n_c}) = \sqrt{\frac{n_0}{n_c}}\left[\frac{(1-n_0/n_c)^{1/2}}{(1-2\sqrt{n_0/n_c})^{1/2}}+1\right]^3 \tag{4.16}$$

or the strongly driven case expression (1.28) where $\Gamma_{PDS} > k_A c_s$ gives

$$\frac{\Delta k_{spr}}{2k_R} = \frac{\Gamma_{PDS}}{2c_s k_R} = 1.56\ 10^{-5}\left[I_{14}\lambda_0^2 \frac{2}{ZT_e}\frac{L}{\lambda_0}\frac{\gamma_A(k_A^{(1)})}{\omega_A^{(1)}}\Xi_{PDS}(\frac{n_0}{n_c})\right]^{1/3} \tag{4.17}$$

$$\Xi_{PDS}(\frac{n_0}{n_c}) = \sqrt{\frac{n_0}{n_c}}\left[\frac{(1-n_0/n_c)^{1/2}}{(1-2\sqrt{n_0/n_c})^{1/2}}+1\right]^4 \tag{4.18}$$

In using our full theoretical model in which the SBS coupling remains intact, we must be careful to maintain the physical validity of our simulations. Because our model can saturate SBS only through the mechanisms of pump depletion or through competition with SRS for pump energy it was necessary to restrict the parameters of table 4.1 to regimes where SBS does not dominate the evolution of the plasma. To insure that the simulations remain valid, parameters have been chosen such that we are either always below the absolute threshold for Brillouin,

or that Brillouin will not grow significantly over the timescale of the experiment. Under these restrictions it is still possible to examine many different regimes which are applicable to current laser-plasma interaction experiments. As is illustrated in Fig. 4.7 the SRS scaling law (3.27), in the presence of the SBS coupling, remains a good approximation for the simulation reflectivity. The reflectivity scaling laws for Brillouin (4.7) and for forward Raman (4.8) scattering also provide reasonable agreement between our analytical theory and numerical simulation. However since these are secondary processes which depend on SRS, the amount of fluctuations in the reflectivity evolution of Brillouin and forward Raman scattering is much larger than that associated with the SRS reflectivity evolution. In deriving the Brillouin scaling law it was assumed that (4.3) properly described the density spectra. In order to maintain the validity of (4.3) it is necessary that, in the density equation (2.58), the electromagnetic ponderomotive potential $\sim \mid \Psi_0 \mid^2$ remain much smaller than the electrostatic ponderomotive force $\sim \mid E \mid^2$. To estimate this limit we assume that density fluctuations produced by SRS will have a constant amplitude in the asymptotic regime. Furthermore we assume that the electromagnetic pump of (4.4) is also constant. These assumptions allow us to write (4.5) as

$$V_B \frac{\partial E_B}{\partial X} = \frac{\omega_p^2}{4\omega_0} N_{k_A^B} E_0 \tag{4.19}$$

where $N_{k_A^B}$ is evaluated using (4.3) at $k = 2k_0$. Integrating (4.19) and using the nonlinear ponderomotive potentials in equation (2.58) leads to the expression

$$\frac{\mid E_L \mid^2}{4\pi n_0^e T_e} \gg \frac{\omega_p^2 N_{k_A^B} v_0^2 L}{2 v_{T_e}^2 \mid k_B \mid c^2} = G_B \frac{8 k_0 \gamma_A(k_A^{(1)})}{k_A^B \omega_A^{(1)}} N_{k_A^B} \tag{4.20}$$

where $G_B = \Gamma_{SBS}^2 L / V_0 \gamma_A(k_A^B)$ is the SBS gain, $\Gamma_{SBS} = \omega_p v_0 \sqrt{\omega_A^B / 8\omega_B v_{T_e}^2}$ is the homogeneous SBS growth rate and $\gamma_A(k_A^B)$ and $\gamma_A(k_A^{(1)})$ are the ion Landau damping

coefficients on the SBS driven ion wave and the first PDI daughter wave at $2k_L - \Delta k$ respectively. Rearranging (4.20) in a more convenient form produces

$$\Delta_{ub} = G_B \frac{8k_0\gamma_A(k_A^{(1)})}{k_A^B\omega_A^{(1)}} N_{k_A^B} \frac{4\pi n_0^e T_e}{\mid E_L \mid^2} < 1 \tag{4.21}$$

where Δ_{ub} represents the upper bound for which it is unnecessary to account for the Brillouin related ponderomotive potential when describing the density fluctuations produced by SRS saturation. In more practical units (4.21) can be written as

$$\begin{aligned} \Delta_{ub} \;=\;& 7.3\frac{I_{14}\lambda_0^2}{T_e}\frac{L}{\lambda_0}\frac{\omega_A^B}{\gamma_A(k_A^B)}\frac{n_0}{n_c} \\ &\times \frac{\exp[-\beta\,(\mid 2k_R - \Delta k \mid /\Delta k_{spr})]}{\left[(1-n_0/n_c)^{\frac{1}{2}} + (1 - 2\sqrt{n_0/n_c})^{\frac{1}{2}}) - (cZm_e/3v_e m_i)\sqrt{n_0/n_c}\right]} \end{aligned} \tag{4.22}$$

where once again L, and λ_0 are in μm, $\gamma_A(k_A^{(1)})/\omega_A^{(1)}$ can be found using (2.63) and I_{14} is the laser intensity in $10^{14} W/cm^2$. The exponential can be approximated by using (4.15) and (4.17).

In the event that (4.21) should be violated, expression (4.3) will overestimate the ion density fluctuations such as shown in Fig. 4.4(a). As can be seen in some of the runs illustrated in Fig. 4.5 under these circumstances the scaling law (4.7) overestimates the Brillouin reflectivity.

In deriving the Brillouin scaling law it was also assumed that a coherent phase description adequately accounted for the evolution of the system. In some of the larger length, higher intensity simulations, (for example the run in Fig. 4.4(b),) a turbulent description of the plasma for which the coherence length is reduced would more accurately describe the system. In these simulations the Brillouin reflectivity would again be overestimated by (4.7) hence providing an upper bound for the reflectivity.

A similar problem to the Brillouin scaling will appear in the estimates for the reflectivity levels of forward Raman scattering. In Fig. 4.6 the comparison between theory, expression (4.8), and simulation gives better agreement than for Brillouin. This is because the presence of forward Raman, due to its lower amplitude, will not modify the expression for the Langmuir spectra (4.2) to the same extent as Brillouin can modify (4.3). However the number of cascades necessary to enhance forward Raman is approximately twice that required to enhance Brillouin. This will produce a more turbulent spectra for forward Raman, and hence the reduced coherence length will produce a smaller reflectivity. Under circumstances where this applies (4.8) will again provide an upper limit for the reflectivity.

In choosing our parameters in table 4.1 we always sought to exceed at least one of the strong enhancement criterion of (4.9) $\Delta_B > 1$ or (4.10) $\Delta_{FR} > 1$. The upper bound Δ_{ub} for accurately predicting the Brillouin reflectivity through (4.3) was usually but not always maintained. One criterion, that of maintaining parameters such that we are always below the absolute Brillouin threshold, was strictly enforced. This limit on parameters is given by

$$\Delta_{abs} = \frac{\Gamma_{SBS}}{\gamma_{abs}} = \frac{v_0 \omega_p}{c \gamma_A (k_A^B)} \sqrt{\frac{Z m_e}{m_i}} \ll 1 \tag{4.23}$$

Each of the criteria Δ_B, Δ_{FR}, and Δ_{ub} depend explicitly on the parameters $I\lambda_0^2 L$, while Δ_{abs} depends only on $I\lambda_0^2$. Because Δ_{abs} is independent of L, we can easily enhance Brillouin and forward Raman while maintaining (4.23). Examples of possible parameter regimes are illustrated in Fig. 4.8, for the three temperatures: Fig. 4.8(a) $T_e \simeq 0.5keV$, Fig. 4.8(b) $T_e \simeq 1keV$, and Fig. 4.8(c) $T_e \simeq 2keV$. In each of the figures the lower bounds for enhanced Brillouin, dotted curve corresponding to $\Delta_B / \frac{2}{3}A = 1$, and forward Raman, dashed curve correspond-

ing to $\Delta_{FR}/\frac{2}{3}A = 1$, are plotted as functions of n_0/n_c and $I\lambda_0^2L$. The dot-dashed curve and solid curve represents $\Delta_{ub} = 1$ for the two different temperature ratios $ZT_e/T_i = 8$ and $ZT_e/T_i = 16$. As is easily seen for each of the temperature regimes, the higher temperature ratio, $ZT_e/T_i = 16$ in this case, drastically limits the parameter regime for which (4.3) remains valid. The reason for this is that the level of ion damping is greatly dependent on the temperature ratios ranging from strongly damped $ZT_e/T_i \simeq 10$ to weakly damped $ZT_e/T_i \simeq 30$. This temperature dependence will also greatly affect the level at which SBS is above the absolute threshold.

The effect of high ZT_e/T_i ratios on the validity of our simulations thus prohibits us from examining high Z targets when Brillouin coupling is present in our model. All our runs containing the Brillouin coupling have been for low Z targets with fairly low temperature ratios. By increasing ZT_e/T_i the temporal threshold for SBS, expression (4.23) is reduced. Large Z targets however increase the threshold for SRS producing a need for higher and higher intensities to over come the SRS temporal threshold. At some point this results in SBS and SRS both growing temporally within the same time scale thus allowing for competition between these two instabilities for pump energy. Under such circumstances the analysis of Chap. 3 may not apply.

4.1.1 The frequency and wave number spectra of scattered radiation

In our full model (2.57)-(2.61) the Brillouin scattering component of the electromagnetic field is an implicit part of the laser pump variable Ψ_0. By analysing the Fourier frequency spectra of this variable one obtains the spectra illustrated in Fig. 4.9 for run parameters $L = 60\,\mu m$, $I = 2 \cdot 10^{14}\,W/cm^2$, $T_e = 1.25\,keV$,

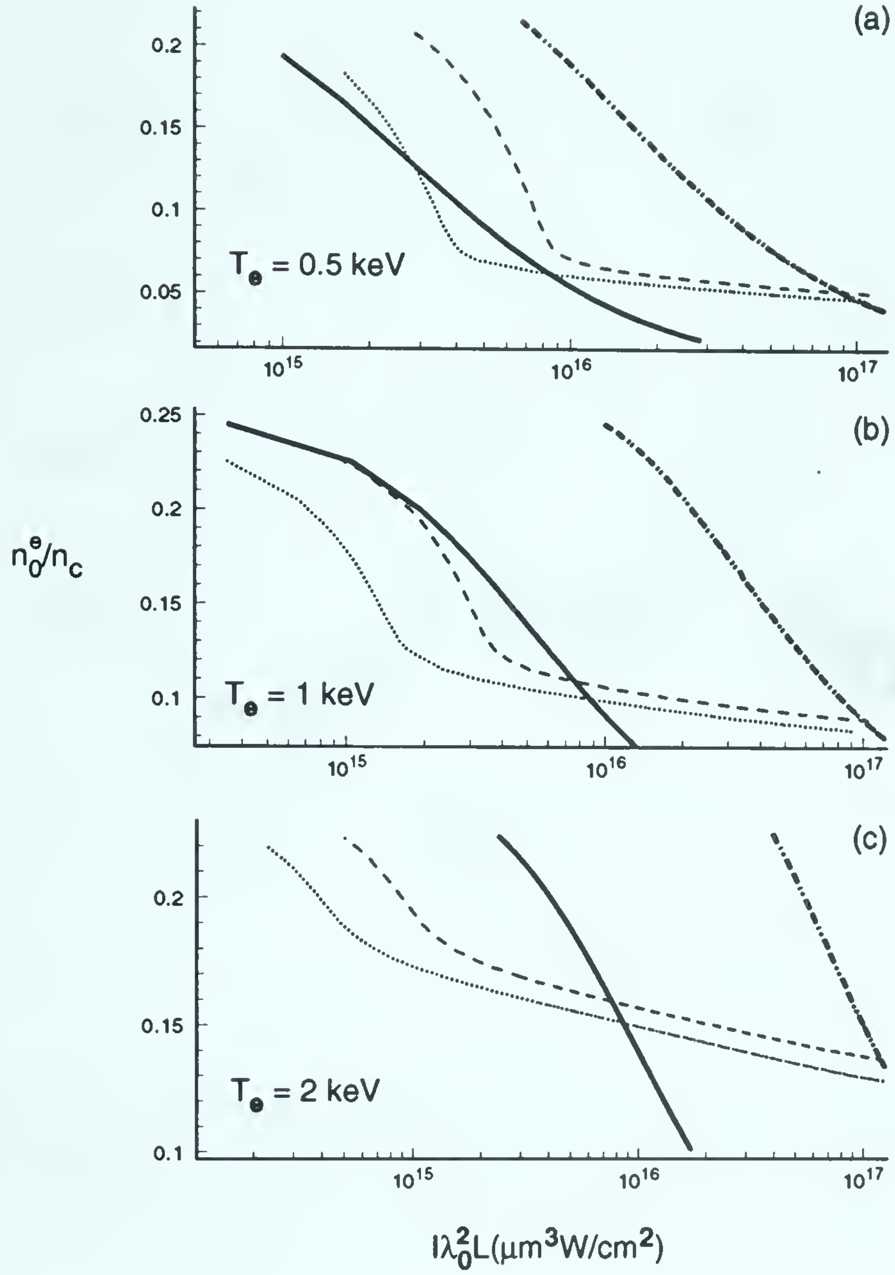

Figure 4.8: *Parameter regime limits of our simulations* $\Delta_B/\frac{2}{3}A = 1$ *(dotted curves),* $\Delta_{FR}/\frac{2}{3}A = 1$ *(dashed curves), and* $\Delta_{ub} = 1$ *for two different temperature ratios* $ZT_e/T_i = 8$ *(dot-dashed curves), and* $ZT_e/T_i = 16$ *(solid curves) for (a)* $T_e = 0.5keV$*, (b)* $T_e = 1keV$*, (c)* $T_e = 2keV$

$ZT_e/T_i = 8$, $Z = 5$, $\lambda_0 = 0.531\,\mu m$, $n_0^e/n_c = 0.2$. In Fig. 4.9 one can easily discern the pump and the Stokes frequency peaks labeled by ω_0 and ω_B which are separated by $\sim c_s k_A^B$. Of great interest is the anti-Stokes peak ω_{B+} separated from ω_0 by $\sim c_s k_A^{B+}$ illustrating how the pump wave must be scattered off ion modes moving in the opposite direction to that of the laser pump. The presence of this anti-Stokes peak is a characteristic feature of enhanced Brillouin scattering, and indicates that the observed Brillouin scattering in our simulations is produced by

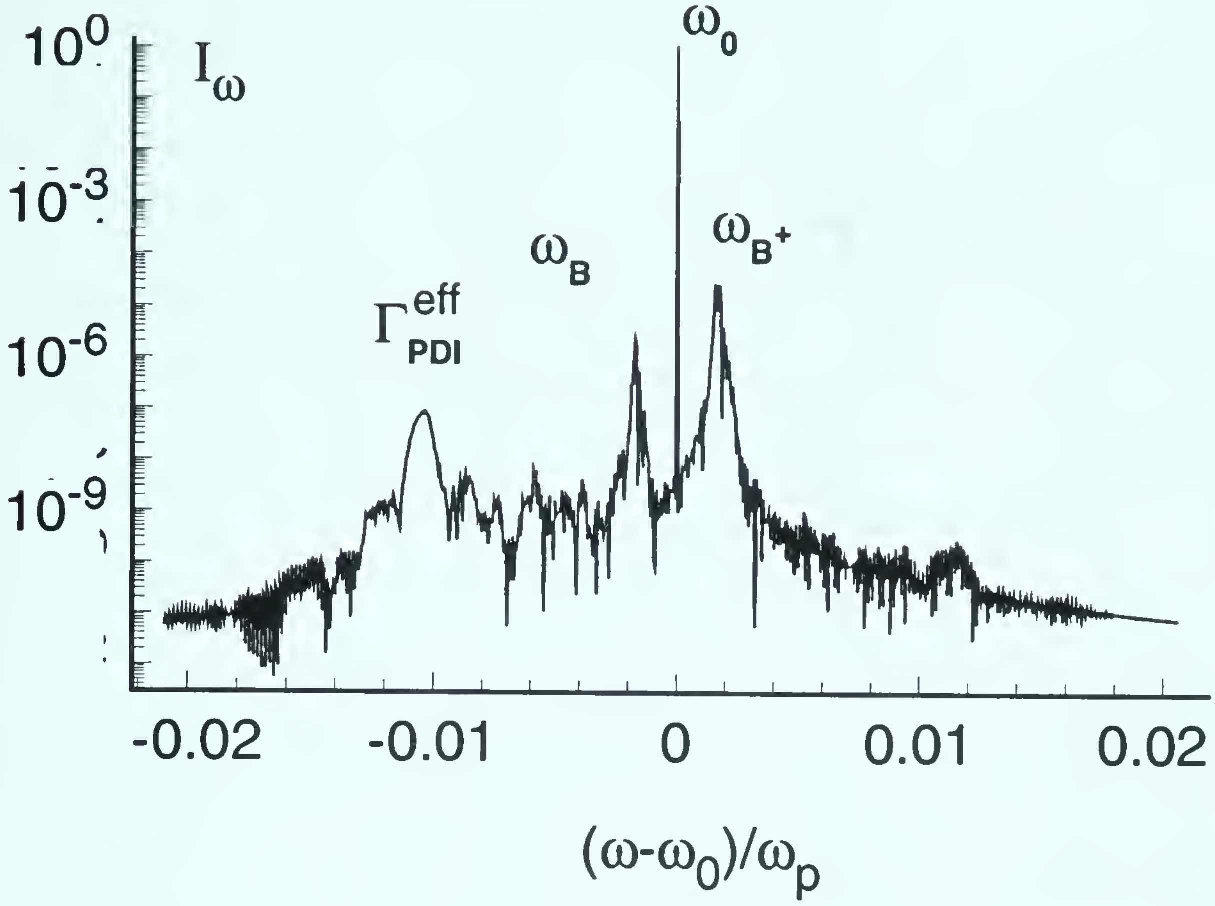

Figure 4.9: *Brillouin reflectivity frequency spectra obtained from numerical solutions of equations (2.57)-(2.61) for run parameters* $L = 60\,\mu m$, $I = 2\cdot 10^{14}\,W/cm^2$, $T_e = 1.25\,keV$, $ZT_e/T_i = 8$, $Z = 5$, $\lambda_0 = 0.531\,\mu m$, $n_0^e/n_c = 0.2$.

the electromagnetic pump wave scattering off the fluctuations produced by saturation of SRS. Since these fluctuations will be a random assortment of left and right moving waves, the frequency spectra for enhanced Brillouin will contain both Stokes and anti-Stokes components. A fourth peak, identifiable as the effective PDI growth rate Γ^{eff}_{PDI}, is also visible in the frequency spectra of Fig. 4.9. This peak is transitory in nature and will disappear as one approaches the asymptotic saturated state of SRS.

In order to clarify the physical processes involved in the production of the enhanced Brillouin frequency peaks three contour plots for the frequency spectra evolution are shown in Fig. 4.10. Each of the runs are for very similar parameters with a slight variation in the density n_0/n_c. As is illustrated in Fig. 4.10 for the

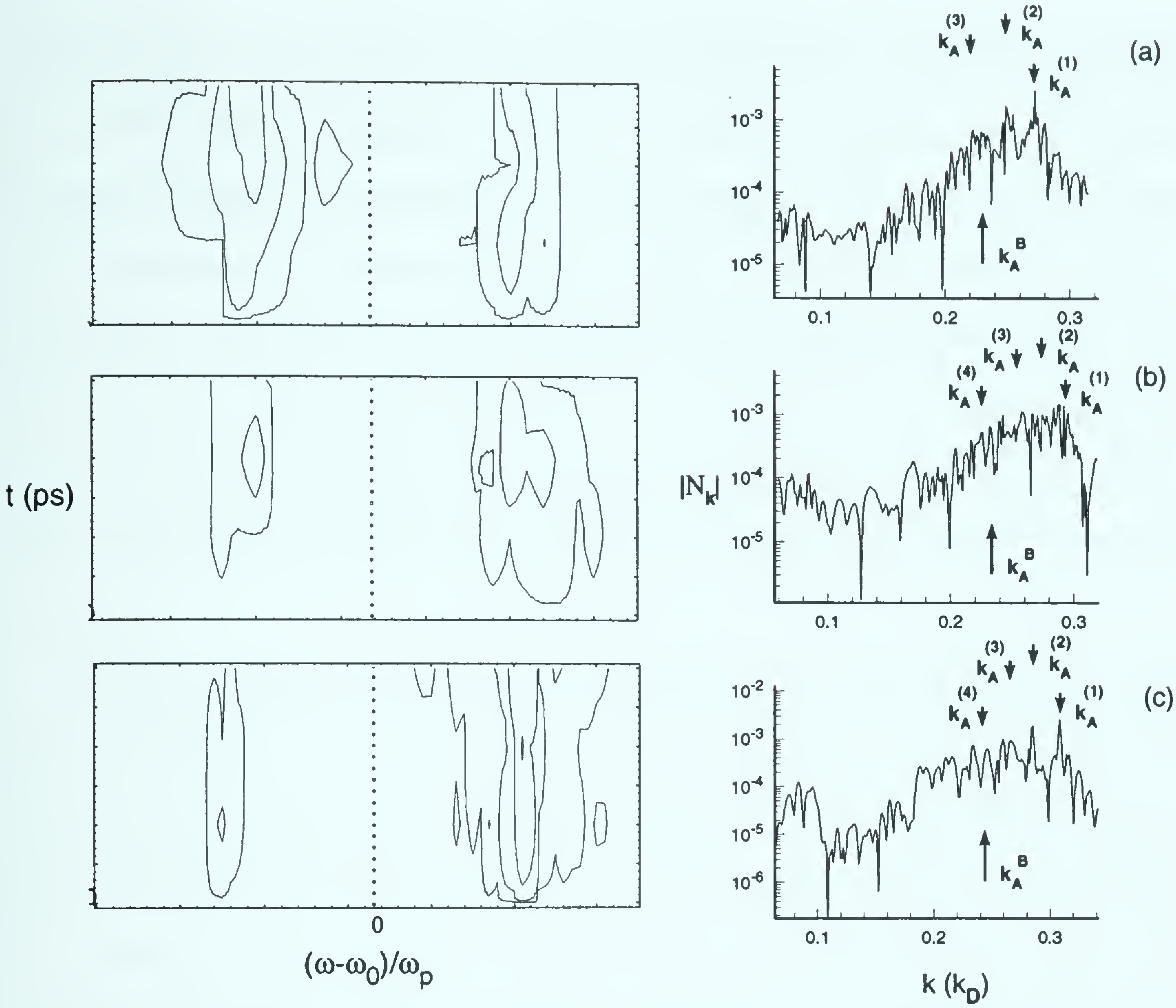

Figure 4.10: *Brillouin reflectivity frequency and wave number spectra obtained from numerical solutions of equations (2.57)-(2.61) for run parameters* $L = 60\,\mu m$, $I = 1.2 \cdot 10^{14}\,W/cm^2$, $T_e = 2\,keV$, $ZT_e/T_i = 8$, $Z = 5$, $\lambda_0 = 0.531\,\mu m$ *for densities (a)* $n_0^e/n_c = 0.229$, *(b)* $n_0^e/n_c = 0.221$, *and (c)* $n_0^e/n_c = 0.21$

run parameters $L = 60\,\mu m$, $I = 1.2 \cdot 10^{14}\,W/cm^2$, $T_e = 2\,keV$, $ZT_e/T_i = 8$, $Z = 5$, $\lambda_0 = 0.531\,\mu m$ both Fig. 4.10(a) ($n_0/n_c = 0.229$) and Fig.4.10(b) ($n_0/n_c = 0.221$) have strong Stokes and anti-Stokes Brillouin peaks in their frequency spectra, while Fig. 4.10(c) ($n_0/n_c = 0.21$) has only a strong anti-Stokes component.

To understand why a small variation in the background density can produce such a large change in the frequency spectra, we have also plotted in Fig. 4.10 the wave number spectra for late times. During the saturation of SRS the PDI density

cascade produces strongly driven modes at intervals of $2\Delta k$, starting from a Stokes peak at $k_A^{(1)}$. Thus using $(k_A^{(1)} - k_A^B)/2\Delta k = m_d$ one can make a crude estimate for whether a Stokes or anti-Stokes peak will be observed. Since the direction of the PDI ion modes will alternate direction, if m_d is odd then one would expect k_A^B to be near an anti-Stokes PDI mode producing a anti-Stokes frequency peak. If m_d is even, then a Stokes peak should be observed and if m_d is a non-integer then one would expect to see evidence of both peaks. In the wave spectra of Fig. 4.10 we have labeled $k_A^{(1)}$, k_A^B and the first four $(n = 1 - 4)$ ion acoustic waves of the PDI cascade.

For the parameters of Fig. 4.10(a) the Brillouin wave number produces a value $(k_A^{(1)} - k_A^B)/2\Delta k = 1.98$, which predicts that a strong Stokes component should be (and is in fact observed) in the frequency spectra. In Fig. 4.10(b) the frequency spectra is dominated by two approximately equal intensity peaks which agrees with the calculation $(k_A^{(1)} - k_A^B)/2\Delta k = 2.47$ for m_d. In the final frequency spectra (Fig. 4.10(c)) one observes a very strong anti-Stokes peak. By calculating m_d one finds a value of 3.11 which again is in agreement with our prediction. Present in each of the frequency spectra of 4.10(a) and 4.10(c) is a second peak corresponding to a mode which would not be strongly enhanced if the only modes generated in the ion spectra were those produced by the PDI cascade. Because of the interaction between the ion density fluctuations and the Langmuir fields permitted by the Zakharov equations, many other resonant waves and waves which do not satisfy the linear dispersion relations (1.1) and (1.2) are also present in the spectra. These waves also permit Brillouin scattering hence producing a more rich spectra that is observed.

4.2 Anti-Stokes forward and backward Raman scattering

The enhancement process can also be extended to explain experimental observations of anti-Stokes forward and backwards Raman [68], [91], [92], [99], [102]. These two scattering processes are characterized by the frequency relation $\omega_{R^+} = \omega_0 + \omega_L$ and in order to satisfy energy conservation, cannot be the result of a unstable three wave process, but instead must be the product of previously excited wave modes. To illustrate how SRS saturation can enhance the levels of the anti-Stokes Raman scattering, we examine the wave spectra plots of Fig. 4.11. Figure 4.11(a) is a late time Langmuir spectra plot for run parameters $L = 45\,\mu m$, $I = 2.5 \cdot 10^{14}\, W/cm^2$, $n_0^e/n_c = 0.2$, $T_e = 1\, keV$, $ZT_e/T_i = 8$, $Z = 3$, $\lambda_0 = 0.531\,\mu m$. For underdense plasmas the Langmuir wave spectra producing the forward anti-Stokes component is very similar to that producing the Stokes component, differing by $\simeq 10\%$ at a density of $0.2 n_0/n_c$. The saturation of SRS by PDI may thus be a possible mechanism for strongly enhancing forward anti-Stokes provided the PDI cascade continues to a point of enhancing forward Raman. With this information one can immediately write down a simple criterion necessary for strong enhancement in the form

$$\frac{2}{3}A > \frac{(k_L - k_L^{FR^+})}{\Delta k} = \Delta_{FR^+} \tag{4.24}$$

which has been met in Fig. 4.11(a) where $1.14\Delta_{FR^+} = \frac{2}{3}A$.

To account for the backward anti-Stokes Raman observed in experiment by using enhancement due to SRS saturation one has to invoke mode coupling of the density components with the Langmuir spectra. This can be seen in Fig. 4.11(b) where the backward anti-Stokes Raman component at $k_L^{BR^+}$ is not located in the region supporting the PDI cascade of the SRS driven Langmuir wave. In order to

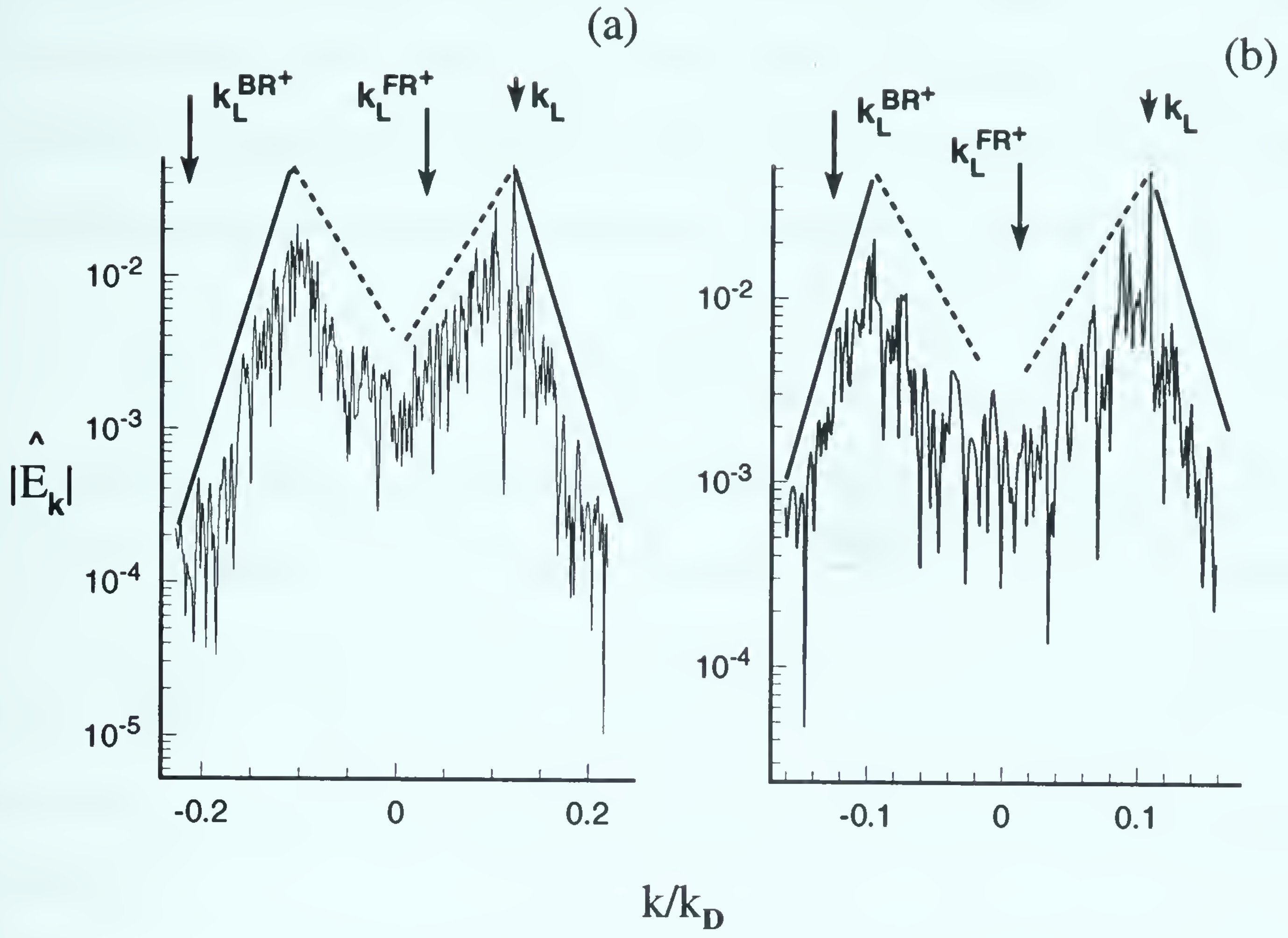

Figure 4.11: *Electrostatic spectra obtained from numerical solutions of equations (2.57)-(2.61) for run parameters: (a)* $L = 45\,\mu m$, $I = 2.5 \cdot 10^{14}\,W/cm^2$, $n_0^e/n_c = 0.2$, $T_e = 1\,keV$, $ZT_e/T_i = 8$, $Z = 3$, $\lambda_0 = 0.531\,\mu m$ *and (b)* $L = 500\,\mu m$, $I = 1 \cdot 10^{12}\,W/cm^2$, $n_0^e/n_c = 0.05$, $T_e = 100\,eV$, $ZT_e/T_i = 8$, $Z = 4$, $\lambda_0 = 10\,\mu m$

produce the necessary Langmuir wave, Langmuir modes at $k > k_L$ or $k < -k_L$, which are associated with the disruption of the PDI cascade and localization of the Langmuir fields, are necessary. The production of these modes begins with the interaction of resonant Langmuir waves travelling in the same direction, producing ion acoustic quasimodes at very low wave numbers. The ion quasimodes then interact with other Langmuir waves broadening the Langmuir spectra.

By using the amplification coefficient $\frac{2}{3}A$ (3.25) to determine the number of modes in a cascade one can estimate the largest Langmuir quasimode in the vicinity of k_L which can be produced. The beating of the SRS driven Langmuir mode and

the last mode in the PDI cascade produces an ion density mode of $k_A = \frac{2}{3}A\Delta k$. The interaction of this density wave with the first PDI Langmuir daughter wave produces a strongly driven mode at $k = k_L^{(1)} - \frac{2}{3}A\Delta k$. If this wave number is larger than the required anti-Stokes wave number such that the criterion

$$\frac{2}{3}A > \frac{\mid k_L^{(1)} - \mid k_L^{BR+} \mid\mid}{\Delta k} = \Delta_{BR+}^{(1)}. \tag{4.25}$$

is met then substantial enhancement of backward anti-Stokes Raman will be observed. This criterion is easily met by the parameters of Fig. 4.11(b) $L = 500\,\mu m$, $I = 1{\cdot}10^{12}\,W/cm^2$, $n_0^e/n_c = 0.05$, $T_e = 100\,eV$, $ZT_e/T_i = 8$, $Z = 4$, $\lambda_0 = 10\,\mu m$ producing $1.67\Delta_{BR^+} = \frac{2}{3}A$. However under most circumstances the anti-Stokes backward Raman component is difficult to produce if the system itself is not strongly turbulent.

A second method for creating the appropriate strongly driven wave number is based on a similar argument. The ion density cascade will have a width given by $k = \frac{4}{3}A\Delta k$, twice that of the Langmuir cascade. If the combination of these modes and the ion quasimodes is greater than the primary PDI ion wave k_A then all modes less that k_A will be strongly driven and hence all Langmuir modes in the vicinity of k_L will also be strongly driven. A simple criterion for this is

$$\frac{2}{3}A > \frac{\mid 2k_L - \Delta k \mid}{3\Delta k} = \Delta_{AB}^{(2)}. \tag{4.26}$$

which if met will once again allow strong enhancement of the backward anti-Stokes component to take place.

As was demonstrated in Chap. 2 the anti-Stokes Raman scattering, though a resonant process, is stable to small perturbations and will not grow due to its lack of any feedback mechanism to drive the instability. The production of anti-Stokes

Raman in our simulations thus relies solely on the Langmuir spectra generated by PDI and the subsequent interaction of the Langmuir and density spectra which produces many resonant modes, that satisfy the linear dispersion relations of (1.1) and (1.2) as well as many quasimodes that do not satisfy (1.1) and (1.2).

The spectral composition in the vicinity of the anti-Stokes wave numbers k_L^{BR+}, and k_L^{FR+} will thus consist of resonant and quasimode components associated with the many wave coupling possibilities available. This suggests that, because the anti-Stokes components are made up of many different waves, the phases of the anti-Stokes wave numbers will be oscillating wildly, producing an almost random phase. Under such circumstances the coherent phase approach used to describe SRS and enhanced Brillouin and forward Raman reflectivity levels will not be accurate in describing the anti-Stokes Raman scattering. Instead we turn to the random phase approximation of Chap. 3.6 and use the resultant expression

$$
\begin{aligned}
R_k = \frac{\mid V_{R+} \mid}{\mid V_0 \mid} \frac{\mid E \mid_{k_{R+}}^2}{\mid E \mid_{k_0}^2} &= \frac{\mid V_{R+} \mid}{\mid V_0 \mid} \frac{\omega_{R+}}{\omega_0} tanh \left[\alpha^2 \int_0^L \mid E \mid_{k_L^{R+}}^2 \, dx \right] \\
&\simeq \frac{\mid V_{R+} \mid}{\mid V_0 \mid} \frac{\omega_{R+}}{\omega_0} \alpha^2 \mid E \mid_{k_L^{R+}}^2 L \qquad (4.27)
\end{aligned}
$$

where $\alpha = ek_L^{R+}/4m_e c^2 \sqrt{k_0 k_{R+}}$. Using $\int \mid E \mid_{k_L^{R+}}^2 dk = \langle E^2 \rangle$ where $\langle E^2 \rangle$ is an averaged amplitude quantity we can estimate the reflectivity by

$$
R = \frac{V_{R+}}{V_0} \frac{\omega_{R+}}{\omega_0} \alpha^2 \langle E^2 \rangle L \qquad (4.28)
$$

In general it is not possible to find the exact value of $\langle E^2 \rangle$. We have however determined through comparison to simulations the crude scaling of

$$
R \propto \frac{I \lambda_0^2 L}{\gamma_L(k_L)} \qquad (4.29)
$$

where $\gamma_L(k_L)$ is the linear electron damping coefficient, I is the laser intensity, L is the interaction length, and λ_0 is the laser wavelength.

To test equation (4.29) two sets of simulations were run for constant n_0/n_c , T_e, ZT_e/T_i and Z, while the laser intensity I and interaction length L were varied. Figure 4.12 displays the integral time averaged reflectivities of a) forward anti-Stokes Raman and Fig. 4.13 (b) backwards anti-Stokes Raman for parameters $L = 50 - 200\,\mu m$, $I = 0.5 - 1.2 \cdot 10^{14}\,W/cm^2$, $n_0^e/n_c = 0.07$, $T_e = 0.6\,keV$, $ZT_e/T_i = 10$, $Z = 4$, $\lambda_0 = 1.06\,\mu m$ (diamonds). The fluctuation levels of these reflectivities vary over orders of magnitude (see for example Fig. 4.1 (d), (e) suggesting that a precise theory describing the other characteristics of the reflectivity scaling would be extremely cumbersome. The reflectivity scaling law (4.29) is thus meant as an estimate describing the dependence on only certain physical characteristics. A further example of the anti-Stokes reflectivities is also illustrated in Fig 4.12 where the parameters $L = 50 - 100\,\mu m$, $I = 4 - 5 \cdot 10^{14}\,W/cm^2$, $n_0^e/n_c = 0.1$, $T_e = 0.5\,keV$, $ZT_e/T_i = 8$, $Z = 3 - 4$, $\lambda_0 = 0.531\,\mu m$ (triangles) have been plotted. In both examples it is possible to draw a straight line which approximates the time averaged simulation reflectivities.

In regimes where the Langmuir spectra is not so turbulent, such that the anti-Stokes wave numbers k_L^{R+} can be enhanced after only a few stages of the PDI cascade, it is possible to find an approximate numerical value for the anti-Stokes reflectivity scaling. We have found that the anti-Stokes reflectivity is linearly dependent on the intensity of the laser I and the length of the simulation box L. We have also found that (4.2) provides a reasonable approximation for the shape of the Langmuir spectrum. However since (3.29) also depends on L (4.2) must overestimate the contribution of the Langmuir waves to the anti-Stokes reflectivity.

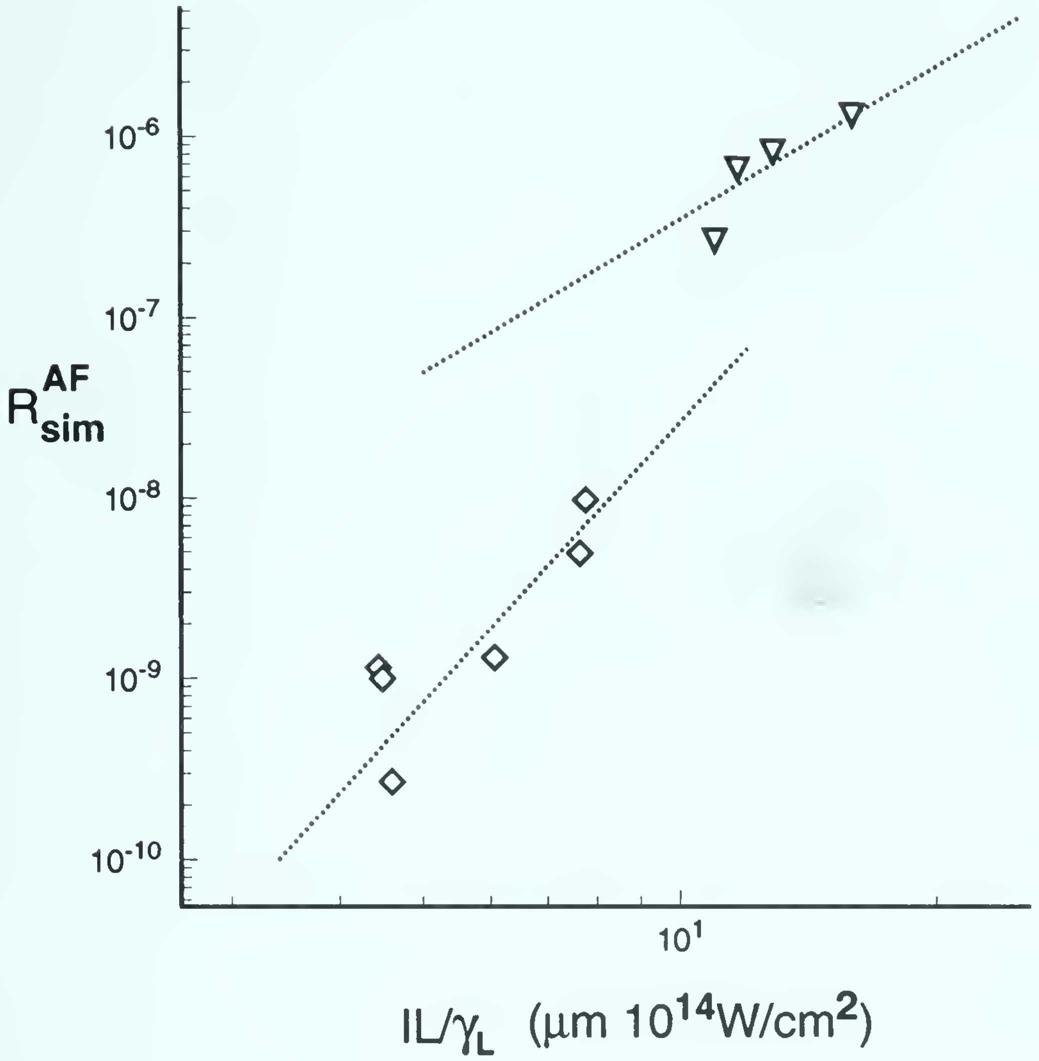

Figure 4.12: *Time integral averaged asymptotic anti-Stokes forward Raman reflectivities plotted as a function of scaling formula, Equation(4.29) for run parameters: (a)* $L = 50 - 200\,\mu m$, $I = 0.5 - 1.2 \cdot 10^{14}\,W/cm^2$, $n_0^e/n_c = 0.07$, $T_e = 0.6\,keV$, $ZT_e/T_i = 10$, $Z = 4$, $\lambda_0 = 1.06\,\mu m$ *(diamonds) and (b)*$L = 50 - 100\,\mu m$, $I = 4 - 5 \cdot 10^{14}\,W/cm^2$, $n_0^e/n_c = 0.1$, $T_e = 0.5\,keV$, $ZT_e/T_i = 8$, $Z = 3 - 4$, $\lambda_0 = 0.531\,\mu m$ *(triangles).*

We thus estimate the reflectivity by using

$$\langle E^2 \rangle = \zeta \left[\frac{64\pi n_0^e T_e \gamma_{k_A}^A \gamma_{0R}^2}{3\omega_p \omega_A \mid V_R \mid} \right] \exp[-2\beta \left(\frac{\mid k - k_L \mid}{\Delta k_{spr}} \right)] \tag{4.30}$$

in expression (4.28). Here ζ is a parameter which is varied to achieve agreement between the simulation and the theoretical reflectivity.

As an example of applying our enhancement criterion, numerous simulations for parameters $L = 25 - 100\,\mu m$, $I = 1 - 10 \cdot 10^{14}\,W/cm^2$, $n_0^e/n_c = 0.2$, $T_e = 1\,keV$, $ZT_e/T_i = 8$, $Z = 3 - 5$, $\lambda_0 = 0.531\,\mu m$ were run. In this case the temperature,

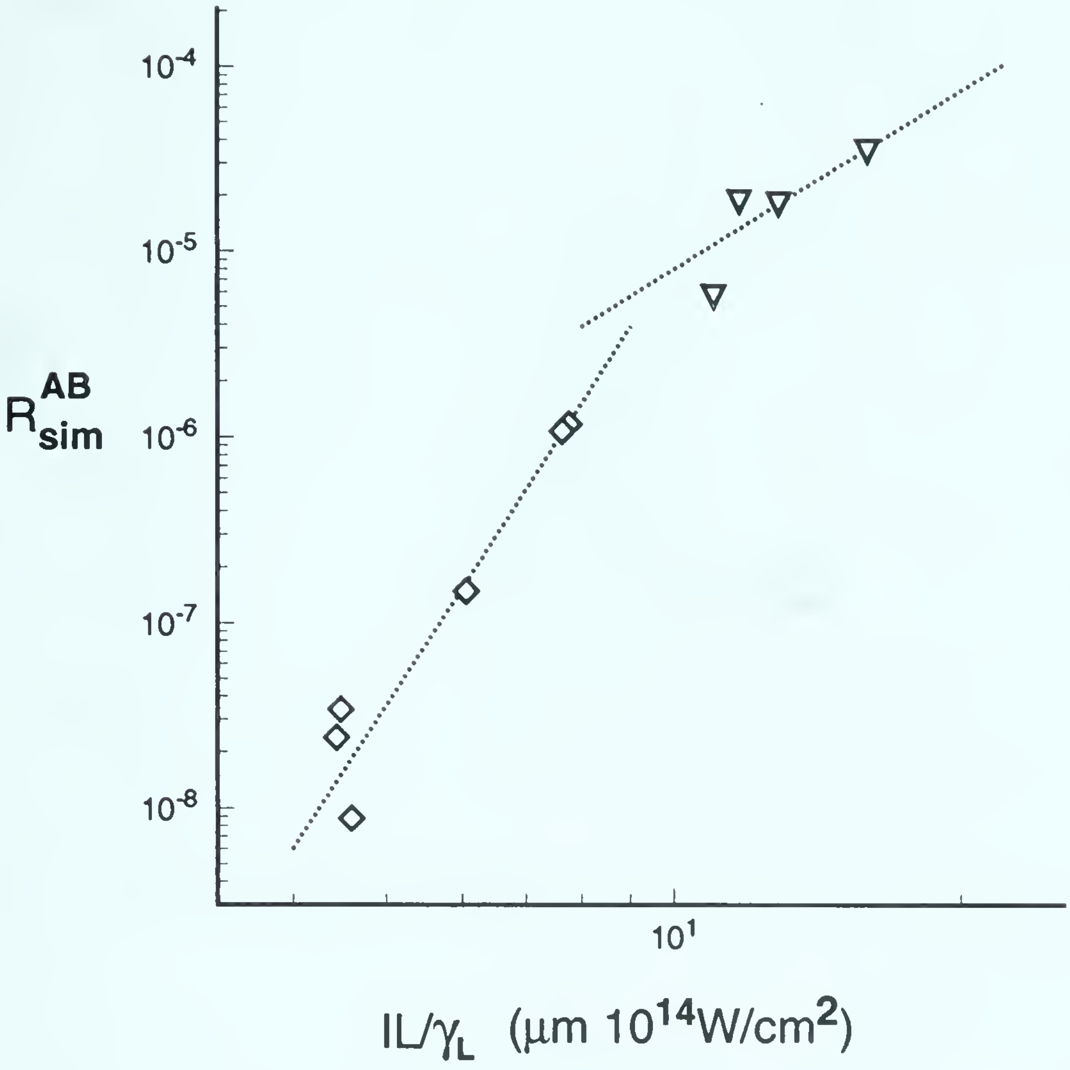

Figure 4.13: *Time integral averaged asymptotic anti-Stokes backward Raman reflectivities plotted as a function of scaling formula, Equation(4.29)for run parameters: (a)* $L = 50 - 200\,\mu m$, $I = 0.5 - 1.2 \cdot 10^{14}\,W/cm^2$, $n_0^e/n_c = 0.07$, $T_e = 0.6\,keV$, $ZT_e/T_i = 10$, $Z = 4$, $\lambda_0 = 1.06\,\mu m$ *(diamonds) and (b)*$L = 50 - 100\,\mu m$, $I = 4 - 5 \cdot 10^{14}\,W/cm^2$, $n_0^e/n_c = 0.1$, $T_e = 0.5\,keV$, $ZT_e/T_i = 8$, $Z = 3 - 4$, $\lambda_0 = 0.531\,\mu m$ *(triangles).*

density, and ZT_e/T_i were fixed while the intensity (I), length (L) and collisional damping (Z) were varied. Provided that the enhancement criteria (4.24) and (4.25) are met, (4.27) can be used to describe both the forward and backward anti-Stokes components.

Figure 4.14 illustrates the anti-Stokes forward reflectivity scaling, and plots (4.27) versus the asymptotic integral time average reflectivity of anti-Stokes forward obtained from our simulations. Reasonable agreement between (4.27) and simulation results were found for a constant value of ζ. Of particular importance

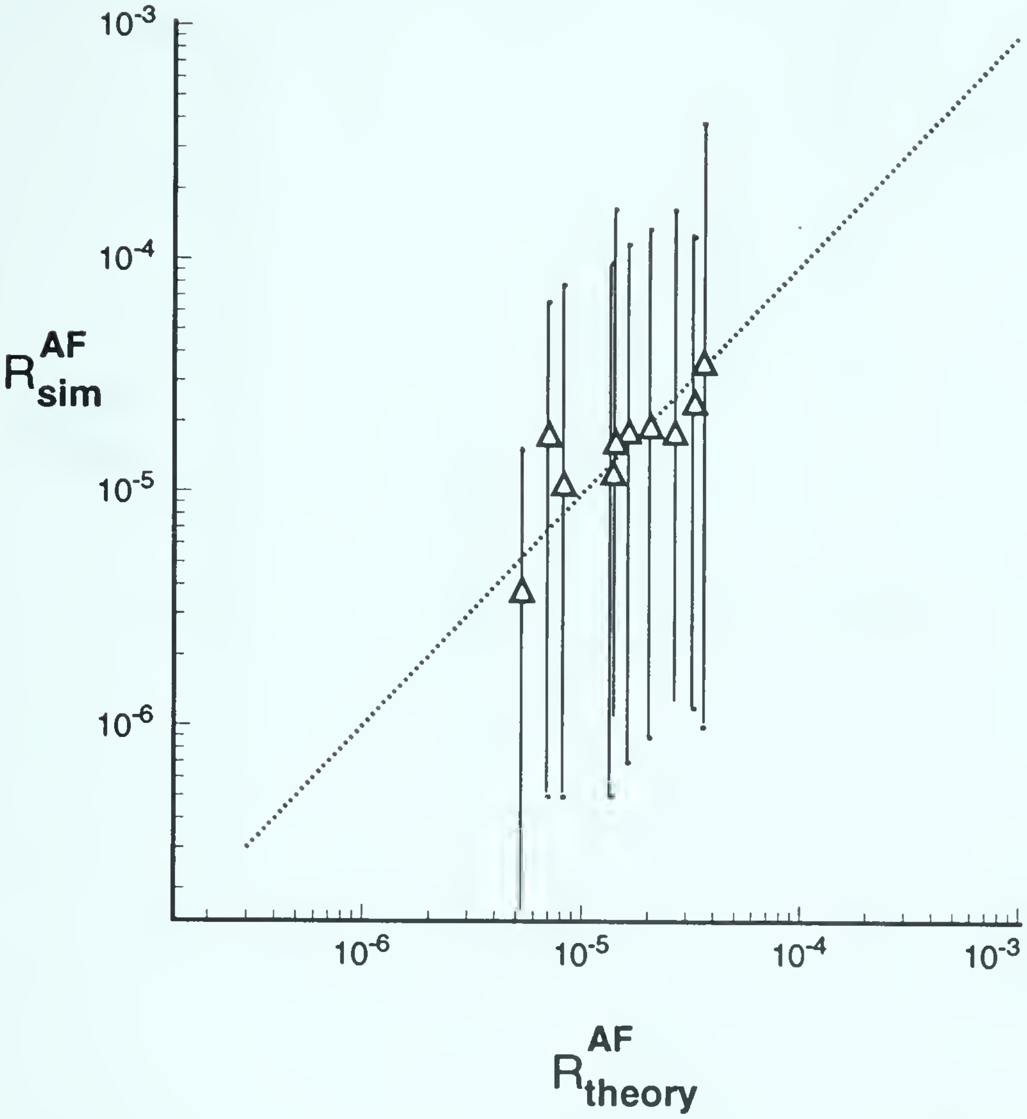

Figure 4.14: *Time integral averaged asymptotic anti-Stokes forward Raman reflectivities plotted as a function of scaling formula, Equation(4.28)for parameters* $L = 25 - 100\,\mu m$, $I = 1 - 10 \cdot 10^{14}\,W/cm^2$, $n_0^e/n_c = 0.2$, $T_e = 1\,keV$, $ZT_e/T_i = 8$, $Z = 3-5$, $\lambda_0 = 0.531\,\mu m$. *Vertical error bars denote the maximum and minimum fluctuations during the asymptotic regime.*

is the observed linear dependence on intensity and length L. The value of ζ corresponding to the forward anti-Stokes was also found to apply to backward component enabling us to verify (4.27) for backward anti-Stokes Raman scattering as well. Once again we plot the simulation reflectivity against expression (4.27) (Fig. 4.15) obtaining good agreement for this specific regime.

The number of regimes for which such analysis can be done is severely limited by the necessity of maintaining model validity. In regimes where the wave spectra separation between k_L and k_L^{R+} is large, intensity and/or length requirements

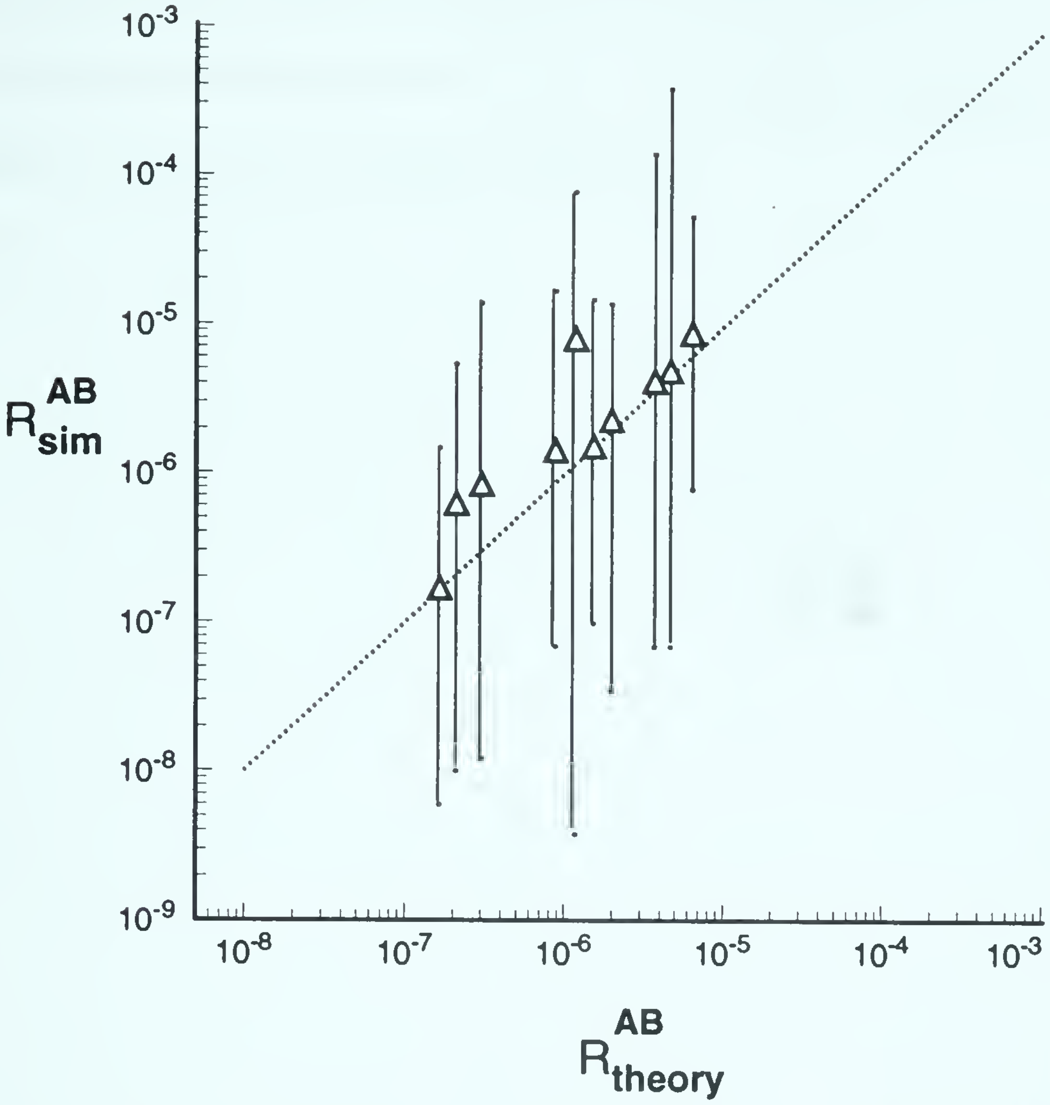

Figure 4.15: *Time integral averaged asymptotic anti-Stokes backward Raman reflectivities plotted as a function of scaling formula, Equation(4.28)for parameters* $L = 25 - 100\,\mu m$, $I = 1 - 10 \cdot 10^{14}\, W/cm^2$, $n_0^e/n_c = 0.2$, $T_e = 1\, keV$, $ZT_e/T_i = 8$, $Z = 3 - 5$, $\lambda_0 = 0.531\,\mu m$ *. Vertical error bars denote the maximum and minimum fluctuations during the asymptotic regime.*

push the model outside the regions for which it applies, or into strongly turbulent regimes for which the analysis breaks down. For parameters that do not meet the enhancement criterion the reflectivity, (4.29) is still applicable however the value of ζ no longer appears to be constant, instead a dependence on I and L are observed to take place. Although this dependence appears to be very weak we were unable to find analytical scaling expressions to properly model the magnitude of $\langle E^2 \rangle$, and could only verify the approximate dependencies on I, L, and $\gamma_L(k_L)$. This result is not surprising, since the spectra of the Langmuir field is strongly dependent on

$\gamma_A(k)$, n_0/n_c and T_e. Once one considers the complex structure of the spectra and the strong laser intensity needed to produce a reasonable enhancement one would not expect to produce a universal scaling law.

Chapter 5

Superthermal electron generation

Superthermal electron production is a concern in laser-plasma interaction because of the detrimental effect it can have on fusion target efficiency [16], [17]. These hot electrons can be produced as a consequence of SRS and forward Raman scattering. The large levels of Langmuir fields generated during SRS accelerate electrons whose phase velocity is near that of the Langmuir waves. In the typical asymptotic regime of region 4 in Fig. 3.1, the Langmuir fields reach a quasistationary state, which extends across the plasma interaction length. Under these circumstances particles at one end of the plasma could be accelerated to very large velocities as they traverse the plasma. As a significant portion of the electrons is accelerated, the distribution function of the electrons will be modified, affecting the level of Landau damping and hence the absolute and convective thresholds of SRS. Such effects are not present in our model (2.57)-(2.61) and hence we must limit our simulations to regimes in which hot electron production does not become a significant factor in the evolution of the plasma. Because production of the hot electrons in the stationary regime will be length dependent, due to the length dependence of the Langmuir field (3.29), this will limit the interaction length for which our simulations will remain valid. Similarly the stationary Langmuir fields in our model have been

shown to be dependent on the intensity of the laser pump. Such a dependence will also affect the electron velocities, introducing a limit on the intensities we can examine with our model.

In order to explore these limits we examine the wave-particle interaction which allows for the transfer of energy from the Langmuir spectra to the electrons within the plasma. Such energy transfer is described by the standard diffusion equation which for a stationary distribution function takes the form:

$$v\frac{\partial f}{\partial x} = \frac{\partial}{\partial v}\left(D_v \frac{\partial f}{\partial v}\right) \tag{5.1}$$

where in a finite length system

$$D_v = \frac{e^2}{4m_e^2}\frac{L}{v} \mid E_{k=\omega_p/v} \mid^2 \tag{5.2}$$

At the present time we are only concerned with estimating the production of hot electrons and their subsequent affect on Landau damping. For this purpose we use our asymptotic expression for the Langmuir spectra in (5.2), which has been shown to be well approximated by the expression

$$\mid E_k \mid^2 = \left[\frac{64\pi n_0^e T_e \gamma_A(k_A^{(1)})\Gamma_{SRS}^2 L}{3\omega_p \omega_A^{(1)} \mid V_R \mid}\right] \exp[-2\beta\left(\frac{\mid k - k_L \mid}{\Delta k_{spr}}\right)], \tag{5.3}$$

where $\beta = 1$ if $\mid k \mid < \mid k_L \mid$ and $\beta = 2$ if $\mid k \mid > \mid k_L \mid$. With this approximation (5.1) can be solved for the steady state distribution as a function of plasma length. This simple model will allow us to test the effects our asymptotic expression for the Langmuir spectra will have on the evolution of a Maxwellian distribution function. When deriving our theoretical model (2.57)-(2.61) we have assumed an ideal gas representation of the pressure tensor, so that during the evolution of the system the overall temperature modifications to the distribution function must be minimal. By

insisting that this assumption remains approximately valid we can find the intensity and length limits of our model by solving (5.1) for the distribution function f. With f we can estimate the hot electron Landau damping and find for what parameters the absolute and convective thresholds are not met. Once f is established it is a trivial matter to find the density of hot electrons n_H and their respective average temperature T_H by

$$\int_0^\infty f dv \mid_{x=L} - \int_0^\infty f dv \mid_{x=0} \simeq \frac{n_H}{2}; \tag{5.4}$$

$$\int_0^\infty f v^2 dv \mid_{x=L} - \int_0^\infty f v^2 dv \mid_{x=0} \simeq \frac{n_H v_H^2}{2} \tag{5.5}$$

Solving (5.1) numerically in the positive velocity space for a thermal Maxwellian distribution of particles traveling through a plasma slab of length L, the energy absorption and spatial evolution of the distribution function is examined. Initially for very short distances $\Delta L \ll L$ the effect of the Langmuir field can be approximated as producing a slight perturbation on the Maxwellian distribution. As the particles proceed further into the plasma, notable particle heating occurs in the vicinity of $v_p = \omega_p/k_L$ significantly altering the distribution function. Once the particles reach the plasma boundary at $x = L$ the final distribution function is well approximated by

$$f = f_0 \exp\left[-\frac{v^2}{2v_T^2}\right] + f_H \exp\left[-\phi(\frac{v}{v_H})\right] \tag{5.6}$$

where a thermal velocity Maxwellian has been combined with a hot electron distribution function.

An example of the numerical solution of (5.1) is given in Fig. 5.1 for parameters $L = 60\,\mu m$, $I = 1 \cdot 10^{15}\,W/cm^2$, $n_0^e/n_c = 0.12$, $T_e = 1\,keV$, $ZT_e/T_i = 10$, $Z = 4$,

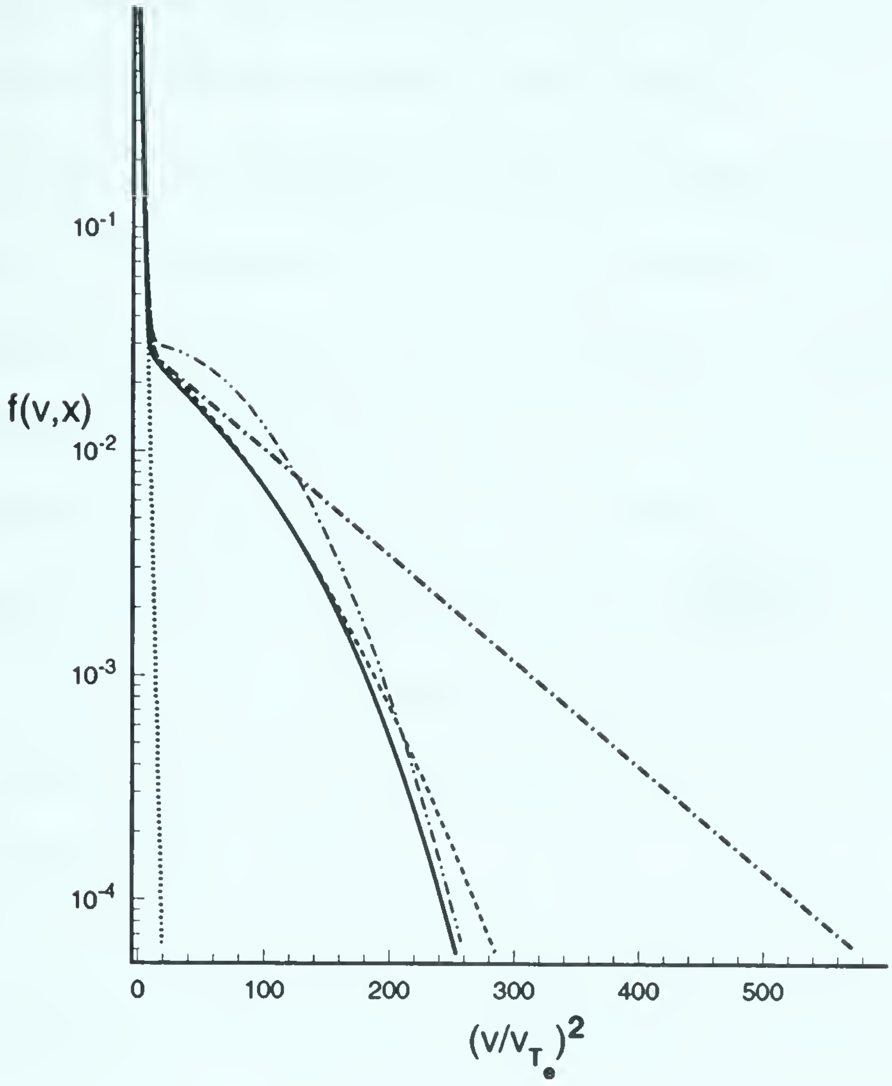

Figure 5.1: *Electron distribution evolution for parameters* $L = 60\,\mu m$, $I = 1 \cdot 10^{15}\,W/cm^2$, $n_0^e/n_c = 0.12$, $T_e = 1\,keV$, $ZT_e/T_i = 10$, $Z = 4$, $\lambda_0 = 0.351\,\mu m$

$\lambda_0 = 0.351\,\mu m$. Initially the distribution is Maxwellian (dotted curve). As the particles move through the plasma wave-particle interactions heat the electrons, producing at the edge of the plasma at $x = L$ Fig. 5.1 (solid curve). Three approximations for $\phi(v/v_H)$ are also shown in Fig. 5.1: (a) $v^2/2v_H^2$ (dot-dash curve), (b) $v^2/2v_H^2 + v^4/12v_H^4$ (dashed curve), and (c) $(v/v_H)^\beta/\alpha$ (dot-dot dash-dash curve). In this particular case $\beta = 4.2$ and $\alpha = 6$. One observes that the Maxwellian form (dot-dash curve) is clearly inadequate to describe the final distribution function. The single term $(v/v_H)^\beta/\alpha$ is also inadequate because the power β can only model a limited region of the curve and is unable to model the entire curve accurately. The polynomial fit can be seen to match a more significant

portion of the electron distribution function and, as one increases the number of terms, gives a reasonable fit to the final distribution.

Both n_H and v_H^2 are determined through evaluating (5.4) and (5.5) from the numerical data. As expected the explicit dependence of (5.3) on I and L will manifest itself in the evolution of the hot electron density and the average energy. Figure 5.2 illustrates the behavior of n_H and $n_H v_H^2 / v_{T_e}^2$ as a function of (a) the interaction length for fixed intensity $I = 5 \cdot 10^{14}\, W/cm^2$ and (b) the laser intensity for fixed length $L \simeq 55\, \mu m$, for parameters $n_0^e/n_c = 0.12, T_e = 1\, keV$, $ZT_e/T_i = 10$, $Z = 4$, $\lambda_0 = 0.351\, \mu m$. One immediately observes the several orders of magnitude increase in n_H and $n_H v_H^2 / v_{T_e}^2$ as the intensity of the laser is varied only over a single order of magnitude (Fig. 5.2(b)).

As the electrons absorb energy from the Langmuir wave spectra altering their distribution function, the effective Landau damping will increase. At this point the damping of the Langmuir waves becomes dependent on both the interaction length and the laser intensity, and subsequently the absolute and convective thresholds will increase. If the system is sufficiently large the particles traveling through the system will eventually reach a length L_{abs} for which the system is below the absolute SRS threshold. At this interaction length SRS will cease to grow absolutely. As the particles progress further into the plasma the convective SRS threshold will be raised to a level which will also stop convective growth (L_{con}). Thus for a given laser intensity and other parameters, a maximum length for absolute (L_{abs}) or for convective (L_{con}) growth can be found.

To obtain the length and intensity limits of our model, the Landau damping due to the hot electrons is found from the best fit $v^2/2v_H^2 + v^4/12v_H^4$ and can be written as

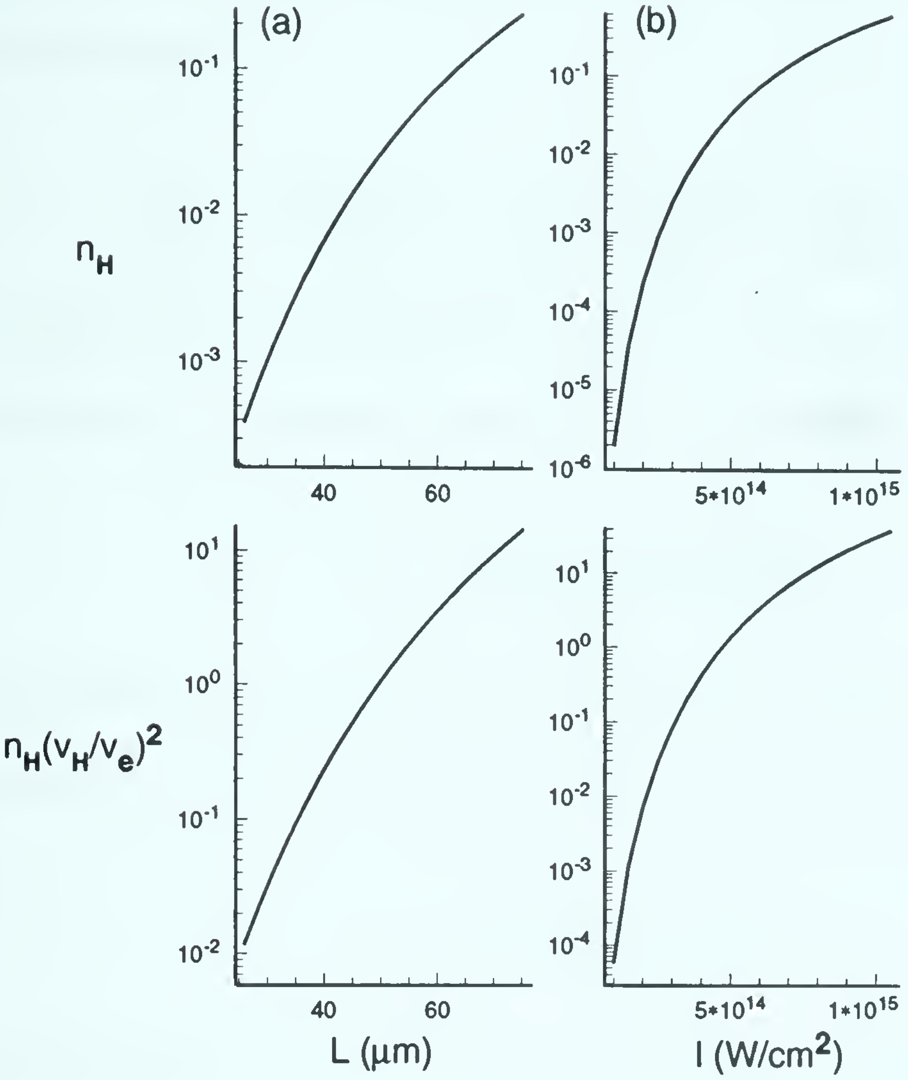

Figure 5.2: *Hot electron density* n_H *and* $n_H v_H^2/v_{T_e}^2$ *as a function of (a) length* ($I = 5 \cdot 10^{14}\,W/cm^2$) *and (b) laser intensity* ($L \simeq 55\,\mu m$) *for parameters* $n_0^e/n_c = 0.12$, $T_e = 1\,keV$, $ZT_e/T_i = 10$, $Z = 4$, $\lambda_0 = 0.351\,\mu m$

$$\gamma_H(I,L) = n_H \sqrt{\frac{\pi}{8}} \frac{\omega_p}{\zeta} [(\frac{v_{T_e} k_D}{v_H k})^3 + \frac{1}{3}(\frac{v_{T_e} k_D}{v_H k})^5] \exp[-\frac{1}{2}(\frac{v_{T_e} k_D}{v_H k})^2 - \frac{1}{12}(\frac{v_{T_e} k_D}{v_H k})^4] \tag{5.7}$$

where n_H and v_H are dependent on both the interaction length L and the laser intensity I. Here

$$\zeta = \sqrt{\frac{\eta}{16}} \exp[\frac{\eta}{16}] K_{\frac{1}{4}}(\frac{\eta}{16}) \tag{5.8}$$

and is the additional normalization constant for the best fit distribution function. $K_{\frac{1}{4}}(\eta/16)$ is the Bessel function of imaginary argument. In order for SRS to grow

absolutely the ratio of the absolute threshold to the SRS convective growth rate must be less than 1.

$$\frac{\gamma_{abs}}{\Gamma_{SRS}} = \left(\frac{\gamma_L(k_L)}{2V_L} + \frac{\gamma_R}{2V_R}\right)\frac{\sqrt{V_L V_R}}{\Gamma_{SRS}} \simeq \frac{\gamma_L(k_L)}{2\Gamma_{SRS}}\sqrt{\frac{V_R}{V_L}} < 1 \tag{5.9}$$

Using a given set of parameters for each laser intensity there will exist a length L_{abs} such that the increased damping due to (5.7) produces

$$\Delta_{abs} = \frac{\gamma_L(k_L) + \gamma_H}{2\Gamma_{SRS}}\sqrt{\frac{V_R}{V_L}} = 1 \tag{5.10}$$

Similarly there exists a length L_{con} such that for a given set of parameters and laser intensity the effective convective threshold is

$$\Delta_{con} = \frac{(\gamma_L(k_L) + \gamma_H)\gamma_R}{\Gamma_{SRS}^2} = 1 \tag{5.11}$$

As an example (5.10) and (5.11) are plotted as a function of I and L for the parameters $n_0^e/n_c = 0.2$, $T_e = 1\,keV$, $ZT_e/T_i = 8$, $Z = 3$, $\lambda_0 = 0.531\,\mu m$.Figure5.3 is a graph of intensity versus length and plots the curves of (5.10) (solid line) and (5.11) (dashed line). Simulation intensity and length must be chosen so that the combination of I, and L remain below the respective curves describing the absolute and convective thresholds. The length and intensity restrictions imposed by insisting that either the temporal or convective thresholds are met provides a much stricter condition than those imposed by the Zakharov model limits where $E_L^2/4\pi n_0^e T_e < 1$. To illustrate this point the curve $E_L^2/4\pi n_0^e T_e = 0.1$ is also plotted in Fig. 5.3. Here the Zakharov validity criterion is plotted as a dotted curve.

With the use of graphs such as Fig. 5.3 we can estimate the length and intensity limits of our simulations. For example should the parameters $n_0^e/n_c = 0.2$, $T_e = 1\,keV$, $ZT_e/T_i = 8$, $Z = 3$, $\lambda_0 = 0.531\,\mu m$ be used in a simulation with

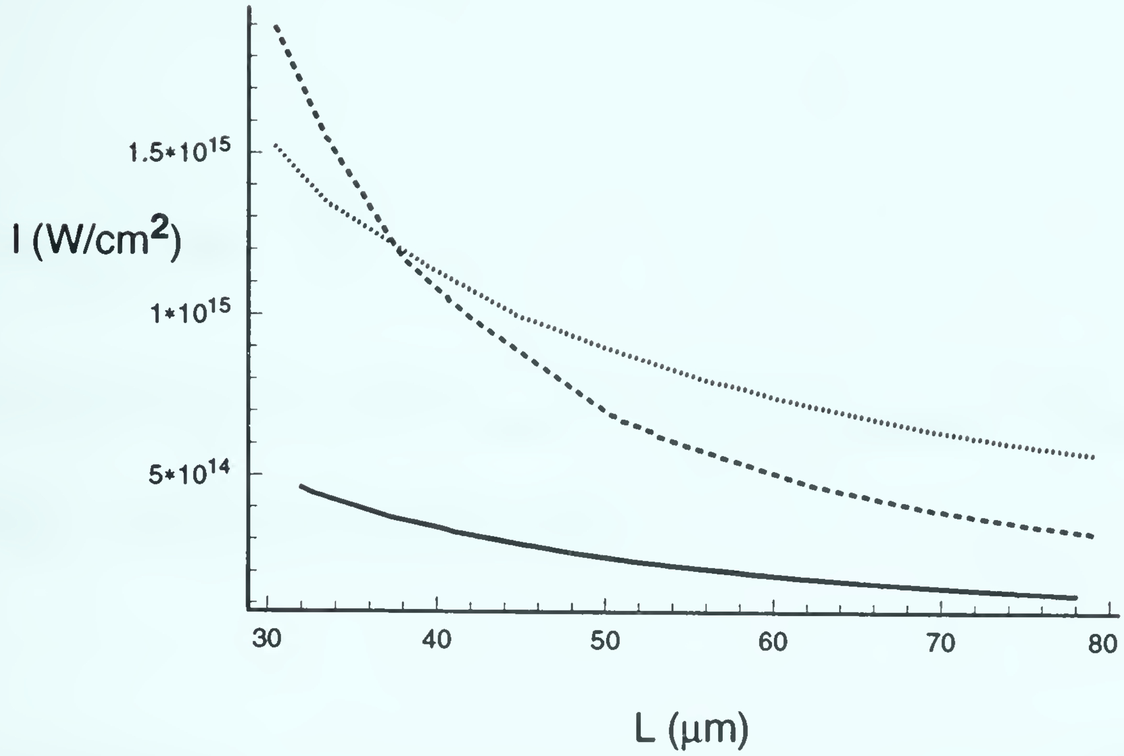

Figure 5.3: *Parameter regime limits of our simulations in terms of the increase in effective Landau damping due to hot electron generation SRS temporal threshold* $\Delta_{abs} = 1$ *(solid curve), SRS convective threshold* $\Delta_{con} = 1$ *(dashed curve), and* 10% *of Zakharov limit* $E_L^2/4\pi n_0^e T_e < 1$ *(dotted curve) for parameters* $n_0^e/n_c = 0.2$, $T_e = 1\,keV$, $ZT_e/T_i = 8$, $Z = 3$, $\lambda_0 = 0.531\,\mu m$

$I = 5 \cdot 10^{14}$, and $L = 50\mu m$, particles traveling across the entire length of the plasma would modify the distribution function sufficiently to drop the system below the absolute threshold before the end of the simulation box was reached. Under such circumstances our simulations may produce questionable results, limiting the interaction length of our model for these parameters to less than $L = 50\mu m$.

Chapter 6

Correspondence between theory and experiments

The present theoretical study analysing the nonlinear evolution of SRS in the presence of the electron-ion coupling described by the Zakharov equations is relevant to many current laser-plasma experiments. Although a detailed comparison between experimental observations is complicated by plasma geometry and hydrodynamical effects, as well as the simplicity of our model, the analysis presented in the previous chapters could be applied to preformed homogeneous plasmas in which parameters such as density and temperature are reasonably well known. We have examined the regime of parameters where the density is always below quarter critical and hence SRS is the fastest growing instability. Theoretically this fact allows the nonlinear evolution of SRS to affect significantly the evolution of other instabilities, such as SBS. One direct method which could be used to determine the applicability of our theory is through the use of Thompson scattering. By determining the frequency and wave number spectra of the relevant wave modes it would thus be possible to assess whether PDI, MI, or some other mechanism, such as wave breaking, is responsible for SRS saturation. Furthermore since the amount of reflectivity from enhanced Brillouin and forward Raman is quite small, one could use the enhance-

ment process of our theory as a diagnostic to determine the behavior inside the plasma.

A recent experiment by Villeneuve et al. [44] provides the first experimental evidence that supports long time SRS saturation produced through the parametric decay of the SRS driven Langmuir wave. By using Thomson scattering, Villeneuve et al. investigated the behavior of the frequency and wave number spectra of the Langmuir waves driven by SRS. When the observed spectra were analysed it was found that the Langmuir waves were consistent with the anticipated linear dispersion relation of SRS. In addition the observed wave number spectra of the Langmuir waves were consistent with that of a weakly driven PDI cascade of the SRS driven Langmuir wave. Wave breaking, which would have resulted in modification of the frequency spectra, was not observed in the experimental results. Simulation run using our full theoretical model (2.57)-(2.61) for typical experimental parameters agreed qualitatively with the experimental results. In particular the characteristics of the wave number spectra showed good agreement between experiment and simulation providing support for our model of SRS saturation. As an illustration of this we present in Fig. 6.1 the late time Langmuir spectra of simulations run for parameters $L = 100\,\mu m$, $I = 1 \cdot 10^{14}\,W/cm^2$, $n_0^e/n_c = 0.07$, $T_e = 0.6\,keV$, $ZT_e/T_i = 10$, $Z = 4$, $\lambda_0 = 1.06\,\mu m$ which are consistent with the Villeneuve et al. experiment. A direct comparison of our results in Fig. 6.1 with those of Villeneuve et al. (Ref. [44], Fig. 4) indicates reasonable agreement. The broader peaks observed in (Ref. [44], Fig. 4) may be accounted for by, for example, small nonuniformities in the background of the experimental density, or the resolution of the experimental data.

By using Thomson scattering as a diagnostic to identify the spectral characteristics of the frequency and wave numbers one could obtain sufficient data to

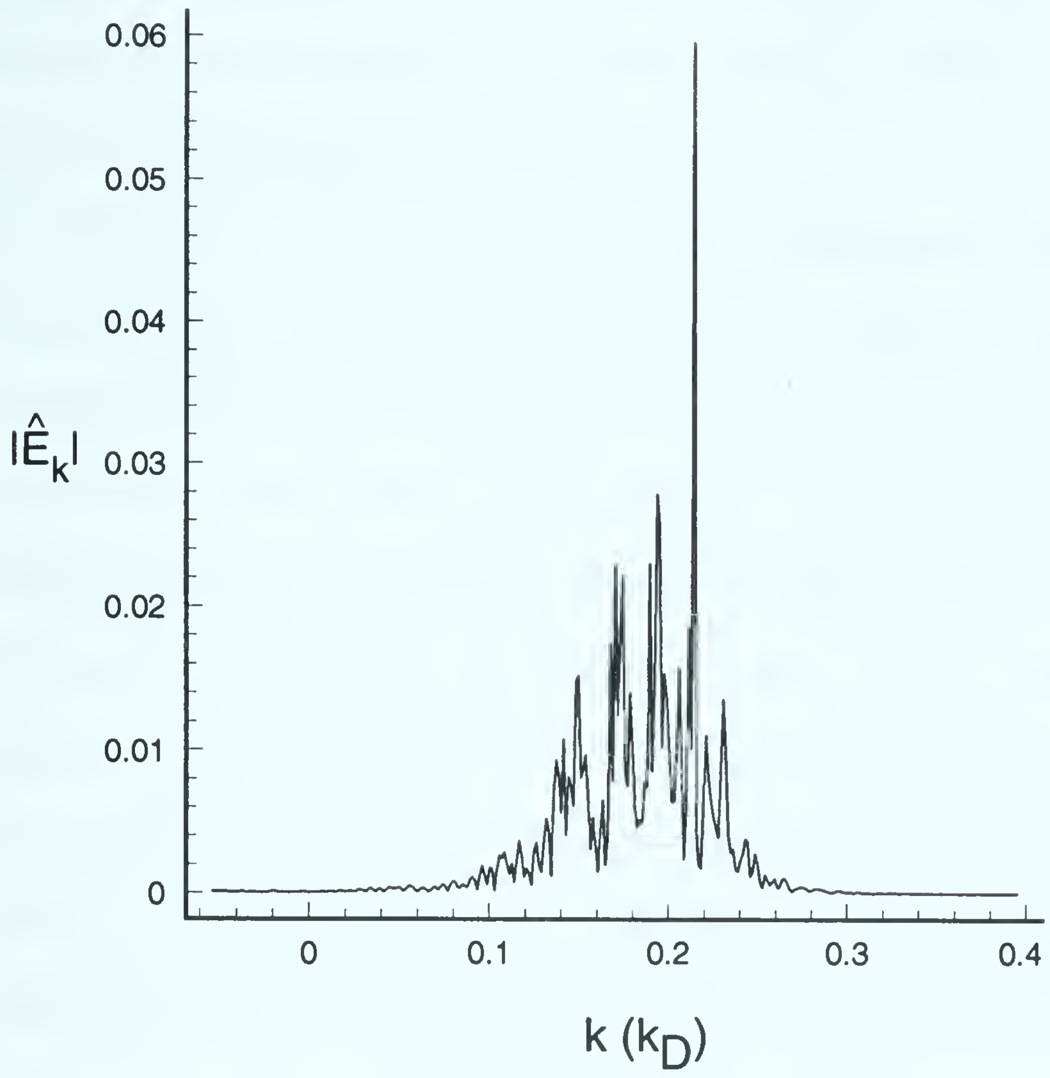

Figure 6.1: *Electrostatic spectra obtained from numerical solutions of equations (2.57)-(2.61) at late time for run parameters* $L = 100\,\mu m$, $I = 1 \cdot 10^{14}\,W/cm^2$, $n_0^e/n_c = 0.07$, $T_e = 0.6\,keV$, $ZT_e/T_i = 10$, $Z = 4$, $\lambda_0 = 1.06\,\mu m$

determine the applicability of our theoretical model. For the experimental parameters in regimes where our model applies, the enhancement of Brillouin and other scattering processes could be used as an additional diagnostic to determine the behavior inside the plasma. An example for which our enhancement theory seems to be consistent with experimental observation is a recent experiment by Baldis et al [88], [89], which reported observations of anomalously high levels of Brillouin reflectivity. In this experiment, a preformed plasma of density $< 0.1 n_c$ was irradiated with a 10 ps pulse of 1 μm light over a wide range of intensities ($I \simeq 10^{13} - 10^{15} W/cm^2$). The observed reflectivity levels vary over approximately two orders of magnitude, beginning with low intensity ($I \simeq 10^{13} W/cm^2$) pulses for

which the reflectivity levels was many orders of magnitude above those predicted by simple Thomson scattering, to high laser pulse ($I \simeq 10^{15} W/cm^2$) experiments for which the Brillouin appeared to saturate.

The experimental results do not correspond to simple three wave interaction. Brillouin scattering, in its three wave form, was investigated by Mounaix et al. [75] who found that the reflectivity levels of the three wave model are strongly dependent on the initial thermal noise levels of the plasma. The Mounaix et al. investigation, which was applied by Baldis et al. to the experimental results, concluded that three wave Brillouin interaction alone was inconsistent, at low laser intensities, with the observed results. In contrast the present analysis provides one possible explanation for the experimentally observed Brillouin levels at low intensities. In our theory only the initial transitory regimes are strongly dependent on the initial thermal levels. The late-time asymptotic levels of Brillouin scattering are dependent on the plasma parameters determining the saturation level of SRS.

Figure 6.2 shows the time integrated reflectivities of Baldis et al. plotted as a function of the laser intensities. Also plotted are reflectivity curves calculated using our theoretical Brillouin reflectivity scaling law (4.7) for the typical experimental parameters of $n_0/n_c = 0.08, T_e = 600eV, Z = 4, ZT_e/T_i = 10$. As one observes, to reproduce the experimentally observed reflectivity slope of Baldis et al. with our theory, the interaction length must be varied with intensity. Physically this would require a decrease in the interaction length as the laser intensity is increased. This is consistent with the results of Chap. 4 where we observed, in simulations, a reduced dependence of the reflectivity levels on length for higher laser intensities. Such a decrease in reflectivity would be expected in turbulent regimes for which the coherent length of interaction is reduced. A second possible explanation is that

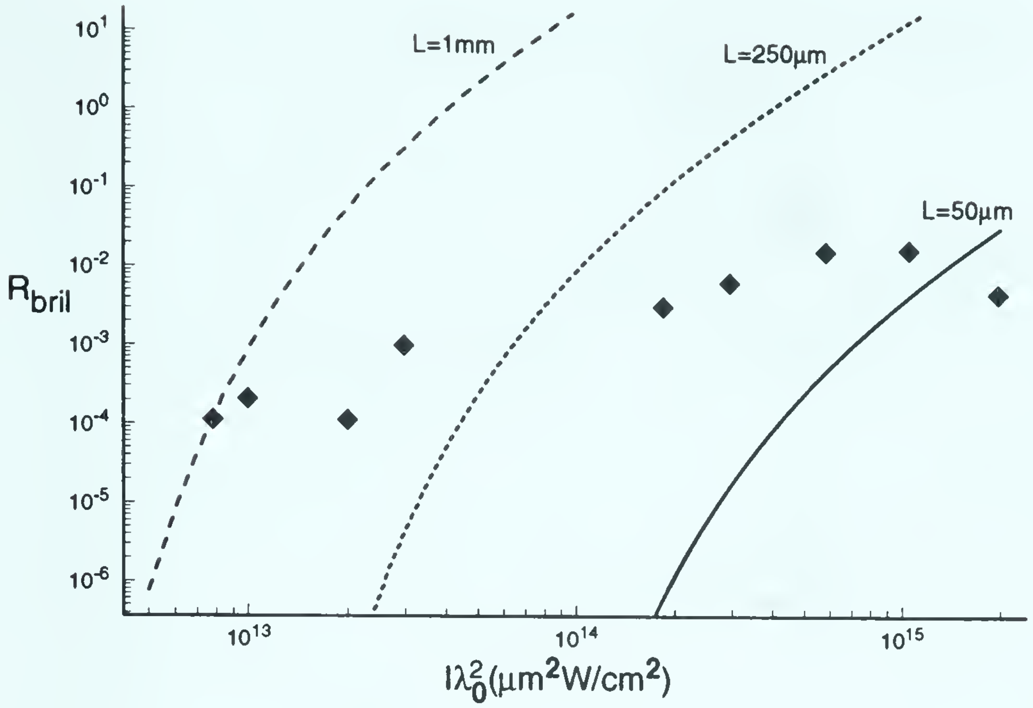

Figure 6.2: *Experimentally observed integral time average Brillouin reflectivity (diamonds) together with enhanced Brillouin reflectivity curves for parameters* $n_0/n_c = 0.08, T_e = 600eV, Z = 4, ZT_e/T_i = 10$

at higher intensities the temperature ratio would change reducing the ion Landau damping and hence the level of enhancement.

As an example the time history of the Brillouin reflectivity together with the SRS evolution for parameters $L = 250\,\mu m$, $I = 5 \cdot 10^{13}\,W/cm^2$, $n_0^e/n_c = 0.08$, $T_e = 0.6\,keV$, $ZT_e/T_i = 12$, $Z = 4$, $\lambda_0 = 1\,\mu m$. is shown in Fig. 6.3. In this particular case the evolution of Brillouin, being dependent on the SRS saturation does not produce a large reflectivity levels until sometime after the 10 ps timescale of the experiment has past.

Figure 6.3 also contains the Brillouin reflectivity level produced through the use of a three wave interaction model (2.75)-(2.77) for identical parameters including the value of initial noise levels. The enhanced Brillouin is orders of magnitude above that of the 3WI reflectivity. Although these results do not give conclusive evidence

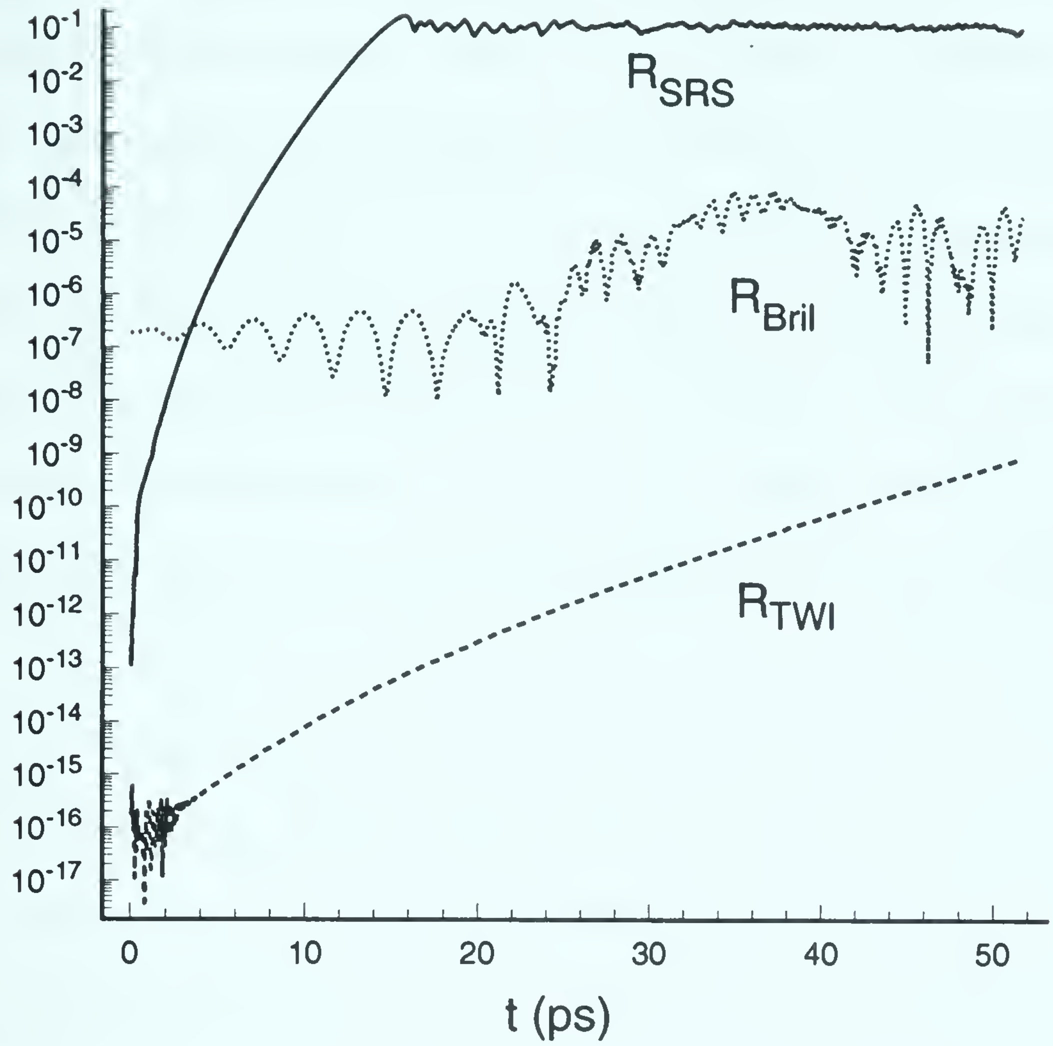

Figure 6.3: *Time history of SRS (solid curve), enhanced Brillouin (dotted curve) and three wave Brillouin (dashed curve) reflectivity for parameters* $L = 250\,\mu m$, $I = 5 \cdot 10^{13}\,W/cm^2$, $n_0^e/n_c = 0.08$, $T_e = 0.6\,keV$, $ZT_e/T_i = 12$, $Z = 4$, $\lambda_0 = 1\,\mu m$

that the experimental reflectivity is caused by the enhancement of noise levels through SRS saturation, qualitatively at least the agreement between simulation and experimental reflectivity scaling suggests that saturation of SRS is a reasonable candidate for the mechanism responsible for enhancing Brillouin in the Baldis et al. experiment.

In a more recent experiment performed using the Nova laser [93], opposing beams were used to study SBS. SBS was observed showing very distinct features: a rapid turn on time, and a complicated frequency spectra, which includes anti-Stokes or blue shifted components and the normal Stokes components. The experimentally observed rapid turn on time is also a characteristic feature of our enhancement

model, and in our case it is a consequence of the first sharp saturation of SRS. In our simulations we also observe both Stokes and anti-Stokes Brillouin scattering.

In the experiment a preformed plasma was produced using one beam of the system, while the second was fired after different time delays. We were able to identify key parameters characterizing two distinct cases by using the results of LASNEX hydrodynamical simulations [69]. We have identified two cases with related delay times, between the firing of the formation beam and the interaction beam, of approximately 400 ps (case 1) and 1000 ps (case 2). The parameters case (1) Fig. 6.4(a) - $n_0/n_c = 0.2$, $T_e = 1.5keV$, $ZT_e/T_i = 8$, $I = 10^{14}W/cm^2$, $L = 60\mu m$; case (2) Fig. 6.4(b)- $n_0/n_c = 0.1$, $T_e = 1keV$, $ZT_e/T_i = 8$, $I = 2.510^{14}W/cm^2$, $L = 60\mu m$ were used, producing results which varied quite dramatically from case to case. Although detailed comparison with experimental results is again complicated by the plasma geometry and hydrodynamical effects, as well as the simplicity of our model, the importance of SRS influence on Brillouin scattering is hard to overestimate once one notices the magnitude of the enhancement effect.

This increase is illustrated in Fig. 6.4, showing the SRS reflectivity (R_{SRS}) and the Brillouin reflectivity R_B produced by laser light scattering from the fluctuations enhanced during nonlinear SRS evolution. Time evolution of R_B shows a very rapid increase of reflectivity and a subsequent decay. Case 1 (Fig. 6.4(a)) displays a much stronger enhancement of Brillouin as compared to case 2 (Fig. 6.4(b)), where R_B after the initial increase decays approximately to the level of detection accuracy for SBS in our numerical simulations (cf.[69]).

Experimentally, both Stokes Brillouin components and blue shifted components, which may be associated with the anti-Stokes Brillouin scattering, were observed in the frequency spectra. Similar anomalous spectral peaks were observed in our

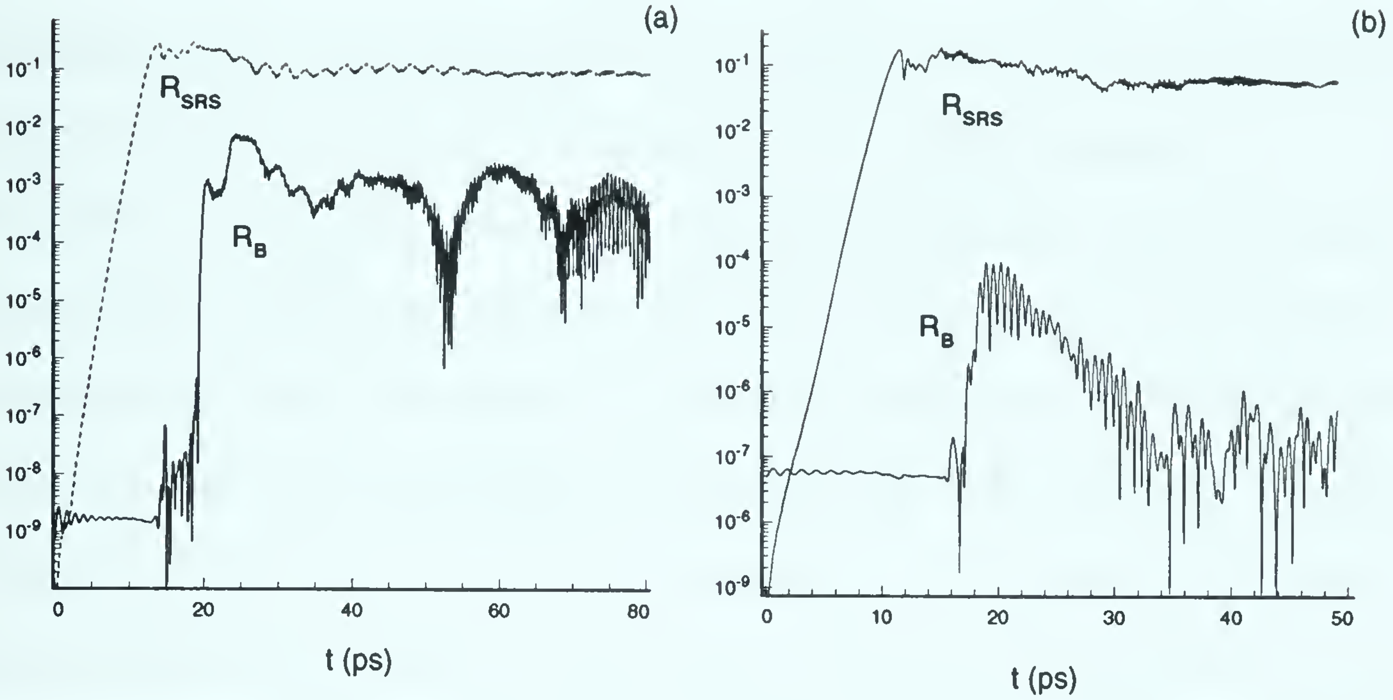

Figure 6.4: *SRS reflectivity R_{SRS} and Brillouin reflectivity R_B as functions of time for the case (1) (a), and the case (2) (b). Brillouin reflectivity corresponds to scattering on the fluctuations enhanced by SRS.*

simulations (cf Chap. 4 Fig. 4.10). As was mentioned in Chap. 4 one of the important parameters describing the level of Brillouin reflectivity is the separation in the ion wave spectra between the components at $k_A^{(1)}$ produced by the PDI of SRS driven Langmuir wave and N_k at $k_A^B = 2k_0$ which participates in Brillouin scattering. Figs. 6.5(a) and 6.6(a) show spectra of density fluctuations at late times in the simulations, when SRS reflectivity has already reached its asymptotic value. For case 1 (Fig. 6.5(a)) we observe strong enhancement of N_k levels and a relatively small separation between $k_A^B = 0.22k_D$ and $k_A = 0.29k_D$ components. The enhanced part of the spectrum is dominated by broad, but distinct peaks corresponding to modes produced by the PDI cascade. The value of $k = k_A^B$ is located very close to the fourth component of the PDI cascade which is a mode propagating in the opposite direction to the pump. Electromagnetic radiation

which is scattered due to interaction with this mode would produce primarily the anti-Stokes component observed in the frequency spectrum (cf. Fig. 6.5(b)). The contour plot (Fig. 6.5(b)) displays the time evolution of the spectral intensity of Brillouin backscattered radiation normalized to the pump intensity at $\omega = \omega_0$. The Stokes and anti-Stokes maxima correspond approximately to the ion acoustic frequency $2k_0c_s$. Since the enhanced part of ion wave spectrum is dominated by nearly discrete peaks, small changes in plasma parameters can move k_A^B component closer to the mode propagating along the pump and produce the strongly enhanced Stokes components in the spectrum. In summary, we have observed that case 1, corresponding to high density and high plasma temperature, is characterized by the strong enhancement of Brillouin scattered light which has a well defined spectral shift (anti-Stokes for this particular simulation).

We observe a quite different situation for case 2, (cf. Fig. 6.6). Due to the weaker SRS a smaller part of the ion spectrum is enhanced. The criterion for the enhancement of the N_k amplitude at $k = k_A^B$ (4.3) is only marginally satisfied for case 2 (cf. Fig. 6.6(a)). Also the $k_A^B = 0.27k_D$ component is separated, to a much larger degree, from the maximum amplitude at $k_A = 0.42k_D$ as compared to the distance between these modes in case 1, reducing the Brillouin reflectivity even further. The frequency spectra of the Brillouin backscattered light (Fig. 6.6(b)) shows weakly enhanced but approximately the same intensity Stokes and anti-Stokes components. The scattering takes place on the ion fluctuations at $k = k_A^B$, which correspond to a continuous part of the spectrum (Fig. 6.6(a)) equally enhanced for waves propagating to the left and to the right.

In both cases which we have examined ion waves enhanced by SRS are the only source of Brillouin scattered light. They contribute to the frequency spectra of the

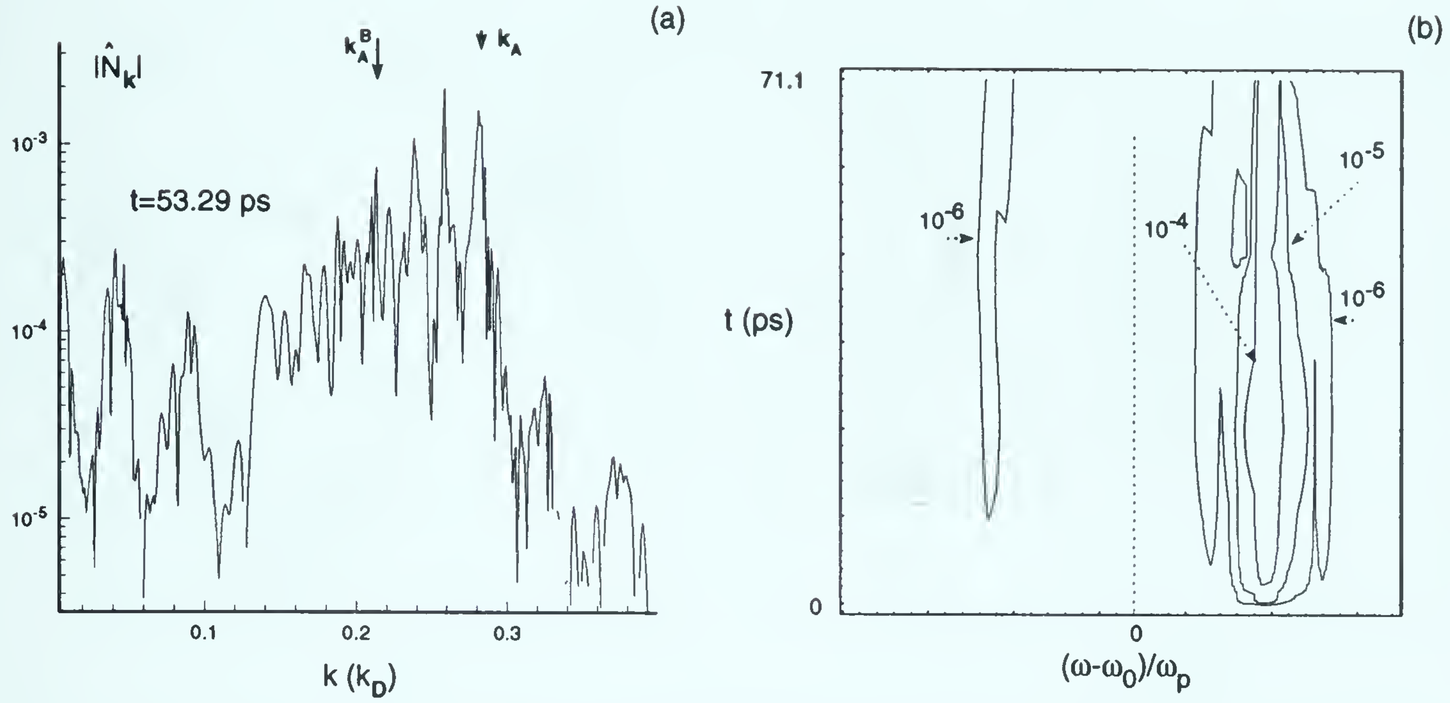

Figure 6.5: *Results from the numerical simulations for the following plasma parameters:* $n_0/n_c = 0.2$, $T_e = 1.5keV$, $ZT_e/T_i = 8$, $I = 10^{14} W/cm^2$, $L = 60\mu m$ *(case (1)). (a) normalized Fourier spectrum of density fluctuations at time t=53.29 ps (cf. Fig. 6.3(a)). (b) contour plot of the Brillouin backscattered spectral intensity normalized to pump intensity.*

Brillouin signal, which contain Stokes and anti-Stokes components. Both components have been observed in experiments [93]. Although our model does produce both Stokes and anti-Stokes components there exists the possibility that hydrodynamical effects, which have not been accounted for, could either act simultaneously with our enhancement mechanism or replace it as the dominant process in plasma.

In Chap. 4 it was shown that the nonlinear evolution of SRS can produce Langmuir modes capable of scattering waves corresponding to the anti-Stokes components of Raman. The enhancement of these anti-Stokes components above the thermal levels expected from Thomson scattering could account for the experimental observation of large levels of anti-Stokes Raman reflectivity. Although direct spectral evidence of the frequency and wave number characteristics of the plasma waves in these experiments were not found, indirectly the experimental evidence

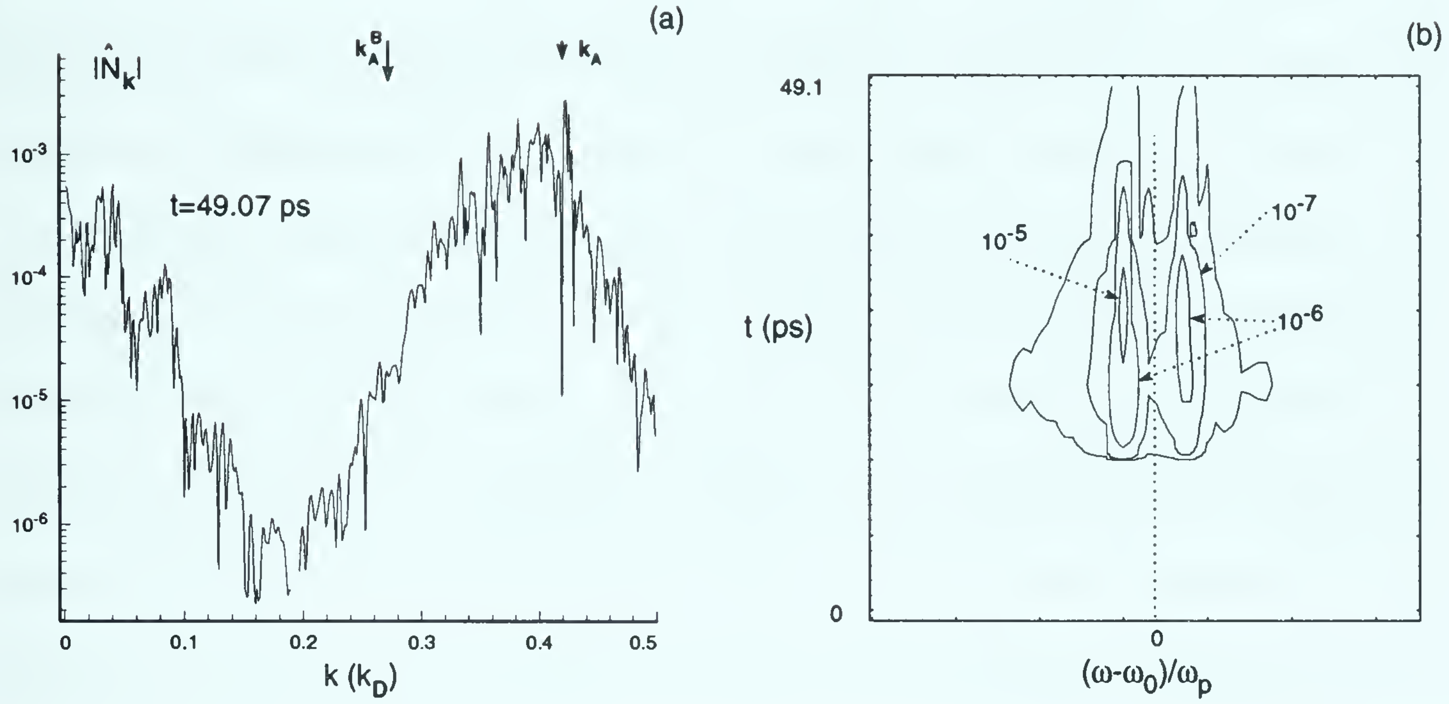

Figure 6.6: *Results from the numerical simulations for the following plasma parameters:* $n_0/n_c = 0.1$, $T_e = 1keV$, $ZT_e/T_i = 8$, $I = 2.510^{14}W/cm^2$, $L = 60\mu m$ *(case (2)). (a) normalized Fourier spectrum of density fluctuations at time t= 49.07 ps (cf. Fig. 6.3(b)). (b) contour plot of the Brillouin backscattered spectral intensity normalized to pump intensity.*

obtained may support our theoretical model of SRS.

Experimental observation of anti-Stokes forward Raman scattering (AFR) was first reported by Turner et al [92] in 1986. Since this time numerous reports of the observation of AFR as well as evidence for the existence of an anti-Stokes component in the backwards direction (ABR) has appeared in the literature [90], [91], [99], [102]. The experiments by Turner et al were performed using one arm of the Nova laser to irradiate CH targets with $0.53\mu m$ light. Although a density gradient was present in the plasma the parameters of the system were such that a qualitative comparison can be done using our model. The observation of SRS was reported to extend from $0.1 \le n_0/n_c \le 0.22$ while FR existed in a more restricted density regime of $0.14 \le n_0/n_c \le 0.22$. The AFR reflectivity, although an order of magnitude or so smaller than FR, was highly correlated with the observed FR

reflectivity. Due to the close proximity of k_L^{FR} to k_L^{FR+} the simultaneous appearance of AFR together with FR is a direct consequence of our enhancement mechanism and could be used to explain the observed results. Furthermore our theory also provides an explanation for the relatively high density required to observe FR. As the density decreases the separation between the primary wave number at k_L and the secondary resonant point at k_L^{FR} increase, requiring a larger amplification coefficient A to produce strong enhancement. The observed experimental ratio between the AFR and FR reflectivity levels can be explained by our theoretical model. FR is an unstable process for which convective growth is possible. AFR however is a stable process relying solely on previously existing Langmuir waves to provide the observed levels.

In order to obtain sufficient simulation data for a comprehensive study of the various reflectivity levels, the key parameters $n_0^e/n_c = 0.2$, $T_e = 1\,keV$, $ZT_e/T_i = 8$, $Z = 3 - 5$, $\lambda_0 = 0.531\,\mu m$ were identified as providing the largest range of laser intensities and interaction lengths while maintaining model validity. To establish a reflectivity scaling for AFR the laser intensity and interaction length were varied, producing the results illustrated in Fig. 6.7. Figure 6.7 shows the time averaged simulation reflectivity versus theoretical reflectivity values for SRS (open diamonds) (3.27), forward Stokes (closed diamonds) (4.8) and anti-Stokes (open circles) (4.28) Raman scattering. A comparison can be made with the reported reflectivities of: (a)backward SRS $\simeq 0.1 - 0.2$, (b)FR $\simeq 10^{-3} - 3 \cdot 10^{-3}$, and (c)AFR $\simeq 5 \cdot 10^{-5}$, which are in quantitative agreement with the simulation reflectivities of Fig. 6.7.

Further examples of experimentally observed anti-Stokes Raman scattering exist in the literature. A recent study by Batha et al. [90] was again performed using the Nova system. In this case a long scale length preformed plasma was irradiated

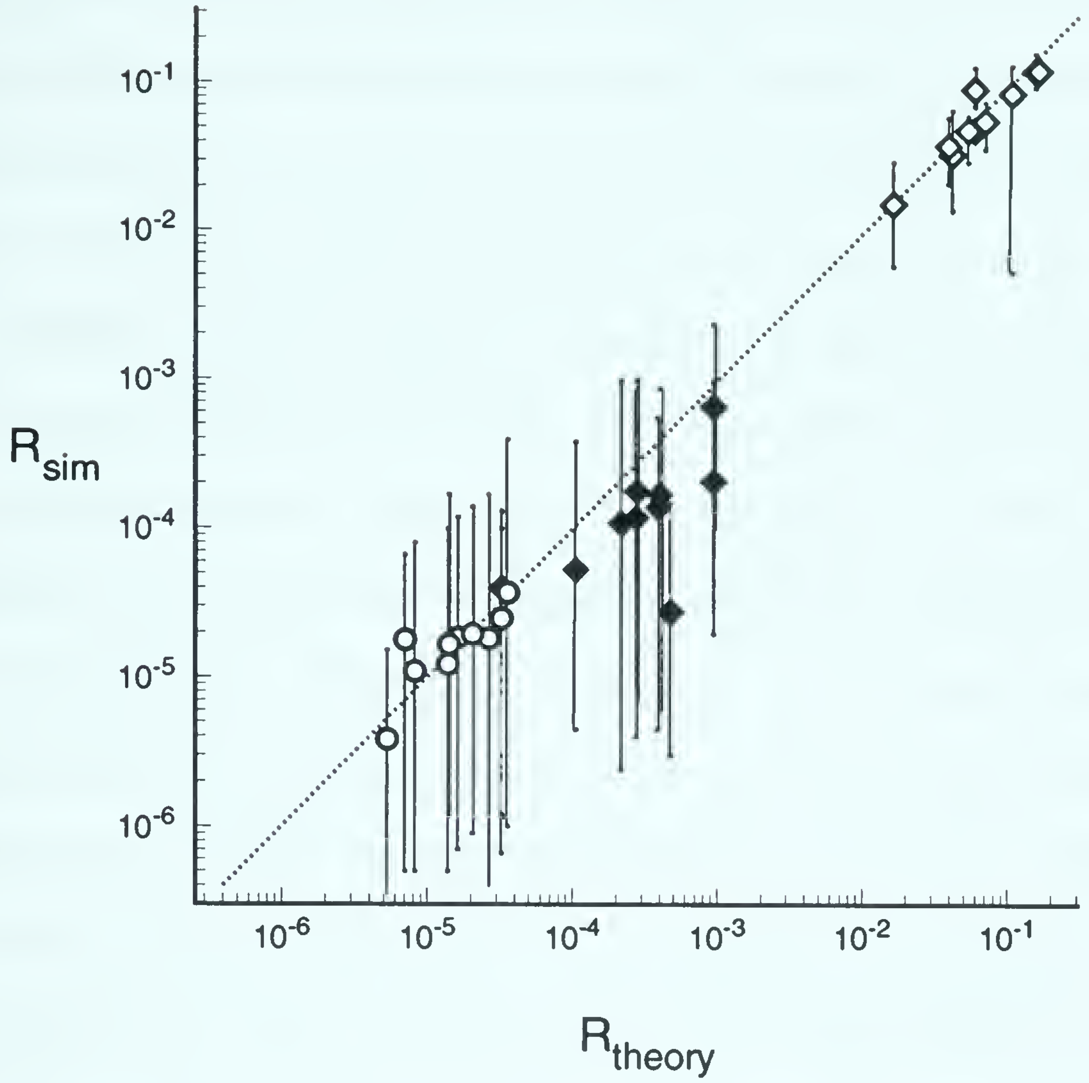

Figure 6.7: *Simulation versus theoretical reflectivity values for SRS (open diamonds)(3.27), forward Stokes (closed diamonds)(4.8) and anti-Stokes (open circles)(4.28) Raman for parameters* $L = 25 - 100\,\mu m$, $I = 1 - 10 \cdot 10^{14}\,W/cm^2$, $n_0^e/n_c = 0.2$, $T_e = 1\,keV$, $ZT_e/T_i = 8$, $Z = 3 - 5$, $\lambda_0 = 0.531\,\mu m$

with a $0.351\mu m$ interaction beam. An approximate density of $0.1 \leq n_0/n_c \leq 0.15$ and temperature of $\simeq 1keV$ was reported. Under such conditions the separation of the primary wave number k_L from both the FR component at k_L^{FR} and the required wave number for ABR is quite large. However the intensity of the interaction beam ($I \simeq 1.5 \cdot 10^{15} W/cm^2$) and the long scale length of the plasma are sufficient to produce a reasonably large amplification coefficient such that significant enhancement of the secondary components can be achieved. It was not possible to produce a universal reflectivity scaling and only some of the physical characteristics of the reflectivity scaling (4.29) were found (see Fig. 4.12(a) and 4.13(a)). However we can

address certain concerns mentioned by Batha et al. as to the nature of the mechanism producing the anti-Stokes component. In particular they expressed concern about the construction of the ion modes which would allow reversal of Langmuir waves to produce the backwards anti-Stokes scattering. As has been demonstrated the saturation of SRS through the nonlinear evolution of the Zakharov equations can supply the necessary wave modes to enhance ABR. Furthermore the spectra is not completely turbulent, allowing for the development of the sharp peaks observed by Batha et al.. Finally in their analysis Batha et al. neglected the continuous part of the spectrum which arises naturally in the PDI cascade process. Such an omission resulted in their rejection of PDI as a source of enhancement based on an argument that any PDI component would have to propagate sufficiently far such that heavy damping would occur. Such propagation is not necessary to produce the correct wave vector. The interaction of the Langmuir and ion acoustic modes generates significant levels of Langmuir waves at the correct wave numbers for enhancement to occur.

As a final note on the phenomenon of anti-Stokes Raman reflectivity, we would like to comment on a recent publication by Labaune et al. [91]. In their investigation they reported observation of ABR correlated with the appearance of a strong Brillouin component. However it is still relevant to discuss this experiment in the context of enhancement processes whether due to SRS saturation of some other possible mechanism for enhancement. In the experimental parameter regime investigated by Labaune et al. the density was always well below quarter critical, and hence, assuming that the plasma was homogeneous, the growth of SRS due to its larger growth rate should have taken place before SBS. Under these circumstances one would expect to see in simulations a similar nonlinear evolution of SRS

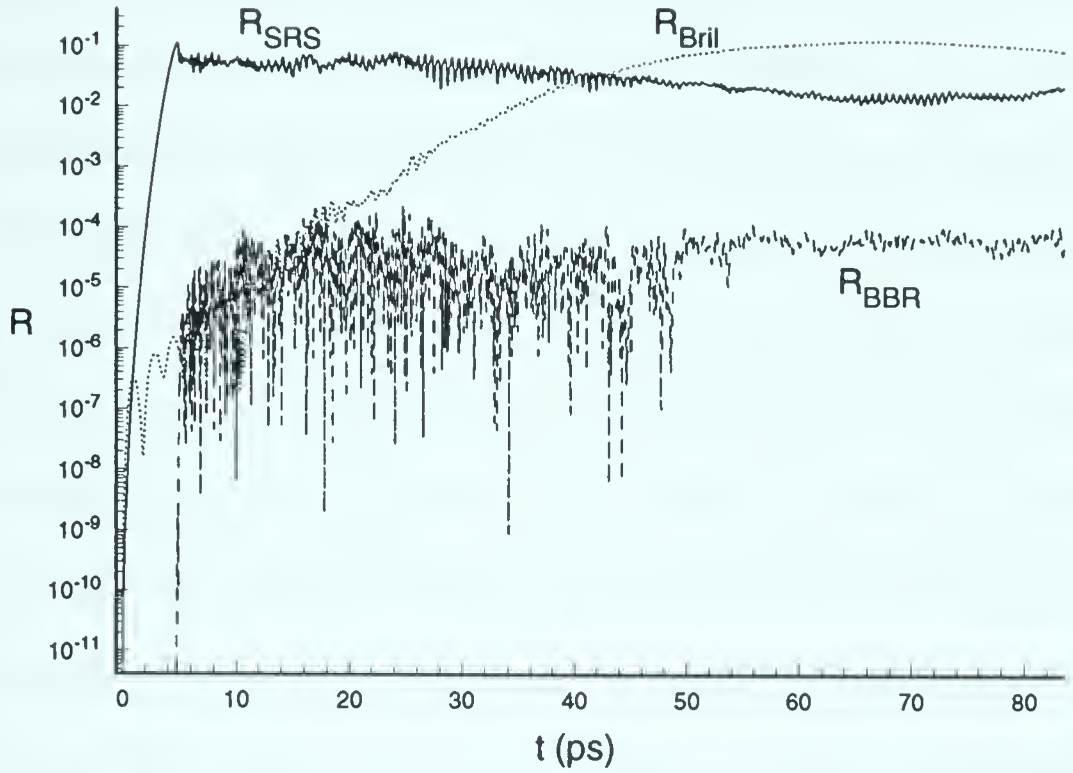

Figure 6.8: *SRS, Brillouin and ABR reflectivity as a function of time obtained from numerical solutions of equations (2.57)-(2.61) for the parameters* $L = 70\,\mu m$, $I = 5\cdot 10^{14}\,W/cm^2$, $n_0^e/n_c = 0.1$, $T_e = 0.5\,keV$, $ZT_e/T_i = 10$, $Z = 4$, $\lambda_0 = 0.531\,\mu m$

to that of Chaps. 3 and 4. As SBS evolves and overtakes SRS the ion modes associated with SBS would grow to large levels producing enhancement of quasi-modes which could affect ABR. As an illustration of this argument Fig. 6.8 plots the simulation time history of SRS, ABR and Brillouin for parameters $L = 70\,\mu m$, $I = 5\cdot 10^{14}\,W/cm^2$, $n_0^e/n_c = 0.1$, $T_e = 0.5\,keV$, $ZT_e/T_i = 10$, $Z = 4$, $\lambda_0 = 0.531\,\mu m$.

For these particular parameters Brillouin is above its absolute threshold, and because our theoretical model (2.57)-(2.61) does not contain an explicit mechanism for SBS saturation, one would expect that Brillouin itself should grow until the simulation reaches unrealistic reflectivity levels. However as is illustrated in Fig. 6.8 the SBS saturates at a level between 10% – 20%. SRS is also saturated, at a level of ~ 1%, and hence, because of the low level of reflectivity, competition between SRS and SBS for pump energy cannot explain the saturation observed.

The reason SBS saturates in this example, if this is actually SBS saturation, is currently not understood. Further analysis of this parameter regime is needed in order to determine what is taking place in the simulation. Regardless of whether we are observing SBS saturation or some dynamical evolution, the simulation of Fig. 6.8 illustrates how absolute SBS can affect the evolution of ABR.

In the context of the Labaune et al. experiment, SBS in our simulation produces a strong density spectral component at k_A^B. This component can couple effectively with the Langmuir spectrum allowing for the production of a more coherent ABR Langmuir component. This coherence can be seen in Fig. 6.8 where, as the SBS becomes the dominant instability ($t > 45$ ps), the fluctuations associated with the anti-Stokes Raman reflectivity are significantly reduced. One also observes that the anti-Stokes reflectivity continues to grow after the saturation of SRS, indicating that the growth of SBS is influencing ABR. Although this simulation evidence does not directly verify the hypothesis that SRS and SBS saturation are the cause of the ABR reflectivity observed in the Labaune experiment, it does provide evidence that SBS can influence the behavior of ABR.

One characteristic, observed in many recent SRS experiments, is a feature known as the Raman gap [90], [104]. The Raman gap refers to a region of very weak emission in the wave spectra of the Raman backscatter near densities approaching the quarter critical density ($\frac{1}{4}n_c$). This gap is not directly predicted by any linear theory of SRS. In the $\frac{1}{4}n_c$ region the wave number of the SRS backscattered electromagnetic wave approaches zero. Thus small modifications in the background density n_0, which were unimportant when one is well below $\frac{1}{4}n_c$, can now affect the SRS dispersion relation. ie.

$$\omega_R^2 = \omega_p^2(1+\delta n) + c^2k_R^2 \tag{6.1}$$

Here we have introduced δn which is associated with the long wavelength ion density fluctuations at $\sim k_A = 0$. These density fluctuations could be produced through the saturation of SRS or two plasmon decay. For argument sake we assume that the fluctuations are produced by the PDI cascade and can be represented by $\delta n = \eta N_A^{(1)}$. Here $N_A^{(1)}$ is the peak noise fluctuation value at $k_A = 2k_L - \Delta k$ and η represents the fraction of the fluctuations which affect the long wavelength regime. Near $\frac{1}{4}n_c$ even small ion fluctuations could adversely affect the Raman scatter by driving the background density above $\frac{1}{4}n_c$ and disrupting the matching conditions of the Raman backscatter.

When calculating the SRS reflectivity, the density fluctuation coupling in the equation describing the Raman scatter (2.60) was ignored and a linear approximation was used instead to describe the SRS wave equation. This omission is valid as long as one is well below $\frac{1}{4}n_c$ ($\leq 0.22n_0/n_c$). For simulations approaching $\frac{1}{4}n_c$ the Raman reflectivity expression (3.27) diverges (cf. Fig. 6.9 (solid line)). To correct for this problem one retains the density nonlinearity in the original electromagnetic equation describing the evolution of the Raman scattering (2.60). By assuming that this electrostatic ponderomotive force can be represented through the use of the asymptotic density fluctuations produced by SRS saturation, expression (3.15), one arrives at the equation

$$V_R\frac{\partial E_R}{\partial X} = -\frac{\omega_p^2\eta}{2\omega_R} \mid E_L \mid^2 E_R + \frac{ek_L}{4\omega_0 m_e}E_0E_L^*. \tag{6.2}$$

Here the coupling constant η describing the fraction of density fluctuations affecting the SRS matching conditions must be determined. We now replace the linear

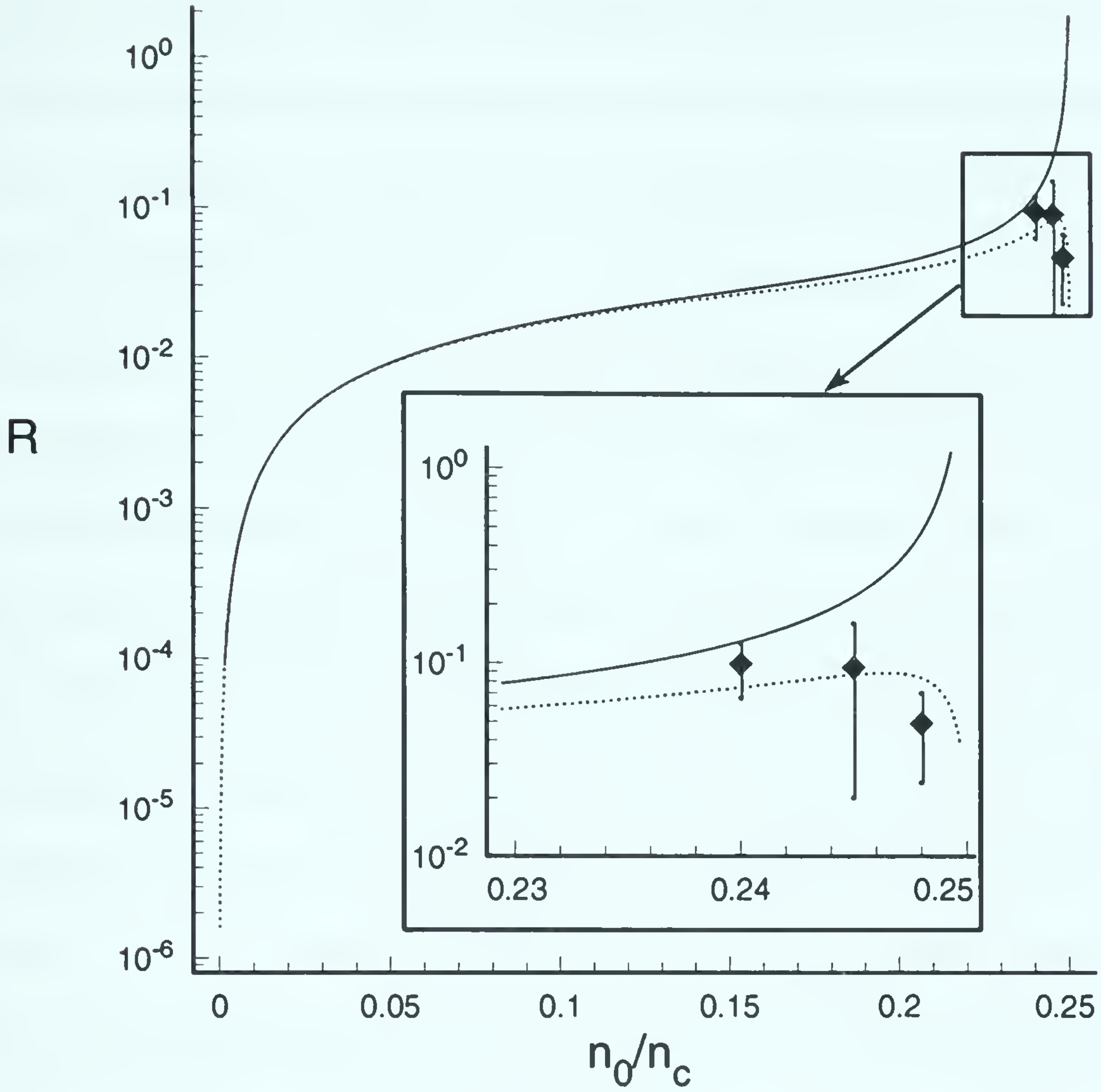

Figure 6.9: *SRS reflectivity expressions (3.27) solid line, and (6.4) dotted line, as a function of density, for parameters* $L = 60\,\mu m$, $I = 1 \cdot 10^{14}\,W/cm^2$, $T_e = 1\,keV$, $ZT_e/T_i = 8$, $Z = 3$, $\lambda_0 = 0.531\,\mu m$. *Diamonds represent time average asymptotic reflectivities obtained from simulations.*

approximation of the SRS evolution, (3.21), with (6.2). Using the relationship we have found between the asymptotic Langmuir and SRS variables, (3.20) written in the form

$$| E_L |^3 = \frac{E_{th}^2}{4\gamma_L(k_L)} \frac{\omega_p k_L}{\omega_R} \frac{eE_0}{\omega_0 m_e} E_R \tag{6.3}$$

and proceeding as in Chap. 3 we obtain the reflectivity expression

$$R_{SRS} = \frac{V_R v_{osc}}{V_0 E_0^2} \frac{\omega_R^2 k_L}{\omega_p^3} \left(\frac{\gamma_L(k_L)}{2\omega_p \eta^3 E_{th}^2} \right)^{\frac{1}{2}} \tanh^3 \left[\frac{L k_L v_{osc} E_{th}}{3 V_R \omega_R} \left(\frac{\omega_p^3 \eta}{8\gamma_L(k_L)} \right)^{\frac{1}{2}} \right] \tag{6.4}$$

where $v_{osc} = eE_0/m_e\omega_0$. When the density is well below $\frac{1}{4}n_c$ it has been shown that (3.27) is a reasonable approximation for the asymptotic reflectivity. This fact allows one to estimate the value of η by matching the reflectivity curves of (3.27) and (6.4) for densities below $0.2n_0/n_c$. One observes that the SRS reflectivity is still independent of $\gamma_L(k_L)$ except possibly through the parameter η. However one can no longer separate the density dependence from the rest of the parameters. The shape of SRS reflectivity, as one varies the density between 0 and $\frac{1}{4}n_c$, now depends explicitly on the parameter regime chosen. If the argument of $\tanh(x)$ is small, (6.4) reduces to (3.27), our usual expression for SRS reflectivity. As one now approaches $\frac{1}{4}n_c$ the reflectivity approaches zero (cf. Fig. 6.9 (dotted line)). Also present in Fig. 6.9 are a number of simulation reflectivity results for densities approaching $\frac{1}{4}n_c$, where η was estimated by examining the density spectra for very low wave numbers. Good agreement between the simulation time averaged reflectivity and the new scaling (6.4) is obtained, indicating that the ion density fluctuations can influence the reflectivity behavior near $\frac{1}{4}n_c$.

However the absence of a density gradient, and other instabilities such as two plasmon decay, in our theoretical model (2.57)-(2.61) makes analyzing this parameter regime difficult. By adding a density gradient to the present model one would be able to investigate the affects such a gradient would have on SRS and allow a much more complete study of the influence of the ion fluctuations on SRS near $\frac{1}{4}n_c$ and their possible contribution towards the Raman gap.

Chapter 7

Summary and conclusions

During this investigation we have obtained scaling laws for the saturated SRS reflectivity level and the associated Langmuir field amplitude. Scaling laws describing the enhanced reflectivity levels of Brillouin and forward Raman scattering as well as criteria for determining their strong enhancement have also been given. Other secondary scattering processes, such as anti-Stokes Raman scattering, have also been described. These results have been compared to several experiments providing new or alternate explanations for observed results.

We have examined the nonlinear behavior of SRS in the presence of the electron-ion coupling associated with the one dimensional Zakharov equations for a uniform bounded plasma. It has been known for many years that secondary parametric processes can disrupt and saturate primary instabilities. Many examples have been studied illustrating this principle within the weak turbulence formalism or wave coupling theories, including the case of SRS. For the parameter regimes studied in this investigation, PDI of the SRS driven Langmuir wave was always observed to be the initial cause of SRS saturation. The new physics in our description of PDI and the PDI cascade is, first of all, related to the different temporal and spatial evolution of both instabilities. SRS is convective and PDI develops locally

with the homogeneous growth rate. Several characteristic features of nonlinear SRS evolution, including disruption of the PDI cascade and Langmuir wave localization, can be explained by spatial nonuniformities of the wave coupling processes.

Secondly, by using the Zakharov theory to describe the resonant wave interaction, we also allowed for nonresonant mode coupling. This nonresonant contribution affects the initial levels of the linear evolution of the secondary components of PDI, introducing enhancement of noise levels well above the thermal levels.

For the asymptotic behavior of SRS, we have found that the final saturation levels are well described by the scaling laws (3.27) and (3.33) derived from simplified PDI theory (3.19), regardless of the many additional nonlinear processes taking part in the SRS evolution. In addition the same scaling predicts a simple proportionality of the Langmuir wave amplitude to the PDI threshold (3.29), and (3.34) with dependence on the intensity and plasma interaction length.

Numerical simulations of our full model (2.57)-(2.61) have shown that in the nonlinear stage of SRS evolution a wide spectrum of plasma fluctuations is excited. The broad fluctuation spectra in the ion density and Langmuir fields result in enhanced levels of Brillouin and forward Raman scattering. Simple reflectivity scaling laws based on the saturation levels of the Langmuir and ion acoustic fluctuations provide good agreement when compared with simulation results. The enhancement of secondary scattering processes can be extended to include the anti-Stokes Raman scattering components. The enhancement of wave numbers corresponding to the anti-Stokes components is more complicated than that of Brillouin or forward Raman scattering. This fact combined with the stable behavior of the anti-Stokes coupling results in a much more turbulent spectrum describing anti-Stokes Raman scattering. A universal scaling law describing the full parameter dependence of

the anti-Stokes reflectivity is thus not possible. We were however able to identify a linear dependence of the anti-Stokes reflectivity on laser intensity and plasma interaction length. This scaling agrees with that derived from a three wave interaction for which a random phase approximation was applied, supporting the observation of a much more turbulent spectrum for the anti-Stokes Raman scattering.

During our investigation we have established criteria necessary for strong enhancement of the secondary processes, and have found limits on the parameter space for which our simulations remain valid. These limits include restrictions on the laser intensity and interaction length of the plasma, which are important parameters in determining the extent of hot electron production. Criteria limiting the amplitude of the Langmuir field and the density fluctuations are provided by the limits imposed of the validity of the Zakharov equations. Within these restrictions our results are still applicable to many current laser plasma interaction experiments. Experiments by Villeneuve et al. [44] and Baldis et al. [88], [89] have provided experimental evidence in support of our model. Our theory also offers plausible explanations for experimental observations of anti-Stokes Raman scattering.

Our theoretical model (2.57)-(2.61), which we have derived in Chap. 2.1, is an extension of the Aldrich et al. model [63], and contains terms describing Brillouin scattering and anti-Stokes Raman scattering. In our study the linear evolution of SRS was well described by the three wave interaction analysis of Chap. 2.2. The numerical simulations of our full model (2.57)-(2.61) in this linear regime compare well with simulations of the three wave model (2.70)-(2.72). Both models have demonstrated linear growth for which the rates are summarized in table 2.2.4. In simulations of our full model, the nonlinear effects always eventually dominated

the evolution of SRS.

The asymptotic reflectivity scaling law of our theory (3.27) partially supports a proposal by Drake and Batha [43] for controlling SRS reflectivity. Drake and Batha suggested that, by designing fusion targets to reduce the PDI threshold one could reduce the SRS reflectivity. Our reflectivity scaling law is directly proportional to the PDI threshold but it is also dependent on the laser intensity and length of the interaction region. The additional possibility of high peaked bursting of SRS reflectivity must also be of some concern if in order to reduce the PDI threshold one reduces the ion damping. Our asymptotic scaling laws are independent of the initial conditions and therefore could be tested using many of the current laser-plasma interaction experiments.

One recent experiment by Villeneuve et al. [44] used Thomson scattering as a diagnostic to analyse the frequency and wave number spectra of the Langmuir modes. The results of this experiment were consistent with our theoretical results of Chap. 3 providing the first direct experimental evidence in support of our theory.

Other ongoing experiments by Batha [105] addressing the question of the saturation of stimulated forward Raman scattering. In this experiment the density and other parameters are such that backwards Raman scattering is very heavily Landau damped ($k_L > 0.4 k_D$) and hence forward Raman is the dominant instability. Batha, in his preliminary analysis of the experimental results, applied the theory of Chap. 3 to describe the forward Raman reflectivity saturation. The plasma interaction length required by our theory to reproduce the observed saturated reflectivity values was considered reasonable and consistent with the physical characteristics of the experiment.

In a recent experiment by Baldis et al. [88], [89] reflectivity levels of Bril-

louin scattering were observed at levels which cannot be explained by a three wave interaction model and the initial thermal fluctuation levels. Although direct experimental evidence of the Langmuir frequency and wave number spectra was not available, the parameter regime of the Baldis et al. experiment is consistent with those regimes in which our model can be applied. Simulations of our full theoretical model were run for parameters typical of the Baldis et al. experiment, producing results in qualitative agreement with the experimental observations.

Although the anti-Stokes coupling is not in itself an instability, the enhanced noise in the Langmuir spectra, produced in our theory by the saturation of SRS, can lead to substantial levels of anti-Stokes Raman scattering. Even though a universal scaling law was not possible we were able to numerically estimate the anti-Stokes Raman reflectivity for parameter regimes consistent with an experiment by Turner et al. [92]. In this experiment Turner et al. observed reflectivity levels of SRS, and both forward Stokes and anti-Stokes Raman scattering. Simulations using the experimental parameters produced results which were in quantitative agreement with the reflectivity levels observed by Turner et al.. The agreement between experiment and simulation in this case suggests that enhancement of noise levels, by the saturation of SRS or other instabilities, is a reasonable candidate to explain the observation of substantial levels of anti-Stokes Raman scattering. The enhanced Langmuir noise of our theory, scattering laser light through the anti-Stokes Raman coupling channels, could also be used to explain the observation of backwards anti-Stokes Raman reflectivity by the experimental groups of Batha et al. [90] and Labaune et al. [91].

In our theoretical description of SRS we have shown that large levels of Langmuir waves can be generated and maintained in the asymptotic stages of SRS

evolution. These enhanced noise levels in the Langmuir spectra were shown in Chap. 5 to be capable of producing large levels of superthermal electrons. Our theoretical model (2.57)-(2.61) does not account for the modification of the electron distribution function produced by the heating of electrons. It is thus necessary for us to estimate for which parameter regimes substantial heating of electrons occurs and limit our simulations to regimes where the modifications are minimal. The parameter regime of our present model could be extended by modifying our phenomenological description of Landau damping to account for superthermal electron production.

There are many other possibilities in which our present analysis of SRS could be extended. For example to maintain the validity of our simulations SBS cannot in general be allowed to grow absolutely. Because our theoretical model does not contain an explicit saturation mechanism for SBS, the parameter regimes examined are restricted to those regimes in which SBS is below absolute threshold. The parameter regime of Fig. 6.8 is a rare exception, illustrating a simulation in which absolute SBS may have saturated at physically realistic values. This possibility should be explored in more detail in order to isolate whether we indeed have SBS saturation or if the evolution is related to some complicated dynamical evolution.

Other forms of limiting SBS growth could come from different sources of ion damping [98], [103]. Furthermore the inclusion of ion nonlinearities in the form of a Boussinesq type density equation may provide a better description than the previous study by Rozmus et al. [94], [95]. In their study a KdV equation was used to describe the ion sound waves. Such a description only allows for the propagation of ion waves in a single direction. This restriction may prohibit the formation of quasimode components which would be present in a more complete

description using a Boussinesq equation allowing for bilateral movement of the ion sound waves. It is also possible that resonant harmonic contributions moving in the opposite direction could adversely affect the resonant matching conditions immensely reducing the saturated reflectivity levels. Finally the affects of two dimensional analysis recently reported in [106] indicates that a two dimensional description may be the only way to properly describe the SBS saturation.

The present analysis can also be expanded in order to provide a more realistic description of an experimental plasma. Of particular relevance is the inclusion of a density gradient in the description of the SRS system. Such a feature is essential to properly model any real plasma experiment because of the inherent presence of density nonuniformities. Apart from producing a more accurate description of the plasma the inclusion of a density gradient would allow for a detailed study of the effects of ion density fluctuations have on the production of SRS near quarter critical. Such a detailed study could lead to many interesting results and further understanding of the Raman gap.

As mentioned previously two dimensional effects should also be investigated in the context of SRS and its saturation. New phenomena such as Raman side scatter and two plasmon decay could be investigated. Two dimensional studies would give rise to more a realistic investigation of the present topics as well. Other possibilities could include the investigation of filamentation [96], [97],[101], or laser hot spots on the development of SRS. Many of these topics are presently being studied both theoretically and experimentally.

Bibliography

[1] L. Tonks, I. Langmuir, Phys. Rev. **33**, 195 (1929).

[2] F. F. Chen, *Introduction to Plasma Physics and Controlled Fusion*, (Plenum press, New York, 1984), Vol. 1

[3] W. L. Kruer, *The Physics of Laser Plasma Interactions*, (Addison-Wesley, New York, 1988).

[4] R. C. Davidson, *Methods in Nonlinear Plasma Theory* (Academic Press, New York, 1972).

[5] V. N. Tsytovich, *Nonlinear Effects in Plasmas* (Plenum Press, New York, 1970).

[6] *Laser-Plasma Interaction*, Les Houches 1980, session XXXIV, R. Balian, and J. Adams editors, (North-Holland , New York, 1982)

[7] A. G. Sitenko, *Fluctuations and Non-linear Wave Interactions in Plasmas*, (Pergamon Press, New York, 1982).

[8] B. B. Kadomtsev, *Plasma Turbulence* (Academic Press, New York, 1965).

[9] S. Ichimaru, *Statistical Plasma Physics*, (Addison-Wesley, New York, 1992).

[10] J. Weiland, H. Wilhelmsson, *Coherent Non-linear Interactions of Waves in Plasmas*, (Pergamon Press, New York, 1977).

[11] A. A. Galeev, R. Z. Sagdeav in *Handbook of Plasma Physics*, A. A. Galeev, R. N. Sudan editors, (North-Holland, New York, 1983) Vol 1 p. 679

[12] A. Bers in *Handbook of Plasma Physics*, A. A. Galeev, R. N. Sudan editors, (North-Holland, New York, 1983) Vol 1 p. 451

[13] K. Mima, K. Nishikawa in *Handbook of Plasma Physics*, A. A. Galeev, R. N. Sudan editors, (North-Holland, New York, 1984) Vol. 2 p. 451

[14] D. R. Nicholson, *Introduction to Plasma Theory*, (John Wiley and Sons, New York, 1983).

[15] D. G. Swanson, *Plasma Waves*, (Academic Press, New York, 1989).

[16] Kent Estabrook, W. L. Kruer, and B. F. Lasinski, Phys. Rev. Lett. **45**, 1399 (1980).

[17] W. Rozmus, W. Tighe, A. A. Offenberger, and Kent Estabrook, Phys. Fluids **28**, 920 (1985).

[18] W. C. Mead, E. M. Campbell, K. G. Estabrook, R. E. Turner, W. L. Kruer, P. H. Y. Lee, B. Pruett, V. C. Rupert, K. G. Tirsell, G. L. Stradling, F. Ze, C. E. Max, M. D. Rosen, and B. F. Lasinski, Phys. Fluids **26**, 2316 (1983).

[19] J. D. Lindl, R. L. McCrory, E. M. Campbell, Phys. Today **45**, 32 (1992).

[20] W. J. Hogan, R. Bangerter, G. L. Kulcinski, Phys. Today **45**, 42 (1992).

[21] J. Delettrez, Can. J. Phys. **64**, 932 (1985).

[22] D. F. DuBois, M. V. Goldman, Phys. Rev. Lett. **14**, 544 (1965).

[23] D. Anderson, H. Wilhelmsson, Physica Scripta **11**, 341 (1974).

[24] L. M. Gorbunov, Sov. Phys. JETP **28**, 1220 (1969).

[25] K. Nishikawa, Journal Phys. Soc. Jap. **24**, 916 (1968).

[26] E. A. Jackson, Phys. Rev. **153**, 235 (1967).

[27] M. Porkolab, R. P. H. Chang, Phys. Fluids **13**, 2054 (1970).

[28] S. P. Kuo, B. R. Cheo, Phys. Fluids **21**, 1753 (1978).

[29] T. W. Johnston, 'Challenges to our understanding of the scattering instabilities of laser fusion',*Inertial Confinement Fusion*, K. Brueckner editor, (1992)

[30] M. S. Sodha, R. P. Sharma, and S. C. Kaushik, J. Appl. Phys. **47**, 3518 (1976).

[31] E. Hiob, A. J. Barnard, Phys. Fluids **26**, 3119 (1983).

[32] D. W. Forslund, J. M. Kindel, E. L. Lindman, Phys. Fluids **18**, 1002 (1975).

[33] D. W. Forslund, J. M. Kindel, E. L. Lindman, Phys. Fluids **18**, 1017 (1975).

[34] J. F. Drake, P. K. Kaw, Y. C. Lee, G. Schmidt, C. S. Liu, M. N. Rosenbluth, Phys. Fluids **17**, 778 (1974).

[35] C. Yamanaka, T. Yamanaka, T. Sasaki, and J. Mizui, Phys. Rev. Lett. **32**, 1038 (1974).

[36] B. H. Ripin, J. M. McMahon, E. A. McLean, W. M. Manheimer, and J. A. Stamper, Phys. Rev. Lett. **33**, 634 (1974).

[37] N. H. Burnett, H. A. Baldis, G. D. Enright, M. C. Richardson, P. B. Corkum, J. App. Phys. **48**, 3727 (1977).

[38] R. G. Watt, R. D. Brooks, Z. A. Pietrzyk, Phys. Rev. Lett. **41**, 170 (1978).

[39] R. P. Drake, R. E. Turner, B. F. Lasinski, E. A. Williams, D. W. Phillion, K. G. Estabrook, W. L. Kruer, E. M. Campbell, K. R. Manes, J. S. Hildum, T. W. Johnston, Phys. Fluids **31**, 3130 (1988).

[40] C. B. Darrow, R. P. Drake, D. S. Montgomery, P. E. Young, K. Estabrook, W. L. Kruer, T. W. Johnston, Phys. Fluids B **3**, 1473 (1991).

[41] W. Seka, R. E. Bahr, R. W. Short, A. Simon, R. S. Craxton, D. S. Montgomery, A. E. Rubenchik, Phys. Fluids B **4**, 2232 (1992).

[42] P. E. Young, R. L. Berger, K. G. Estabrook, Phys. Fluids B **4**, 2605 (1992).

[43] R. P. Drake, S. H. Batha, Phys. Fluids B **3**, 2936 (1991).

[44] D. M. Villeneuve, K. Baker, R. P. Drake, B. Sleaford, B. La Fontaine, K. Estabrook, Phys. Rev. Lett. **71**, 368 (1993).

[45] D. M. Villeneuve, H. A. Baldis, Phys. Fluids **31**, 1790 (1988).

[46] C. J. Walsh, D. M. Villeneuve, H. A. Baldis, Phys. Rev. Lett. **53**, 1445 (1984); D. M. Villeneuve, H. A. Baldis, J. E. Bernard, Phys. Rev. Lett. **59**, 1585 (1987).

[47] H. A. Baldis, P. E. Young R. P. Drake, W. L. Kruer, K. Estabrook, E. A. Williams, T. W. Johnston, Phys. Rev. Lett. **62**, 2829 (1989).

[48] H. A. Baldis, D. M. Villeneuve, C. Labaune, D. Pesme, W. Rozmus, W. L. Kruer, P. E. Young, Phys. Fluids B **3**, 2341 (1991).

[49] H. A. Rose, D. F. DuBois, B. Bezzerides, Phys. Rev. Lett. **58**, 2547 (1987).

[50] V. E. Zakharov, Sov. Phys. JETP **35**, 908 (1972).

[51] S. G. Thornhill and D. ter Haar, Phys. Reps. **43**, 43 (1978).

[52] M. V. Goldman, Rev. Mod. Phys. **56**, 709 (1984).

[53] D. Russell, D. F. DuBois, H. A. Rose, Phys. Rev. Lett. **56**, 838 (1986).

[54] G. D. Doolen, D. F. DuBois, H. A. Rose, Phys. Rev. Lett. **54**, 804 (1985).

[55] W. L. Kruer, E. J. Valeo, Phys. Fluids **16**, 675 (1973).

[56] P. K. Kaw, A. T. Lin, J. M. Dawson, Phys. Fluids **16**, 1967 (1973).

[57] A. A. Vedenov and L. I. Rudakov, Sov., Phys. Doklady **9**, 1073 (1965).

[58] R. Pellat in *Laser-Plasma Interaction*, Les Houches 1980, session XXXIV, R. Balian, and J. Adams editors, (North-Holland , New York, 1982) p. 415

[59] D. F. DuBois, and H. A. Rose, *Nonlinear and Chaotic Phenomena in Plasmas, Solids and Fluids*, W. Rozmus, J. A. Tuszynski editors, (World scientific, Singapore, 1991), p. 266

[60] D. F. DuBois, H. A. Rose, D. Russell, Phys. Rev. Lett. **66**, 1970 (1991).

[61] P. A. Robinson, D. L. Newman, and A. M. Rubenchik, Phys. Fluids B **4**, 2510 (1992).

[62] L. M. Degtyarev, R. Z. Sagdeev, G. I. Solov'ev, V. D. Shapiro, and V. I. Shevchenko, Sov. J. Plasma Phys. **6**, 263 (1980).

[63] C. H. Aldrich, B. Bezzerides, D. F. DuBois, and H. A. Rose, Comments Plasma Phys. Controlled Fusion **10**, 1 (1986).

[64] W. Rozmus, R. P. Sharma, J. C. Samson, W. Tighe, Phys. Fluids **30**, 2181 (1987).

[65] B. Bezzerides, D. F. DuBois, H. A. Rose, Phys. Rev. Lett. **70**, 2569 (1993).

[66] O. Willi, D. Bassetti, A. Giuletti, and S. J. Karttunen, Opt. Commun. **70**, 487 (1989).

[67] T. Kolber, W. Rozmus, V. T. Tikhonchuk, Phys. Fluids B **5**, 183 (1993).

[68] T. Kolber, W. Rozmus, V. T. Tikhonchuk, Ph. Mounaix and D. Pesme, Phys. Rev. Lett. **70**, 1810 (1993).

[69] T. Kolber, W. Rozmus, V. T. Tikhonchuk, H. A. Baldis, K. Estabrook, Proc. SPIE (1993) in press.

[70] W. H. Press, S. A. Teukolsky, W. T. Vetterling, B. P. Flannery, *Numerical Recipes* (Cambridge University Press, New York, 1986).

[71] C. Oberman, and G. Auer, Phys. Fluids **17**, 1980 (1974).

[72] R. L. Berger, E. A. Williams, A. Simon , Phys. Fluids B **1**, 414 (1989).

[73] M. M. Kroll, J. Appl. Phys. **36**, 34 (1965).

[74] T. W. Johnston, G. R. Mitchel, and H. Pepin, Phys. Fluids **25**, 179 (1982).

[75] Ph. Mounaix, D. Pesme, W. Rozmus, M. Casanova, Phys. Fluids B **5**, 3304 (1993).

[76] V. P. Silin and V. T. Tikhonchuk, Phys. Rep. **135**, 1 (1986).

[77] S. J. Karttunen, Phys. Rev. A **23**, 2006 (1981).

[78] J. A. Heikkinen, S. J. Karttunen, Phys. Fluids **29**, 1291 (1986).

[79] K. Estabrook, W. L. Kruer, M. G. Haines, Phys. Fluids B **1**, 1282 (1989).

[80] Kent Estabrook, W. L. Kruer, Phys. Fluids **26**, 1892 (1983).

[81] G. Bonnaud, D. Pesme, R. Pellat, Phys. Fluids B **2**, 1618 (1990).

[82] G. Bonnaud, Laser and Particle Beams **5**, 101 (1987).

[83] G. Bonnaud, D. Pesme, *Laser Interactions and Related Plasma Phenomena*, H. Hora, G. H. Miley editors (Plenum Press, New York, 1988).

[84] R. P. Drake, Comments Plasma Phys. Controlled Fusion **12**, 181 (1989).

[85] R. E. Turner, Kent Estabrook, R. L. Kauffman, D. R. Bach, R. P. Drake, D. W. Phillion, B. F. Lansinski, E. M. Campbell, W. L. Kruer, and E. A. Williams, Phys. Rev. Lett. **54**, 189 (1985).

[86] R. P. Drake, E. A. Williams, P. E. Young, K. Estabrook, W. L. Kruer, D. S. Montgomery, H. A. Baldis, T. W. Johnston, Phys. Fluids B **1**, 2217 (1989).

[87] R. P. Drake, E. A. Williams, P. E. Young, K. Estabrook, W. L. Kruer, D. S. Montgomery, H. A. Baldis, T. W. Johnston, Phys. Rev. A **39**, 3536 (1989).

[88] H. A. Baldis, H. C. Barr, D. M. Villeneuve, G. D. Enright, C. Labaune, and S. Baton, Proc. SPIE **1229**, 144 (1990).

[89] H. A. Baldis, D. M. Villeneuve, B. La Fontaine, G. D. Enright, C. Labaune, S. Baton, P. Mounaix, D. Pesme, M. Casanova, W. Rozmus, Phys. Fluids B **5**, 3319 (1993).

[90] S. H. Batha, D. D. Meyerhofer, A. Simon, R. P. Drake, Phys. Fluids B **3**, 448 (1991).

[91] C. Labaune, H. A. Baldis, S. D. Baton, D. Pesme, and T. Jalinaud, Phys. Rev. Lett. **69**, 285 (1992).

[92] R. E. Turner, Kent Estabrook, R. P. Drake, E. A. Williams, H. N. Kornblum, W. L. Kruer, and E. M. Campbell, Phys. Rev. Lett. **57**, 1725 (1986).

[93] J. D. Moody, H. A. Baldis, D. S. Montgomery, C. Labaune, R. L. Berger, S. Dixit, K. Estabrook, W. L. Kruer, and E. A. Williams, APS Bulletin **37**, 1441 (1992).

[94] W. Rozmus, M. Casanova, D. Pesme, A. Heron, J-C. Adam, Phys. Fluids B **4**, 576 (1992).

[95] J. Candy, W. Rozmus, V. T. Tikhonchuk, Phys. Rev. Lett. **65**, 1889 (1990).

[96] C. S. Liu, V. K. Tripathi, Phys. Fluids **29**, 4188 (1986).

[97] H. C. Barr, T. J. M. Boyd, G. A. Coutts, Phys. Fluids **31**, 641 (1988).

[98] C. J. Randall, Phys. Fluids **25**, 2231 (1982).

[99] S. H. Batha, R. Bahr, L. M. Goldman, W. Seka, and A. Simon, Phys. Fluids **31**, 3667 (1988).

[100] C. Labaune, H. A. Baldis, E. Fabre, F. Briand, D. M. Villeneuve, and K. Estabrook, Phys. Fluids B **2**, 166 (1990).

[101] T. Afshar-rad, S. E. Ceo, O. Willi, and M. Desselberger, Phys. Fluids B **4**, 1017 (1992).

[102] D. Umstadter, W. B. Mori, C. Joshi, Phys. Fluids B **1**, 1017 (1989).

[103] E. M. Epperlein, R. W. Short, A. Simon, Phys. Rev. Lett. **69**, 1765 (1992).

[104] H. Figueroa, C. Joshi, and C. E. Clayton, Phys. Fluids **30**, 586 (1987).

[105] S. Batha, K. S. Bradley, R. P. Drake, Kent Estabrook, W. L. Kruer, D. S. Montegomery, and B. A. Remington, *Intensity scaling and saturation of stimulated Raman forward scattering* Preprint (1993).

[106] M. R. Amin, C. E. Capjack, P. Frycz, W. Rozmus, V. T. Tikhonchuk, Phys. Rev. Lett. **71**, 81 (1993). M. R. Amin, C. E. Capjack, P. Frycz, W. Rozmus, V. T. Tikhonchuk, "Two dimensional studies of stimulated Brillouin scattering, filamintation and self-focussing instabilities of laser light in plasmas", In press Phys. Fluids B (1993).

[107] *Handbook of Mathematical Functions*, M. Abramowtiz, I. A. Stegun editors, (Dover publications, New York, 1972)

.1 Thermal noise levels

In order to model a realistic plasma thermal noise sources, corresponding to the fluctuations produced by particle discreteness, must be accounted for [71], [72]. We assume a priori that these fluctuations will only affect the linear evolution of the plasma, and their influence will be negligible once nonlinear effects become important. The object of including noise source terms is, in the absence of nonlinear contributions, to model a plasma in thermal equilibrium.

In a three dimensional infinite plasma the spectral distribution of the electric field fluctuations is given by (cf. Ref. [7] Eq. 6.88)

$$\langle E^2 \rangle_{\vec{k},\omega} \quad = \left(\frac{4\pi e}{k}\right)^2 \frac{\langle \delta n_e^2 \rangle^0_{\vec{k},\omega} + \langle \delta n_i^2 \rangle^0_{\vec{k},\omega}}{\mid \epsilon(\vec{k},\omega) \mid^2} \tag{.1}$$

where

$$\langle \delta n_e^2 \rangle^0_{\vec{k},\omega} = 2\pi \int d\vec{v} f_{0\alpha}(\vec{v}) \delta(\omega - \vec{k} \cdot \vec{v}) = \frac{\sqrt{2\pi} n_0^\alpha}{k v_{T_\alpha}} \exp[-\frac{m_\alpha \vec{v}^2}{2T_\alpha}] \tag{.2}$$

is the spectral distribution of particle fluctuations in the absence of Coulomb interaction, and where we used a Maxwellian distribution $f_{0\alpha}(\vec{v})$ for the electron $\alpha = e$ and ion $\alpha = i$ species. Here

$$\epsilon = 1 + \chi_e + \chi_i \tag{.3}$$

is the longitudinal dielectric permittivity, and

$$\chi_\alpha = \frac{\omega_\alpha^2}{k^2} \int d\vec{v} \frac{1}{\omega - \vec{k} \cdot \vec{v}} \vec{k} \cdot \frac{\partial f_{0\alpha}}{\partial \vec{v}} \tag{.4}$$

are the partial components of the linear plasma susceptibility. By expanding ϵ around the solution ω, k to produce

$$\epsilon(\vec{k},\omega) = \epsilon_1(\vec{k},\omega) \mid_{\vec{k},\omega_{\vec{k}}} + \frac{\partial \epsilon_1(\vec{k},\omega)}{\partial \omega} \mid_{\vec{k},\omega_{\vec{k}}} (\omega - \omega_{\vec{k}}) + i\epsilon_2(\vec{k},\omega) \mid_{\vec{k},\omega_{\vec{k}}} \simeq 0 \qquad (.5)$$

where $\omega_{\vec{k}} \simeq \omega - i\gamma_L(\vec{k})$ and using the identity

$$\lim_{\eta \to 0} \frac{\eta}{x^2 + \eta^2} = \pi\delta(x) \qquad (.6)$$

one finds

$$\frac{1}{\mid \epsilon(\vec{k},\omega) \mid^2} = \frac{\pi\delta(\omega - \omega_{\vec{k}})}{\mid \partial\epsilon_1(\vec{k},\omega)/\partial\omega \mid^2_{\vec{k},\omega_{\vec{k}}} \gamma_L(\vec{k})} \qquad (.7)$$

In the high frequency $\mid \omega \mid \gg v_{T_e} k$ long wavelength limit $k_D \gg k$ one can easily show (cf. Ref. [9])

$$\begin{aligned} \epsilon(k,\omega) &= 1 + \frac{k_D^2}{k^2}\left(-\frac{k^2 v_{T_e}^2}{\omega^2} - \frac{3k^4 v_{T_e}^4}{\omega^4}\right) + \frac{k_{D_i}^2}{k^2}\left(-\frac{k^2 v_{T_i}^2}{\omega^2} - \frac{3k^4 v_{T_i}^4}{\omega^4}\right) \\ &+ i\sqrt{\frac{\pi}{2}}\left(\frac{k_D^3}{k^3}\frac{\omega}{\omega_{p_e}} \exp\left[-\frac{\omega^2}{2k^2 v_{T_e}^2}\right] + \frac{k_{D_i}^3}{k^3}\frac{\omega}{\omega_{p_i}} \exp\left[-\frac{\omega^2}{2k^2 v_{T_i}^2}\right]\right) = 0 \qquad (.8) \end{aligned}$$

which can be used to find

$$\frac{\partial \epsilon_1}{\partial \omega} \simeq \frac{2\omega_p^2}{\omega^3} + \frac{12\omega_p^2 v_{T_e}^2 k^2}{\omega^5} \simeq \frac{2}{\omega_p} \qquad (.9)$$

and

$$\gamma_L(k) = \sqrt{\frac{\pi}{8}}\omega_p \frac{k_D^3}{k^3} \exp[-\frac{1}{2}(3 + \frac{k_D^2}{k^2})] \qquad (.10)$$

Equation (.1) can be written in the general form

$$
\begin{aligned}
\langle E_{\vec{k}}(\omega)E'_{\vec{k}}(\omega')\rangle &= \langle E^2\rangle_{\vec{k},\omega}(2\pi)^3\delta(\vec{k}+\vec{k}')\delta(\omega+\omega') \\
&= \frac{(4\pi e)^2}{\vec{k}\vec{k}'}n_0^e\frac{k^2}{k_D^2}\frac{\pi}{2}\sum_\beta \delta(\omega-\omega_{\vec{k}}^\beta)(2\pi)^3\delta(\vec{k}+\vec{k}')\delta(\omega+\omega') \quad (.11)
\end{aligned}
$$

Here the sum over β takes into account both possible solutions of $\omega_{\vec{k}}$. Inverting the transforms gives

$$
\begin{aligned}
&\int d\omega d\omega' \int \frac{d\vec{k}}{(2\pi)^3}\frac{d\vec{k}'}{(2\pi)^3}\exp[i\vec{k}\cdot\vec{x}+i\vec{k}'\cdot\vec{x}'-i\omega t-i\omega' t']\langle E_{\vec{k}}(\omega)E'_{\vec{k}}(\omega')\rangle \\
&\qquad = \int d\omega \int \frac{d\vec{k}}{(2\pi)^3}\exp[i\vec{k}\cdot(\vec{x}-\vec{x}')-i\omega(t-t')]\langle E^2\rangle_{\vec{k},\omega} \quad (.12)
\end{aligned}
$$

Using

$$
\int d\vec{k} = \int_0^\infty dk k^2 \int d\Omega \quad (.13)
$$

and looking the projection onto a finite one dimensional system we have

$$
\int_0^\infty dk \to \frac{2\pi}{2L}\sum_k; \quad \int d\Omega \to \Delta\Omega \quad (.14)
$$

allowing us to approximate (.12) as

$$
\langle E(x,t)E(x',t')\rangle = \frac{\Delta\Omega}{2(2\pi)^2 L}(4\pi e)^2 n_0^e \sum_k \frac{k^2}{k_D^2}\exp[ik(x-x')-i\omega_k(t-t')] \quad (.15)
$$

In our full model (2.57)-(2.61) we have enveloped the Langmuir fields over the high frequency ω_p, thus $\omega_k = \frac{3}{2}v_{T_e}^2 k^2/\Omega_p$. The argument of the exponential in (.15) can be rewritten as

$$ikx - i\omega_k t + i\phi_k \tag{.16}$$

where ϕ_k is a random phase constant for each k, allowing us to write

$$E_{in} = \langle E(x,t)E(x',t')\rangle^{1/2} \simeq \left(\frac{\Delta\Omega}{2(2\pi)^2 L k_D^2}(4\pi e)^2 n_0^e\right)^{1/2} \tag{.17}$$
$$\times \sum_k k\alpha_k \cos[ikx - i\omega_k t + \phi_k] + i\beta_k \sin[ikx - i\omega_k t + \phi_k]$$

where α_k, and β_k are random amplitudes between 0 and 1.

In our full model (2.57)-(2.61) the enveloped equations of the high frequency Langmuir waves in the absence of nonlinear terms is given by

$$i(\frac{\partial E}{\partial t} + \gamma_L * E) + \frac{3}{2}\frac{v_{T_e}^2}{\omega_p}\frac{\partial^2 E}{\partial x^2} = S_L(x,t) \tag{.18}$$

By finding analytically a solution E_{in} for the inhomogeneous equation, we can then construct a full solution by adding, at each timestep, E_{in} to the linear homogeneous (and eventually the nonlinear) solution found from solving the full system of equations. When the system is dominated by the nonlinear evolution we continue to add E_{in} to the numerical solution to maintain a realistic conversion of the Langmuir wave energy into thermal energy through Landau damping.

A similar method can be applied to obtain the thermal noise levels for the ion density. Using the spectral distribution for the ion density fluctuations given by (cf. Ref. [7] Eq. 6.84)

$$\langle \delta n_i^2\rangle_{\vec{k},\omega} = \frac{(1+\chi_e)\langle \delta n_i^2\rangle^0_{\vec{k},\omega} + \chi_i\langle \delta n_e^2\rangle^0_{\vec{k},\omega}}{\mid \epsilon(\vec{k},\omega)\mid^2} \tag{.19}$$

using equations (.5), (.6), and (.7) with $\omega_{\vec{k}} = \omega - i\gamma_A(\vec{k})$

$$\frac{1}{\mid \epsilon(\vec{k},\omega)\mid^2} = \frac{\pi\delta(\omega-\omega_{\vec{k}})}{\mid \partial\epsilon_1(\vec{k},\omega)/\partial\omega \mid^2_{\vec{k},\omega_{\vec{k}}} \gamma_A(\vec{k})} \qquad (.20)$$

In the intermediate frequency regime where $v_{T_e}k \gg \mid \omega \mid \gg v_{T_i}k$ for the long wavelength limit $k_D \gg k$ one can easily show (cf. Ref. [9])

$$\epsilon(k,\omega) = 1 + \frac{k_D^2}{k^2} + \frac{k_{D_i}^2}{k^2}\left(-\frac{k^2 v_{T_i}^2}{\omega^2} - \frac{3k^4 v_{T_i}^4}{\omega^4}\right)$$
$$+i\sqrt{\frac{\pi}{2}}\left(\frac{k_D^3}{k^3}\frac{\omega}{\omega_{p_e}}\exp\left[-\frac{\omega^2}{2k^2v_{T_e}^2}\right] + \frac{k_{D_i}^3}{k^3}\frac{\omega}{\omega_{p_i}}\exp\left[-\frac{\omega^2}{2k^2v_{T_i}^2}\right]\right) = 0 \qquad (.21)$$

for the low frequency ion contribution. Repeating the same procedure for ion acoustic wave frequencies with

$$\frac{\partial\epsilon_1}{\partial\omega} \simeq \frac{2\omega_{p_i}^2}{\omega^3}\left(1 + \frac{6k^2v_{T_i}^2}{\omega^2}\right) \qquad (.22)$$

and

$$\gamma_A(k) = \sqrt{\frac{\pi}{8}}c_s k\left(\sqrt{\frac{Zm_e}{m_i}} + \left(\frac{ZT_e}{T_i}\right)^{3/2}\exp[-(\frac{3}{2}+\frac{ZT_e}{2T_i})]\right), \qquad (.23)$$

one arrives at

$$\langle\delta n^2\rangle^i_{\vec{k},\omega} = n_0^e\pi\delta(\omega-\omega_{\vec{k}})\frac{1+Zv_{T_e}Q/v_{T_i}}{1+ZT_e v_{T_e}Q/T_i v_{T_i}} \qquad (.24)$$

where $Q = \exp[-3/2 - ZT_e/2T_i]$, and we have used $ZT_e/T_i \gg 1$ so that

$$\frac{1+3T_i/ZT_e}{1+9T_i/ZT_e} \simeq 1 \qquad (.25)$$

Inverting the transforms, taking the one dimensional projection and using $\omega_k = \pm c_s k$ gives

$$
\begin{aligned}
&\langle \delta n^i(x,t)\delta n^{i*}(x',t')\rangle \frac{1}{n_0^{i2}} = \qquad (.26)\\
&\frac{\Delta\Omega}{2L(2\pi)^2 n_0^e}\frac{1 + Z v_{T_e} Q/v_{T_i}}{1 + Z T_e v_{T_e} Q/T_i v_{T_i}} \sum_k k^2 \exp[ik(x-x') - i\omega_k(t-t')]
\end{aligned}
$$

Once again the argument of the exponential can be written in the form of expression (.16) and

$$
\begin{aligned}
N_{in} &= \left(\langle \delta n^i(x,t)\delta n^{i*}(x',t')\rangle \frac{1}{n_0^{i2}}\right)^{1/2} \simeq \left(\frac{\Delta\Omega}{2L(2\pi)^2 n_0^e}\frac{1 + Z v_{T_e} Q/v_{T_i}}{1 + Z T_e v_{T_e} Q/T_i v_{T_i}}\right)^{1/2}\\
&\times \sum_k k\alpha_k \cos[ikx - i\omega_k t + \phi_k] + i\beta_k \sin[ikx - i\omega_k t + \phi_k] \qquad (.27)
\end{aligned}
$$

Here again ϕ_k is random phase constant for each k, and α_k, and β_k are random amplitudes between 0 and 1.

Numerically these source terms are achieved by adding stochastic amplitudes of width $(\Gamma_{SRS}/V_L)(L/2\pi)$ in Fourier space in the vicinity of the resonantly driven SRS Langmuir mode and the first PDI daughter components in the Langmuir. The ion density equation is split into two first order time equations to which the stochastic amplitudes are added separately.

.2 Partial/ordinary differential equation solver algorithm

.2.1 System of equations

In this investigation each of the systems of differential equations was solve numerically using the same basic algorithm. The core of this algorithm was designed to accommodate an arbitrary number (NE) of nonlinear partial and ordinary differential equations for an initial value problem with nonperiodic boundary conditions. It is assumed that the equations can be written in a form such that the derivatives are first order in time and up to second order in space, ie.

$$\sigma^i \partial_t u^i = f^i \left(\{u^i\}, \{\frac{\partial u^i}{\partial x}\}, \{\frac{\partial^2 u^i}{\partial x^2}\} \right) \quad (i = 1, \ldots, NE) \tag{.28}$$

Here $\sigma^i = 0$ for an ordinary differential equation and $\sigma^i = 1$ for a partial differential equation,u^i represents the variables and f^i is the spatial components of the differential equations. For example Burgers equation would be written as

$$\frac{\partial u^i}{\partial t} = \eta \frac{\partial^2 u^i}{\partial x^2} - u^i \frac{\partial u^i}{\partial x} = f^i \left(\{u^i\}, \{\frac{\partial u^i}{\partial x}\}, \{\frac{\partial^2 u^i}{\partial x^2}\} \right) \quad (i = 1) \tag{.29}$$

The system is assumed to exist in a finite one dimensional region $x \in [a, b]$, with similar equations to (.28) which hold on the boundaries $x = a$ and $x = b$. In order to solve (.28) numerically the spatial and temporal domains are discretized according to

$$\{x_1, \ldots, x_{NP}\}; \quad \{t^0, \ldots, t^m, \ldots\} \tag{.30}$$

such that $\Delta t = t^{m+1} - t^m$ and $\Delta x = x_{k+1} - x_k$. The temporal derivative is represented by a two point forward difference approximation while the spatial derivatives

are found using a five point centered difference approximation. The discrete system is thus represented by $NP \times NE$ equations which connect the m and $m+1$ time points:

$$\sigma_k^i[\frac{u_k^{i,m+1} - u_k^{i,m}}{\Delta t}] = \frac{f_k^{i,m+1} + f_k^{i,m}}{2} \tag{.31}$$

where $(i = 1, \ldots, NE)$, NE is the number of equations and $(k = 1, \ldots, NP)$, where NP is the number of spatial grid points.

In (.31), the spatial derivatives have been replaced by the difference approximations shown in appendix .2.3. This ensures that the algorithm is accurate to 4^{th} order in the interior $\{x_3, \ldots, x_{NP-2}\}$ and to 2^{nd} order at the boundaries $\{x_1, x_2\}$ and $\{x_{NP-1}, x_{NP}\}$. Furthermore, the differencing (.31) is accurate to 2^{nd} order in time. It should be realized, however, that the user must *explicitly* replace all of the f^i's by their difference approximations f_k^i. After doing so, one is left with $NP \times NE$ algebraic equations in $NP \times NE$ variables $\{u_k^{i,m+1}\}$; as we assume that the numbers $\{u_k^{i,m}\}$ are known. A natural way to rewrite (.31) is

$$f_k^{i,m+1} - [\sigma_k^i[\frac{u_k^{i,m+1} - u_k^{i,m}}{h}] - f_k^{i,m}] \equiv g_k^i(\{u_k^{i,m+1}\}) = 0 \tag{.32}$$

where $h = \Delta t/2$. Thus, in what follows, we can suppress the time superscripts on $u_k^{i,m+1}$, and simply write u_k^i. Similarly we can write $u_k^{i,m}$ as u_{0k}^i.

We assume that the variation of u_k^i in time is sufficiently small so that we may write

$$u_k^i = u_{0k}^i + \epsilon_k^i + O(\epsilon_k^{(i)^2}) \tag{.33}$$

where ϵ_k^i is a small correction. Expanding (.32) to first order around the solution set $\{u_k^i\}$ we have

$$g_k^i(\{u_{0k}^i\}) + \sum_{i=1}^{NE}\sum_{k=1}^{NP} \mathcal{J}_k^{(i)}(\{u_{0k}^i\})\epsilon_k^i = O(\epsilon_k^{(i)^3}) \tag{.34}$$

where the elements of the Jacobian matrix $\vec{\mathbf{J}}$ are given by

$$\mathcal{J}_k^{(i)}(\{u_{0k}^i\}) \equiv \frac{\partial g_k^i(\{u_k^i\})}{\partial u_k^i}, \tag{.35}$$

Here we use boldface vector quantities to designate matrices. In matrix form (.34) can be written

$$\vec{\mathbf{G}} = -\vec{\mathbf{J}} \cdot \vec{\mathbf{E}} \tag{.36}$$

where $\vec{\mathbf{E}} \equiv (\epsilon_k^{(1)}, ...\epsilon_k^{(NE)})^T = \vec{\mathbf{u}} - \vec{\mathbf{u}}_0$ and $\vec{\mathbf{G}} \equiv (g_k^{(1)}, ...g_k^{(NE)})^T$. This makes it clear that $\vec{\mathbf{J}}$ should be an NPxNP block matrix of NExNE blocks. By inverting $\vec{\mathbf{J}}$ one can thus calculate a closer approximation for $\vec{\mathbf{u}}$ by using

$$\vec{\mathbf{u}} = \vec{\mathbf{u}}_0 - \vec{\mathbf{J}}^{-1} \cdot \vec{\mathbf{G}} \tag{.37}$$

The new value of $\vec{\mathbf{u}}$ then replaces the old approximation $\vec{\mathbf{u}}_0$ and the procedure is iterated to obtain the desired accuracy. Once the desired accuracy is obtained the time is increased by one timestep Δt and the entire procedure is repeated. The whole process is illustrated in diagrammatic form in Fig. .1

To invert the matrix $\vec{\mathbf{J}}$ we must invert a band matrix consisting of five elements by NP elements where each element is itself an $NE \times NE$ matrix. $\vec{\mathbf{J}}$ has the explicit form

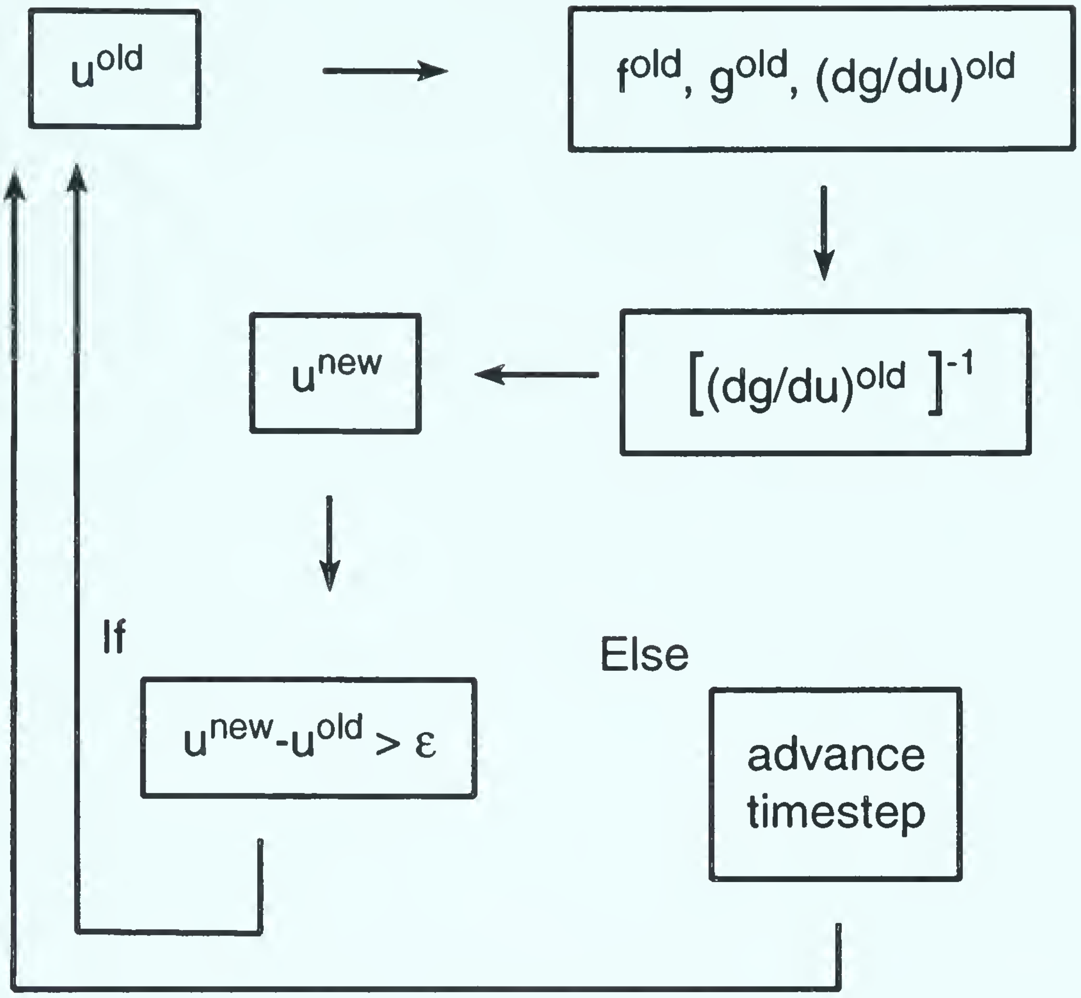
u^old
f^old, g^old, (dg/du)^old
[(dg/du)^old]^-1
u^new
If
Else
u^new-u^old > ε
advance timestep

Figure .1: *Schematic diagram of numerical solver program.*

$$\vec{\mathbf{J}} = \begin{bmatrix}
c_1 & d_1 & e_1 & a_1 & b_1 & 0 & 0 & \ldots\ldots & 0 \\
b_2 & c_2 & d_2 & e_2 & a_2 & 0 & 0 & \ldots\ldots & 0 \\
a_3 & b_3 & c_3 & d_3 & e_3 & 0 & 0 & \ldots\ldots & 0 \\
0 & a_4 & b_4 & c_4 & d_4 & e_4 & 0 & \ldots\ldots & 0 \\
0 & 0 & a_5 & b_5 & c_5 & d_5 & e_5 & \ldots\ldots & 0 \\
0 & . & . & . & . & . & . & . & 0 \\
0 & . & . & . & . & . & . & . & 0 \\
0 & 0 & \ldots\ldots & a_{NP-3} & b_{NP-3} & c_{NP-3} & d_{NP-3} & e_{NP-3} & 0 \\
0 & 0 & \ldots\ldots & 0 & a_{NP-2} & b_{NP-2} & c_{NP-2} & d_{NP-2} & e_{NP-2} \\
0 & 0 & \ldots\ldots & 0 & e_{NP-1} & a_{NP-1} & b_{NP-1} & c_{NP-1} & d_{NP-1} \\
0 & 0 & \ldots\ldots & 0 & d_{NP} & e_{NP} & a_{NP} & b_{NP} & c_{NP}
\end{bmatrix}$$

where each element of NE×NE block matrix form is defined by:

$$\begin{array}{ll}
(a_{i,j})_1 = \frac{\partial f_1^i}{\partial u_4^j}; \quad (b_{i,j})_1 = \frac{\partial f_1^i}{\partial u_5^j} & k = 1 \\
(a_{i,j})_2 = \frac{\partial f_2^i}{\partial u_5^j} & k = 2 \\
\left[\begin{array}{lll} (a_{i,j})_k = \frac{\partial f_k^i}{\partial u_{k-2}^j}; & (b_{i,j})_k = \frac{\partial f_k^i}{\partial u_{k-1}^j}; & (c_{i,j})_k = \frac{\partial f_k^i}{\partial u_k^j} \\ (d_{i,j})_k = \frac{\partial f_k^i}{\partial u_{k+1}^j}; & (e_{i,j})_k = \frac{\partial f_k^i}{\partial u_{k+2}^j} & \end{array} \right] & k = 3, NP-2 \\
(e_{i,j})_{NP-1} = \frac{\partial f_{NP-1}^i}{\partial u_{NP-4}^j} & k = NP-1 \\
(e_{i,j})_{NP} = \frac{\partial f_{NP}^i}{\partial u_{NP-3}^j}; \quad (d_{i,j})_{NP} = \frac{\partial f_{NP}^i}{\partial u_{NP-4}^j} & k = NP
\end{array}$$

The reader must realize that f_2^i and f_{NP-1}^i are differenced using 4 or 5 point unsymmetric formulas. f_1^i and f_{NP}^i are defined using boundary equations as well as unsymmetric differences.

In order to manipulate the matrix elements we must maintain matrix arithmetic. To invert $\vec{\mathbf{J}}$ we use a generalized form of the upper-lower triangular decomposition or LUD matrix inversion algorithm. This generalized form is summarized in the next section.

.2.2 Inversion algorithm

The matrix $\vec{\mathbf{J}}$ can, in general, be factored into the product of a lower triangular matrix $\vec{\mathbf{L}}$ and an upper triangular matrix, $\vec{\mathbf{U}}$ according to

$$\vec{\mathbf{J}} = \vec{\mathbf{L}}\vec{\mathbf{U}} \tag{.38}$$

where $\vec{\mathbf{L}}$ and $\vec{\mathbf{U}}$ have the form

$$\vec{\mathbf{L}} = \begin{bmatrix}
\gamma_1 & 0 & 0 & 0 & 0 & 0 & 0 & \ldots\ldots & 0 \\
\beta_2 & \gamma_2 & 0 & 0 & 0 & 0 & 0 & \ldots\ldots & 0 \\
\alpha_3 & \beta_3 & \gamma_3 & 0 & 0 & 0 & 0 & \ldots\ldots & 0 \\
0 & . & . & . & . & . & . & . & 0 \\
0 & . & . & . & . & . & . & . & 0 \\
0 & 0 & \ldots\ldots & 0 & \alpha_{NP-2} & \beta_{NP-2} & \gamma_{NP-2} & 0 & 0 \\
0 & 0 & \ldots\ldots & 0 & \epsilon_{NP-1} & \alpha_{NP-1} & \beta_{NP-1} & \gamma_{NP-1} & 0 \\
0 & 0 & \ldots\ldots & 0 & \delta_{NP} & \epsilon_{NP} & \alpha_{NP} & \beta_{NP} & \gamma_{NP}
\end{bmatrix}$$

and

$$\vec{\mathbf{U}} = \left[\begin{array}{ccccccccc} 1 & \delta_1 & \epsilon_1 & \alpha_1 & \beta_1 & 0 & 0 & \ldots\ldots & 0 \\ 0 & 1 & \delta_2 & \epsilon_2 & \alpha_2 & 0 & 0 & \ldots\ldots & 0 \\ 0 & 0 & 1 & \delta_3 & \epsilon_3 & 0 & 0 & \ldots\ldots & 0 \\ 0 & . & . & . & . & . & . & . & 0 \\ 0 & . & . & . & . & . & . & . & 0 \\ 0 & 0 & 0 & 0 & \ldots\ldots & 0 & 1 & \delta_{NP-2} & \epsilon_{NP-2} \\ 0 & 0 & 0 & 0 & 0 & \ldots\ldots & 0 & 1 & \delta_{NP-1} \\ 0 & 0 & 0 & 0 & 0 & 0 & \ldots\ldots & 0 & 1 \end{array} \right]$$

For $NP > 7$, the matrices $\alpha_k, ..., \epsilon_k$ are given in terms of the known matrices $a_k, ..., e_k$ by the formulae:

$$\begin{array}{lll} \gamma_1 = c_1 & \beta_2 = b_2 & \alpha_3 = a_3 \\ \delta_1 = \gamma_1^{-1} d_1 & \gamma_2 = c_2 - \beta_2 \delta_1 & \beta_3 = b_3 - \alpha_3 \delta_1 \\ \epsilon_1 = \gamma_1^{-1} e_1 & \delta_2 = \gamma_2^{-1}(d_2 - \beta_2 \epsilon_1) & \gamma_3 = c_3 - \alpha_3 \epsilon_1 - \beta_3 \delta_2 \\ \alpha_1 = \gamma_1^{-1} a_1 & \epsilon_2 = \gamma_2^{-1}(e_2 - \beta_2 \alpha_1) & \delta_3 = \gamma_3^{-1}(d_3 - \alpha_1 \alpha_3 - \beta_3 \epsilon_2) \\ \beta_1 = \gamma_1^{-1} b_1 & \alpha_2 = \gamma_2^{-1}(a_2 - \beta_1 \beta_2 & \epsilon_3 = \gamma_3^{-1}(e_3 - \alpha_3 \beta_1 - \beta_3 \alpha_2) \end{array}$$

$$\begin{array}{ll} \alpha_4 = a_4 & \alpha_k = a_k \\ \beta_4 = b_4 - \alpha_4 \delta_2 & \beta_k = b_k - \alpha_k \delta_{k-2} \\ \gamma_4 = c_4 - \alpha_4 \epsilon_2 - \beta_4 \delta_3 & \gamma_k = c_k - \alpha_k \epsilon_{k-2} - \beta_k \delta_{k-1} \\ \delta_4 = \gamma_4^{-1}(d_4 - \alpha_4 \alpha_2 - \beta_4 \epsilon_3) & \delta_k = \gamma_k^{-1}(d_k - \beta_k \epsilon_{k-1}) \\ \epsilon_4 = \gamma_4^{-1} e_4 & \epsilon_k = \gamma_k^{-1} e_k \end{array}$$

$$\begin{array}{l} \epsilon_{NP-1} = e_{NP-1} \\ \alpha_{NP-1} = a_{NP-1} - \epsilon_{NP-1} \delta_{NP-4} \\ \beta_{NP-1} = b_{NP-1} - \alpha_{NP-1} \delta_{NP-3} - \epsilon_{NP-1} \epsilon_{NP-4} \\ \gamma_{NP-1} = c_{NP-1} - \alpha_{NP-1} \epsilon_{NP-3} - \beta_{NP-1} \delta_{NP-2} \\ \delta_{NP-1} = \gamma_{NP-1}^{-1}(d_{NP-1} - \beta_{NP-1} \epsilon_{NP-2}) \\ \delta_{NP} = d_{NP} \\ \epsilon_{NP} = e_{NP} - \delta_{NP} \delta_{NP-4} \\ \alpha_{NP} = a_{NP} - \epsilon_{NP} \delta_{NP-3} - \epsilon_{NP-4} \delta_{NP} \\ \beta_{NP} = b_{NP} - \alpha_{NP} \delta_{NP-2} - \epsilon_{NP} \epsilon_{NP-3} \\ \gamma_{NP} = c_{NP} - \beta_{NP} \delta_{NP-1} - \alpha_{NP} \epsilon_{NP-2} \end{array}$$

Only the matrices $\gamma_1, ..., \gamma_{NP-1}$ must be inverted. Since these matrices are characteristicly very dense, a general purpose inversion routine is used to invert these elements (cf. Ref. [70] subroutines LUDCMP and LUBKSB). To obtain a complete solution to (.35), it was also necessary to invert γ_{NP}. The factorization

(.38) allows us to obtain such a complete solution directly. First an equation of the form (simply (.35) expressed in new notation)

$$\vec{\mathbf{J}}\hat{\underline{\varepsilon}} = -\hat{\underline{g}} \tag{.39}$$

where $\hat{\underline{\varepsilon}} \equiv (\underline{\varepsilon}_1, ..., \underline{\varepsilon}_{NP})^T$ and $\hat{\underline{g}} \equiv (\underline{g}_1, ..., \underline{g}_{NP})^T$, may be written

$$(\vec{\mathbf{L}}\vec{\mathbf{U}})\hat{\underline{\varepsilon}} = -\hat{\underline{g}} \tag{.40}$$

Then, we solve the system

$$\vec{\mathbf{L}}\hat{\underline{y}} = -\hat{\underline{g}}; \qquad \hat{\underline{y}} \equiv (\underline{y}_1, ..., \underline{y}_{NP})^T \tag{.41}$$

For the unknown vector $\hat{\underline{y}}$ directly using the forward substitution:

$$\begin{aligned}
&\underline{y}_1 = -\gamma_1^{-1}\underline{g}_1 \\
&\underline{y}_2 = -\gamma_2^{-1}(\underline{g}_2 + \beta_2\underline{y}_1) \\
&\underline{y}_k = -\gamma_k^{-1}(\underline{g}_k + \beta_k\underline{y}_{k-2} + \alpha_k\underline{y}_{k-1}) \,\big|_{k=3}^{k=NP-2} \\
&\underline{y}_{NP-1} = -\gamma_{NP-1}^{-1}(\underline{g}_{NP-1} + \beta_{NP-1}\underline{y}_{NP-2} + \alpha_{NP-1}\underline{y}_{NP-3} + \epsilon_{NP-1}\underline{y}_{NP-4}) \\
&\underline{y}_{NP} = -\gamma_{NP}^{-1}(\underline{g}_{NP} + \beta_{NP}\underline{y}_{NP-1} + \alpha_{NP}\underline{y}_{NP-2} + \epsilon_{NP}\underline{y}_{NP-3} + \delta_{NP}\underline{y}_{NP-4})
\end{aligned}$$

Finally, knowing $\hat{\underline{y}}$,we solve the system

$$\vec{\mathbf{U}}\hat{\underline{\varepsilon}} = -\hat{\underline{y}} \tag{.42}$$

for $\hat{\underline{\varepsilon}}$ using backward substitution. It is easy to see that $\hat{\underline{\varepsilon}}$ is given explicitly by

$$\begin{aligned}
&\underline{\varepsilon}_{NP} = \underline{y}_{NP} \\
&\underline{\varepsilon}_{NP-1} = \underline{y}_{NP-1} - \delta_{NP-1}\underline{\varepsilon}_{NP} \\
&\underline{\varepsilon}_k = \underline{y}_k - \delta_k\underline{\varepsilon}_{k+1} - \epsilon_k\underline{\varepsilon}_{k+2} \,\big|_{k=3}^{k=NP-2} \\
&\underline{\varepsilon}_2 = \underline{y}_2 - \delta_2\underline{\varepsilon}_3 - \epsilon_2\underline{\varepsilon}_4 - \alpha_2\underline{\varepsilon}_5 \\
&\underline{\varepsilon}_1 = \underline{y}_1 - \delta_1\underline{\varepsilon}_2 - \epsilon_1\underline{\varepsilon}_3 - \alpha_1\underline{\varepsilon}_4 - \beta_1\underline{\varepsilon}_5
\end{aligned}$$

This completes the solution of (.36)

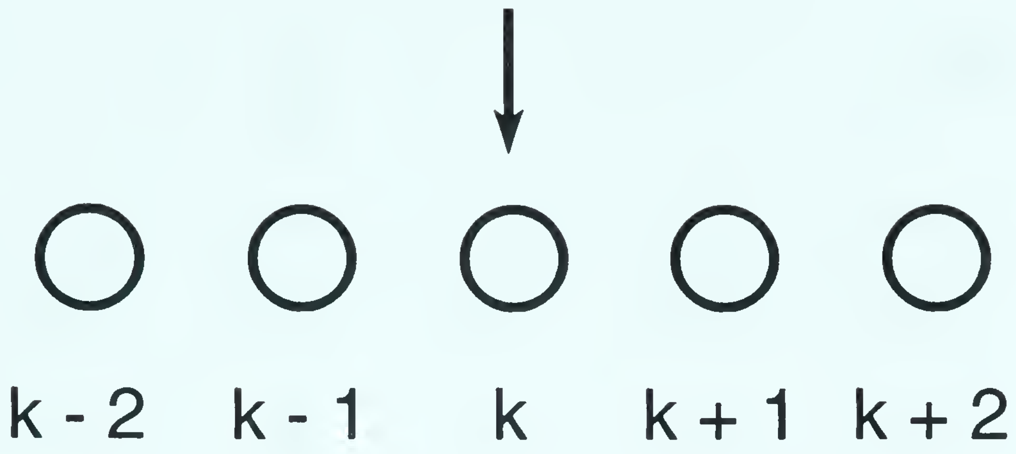

Figure .2: *Centered difference*

.2.3 Derivative differencing

Standard 4 and 5 point differencing formulas [107] are used to approximate first and second spatial derivatives.

$$\frac{\partial u_k}{\partial x} = D1(u_{k-2} - 8u_{k-1} + 8u_{k+1} - u_{k+2}) + O(\Delta x^4) \qquad (.43)$$

$$\frac{\partial^2 u_k}{\partial x^2} = D2(-u_{k-2} + 16u_{k-1} - 30u_k + 16u_{k+1} - u_{k+2}) + O(\Delta x^4) \qquad (.44)$$

$k \neq 1, 2, NP-1, NP$ The derivatives are centered evenly around the derivative point as in figure (.2)

The second and second last points have derivatives in the unsymmetric form of

$$\frac{\partial u_2}{\partial x} = D1(-4u_1 - 6u_2 + 12u_3 - 2u_4) + O(\Delta x^3) \qquad (.45)$$

$$\frac{\partial^2 u_2}{\partial x^2} = D2(11u_1 - 20u_2 + 6u_3 + 4u_4 - u_5) + O(\Delta x^3) \qquad (.46)$$

$$\frac{\partial u_{NP-1}}{\partial x} = D1(4u_{NP} + 6u_{NP-1} - 12u_{NP-2} + 2u_{NP-3}) + O(\Delta x^3) \qquad (.47)$$

$$\begin{aligned}\frac{\partial^2 u_{NP-1}}{\partial x^2} &= D2(11u_{NP} - 20u_{NP-1} + 6u_{NP-2} + 4u_{NP-3} - u_{NP-4}) \\ &+ O(\Delta x^3) \qquad (.48)\end{aligned}$$

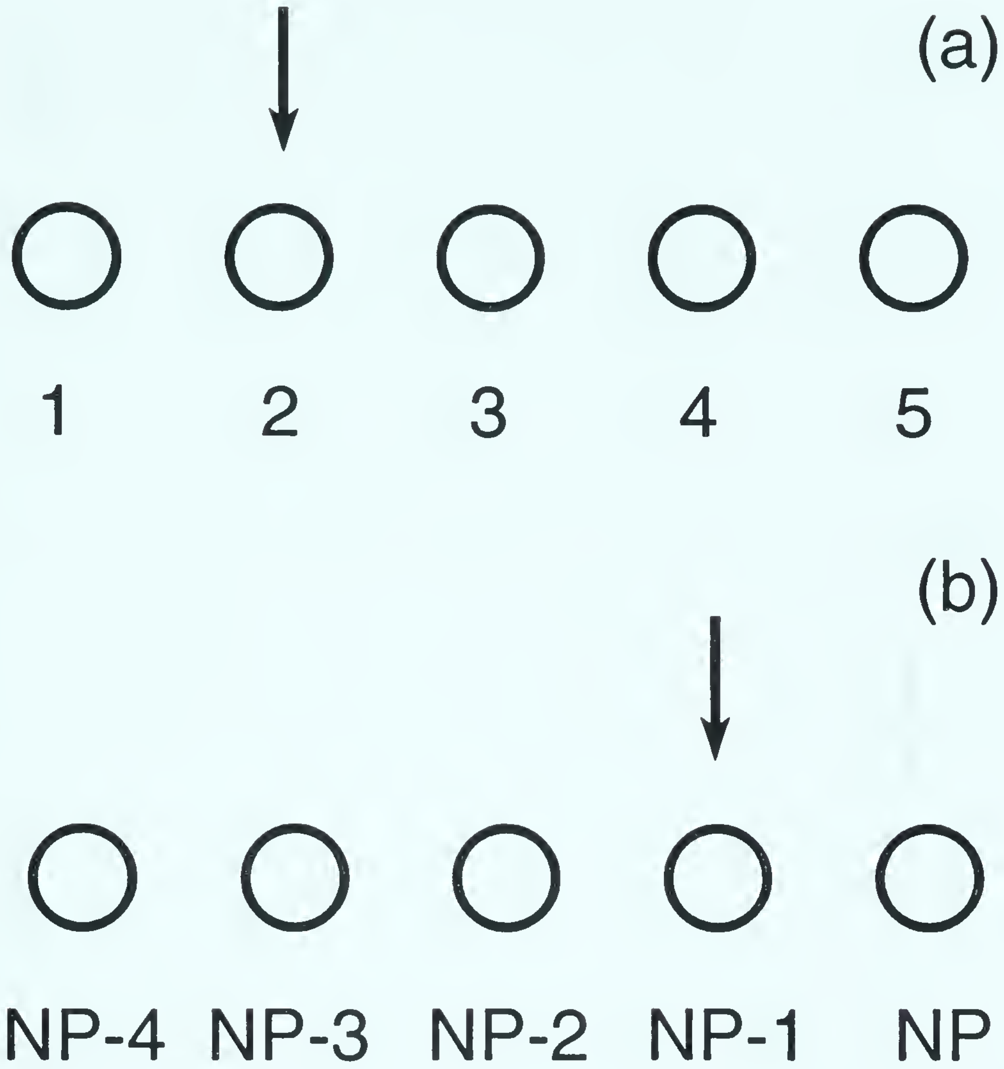

Figure .3: *Unsymmetric difference for points (a) n = 2 and (b) n = NP-1 respectively*

where figure (.3) gives the position of the derivative for the left and right side of the box

The boundary derivatives are also of an unsymmetric form given by

$$\begin{aligned}
\frac{\partial u_1}{\partial x} &= D1(-22u_1 + 36u_2 - 18u_3 + 4u_4) + O(\Delta x^3) && (.49)\\
\frac{\partial^2 u_1}{\partial x^2} &= D2(35u_1 - 10u_2 + 11u_3 - 56u_4 + 11u_5) + O(\Delta x^3) && (.50)\\
\frac{\partial u_{NP}}{\partial x} &= D1(22u_{NP} - 36u_{NP-1} + 18u_{NP-2} - 4u_{NP-3}) + O(\Delta x^3) && (.51)\\
\frac{\partial^2 u_{NP}}{\partial x^2} &= D2(35u_{NP} - 10u_{NP-1} + 11u_{NP-2} - 56u_{NP-3} + 11u_{NP-4})\\
&+ O(\Delta x^3) && (.52)
\end{aligned}$$

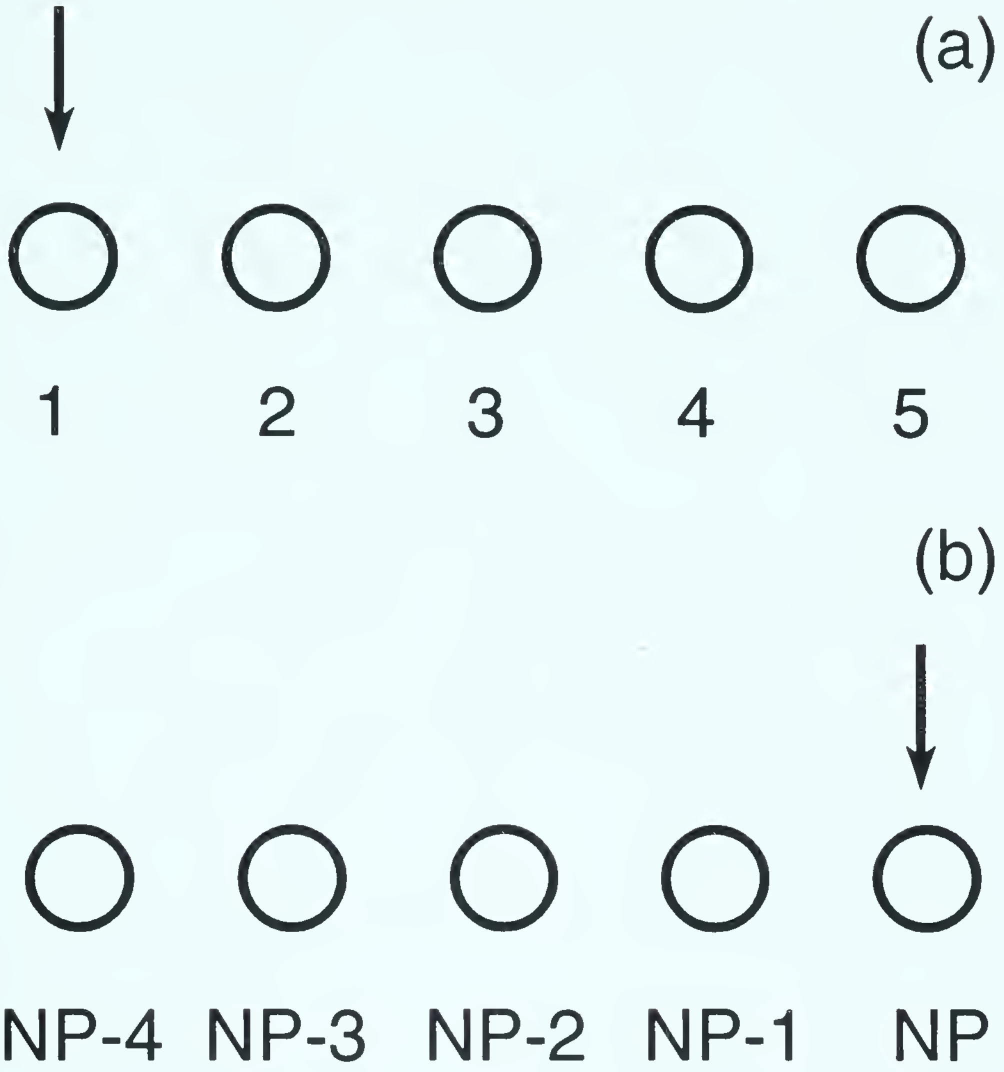

Figure .4: *Unsymmetric difference for boundary points (a)* $n = 1$*, and (b)* $n = NP$

where figure (.4) gives the position of the derivative for the left and right boundaries For all the derivative differences $D1 \equiv 1/12\Delta x$ and $D2 \equiv 1/12\Delta x^2$.

University of Alberta Library

0 1620 0110 6523

B44940